Astronomy Unit

School of Physics and Astronomy

Queen Mary, University of London

The Design and Construction of High-Resolution Spectrometers for Exoplanet Discovery and Characterisation

Clark Baker

Supervised by Guillem Anglada-Escudé and Richard Nelson

Submitted in partial fulfillment of the requirements of the Degree of Doctor of Philosophy

Declaration

I, Clark Baker, confirm that the research included within this thesis is my own work or that where it has been carried out in collaboration with, or supported by others, that this is duly acknowledged below and my contribution indicated. Previously published material is also acknowledged below.

I attest that I have exercised reasonable care to ensure that the work is original, and does not to the best of my knowledge break any UK law, infringe any third party's copyright or other Intellectual Property Right, or contain any confidential material.

I accept that the College has the right to use plagiarism detection software to check the electronic version of the thesis.

I confirm that this thesis has not been previously submitted for the award of a degree by this or any other university. The copyright of this thesis rests with the author and no quotation from it or information derived from it may be published without the prior written consent of the author.

replicable, low-cost, portable, general-purpose, high-resolution spectrometer with applications in stellar studies and exoplanet science", Proc. SPIE 11117, Techniques and Instrumentation for Detection of Exoplanets IX, 111171M (9 September 2019); https://doi.org/10.1117/12.2529290

Signature: Clark Baker
Date: 26/07/2020

Abstract

In this thesis, we discuss the design and construction of high-resolution spectrometers for exoplanet discovery and characterisation across the entire scope of project budgetary regimes. As with all aspects of astronomy, light and more specifically electromagnetic waves are our greatest key to unlocking the secrets of exoplanetary systems. The radial velocity method, in which analysis of the Doppler shift of star light can infer the existence and minimum mass of an exoplanetary system, relies wholly on the application of high-resolution, stable spectrometer systems. Alongside this, powerful spectroscopic techniques such as: transit and cross-correlation spectroscopy (used to probe the atmospheric characteristics of planets), the Rossiter–McLaughlin effect (which can infer spin-orbit characteristics of the planetary system) and reflected light analysis of a planet (that allow us to discover orbital characteristics and true mass of a planet) require field leading spectrometer design.

These investigative techniques alone more than warrant the existence of large, high-cost, ultra-stable, high-resolution spectrograph systems, such as HARPS, PFS, ESPRESSO e.t.c. However, with ever changing science goals, there is scope for a new kind of instrument. With growing discussion amongst the exoplanet community on the application of combined high contrast imaging and high dispersion spectroscopy in exoplanet science, there is a need for replicable, low-cost, stable, high-resolution spectrometer systems for integral field applications; which can be efficiently coupled to high contrast imagers.

This thesis presents the design and construction of such an instrument, with a proof of concept prototype spectrometer produced which is compact (comparable in size to a 3U CubeSat chassis), low-cost ($<£10,000$), highly-replicable (utilising mostly commercially-off-the-shelf components), stable (demonstrated RV precision of approximately 20m/s) and high-resolution (resolving power $> 60,000$).

Sub-systems for this instrument, a fibre coupling system and a data-reduction pipeline, are designed and constructed with the complete instrument successfully tested on-sky at the QMUL Astronomy Unit Observatory.

The design aspects of this system are further employed in the design study of a large-scale, high-budget, ultra-stable, red-NIR, high-resolution spectrometer concept: NEREA (Near Earths and high-Res Exoplanet Atmospheres). If funded, this instrument is to be efficiently coupled to The Gran Telescopio Canarias (GTC). The combination of the 10m aperture of the GTC and the high-resolution, stable spec-

troscopy of NEREA will open up opportunities to investigate exoplanetary systems which are currently unobtainable with contemporary instrumentation.

Finally, all of the experience gained through the completion of these projects is channelled into the construction of a 'Spectrometer Design Toolkit' software which aids in the rapid design of spectrograph concepts. This system is tested in the re-design of the collimating/re-focussing lens for EXOhSPEC (EXOplanet high resolution SPECtrograph), a compact, high-resolution spectrograph in development at the University of Hertfordshire for the Thai National Observatory (TNO).

Acknowledgements

Firstly, I would like to thank my supervisor, Guillem Anglada-Escudé. His support, patience and tutelage throughout these four years has been invaluable. The lessons he has taught me and opportunities he has provided will stay with me throughout the rest of my career.

I would like to give special thanks to Richard Nelson for his continued support of me and this project throughout. His efforts and encouragement have enabled us to achieve the results that are outlined in this thesis. Without his support, I am certain that this would not have been possible; I am very grateful.

I want to give a huge thanks to John Strachan for all of the time he freely and openly gave to aid me throughout the years. The concepts he helped me to understand, his guidance in navigating the life of a PhD student and the time he spent helping me prepare for post-doc interviews has helped me immensely; thank you.

Thank you to my collaborators at The University of Hertfordshire, Hugh Jones and Bill Martin, for their support, openness, teachings and shared resources; their contributions have been crucial to allow this project to take place. I hope that my contributions to future collaborations can begin to show my gratitude for this. I would also like to thank Piyamas Choochalerm and Ronny Errmann for their assistance over the years in remotely accessing the resources that I needed.

I would also like to give many thanks to my collaborators at the IAC, Enric Pallé, Roberto López López and José Luis Rasilla. Their great collaboration, teachings and discussion helped me to make substantial breakthroughs in my understanding of this topic and re-ignited my passion for this work. I want to give a special thanks to Enric Pallé for his continued advice, infectious enthusiasm and for writing me a very positive reference.

Thank you to Steve Thomas for his keenness and enthusiasm for my project throughout and his assistance in observatory matters.

When I was interviewed for this PhD position I was asked something to the effect of: "Are you sure you want to do this instrumentation project here, we are primarily a theory group" to which my answer was a resounding "Yes". I want to thank all of the Astronomy Unit staff that made this very out-of-the-ordinary PhD project possible and furthermore for fostering such a positive work environment. I have never known another group where everyone is as caring, friendly and open as the Astronomy Unit.

I would also like to take this opportunity to thank my examiners, Dr. Edward Gillen and Prof. John Girkin, for all of their efforts in assessing this thesis, their very helpful comments and suggestions, and for fostering a thoroughly enjoyable viva experience.

I would now like to thank those that kept me sane over the years. Firstly my

fellow PhD students, I would like to thank all of those who were my companions throughout this process - both those who have long since submitted and those that are still studying. You have been amazing, I couldn't imagine a better bunch of people!

I will now give some special mentions:

- Those that are collectively referred to as the "North Wing": Domenico Trotta, John Ronayne, Paul Hallam, Francesco Lovascio, John Strachan, Callum Boocock, Jesse Coburn, Sandy Zeng, Ali Barlas and George Turpin - with honorary mentions to Sanson Poon, Frini Taifakou and Rebeca Carrillo.

- My fellow 502 office mates: Charalambos 'Charlie' Pittordis, Pedro Carrilho, Shailee Imrith, Louis Coates, Eline de Weerd, Viraj Sanghai, Jessie Durk, Sophia Goldberg, Ahdab Althukair and Usman Gilani.

- My finishing-up-office mates: Jack Skinner, Jorge Fuentes, Kit Gallagher, Joanna Borowiec and Paul Miyagawa.

- The rest of the gang: Alice Giroul, Fraser Kennedy, George Montagnon, Paula Soares, Pedro Fernandes, Kevin Chan.

- The post-docs: Maritza Soto, Colin McNally, Gavin Coleman, Luca Franci and Julian Adamek.

Thank you all for making this the place that it is!

I would also like to take this opportunity to thank some of my closest friends:

- "Teem Azeem": Peter Shatwell, James Fernandes, Akash Jyoti, Rhea Mole, Serena Yuen, Emma Davies, Christian Storm, Aalisha Rahim and Liam Smith.

- My friends in Tenerife: Nushkia Chamba, Efşan Sökmen and James Angthopo.

I want to give my thanks to my A-level Physics teacher, Ian Roche, for igniting my passion for Physics and for all of the time after lessons he spent answering my endless questions. Following his teachings I was able to achieve more than I could have ever imagined.

Finally, and most of all, I would like to thank my parents, grandparents and siblings. Without their support, encouragement and inspiration, I wouldn't have been able to pursue any of this and most definitely wouldn't be where I am today.

Contents

<div align="center">Contents</div>

1 Introduction

1.1 Exoplanets, Motivation for their Study and Motivation for Compact Spectrometers

The big questions that motivate me are 'how did we come into being?' and furthermore, 'could others come about in the same way, are we really alone?'. I believe the study of other worlds will give us the best chance of beginning to answer these questions within my life-time.

Over the last few decades, the greater scientific community has come to realise that the universe is the best laboratory we have available to us. From particle physics to cosmology, we are beginning to see that the only feasible place where we can observe and re-create the extreme conditions of the universe is by observing them in the universe itself.

In order to begin to unravel my proposed questions, we must first understand the formation of planetary systems: from proto-planetary disks, to the formation of planetesimals and in-turn the formation of planets; and their migration to stable states. Then, we must understand the conditions on these planets as they evolve, their chemical make-up and atmospheric characteristics, and how their orbital parameters effect this. Only by filling in a 'planetary census' can we begin to understand what system layouts are possible and how common planets (and planetary systems) like our own really are. Furthermore, by observing these many snapshots in the evolution of planetary systems, we can bolster our understanding of their formation mechanisms.

Once the formation of planetary systems is understood, to answer the proposed questions fully we must then understand the origin of life. We must decipher the necessary mechanisms and conditions that are required for the formation of life and understand the criteria for how these conditions can be met on the surface of exoplanets. Studies such as the 'Universal Life Project' (Rimmer et al., 2018) suggest that for what is understood to be the necessary life-forming prebiotic chemistry to occur, the UV flux level on a planet's surface must be above a specific threshold. This

threshold intersects with the planetary habitable zone, the orbital distance where liquid water can exist on a planet's surface, for only a handful of planetary system types. The primary system which fulfils this criteria without the need for events of stellar activity is that of Earth-like, terrestrial planets orbiting around Sun-like stars. This suggests that systems of this type could be a key source of life formation in the universe. Hence, in order to study the origin of life and probe the universe for signs of life beyond our planet, we should be observing Earth/Sun-analogue systems.

This becomes an issue as with current instrumentation and observational techniques, using reflected light in the visible wavelength range as an example, we can only probe exoplanetary atmospheres for systems down to a planet-star flux ratio limit of 10^{-5}. Whilst this allows us to study short period hot-Jupiters around sun-like stars or close-in, rocky, terrestrial planets around M-dwarf stars (with typical contrast ratios down to around $10^{-4} - 10^{-5}$) (Cameron et al., 1999; Leigh et al., 2003; Brogi et al., 2012; Birkby et al., 2013b), this leaves the observation of Earth-like planets orbiting in the habitable zone of Sun-like stars out of reach; which have a flux ratio of approximately 10^{-10} (Traub & Oppenheimer, 2010; Martins et al., 2016).

As such, new approaches to instrumentation design and new observational methodologies must be investigated in order to reach these flux levels. One such technique, proposed by Snellen et al. (2015), couples high-resolution, stable spectrometers in the form of an IFS (integral field spectrometer) to a high-contrast imager. The high-contrast imager will inevitably leave behind some residual speckle from the stellar signal, which the spectrometers can disentangle from the planetary signal as they have a different wavelength dependence; due to their relative motion. High-contrast imagers alone are able to reach a planet-star flux level of 10^{-5} and high-dispersion spectroscopy can also reach a planet-star flux level of 10^{-5} alone. By combining these techniques and following the methodology outlined, it is theorised that one could reach a flux level of $10^{-5} \times 10^{-5} = 10^{-10}$; enough to observe and study Earth-analogue systems (Snellen et al., 2015).

In order to build such an instrument, one would need at least a 4×4 array of high-resolution, stable spectrometers; more than 16 in total. With current, mainstream design of such spectrographs, each of these 16 individual instruments would cost in the order of £1million and, with thermal and pressure control systems attached, would take up a form factor volume comparable in size to a car (Pepe et al., 2000; Crane et al., 2006; Pepe et al., 2010). For budgetary reasons alone, this leaves such a coupled instrument unfeasible. With this, an alternative approach to the design of such spectrographs must be taken. In this thesis, we discuss the design and

construction of a proof-of-concept, prototype, low-cost, compact, high-resolution spectrometer with comparable resolving power performance to its large scale counterparts but produced within a budget of only $\sim£10,000$ and within a form factor smaller than a 'shoe-box'.

The design philosophy and experience acquired in the development of the compact spectrometer system is further applied to the design of a spectrometer concept, NEREA, for the Gran Telescopio Canarias (GTC). If constructed, NEREA would aid in the completion of the planetary census of our stellar neighbourhood, as well as vastly increase the number of attainable planetary targets for atmospheric characterisation.

Finally, the culmination of the knowledge gained in the completion of this PhD is fed into the production of a 'Spectrometer Design Toolkit' software which models the spectrometer system's operating parameter for a given set of component specifications. This allows the rapid prototyping of high-resolution spectrometer systems which is demonstrated in a test-case of the re-design of EXOhSPEC, a compact spectrometer system for the Thai National Observatory (TNO).

Following the discussion of the motivation for this work here, the proceeding sections of this introduction chapter will work backwards from the exoplanet science being undertaken, to the ways we extract the data used for this science and the current state of the field. This will then lead into the following chapter which discusses the design principles of the instrumentation that makes these studies possible.

Now I will provide an outline on the current exoplanet detection and characterisation methods, culminating in a brief review of the exoplanet discoveries to date.

1.2 Exoplanet Discovery

Our perspective on the universe, and the place of our planet within it, changed in 1992 with the discovery of the first planet orbiting a star outside of our solar system (Wolszczan & Frail, 1992). Furthermore, this discovery perplexed scientists of the time as the two confirmed planets were found to be orbiting a pulsar; a rapidly rotating neutron star formed from the supernova of a massive main sequence star. Whilst the form of this stellar object led to questions about the formation mechanisms of the planetary system, the nature of the pulsar itself was crucial to this discovery. The technique which allowed these first exoplanets to be discovered was the pulsar timing method.

1.2.1 Pulsar Timing Method

Millisecond radio pulsars are old ($\sim 10^9 yr$), rapidly rotating neutron stars believed to be spun up by accretion of matter from their stellar companions. These pulsars emit a collimated beam of EM radiation from their magnetic poles, parallel to their dipole axis. If the star's rational axis and magnetic dipole axis are misaligned, the orientation of the EM beam will rotate. For radio telescope observations of a lone pulsar, this beam will appear as a regular periodic pulse. If a planet is orbiting the pulsar, the pulsar and planet will instead orbit around their barycentre; the centre of mass of the system of bodies. This alteration in the rotation of the pulsar will lead to slight variations in the timing between pulses. Combining this with models of the orbiting bodies and the known mass of the pulsar enables the calculation of the minimum mass and semi-major axis of the planet (Wolszczan & Frail, 1992). We are only able to calculate the minimum mass as this observation gives us no information on the inclination of the orbit of the planet; this concept is further seen in the radial velocity technique.

1.2.2 Radial Velocity Technique

The second groundbreaking discovery occurred just three years later, in 1995, with the detection of an exoplanet orbiting a sun-like star; 51 Pegasi (Mayor & Queloz, 1995). This planet was detected using the radial velocity technique; a technique first suggested by Struve (1952) in 1952. This method holds some similarity to the pulsar timing technique in its use of the barycentric motion of the host star to imply the existence of a planet. Essentially, as long as the orbital plane of the planet is not perfectly perpendicular to our line of sight, the orbit of the planet will induce some motion in the parent star parallel to our line of sight. As the star oscillates, the EM radiation it emits is Doppler shifted. As the star moves towards us, its light is blue-shifted and as it moves away, its light is red shifted. By measuring this Doppler shift we can calculate the radial velocity of the star,

$$\Delta v_{rad} = c \frac{\Delta \lambda}{\lambda}, \tag{1.1}$$

where c is the speed of light in a vacuum and $\Delta \lambda$ is the change in wavelength induced by the radial velocity Doppler shift for a given wavelength, λ. By taking many observations of the radial velocity of the star during its orbital motion, it is possible to fit an accurate curve to the radial velocity of the star against time (fitting for period, phase and amplitude), as described in figure 1.1. By applying
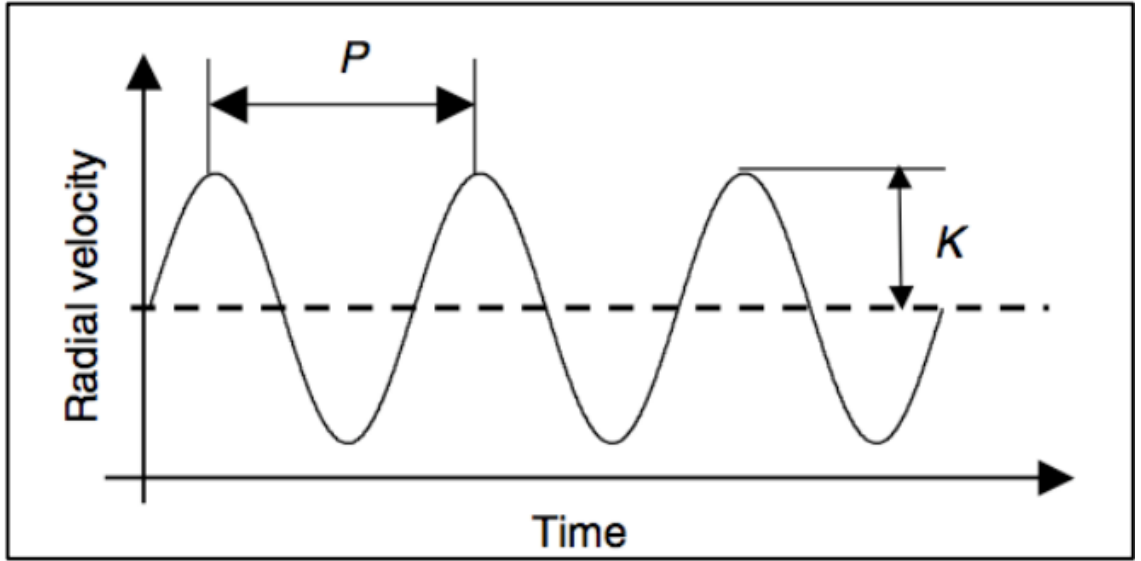
Figure 1.1: Plot of radial velocity against time for the host star indicating how the period, P, and radial velocity semi-amplitude, K, can be determined from the data (Zucker, 2007).

Kepler's third law of planetary motion and assuming that the mass of the star is much greater than that of the planet, an expression can be derived which relates the observable parameters of this technique:

$$K = \left(\frac{2\pi G}{P}\right)^{\frac{1}{3}} \frac{m_p \sin(i)}{M_*^{\frac{2}{3}}} \frac{1}{\sqrt{1 - e^2}} \,, \tag{1.2}$$

where K is the radial velocity semi-amplitude of the star's orbit, P is the orbital period, G is the gravitational constant, m_p is the mass of the planet, M_* is the mass of the star, i is the inclination of the orbit relative to the line of sight (as visualised in figure 1.2) and e is the eccentricity of the orbit. Using the period, P, radial velocity semi-amplitude, K, (found by fitting the radial velocity data) and the star's mass (estimated by colour temperature), it can be seen that equation 1.2 has three remaining free parameters: m_p, i and e. For many cases, especially for systems with a small period and semi-major axis (on the order of 0.1AU), which the radial velocity method is biased to better detect, one can ascertain a reasonably good fit to the radial velocity data by setting $e = 0$ (Kane et al., 2012). In order to attain an accurate eccentricity value for longer period systems, e can be determined by leaving it as a free parameter in the fit to the radial velocity curve. With all of these parameter values set, a value for $m_p \sin(i)$ can be calculated, obtaining a minimum mass value for the planet. As the radial velocity observation only gives us
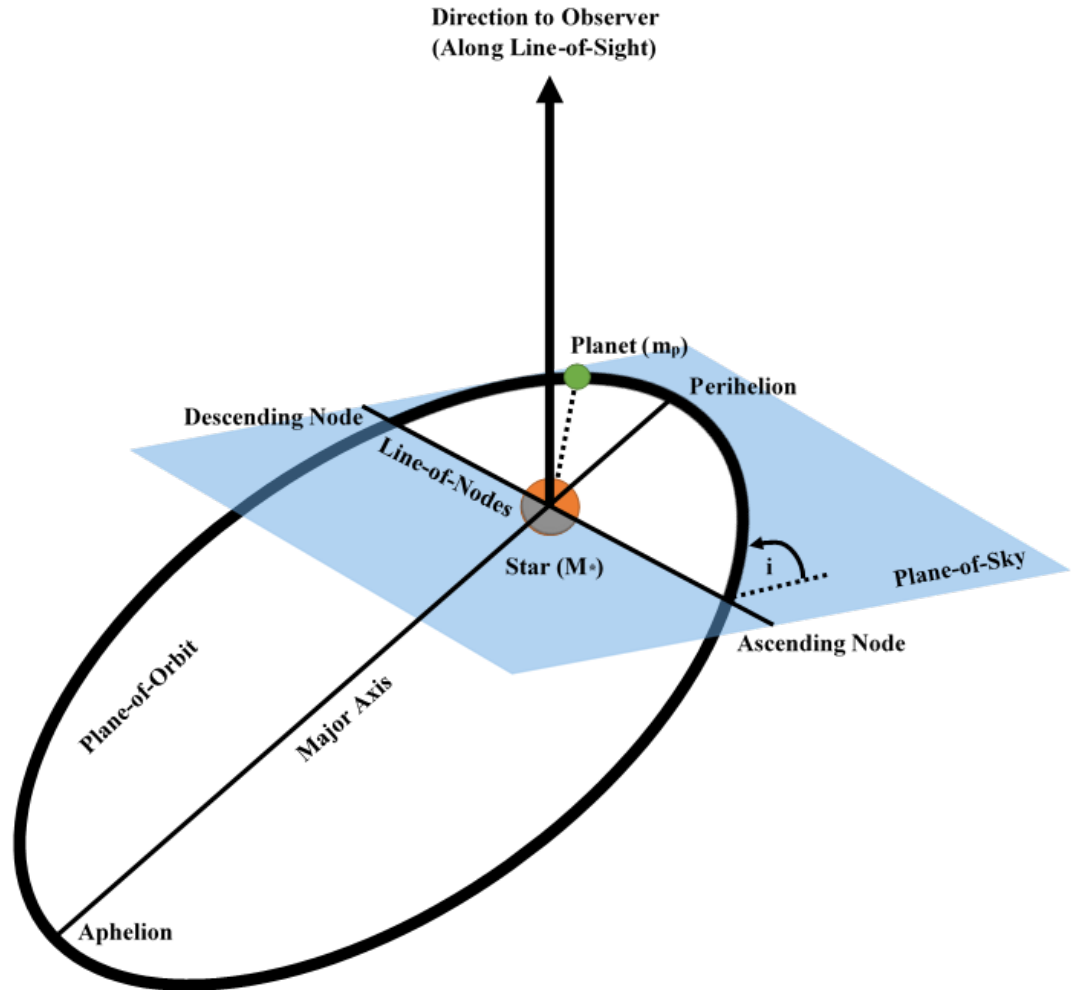
Figure 1.2: Diagram depicting orbital orientation, where i is the orbital inclination.
The ellipse shape of the orbit is dictated by the eccentricity (e) of the
planet's orbit. The ascending and descending nodes are the points in the
planet's orbit where it passes through the plane of the sky whilst moving
towards or away from the observer, respectively. Furthermore, the 'line
of nodes' is the intersection of the object's orbital plane with the plane
of the sky, passing through the ascending and descending node. The
perihelion is the point of closest approach of the orbit to the star and
the aphelion is the point at which the orbit strays furthest from the star.
The major axis is the length of the longest dimension of the elliptical
orbit.

radial velocity information in the line of sight, there is no way to determine system inclination with this technique alone. Hence, without further observation, such as a transit, there is no way to break the degeneracy between inclination and planetary mass; leaving sole application of the radial velocity technique unable to provide an accurate mass value.

1.2.3 Transit Photometry

The record for highest number of exoplanets discovered by a single mission, with a total of almost 2500 planets, is currently held by the Kepler mission. Kepler used the transit photometry technique which is well suited to large surveys (Borucki et al., 2010). This method was, again, first suggested by Struve (1952) in their 1952 paper.

The application of this technique requires the observed planet's orbit to be 'edge-on', such that it travels between the line of sight of the observer and the parent star. In this way, the planet blocks some of the stellar flux of the parent star. In short, as the planet travels in front of the star it will block an increasing amount of stellar flux until the entire planet's cross-sectional surface area is sat within the star's cross-section. For the duration of the transit, the stellar flux level (ignoring limb darkening, noise or other physical phenomena) will remain approximately constant until the star leaves the transit; where the observed stellar flux level will increase again. This is depicted in figure 1.3.

The depth of the reduction seen in stellar flux level on a transit light curve, ignoring limb darkening, is proportional to the ratio in cross-sectional area of the planet and the star,

$$\frac{\Delta F_*}{F_*} = \left(\frac{R_p}{R_*}\right)^2 , \tag{1.3}$$

where ΔF_* is the change in stellar flux at the deepest part of the transit, F_* is stellar flux outside of the transit, R_p is the radius of the planet and R_* is the radius of the star.

Unfortunately, as the geometric probability of a system to transit is given by R_*/a_p, where a_p is the semi-major orbital axis of the planet, transit photometry is biased to better detect close-in, large planets. Furthermore, assuming currently discovered systems to be representative of the whole planetary census, orbital geometry suggests that only 2% of exoplanetary systems are detectable by transit photometry (Borucki & Summers, 1984; Deeg & Alonso, 2018). Hence, while transit photometry is well suited to surveying large numbers of stars, its results cannot tell us the full picture.
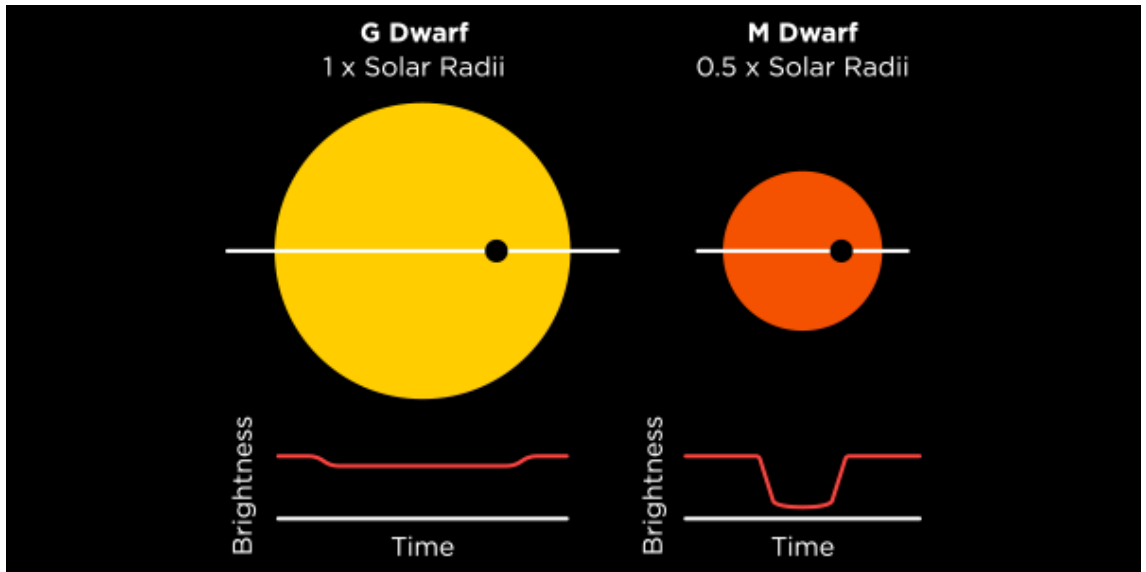
Figure 1.3: Image depicting transit light curve observation for a planet transiting a Sun-like star and the same planet transiting an M-dwarf star with half the radius of the Sun. The transit depth is larger for a larger star-planet radius ratio as described by equation 1.3 (Vanderburg, 2020).

For planets which a transit can be observed, this technique can give great insight into the characteristics of the planetary system. From photometric transit observations, using equation 1.3 and a priori knowledge of the star's radius, one is able to calculate the planet's effective radius in the wavelength band of the observation. By observing multiple transits (more than three), it is also possible to accurately measure the period of the exoplanet's orbit. Further to these measurements, by fitting an orbital model to the photometric light curve, an estimate of orbital inclination, transit impact parameter and semi-major axis can be obtained (Brown, 2009; Gillon et al., 2017).

For the 2% of transiting planets, through a combination of photometric observations with a radial velocity follow-up campaign, it is possible to break the degeneracy between planetary mass and inclination found in the application of the radial velocity technique alone; allowing accurate mass values to be obtained. Thereby, with an accurate mass and radius value found, planetary density can be calculated. This, amongst other things, gives insight into whether the planet is terrestrial or gaseous.

For multi-body systems, the orbit of the observed planet may be perturbed by another object. These perturbations will result in slight variations in the period of the orbit and also the length of the transit of the planet. The measurement and analysis of these variations is known as the transit timing variation technique (TTV). Through the fitting of models and the application of TTV, one can obtain

planetary mass estimates as well as an upper bound on orbital eccentricity (Agol et al., 2005; Holman & Murray, 2005).

Due to atmospheric extinction and scintillation, ground based photometric observations are limited to a precision of $\sim 0.1\%$. This limits ground based photometric campaigns, such as SPECULOOS and NGTS, to the observation of Jupiter-sized objects around sun-like stars or Earth-sized planets around M-dwarfs (with transit depths of 0.1% up to the order of a few percent), but this leaves Earth-like planets orbiting around Sun-like stars out of reach (which require transit precision at, and better than, 0.01%) (Burdanov et al., 2018; Wheatley et al., 2017). This issue is overcome through the use of space-based photometretry from missions like CoRoT, Kepler and TESS, which allow for higher photometric precision; only limited by instrument or stellar noise (Auvergne et al., 2009; Koch et al., 2004; Ricker et al., 2014).

1.2.4 Direct Imaging

The first exoplanet to be discovered by direct imaging occurred in 2004 and was later confirmed in 2005. It was a giant planet orbiting a brown-dwarf star; a system typical of those discoverable with direct imaging (Chauvin et al., 2004, 2005).

Direct imaging allows the planet's orbital parameters to be accurately measured. Furthermore, through the use of evolutionary models combined with a set of physical parameters, e.g. luminosity and age of planet, it is possible to infer a loose constraint on planetary mass. Similarly, estimates of the radius can be made from evolutionary models (Bowler, 2016).

This technique is arguably the simplest in theory but one of the most difficult in application due to technical limitations. Essentially, as the name suggests, direct imaging is the imaging of an exoplanet system such that the image of the star and image of the planet are independently resolvable.

The limit of resolvability of the planet and star occurs at the same point as any other imaged system, when the Rayleigh criterion is fulfilled. This occurs such that the peak of the planet's imaged point spread function (PSF) is at the first diffractive Airy minima of the star's PSF; as demonstrated in figure 1.4. The PSF describes the resultant imaging response of an optical system when imaging a point source; in this case, a star or planet can be considered a point source.

The direct imaging technique is limited due to a number of factors. Primarily, the flux ratio between the planet and the star. As mentioned in section 1.1, typical planet-star flux ratios can vary all the way from 10^{-4} down to 10^{-10} for Earth sized
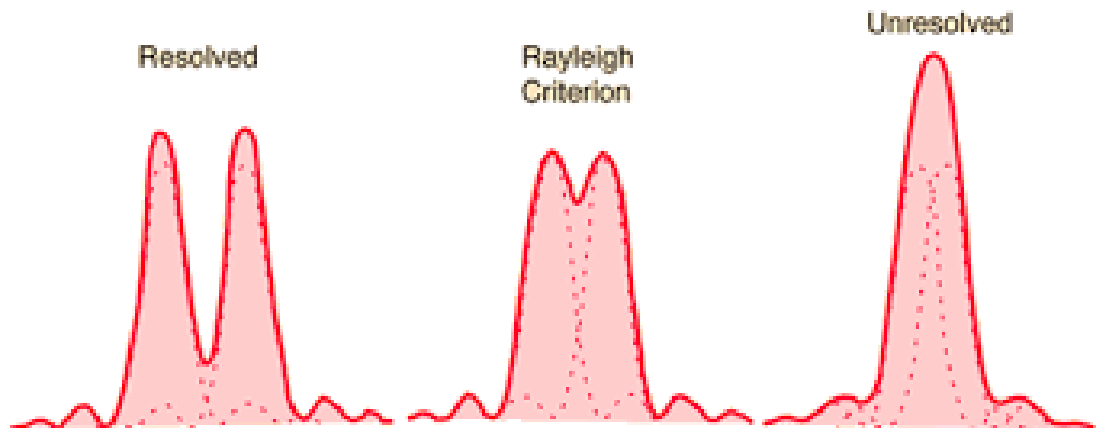
Figure 1.4: Graphical representation of two overlapping Airy functions demonstrating the resolved case, the case where the Rayleigh criteria is fulfilled and the unresolved case (Nave, 2016).

planets in optical and IR wavebands; depending on their star's characteristics and the planet's emissivity and reflectance. As such, the planet's imaged PSF amplitude is often much lower than even the Airy wings of the star's signal; as is demonstrated in figure 1.5. Therefore, this technique is much better suited to large planets orbiting far (on the order of $10AU$) from their dim host star. This way, a large planet will reflect a higher proportion of the star's light and its own thermal emission will be comparatively greater, leading to a more favourable planet-star flux ratio. The great spatial separation will increase the perceived angular separation of the image of the star and planet, leading to less stellar flux at the point in which the planet is imaged and ultimately resulting in a higher signal-to-noise image of the planet.

There are a number of ways to improve the planet-star contrast ratio in the image. The first technique we shall discuss is essentially a 'brute-force' method, achieving the best image resolution possible purely by maximising the quality of the optics. This is more or less a prerequisite for direct imaging, one must use a telescope with, or close to, diffraction limited performance (one where optical aberrations result in a spot size smaller than that imposed by diffraction through the physical aperture of the telescope, this shall be discussed further in section 2.0.5).

To achieve this, the telescope must be designed to minimise or cancel all optical aberrations. It must then be constructed to stringent tolerances in parameters such as mirror radius, conic constant, element separation, tip/tilt alignment and surface irregularity to ensure that the manufactured instrument performs as designed. With this in place, the star (which can be thought of as an ideal point source) when imaged with a diffraction limited 'ideal' telescope will produce a PSF which follows the Airy
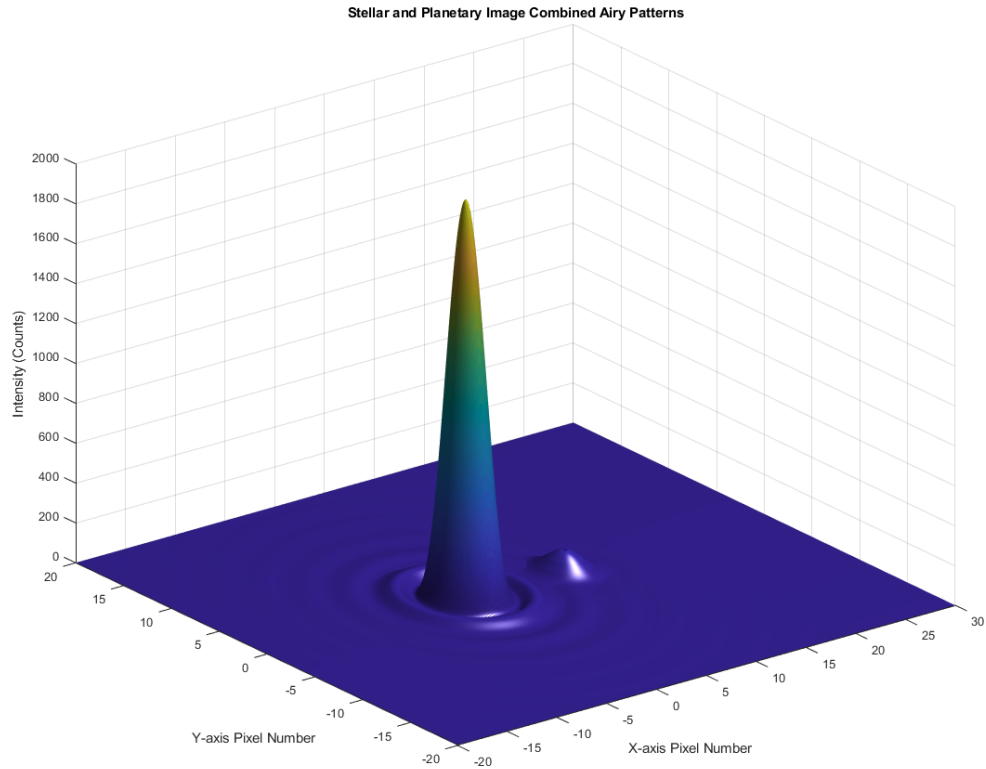
Figure 1.5: Simulated intensity plot for the image of a star and planet. The star and planet are imaged through an optical device with a perfect circular aperture, such that their diffraction pattern can be described by an Airy function. The star's image is demonstrated by the large, central Airy pattern. The planet's image is demonstrated by the smaller secondary Airy pattern, with its peak at the third minima of the stellar Airy pattern. This example is a resolved case and is exaggerated for demonstration purposes. For typical direct detection observations of real planetary systems, one would expect the planetary signal to be many orders of magnitude weaker relative to the stellar signal. The maxima of the two signals would also be closer, such that the higher intensity parts of the stellar Airy wings better conceal the planetary signal.

disk profile, as demonstrated in figure 1.5.

The Airy Disk

An Airy disk's first minima occurs following, $\sin\theta = 1.22\frac{\lambda}{D}$, where θ is the angular separation of the centre of the star's PSF and the first Airy minima, λ is the wavelength of the light and D is the diameter of the telescope. From this it can be seen that for a larger diameter telescope, the first Airy minima will be closer to the centre of the PSF. Therefore, the overall light intensity will be more tightly packed to the centre of the the star's PSF; leaving less light intensity in the Airy 'wings' and decreasing the amount of stellar signal overlaying the planetary signal. The same effect will occur for the planet's image, increasing the concentration of light at the centre of the PSF and increasing the signal strength. Therefore, a larger aperture telescope will lead to better image resolution.

Unfortunately, there is a limitation on the feasible manufacturable size of telescopes, due to budgetary requirements and the structural strength of current mounting materials. Current 'very-large' class telescopes have a diameter of, for example, 8.2m for a VLT primary mirror and 10.4m for the GTC. Notably, prior to the advent of adaptive optics, which we shall discuss subsequently, there was little gain in constructing telescopes with diameters larger than this, as atmospheric effects would dominate the diffraction limited performance. Upcoming 'extremely-large' class telescopes however will take measures to mitigate these atmospheric effects and therefore are constructed with much greater diameters; for example, the E-ELT will boast a total primary diameter of 39.3m. With these telescope aperture considerations in mind, a lower limit is set on the diffraction limited spot size achievable with these optics. For example, in order to resolve a $2K \times 2K$ pixel diffraction limited image of Earth around Proxima Centauri (our closest neighbour), one would require a telescope with the diameter of the Earth. Beyond this, for more distant systems, even with a telescope of such epic proportions, an observer would be lucky to produce a 10×10 pixel image of an Earth analogue. Hence, imaging exoplanets in detail is unfeasible; but resolving their PSF when considering the planet as a point source is possible.

Adaptive Optics

Another degradation in optical performance that occurs for ground based observations (where the largest aperture telescopes are available) comes from wave-front distortions introduced by turbulence of the atmosphere. This effect is known as
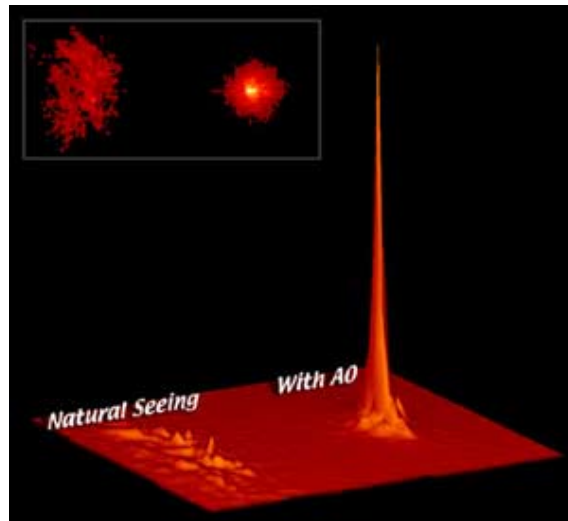
Figure 1.6: Image demonstrating the observed intensity of an imaged point source with natural seeing and then with adaptive optics enabled (Australian Telescope National Facility, 2018).

atmospheric seeing. The distortion causes different parts of the distorted wave-front to come to focus at different points on the telescope focal plane, leaving a speckle effect as depicted in figure 1.6.

To correct for this 'speckle', in 1953, Babcock (1953) proposed a system in which continuous measurement of the wave-front distortion could be coupled, via a feedback loop, to an adaptive element which could compensate for this distortion. This system would come to be possible in the 1990's with the advent of computer technology and go on to be known as 'adaptive optics'. The majority of contemporary adaptive optics systems loosely follow the the schematic layout shown in figure 1.7.

The light from the telescope focus is re-collimated and reflected off of the adaptive element (a deformable mirror in this case) and then passes through a dichroic element. The dischroic element will allow the required wavelengths to pass through to the camera to be observed, while wavelengths out of the region of interest will be reflected onto a wave-front sensor (such as a Shack-Hartmann wave-front sensor) for use by the AO system in calculating the required correction (Hartmann, 1900; Platt & Shack, 2001). The wave-front sensor measures the distortion of the wave-front and, through a closed feedback control loop, will alter the shape of the deformable mirror to correct for this wave-front distortion. This process must happen continuously and often at a rate greater than 20 times a second in order for the rapidly changing wave-fronts to be corrected as required.
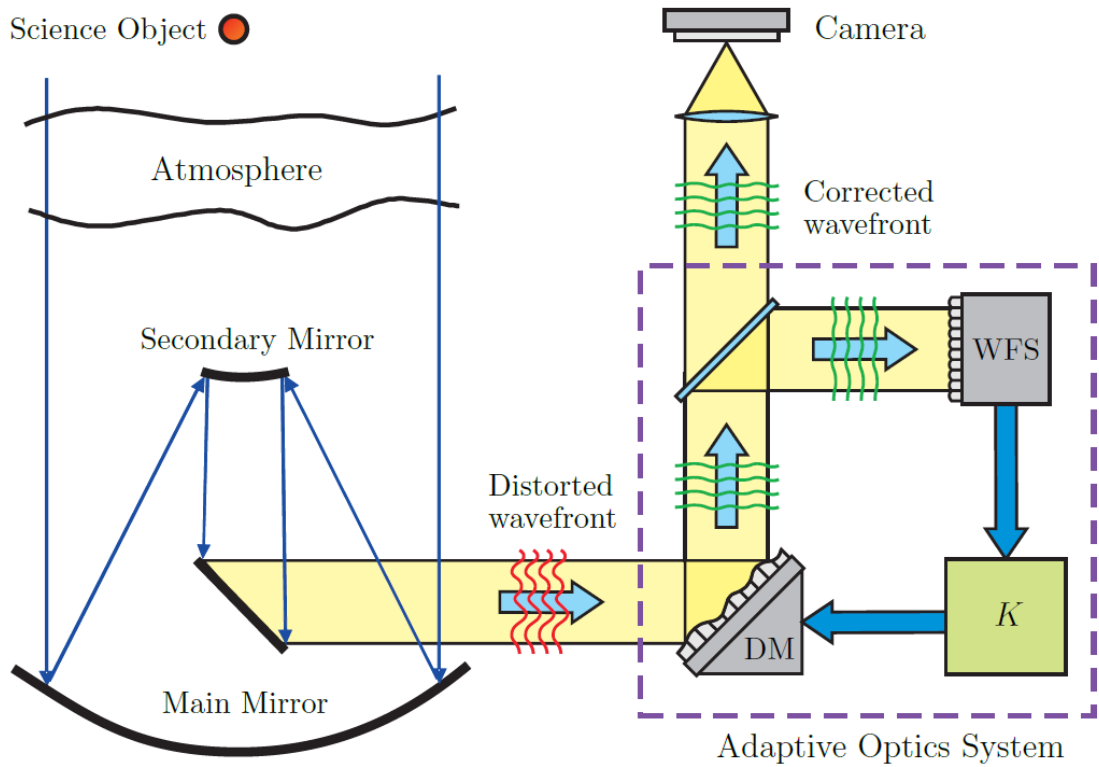
Figure 1.7: Schematic layout of an adaptive optics system. This diagram demonstrates the distortion of the wave-front by the atmosphere and subsequent correction by the adaptive optics system. Depicted here, the adaptive optics system consists of a wave-front sensor (WFS), a closed-loop feedback control system controller (K) and a deformable mirror (DM) (Lessard, 2011).

Light propagation direction

| Entrance pupil plane A | Focal plane B | Exit pupil plane C | Image plane D |

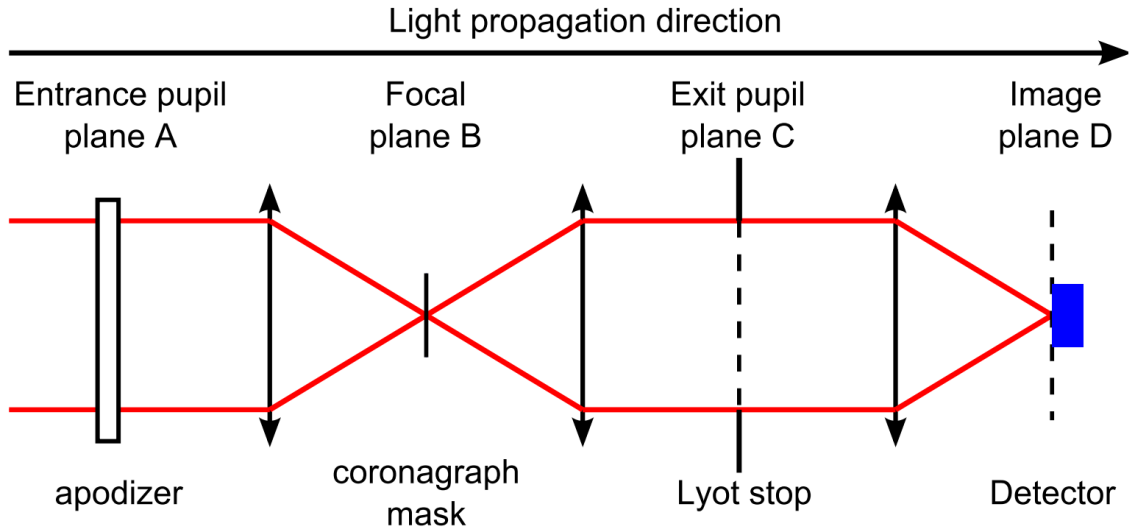apodizer

coronagraph mask

Lyot stop

Detector

Figure 1.8: Diagram of a classical Lyot coronagraph demonstrating the placement of the coronagraph mask at the focal plane and the placement of the Lyot stop at the exit pupil; in order to remove resultant light diffracted around the coronagraph mask (N'diaye et al., 2015).

Coronagraphs

With diffraction-limited optical performance attained, another option to improve the planet-star flux ratio is to remove the stellar flux. This is achieved using a device known as a coronagraph, which acts as an extreme angular filter; removing on-axis starlight and leaving behind the off-axis planetary image.

Coronagraphs have been in common use since their invention by Lyot in 1939 for solar corona observations (Lyot, 1939). A classical Lyot coronagraph, as seen in figure 1.8, places an opaque disk with a diameter of the order $\frac{\lambda}{D}$ at the focal plane of the telecope. This disk will block most of the starlight but due to its hard edges, some of the light will diffract around it. To remove this scattered light, another stop, known as a Lyot stop, is placed at the exit pupil of the optical system; as through the definition of the exit pupil, this is where the scattered light will come to focus.

This form of coronagraph can reduce stellar intensity by several orders of magnitude (Noll, 1973) and more sophisticated systems have been proposed which can theoretically remove the stellar intensity completely for an aberration free incoming stellar image (Foo et al., 2005).

Another form of coronagraph, known as a pupil plane coronagraph, places a phase plate in the pupil of the telescope. These phase plates are designed in such a way that they cause stellar light to interfere destructively at the focal plane of the system, leaving 'dark holes' where planets can be observed without stellar flux (Snik et al.,

2018).

With these advancements in coronagraph capabilities, direct imaging is becoming a strong candidate for future large scale exoplanet detection and characterisation campaigns. For example, NASA's decadal mission concepts LUVIOR and HabEx both have a strong emphasis on direct imaging (Pueyo et al., 2019; Martin et al., 2019).

1.2.5 Microlensing

The first detection of a planetary signal in a microlensing event occurred in 2004, with observations of OGLE 2003-BLG-235 (Bond et al., 2004). Whereby a 1.4 Jupiter mass object was discovered orbiting 3 AU from its host star.

When an observed star travels between a distant star and the line of sight of an observer, the mass of the foreground star and its associated bending of space-time can act as a lens. This distorts the path of light from the background star and produces a bright 'halo' around the foreground star. As discussed in section 1.2.4, this halo is not resolvable via imaging but it is observable through photometry. The increase in flux from the star seen in a microlensing event is detectable as a symmetric peak in the light curve.

If a planet is orbiting the foreground star, the planet will also microlens the distant star. This secondary microlensing event will introduce a further smaller peak to the lightcurve, as can be seen in figure 1.9.

Unlike other techniques, microlensing is a one-off event, so an observer must be 'lucky' to observe such an event for a star of interest. Microlensing allows us to calculate details about the planet-star mass ratio and the transverse distance between the star and the planet. Microlensing is currently our best technique for detecting distant Earth-like systems (Beaulieu et al., 2006).

1.2.6 Astrometry

The first confirmed planet discovery by astrometry occurred in 2010, with HD 176051 b, but attempts at discovering planets with this technique date back to the 1940's with further notable claims in the 1960's (Muterspaugh et al., 2010; van de Kamp, 1963).

As seen in other detection techniques, astrometry relies on the barycentric motion of the star-planet system. The technique measures the motion of the star on the sky-plane relative to some reference object. With this in mind, astrometry is
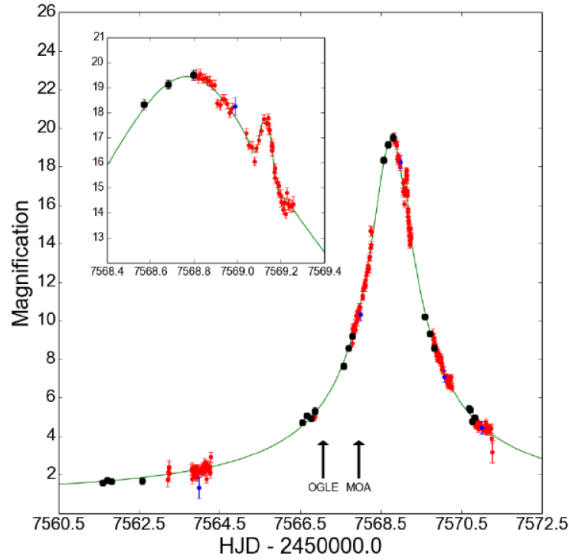
Figure 1.9: Lightcurve from microlensing event OGLE 2016–BLG–1195Lb. The symmetric peak for the foreground star microlensing event is clearly visible, with the secondary peak from the planetary microlensing signature shown in the insert. (Bond et al., 2017)

most applicable to face-on systems. From the measured barycentric motion, orbital parameters and the minimum mass of the planet can be inferred.

Currently, only a handful of planets have been detected with astrometry; far fewer than all of the other discussed techniques. This is expected to change with the 5 year data release from the Gaia space mission, where it is predicted that over 21,000 planets could be detected by astrometry (Perryman et al., 2014). However, as of writing, no new planets have been discovered through Gaia astrometry alone.

1.3 Exoplanet Characterisation with High-Resolution, Stable Spectroscopy

Beyond the detection of planets and their basic characteristics examined in section 1.2, we can use high resolution, stable spectroscopy and applications of the radial velocity method to give greater insight into the atmospheric characteristics and physical phenomena associated with exoplanetary systems. We shall discuss a few examples of this here.

1.3.1 Measurement of High-Precision Radial Velocities from High-Resolution Spectroscopy

In order to conduct any form of Doppler analysis of spectral data, the radial velocities of the objects of interest must first be extracted. As discussed in section 1.2.2, the calculation of radial velocities from spectroscopy is a relative measurement. The change in radial velocity is measured through the spatial shift of the centre of the spectral lines between your observed spectrum and some reference spectra, measured on the detector of the spectrograph. This spatial shift is due to the change in the wavelength of the spectra induced by the Doppler effect and, as the spectrograph is wavelength calibrated, this spatial shift can be measured as the change in wavelength of the spectra. Following equation 1.1, it is then possible to convert this change in wavelength induced by the Doppler shift into a radial velocity measurement (in m/s).

Early attempts to reach a radial velocity precision on the order of $10m/s$ used the Earth's telluric absorption lines as the reference measurement (Griffin, 1973). In short, as the exoplanet orbits its parent star and the star moves in its barycentric orbit, the Doppler shift of the starlight will be observed on the spectroscope as the movement of the spectral lines. As the spectrograph is ground based, the starlight will pass through the Earth's atmosphere and telluric absorbtion features will be introduced into the spectrum; primarily from water and oxygen. As the spectrograph is moving with the Earth, the Earth's telluric lines will have no Doppler shift, leaving them effectively static on the spectrometer's detector. Hence, one can measure the extent of the star's Doppler shift by observing the shift of the starlight's spectral features relative to the static telluric lines. Unfortunately, through the use of telluric lines as a reference alone, a precision greater than $\sim 10m/s$ cannot be reached due to the lack of wide-range spectral coverage of the telluric lines and their innate variability.

To overcome these issues an absorption cell can be applied. These cells are placed in front of the spectrograph's slit and are filled with a gas with a greater absorption line coverage across the waveband of interest than the Earth's telluric lines. These cells also exhibit substantially less variability than atmospheric telluric lines. Following the trial of multiple gases for this application, the community came to a consensus on the use of Iodine; for its large wavelength coverage, sharp lines and safety of operation. Given this, this method is commonly referred to as the 'Iodine Cell Technique' (Marcy & Butler, 1992). With this technique, radial velocity measurements at a precision of $\sim 1m/s$ can be achieved. One of the advantages

of this technique is that as the reference/calibration spectrum is superimposed into the science spectrum, the calibration spectrum passes through the same parts of the instrument and is imaged on the same pixels as the science spectra. This means that the instrumental profile and instrumental shifts are well characterised for the science spectra, increasing the accuracy of the calibration and negating the need for the spectrograph to be stabilised. A disadvantage of this technique is also that the reference/calibration spectrum is superimposed into the science spectrum. Similarly to the telluric absorption lines, regions where there are many absorption lines from the cell may leave the science spectra 'contaminated' and unusable. This technique is also computationally expensive but is still in common application at instruments such as the Coudé Echelle Spectrograph at the Karl Schwarzschild Observatory (TLS Tautenburg, 2020).

An alternative technique, which has become prevalent in the field of exoplanet science, is the 'Simultaneous Reference Technique'. To reach high radial velocity precision, this method relies on an ultra-stable spectrograph and the use of a separate calibration source; such a a Thorium Argon emission lamp, Fabry–Pérot Etalon or a laser frequency comb. Typically, these spectrometers will be fibre-fed and have two fibre inputs on the object plane; one for science and the other for calibration. The instrument is commonly kept stable using a vacuum chamber, to mitigate pressure variations, and a temperature control system, to reduce temperature variations. ESPRESSO is a very good example of this, utilising stacked enclosures to achieve an instrument temperature stabilised to $0.001K$ and pressure stabilised below $5 \times 10^{-3} mbar$ (Mégevand et al., 2014). To further increase stability, the optical fibres are mode scrambled. All of these measures ensure that the instrument profile is stable and will only vary minimally and in a smooth, continuous way.

To measure any of the small variations that may arise over the period of observation, wavelength calibration is periodically undertaken using calibration frames (implementing the sources discussed) to characterise any velocity shift that the instrument may introduce.

Early methods to extract high-precision radial velocities from stellar spectra using the simultaneous reference technique involved the cross-correlation of the spectra with a binary mask (Baranne et al., 1979). This binary mask is a model of the stellar spectrum for the type of star under investigation. The mask has emission lines of constant amplitude at the centre of the stars absorption lines and is zero everywhere else. This method was later improved by Pepe et al. (2002) through the use of stellar masks with line amplitudes corresponding to the stellar absorption line depths. This allowed a radial velocity precision on the order of $\sim 1 m/s$ to be

achieved through the simultaneous reference technique.

The method of construction of the cross-correlation function (CCF) through the use of cross-correlation can be seen in figure 1.10.

The resultant CCF will have a profile comparable to a single spectral line but will have a signal-to-noise ratio (SNR) that is stronger than the stellar spectrum by a factor of $\sqrt{n}$, where n is the number of spectral lines identified in the mask (Baranne et al., 1996; Martins et al., 2013). This allows analysis to be undertaken on the spectral lines profile that would otherwise not be possible due to low SNRs. To calculate the radial velocity from the CCF, the CCF's centroid is found by fitting a Gaussian; this allows sub-pixel precision in the calculation of the off-set of the CCF's peak relative to the reference spectra. In essence, the shift of the CCF's peak gives the radial velocity value.

Further work on the extraction of radial velocities has lead to more refined methods, such as the differential method exhibited in HARPS-TERRA by Anglada-Escudé & Butler (2012), the analysis of the RV of individual lines demonstrated by Dumusque (2018) or the use of Gaussian processes to model and align pairs of spectra with each other, outlined by Rajpaul et al. (2020).

Instruments like ESPRESSO have demonstrated that through the use of the simultaneous reference technique, radial velocities with a precision of the order of $10cm/s$ can be achieved (Pepe et al., 2014a). It is exceedingly important at these levels of precision that measures are taken to mitigate noise from sources such as stellar activity.

This stellar activity can be broken down into a number of sources and we will briefly discuss some examples of these here. Convection in the star can excite pressure waves, known as P-modes, which can collectively introduce RV errors of up to several m/s. These P-mode signals can be averaged out by integrating over more than 1-2 oscillation periods, usually equating to exposures of 15 minutes. Furthermore, convection in the form of granulation is seen to introduce an average RV signal on the order of a m/s and occurs over time scales of 10 minutes to a day; this signal can be mitigated somewhat by binning several observations. Magnetic activity of the star will lead to star spots and plages on the stellar surface. Their irregular coverage over the blueshifted and the redshifted parts of the stellar disk as it rotates will lead to changes in the shape of the spectral lines and introduce modulations in the measured radial velocities over the time-scale of the stellar rotation period. Around young stars, RV variations of $10 - 100m/s$ can be introduced by stellar activity, hence it is extremely important to find ways to reduce this. Fortunately, dense sampling, averaging and binning of the data over timescales similar to the
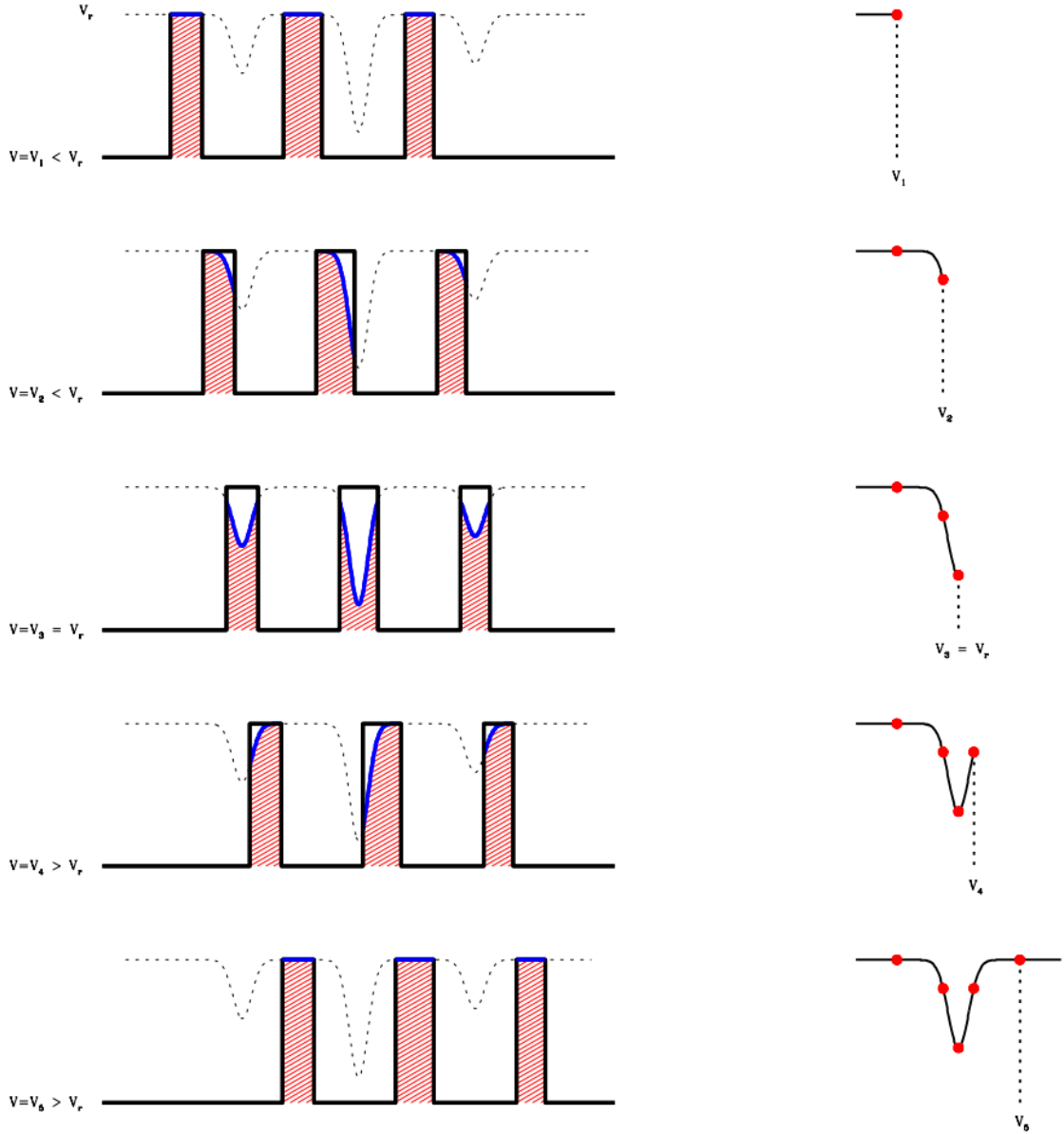
Figure 1.10: Illustration of the construction of the cross-correlation function. Diagrams on the left represent the stellar spectrum (dashed lines) and the binary mask (solid lines). The graphs on the right show the result of the cross-correlation process (Eggenberger & Udry, 2010).

stellar rotation period can allow RV surveys to reach precisions lower than $1m/s$ (Lovis & Fischer, 2010).

With processes in place to extract radial velocities from the spectral data, it is now possible to apply them in the analysis of exoplanetary system features. One such phenomena which is examinable with radial velocity data is the Rossiter–McLaughlin effect.

1.3.2 Rossiter–McLaughlin Effect

The Rossiter–McLaughlin effect was first observed for an eclipsing binary system, Beta Lyrae, in 1924 (Rossiter, 1924; McLaughlin, 1924). The first detection of this effect for an exoplanetary system, around the star HD209458, took place in the year 2000 (Queloz et al., 2000).

The Rossiter–McLaughlin effect is a spectroscopic phenomena observable for transiting exoplanets. As the parent star rotates on its axis, half of the star's face will be rotating towards the observer and as such experience a blue-shift. The other half of the face will be moving away from the observer and experience a red-shift. Without a transiting planet, these shifts would be observed as a broadening of the star's spectral lines; known as rotational broadening. When the planet transits the star, it blocks part of the stellar face, preventing some of this shifted light from reaching the observer. This alters the overall observed mean red-shift of the star, causing it to vary from its out-of-transit value. Additionally this also leads to a change in the shape of the stellar spectral lines, as depicted in figure 1.11.

As long as the star's rotation axis and the planet's orbital axis aren't perpendicular, as the planet transits across the star it will switch from blocking red- or blue-shifted parts of the stellar face, leading to a change in sign of the observed mean stellar red-shift value; as demonstrated in figure 1.12.

The Rossiter–McLaughlin effect provides information on the spin-orbit alignment of the exoplanetary system; more specifically, information on the projected angle between the planetary orbit axis and the stellar spin axis, Λ, and the projected stellar spin velocity, $V \sin I_*$, where I_* is the angle between the stellar rotational axis and the line of sight to the observer (Ohta et al., 2005).

The Rossiter–McLaughlin effect is a powerful tool in the characterisation of exoplanetary systems and has a number of broader applications, such as the recent use of an anomaly in the Rossiter–McLaughlin effect to aid in the detection of iron condensation on the night side of tidally locked WASP-76b (Ehrenreich et al., 2020).
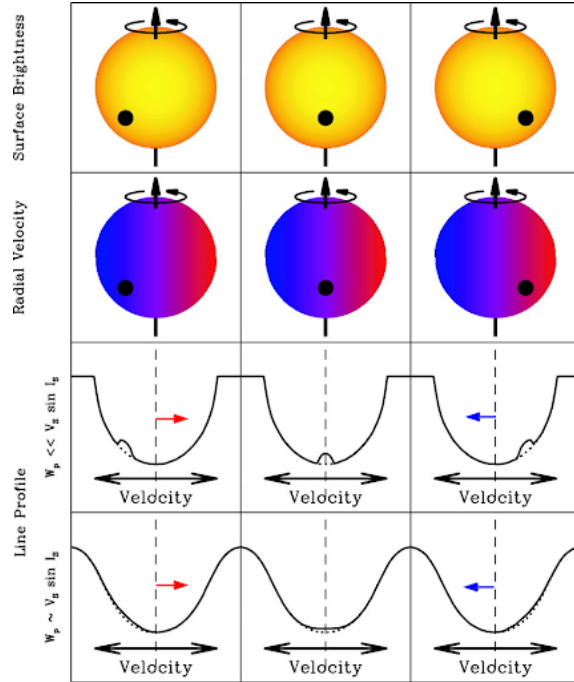
Figure 1.11: Diagram depicting the effect of the Rossiter-McLaughlin effect on the shape of the line profile for both the rotational broadening dominated case (upper panel) and the non-rotational broadening dominated case (lower panel) (Gaudi & Winn, 2007).
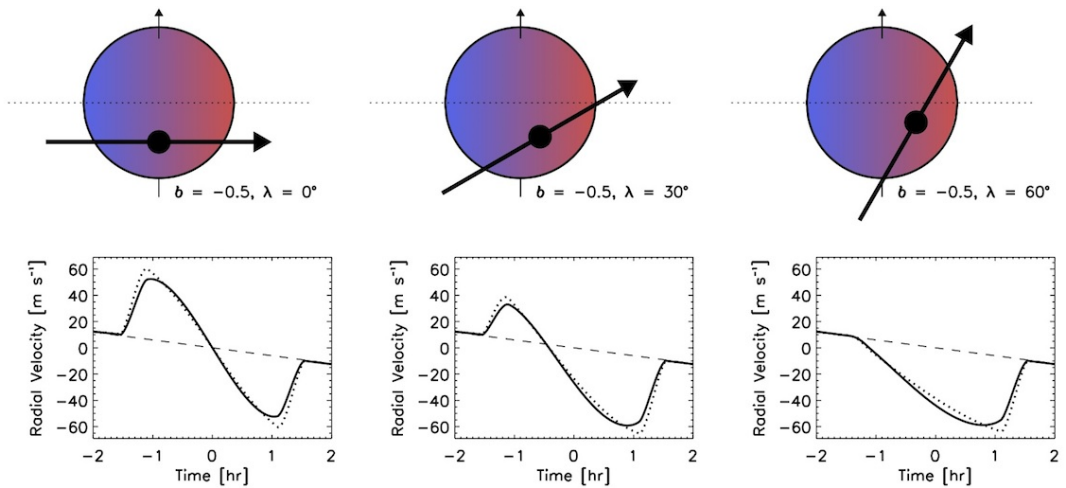

Figure 1.12: Diagram depicting how the Rossiter-McLaughlin effect alters the mean radial velocity measurement of the star for three different spin-orbit scenarios (Addison, 2016).

1.3.3 Transmission Spectroscopy

When a planet with an atmosphere transits its star, some of the starlight will pass through the planet's atmosphere. During this process the atmosphere will absorb certain wavelengths of stellar emission dependent upon the atmosphere's chemical composition. By analysing this absorption, we can determine the composition and characteristics of the atmosphere.

Currently, the most ubiquitous form of transmission spectroscopy is undertaken in the low-resolution regime. Using filters, photometric observations are binned into different wavebands. A heavily absorbing waveband of the atmosphere will block more light and give a deeper transit depth than a more transparent waveband. Hence, by measuring the stellar flux, one can reconstruct the planetary atmospheric absorption spectrum (Kreidberg, 2017). Observations of this form are best undertaken from space-based instruments, where telluric absorption features from the Earth's own atmosphere can be avoided. One such instrument is the Hubble space telescope's WF3, which operates in the near-IR ($1.1 - 1.7\mu m$).

Clouds on planets can be detected and in some circumstances are a dominating factor in transmission spectroscopy observations. They block light from travelling through the atmosphere below them, flattening out the spectra at longer wavelengths, leaving a featureless spectrum (Seager, 2014).

The majority of ground-based, high-resolution spectroscopy studies focus on detecting the day-side thermal emission of planets, but a number of studies also observe the planet during its transit; highlighting that traditional transmission spectroscopy is also possible in the high-resolution regime (Birkby, 2018). Recent studies have shown that high-resolution transmission spectroscopy, through the use of the cross-correlation technique, is capable of detecting sodium, potassium and water absorption features in low-mass planetary atmospheres (Deibert et al., 2019). Thus, with the promise of the upcoming 40m class telescopes, characterisation of exoplanet atmospheres during transits using high-resolution spectroscopy is a growing and promising field.

1.3.4 Occultation Spectroscopy

There are other sources of light that we can use to analyse the planetary atmospheric spectrum. Two of these are thermal emission by the planet and reflected starlight from the planet (which is at maximal flux just before and just after the secondary eclipse).
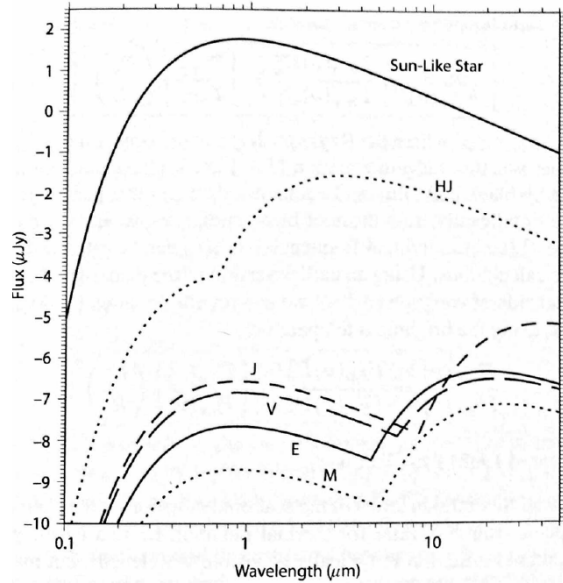
Figure 1.13: Plot of stellar and planetary flux. The planets exhibit a double peak, the shorter wavelength peak is from reflected starlight and as such exhibits the same wavelength dependence as the stellar flux, while the longer wavelength peak is from planetary thermal emission (Seager, 2010).

Thermal Emission

The majority of exoplanets studied via thermal emission are those with a short period; such that their dominant thermal emission source is re-emission of absorbed stellar flux. With this in mind, their emission signal can be predicted from the planet's equilibrium temperature. As the planet is substantially cooler than the star, through Wien's displacement law, we see that the peak planet-star flux ratio is seen at longer wavelengths, typically in the near-IR; as demonstrated in figure 1.13.

The emitted light originates from the planet's photosphere, thus the observed component must travel through the rest of the planetary atmosphere to reach the observer, leaving spectral absorption features. The size and shape of spectral features depend on the temperature-pressure profile of the atmosphere. Due to this, if the temperature increases with altitude (known as a thermal inversion) spectral features can be seen in emission rather than absorption. Thermal emission spectroscopy is therefore a useful probe of temperature structure in addition to atmospheric composition (Kreidberg, 2017).

As the planet orbits, its radial velocity will vary substantially more than, and differently to, its parent star. Thus, through the use of high-resolution, stable

spectroscopy and cross-correlation with model spectra allows the planet's thermal spectra to be decoupled from the stellar spectrum. CRIRES, a $R \sim 100,000$, NIR-IR spectrograph at the VLT was designed for this purpose (Birkby, 2018; Wiedemann, 2000). One such observation using CRIRES detected a water signature on 51 Peg b (Birkby et al., 2017).

Reflected Light

As the planet orbits its parent star, it will reflect and scatter the starlight. This occurs in phases, similar to that of the moon, whereby minimum flux is reflected to the observer when the planet's night side is facing us and maximal flux when the planet's dayside is facing us. For transiting planets this is just before or after it's secondary transit, where the planet is out of occlusion.

In a similar manner to thermal emission spectra, after removal of Earth's telluric absorbtion features, the reflected planetary signal can be decoupled from the stellar light using the difference in their radial velocity. By cross-correlation with a model stellar spectra it is possible to remove the stellar signal, leaving the planetary spectra only.

With a succesful reflected light detection, one can accurately measure the radial velocity semi-amplitude of the planet's orbit and hence attain an accurate planetary mass value. This further allows the deduction of planetary orbital inclination. With high signal to noise observations, it is also possible to constrain the albedo of the planet. In 2015, Martins et al. (2015) successfully measured a reflected light signal from 51 Peg b. With this first observation, the study of reflected light with high-resolution spectroscopy has become a fast growing and exciting research field.

One of the ultimate aims of atmospheric characterisation techniques like these is the successful detection of biosignatures; indicators for life. These include the detection of spectral features that stipulate the presence of oxygen, water, carbon dioxide, methane and ozone on the planet's surface. Essentially, we are looking for features that suggest an Earth-like, habitable atmosphere. Another such phenomena which could allude to this is a Rayleigh scattering slope (Pallé et al., 2009). Currently, no planet has been detected exhibiting a significant number of these features but with the upcoming E-ELT HIRES and JWST, it is promising that the higher accuracy and signal-to-noise ratios achievable with these instruments will allow a planet with an Earth-like atmosphere to be detected in the next decade.
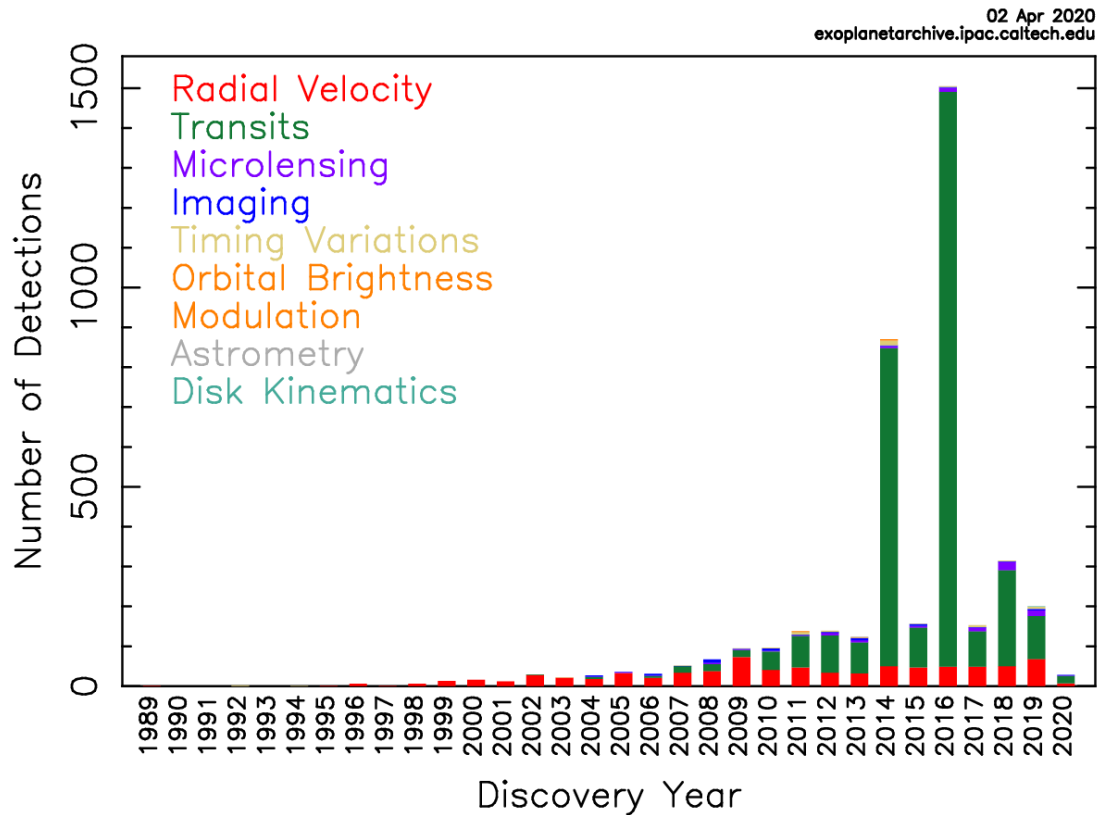
Detections Per Year

Figure 1.14: Stacked histogram displaying the distribution of the number of exoplanets discovered against year of discovery. This figure was produced using data from the NASA Exoplanet Archive (NASA Exoplanet Science Institute, 2020).

1.4 Current State of the Field

1.4.1 Exoplanet Census

As of the time of writing, using data from 'The Extrasolar Planet Encyclopedia', it can be seen that over 4100 validated exoplanets have been discovered (Roques, 2020). The timeline of these discoveries is displayed in figure 1.14. The effect of Kepler's operation (2009-2013) on the number of planets discovered by transit photometry is clear to see; it is hopeful that TESS, as well as ground based observational programs such as NGTS and SPECULOOS, will further increase this number substantially.

The mass-period relation of the planets with available mass data out of the 4100 detected can be seen in figure 1.15. The planets are broken up into five classifications dependent upon their properties; including where they sit on this graph.

These are:
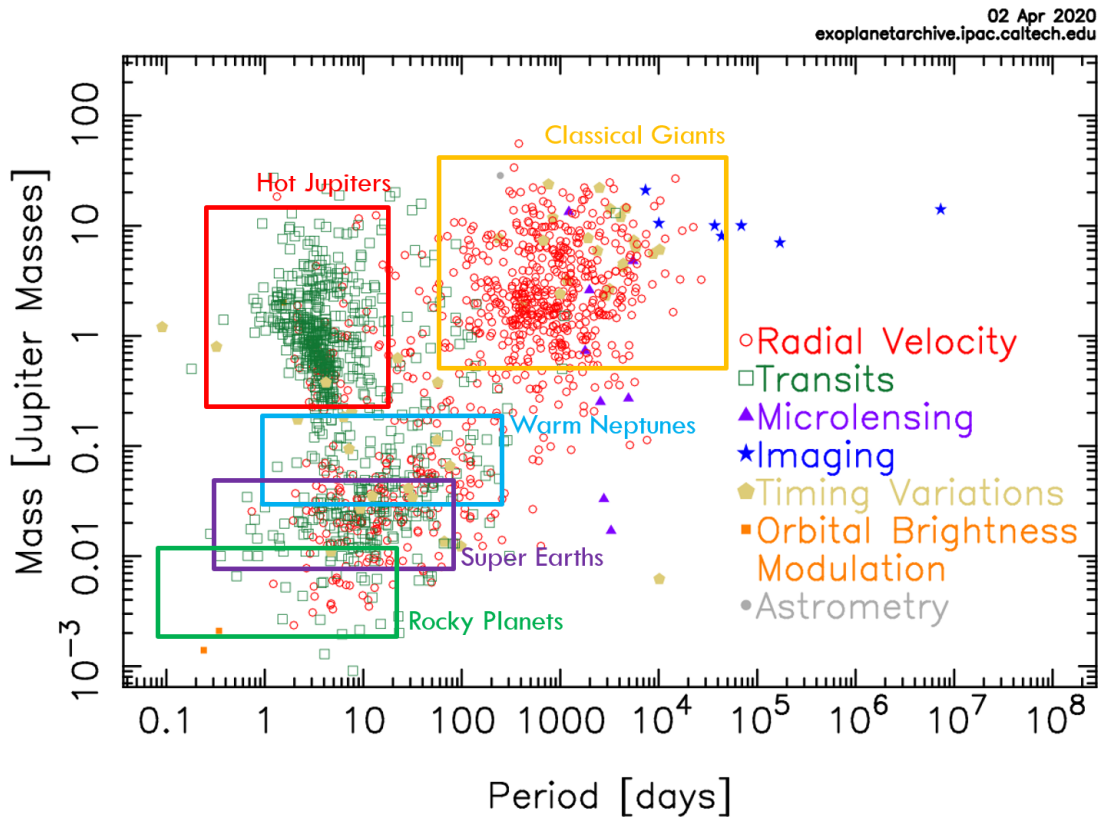
Figure 1.15: Scatter plot of the period of discovered exoplanets against their mass. This figure was produced using data from the NASA Exoplanet Archive (NASA Exoplanet Science Institute, 2020).

1. 'Classical Giants'. Giant gas planets like Jupiter and Saturn reside in this category.

2. 'Hot Jupiters'. These are giant gas planets orbiting on short periods, close to their parent star.

3. 'Warm Neptunes'. Giant planets with similar properties and mass to that of Neptune, orbiting on shorter period orbits.

4. 'Super Earths'. There is no planet representative of this classification in our solar system. It is defined as a planet with mass greater than the Earth's but substantially lower than the solar system's ice giants, Uranus and Neptune.

5. 'Rocky Planets'. These are planets composed primarily of silicate rocks or metals, like Mercury, Venus, Earth, and Mars.

Note how direct imaging is able to detect longer period, higher mass objects than

all other techniques. Microlensing also has a niche and is able to detect lower mass, long period object than other conventional methods. This makes direct imaging and microlensing our current best methods to fill in the gaps we see in the long period planetary census.

Prior to the 'Kepler Planet Bonanza' announcement on Feb. 26, 2014, the majority of all known exoplanets were giant planets (Hot Jupiters and Classical Giants). This was due to the relative ease of detection of giant planets with the transit method; as their large planetary radii obscure more of the stellar disk leading to deeper transits. Following the 2014 Kepler announcement, outlined by Rowe et al. (2014), which nearly doubled the number of validated planets at the time of release, the histogram of detected planets against planet radius changed significantly. Refinements in the application of the transit method allowed more planets with smaller radii to be detected. With this, the most commonly detected planet type was skewed towards those in the 'super-Earth/sub-Neptune' regime. This has since been further compounded with the 2016 Kepler announcement and proceeding discoveries (Morton et al., 2016). This discussion highlights the amount in which the application of the detection method has an impact on the resultant planets which are detected, demonstrating the importance of understanding our observational bias when conducting population synthesis studies. Following the removal of understood observational biases, Fressin et al. (2013) suggest that the occurrence rate of sub-Neptunes is approximately 31% out to periods of 245 days and 30% up to a period of 145 days for super-Earths. This is in stark contrast to the overall frequency of giant planets, which is thought to be close 5.2% for periods up to 418 days. This is further compounded with subsequent work, within the margin of error of the study, by Hsu et al. (2019). However, to gain a clearer picture of the true planetary census, more data and more variety in data is required. With subsequent discoveries, false positive and observational bias studies, the accuracy and precision of our understanding of the distribution of planets continues to improve.

In order to complete the low-mass (bottom) regime of the mass-period diagram, we need to be able to detect Earth-like planets and beyond. To achieve this with the radial velocity technique we need to reach a radial velocity precision of $\sim 10cm/s$ for rocky planets orbiting at $\sim 1AU$ - and greater than this for longer period planets. Instruments such as ESPRESSO, and soon HARPS-3, aim to achieve an on-sky radial velocity precision of $\sim 10cm/s$ and are expected to begin to open up this low-mass regime to investigation (Spanò et al., 2010; Thompson et al., 2016).

The radius-period relation of the current total discovered planets with available radius data is plotted in figure 1.16. The figure is dominated by planets discovered
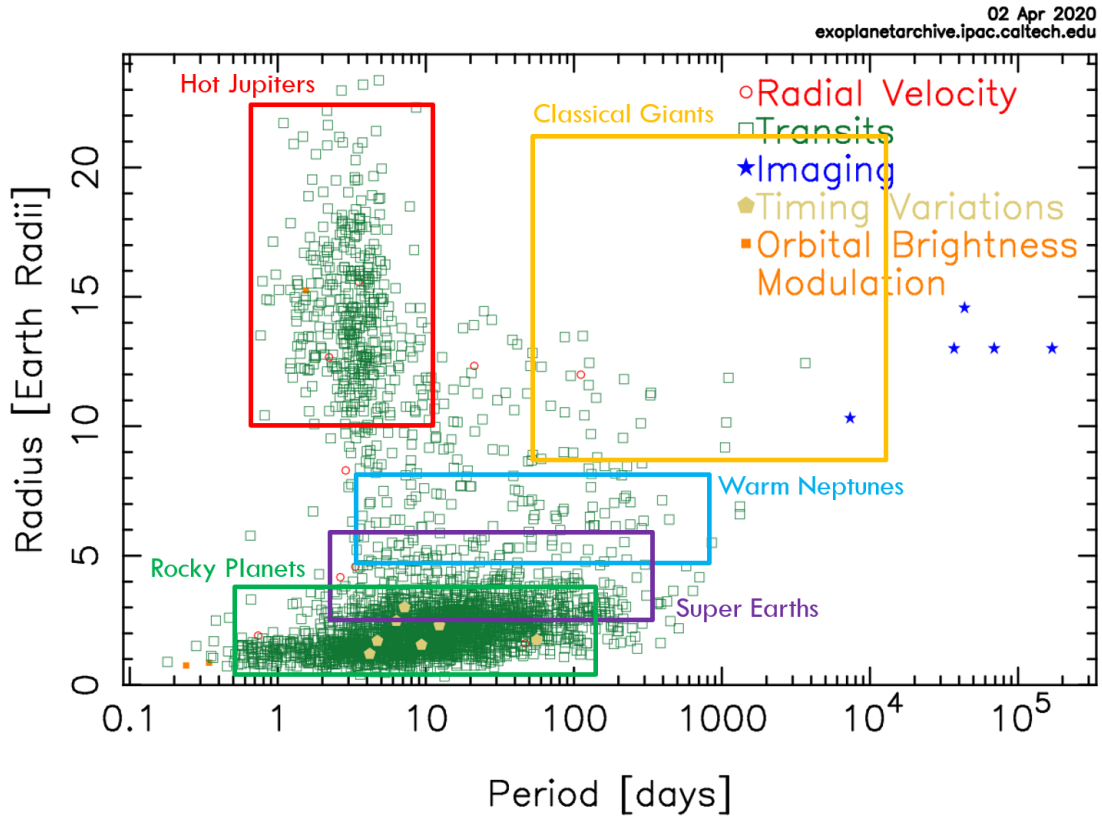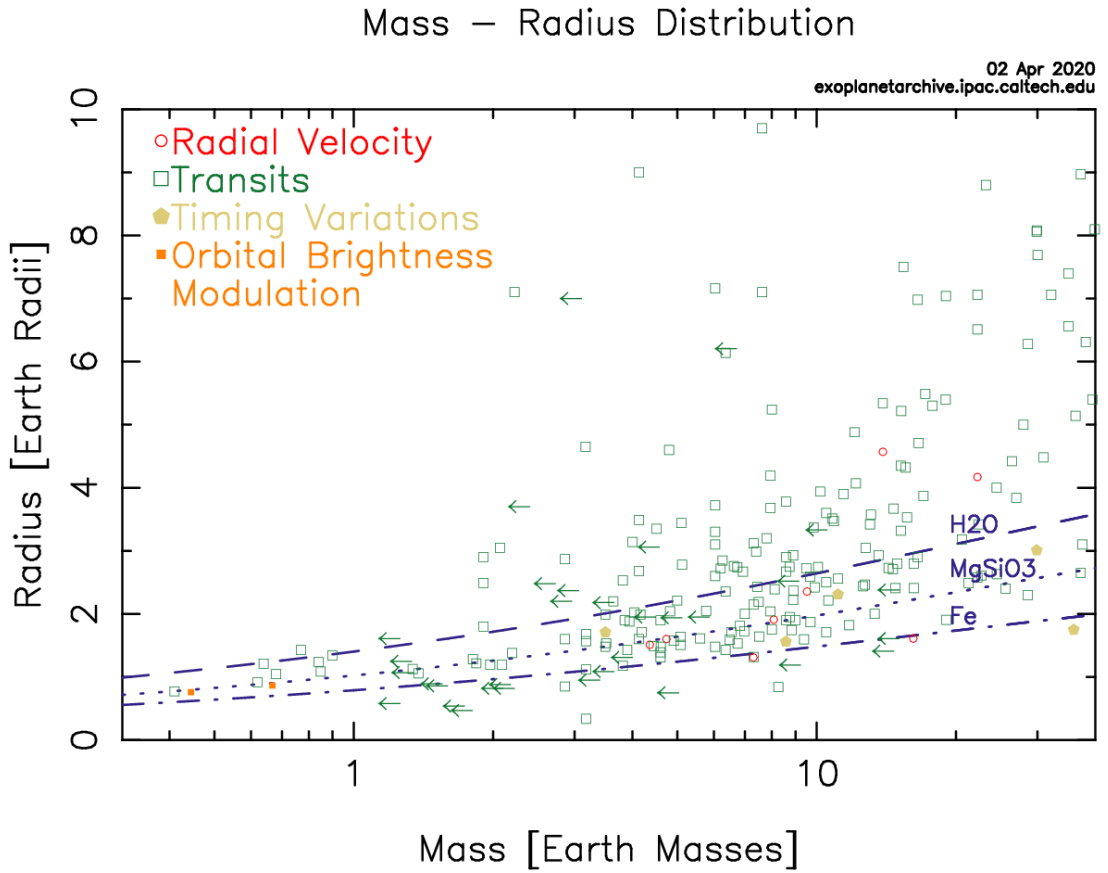
Figure 1.16: Scatter plot of the period of discovered exoplanets against their radius. This figure was produced using data from the NASA Exoplanet Archive (NASA Exoplanet Science Institute, 2020).

by transit photometry not only because of the large number of planets discovered by this method but also due to the fact that this is our primary technique for determining planet radius. Again, these observations have an associated bias of detecting short period planets with a large planet-star radius ratio. Note, again, no planets with properties close to an Earth analogue are present on this plot.

For planets with both a radius and a mass value, their density can be determined. A plot of the mass-radius relation of these exoplanets is seen in figure 1.17. Terrestrial exoplanets sit between the density of iron and water, close to the $MgSiO_3$ line (Zeng et al., 2019). Warm Neptunes, which can consist of a high quantity of volatiles, sit near the $H_2 0$ line and gas giants, which are the lowest density, sit high above the water line with large radii relative to their mass.

Figure 1.17: Scatter plot of the mass of discovered exoplanets against their radius. This figure was produced using data from the NASA Exoplanet Archive (NASA Exoplanet Science Institute, 2020). The typical error in the measurements of the planetary mass plotted here can be on the order of 5% of the given mass value. Similarly, the typical error in the measurements of the planetary radius plotted here can be on the order of $5 - 10\%$ of the given radius value. However, these values are highly variable with the planetary system studied, the measurement technique applied and the instrumentation used. Given this, it is highly unlikely that the planets plotted here with a density higher than iron are truly more dense than iron; which has a low-feasibility within our understanding of planetary formation. Within the error bars of these measurements are planetary density solutions that are less dense than iron, which is thought to far more likely be the accurate solution.

1.4.2 Formation and Evolution

This growing census of exoplanets not only informs us of the variety and ubiquity of planetary systems in the observable universe but it also provides a valuable resource from which we build our understanding of protoplanetary disk evolution and planetary formation.

Prior to the discovery of the first exoplanet, planetary system formation theories were focused on recreating the planets and structure found in our own solar system. These models would produce pro-grade orbiting, coplanar systems with an inner-band of terrestrial planets surrounded by ice/gas-giant planets; with Kuiper belt and Oort cloud analogies beyond those. The diversity of exoplanet discoveries has led to a re-evaluation of planetary system formation and evolution (Perryman, 2018).

The current field of study aims to improve our understanding of these formation and evolution mechanisms by creating models which both describe individual systems and the statistics of the population as a whole; known as population synthesis. The main challenges faced in modelling the catalogue of discovered exoplanets can be broken down into two parts: simulating the environments in which these systems form and evolve, and evaluating the physical phenomena which play a role in these processes.

The idea that planets form and evolve in a protoplanetary disk was first suggested in 1755 and has remained a core concept ever since (Kant et al., 1755). Essentially, from collapse caused by gravitational instabilities in the dust and gas of a nebula, a protostar is formed. The remaining material that surrounds the protostar is then arranged into a disk by conservation of angular momentum. From this material, the planets and other bodies are formed. The leading hypothesis on planetesimal formation is that small-scale clustering of solids is caused by a linear instability of aerodynamically coupled mixtures of particles and gas in the disk; this is known as the streaming instability (Youdin & Goodman, 2005). Once these clusters are formed, there are a number of mechanisms cited to allow the growth of these planetesimals to planets; two of which are core accretion and disk instability. In core accretion, the small clusters of dust grains are thought to coagulate into larger rocks, which then go on to form planetary sized bodies. This method is often cited in the formation of short period terrestrial planets, but its effectiveness in forming the long period, gas giant planets observed through direct imaging is under debate. The other mechanism which can explain the existence of these planets is disk instability, whereby if the disk is massive enough, parts of the material can fragment and collapse under their own self-gravity in order to form giant planets. For those inter-

mediate planets, one suggested hypothesis is the downsizing of giant planets as they evolve (Perryman, 2018). Throughout these processes, the protostar will continue to accrete mass from the disk and evolve into a pre-main sequence star (Safronov, 1972).

This picture can explain the structure of our solar system, where rocky terrestrial planets are formed in the inner system and ice/gas-giants are formed beyond the snow/ice-line; where the volatiles which are required for their formation are available. However, this theory alone cannot explain the existence of exoplanets such as hot-Jupiters, which are gas-giants found within the snow/ice-line. Some form of 'migration' must occur to allow these planets to move inwards from where they are formed to where they are observed.

This migration has been attributed to several mechanisms, one such sub-set of these processes sit under planet-planet interactions. Through, for example, collisions, resonances or gravitational interactions, the orbits of planets can be altered significantly; which may play a role in explaining the diversity of exoplanet observations (Davies et al., 2014). However, the dominant mechanism of migration is thought to be through gravitational interactions between the protoplanetary disk and the embedded planets (Goldreich & Tremaine, 1979).

Hence, it is important to understand the structure of protoplanetary disks. By observing protoplanetary disks in multiple wavebands it is possible to study their temperature and pressure profiles; via the connection of emission features with radial locations in the disk. This is additionally important as the temperature and pressure structures will impact the formation and evolution of planets (Armitage, 2018). Observations with instruments such as the ALMA telescope array have shown that protoplanetary disks can have complex temperature and pressure profiles in, for example, the form of ring structures; as is displayed in figure 1.18. Observations like these feed back into the improvement and refinement of our theoretical models.

1.5 Conclusion

In this chapter, we have touched on the methods currently in common application in the discovery of exoplanetary systems; discussing their implementation, observables and weaknesses. With this summary in place, we took a deeper dive into the further applications of high-resolution spectroscopy in the characterisation of exoplanets. We broke down the methods for extracting radial velocity measurements, with a focus on the cross-correlation technique, and highlighted how these observations
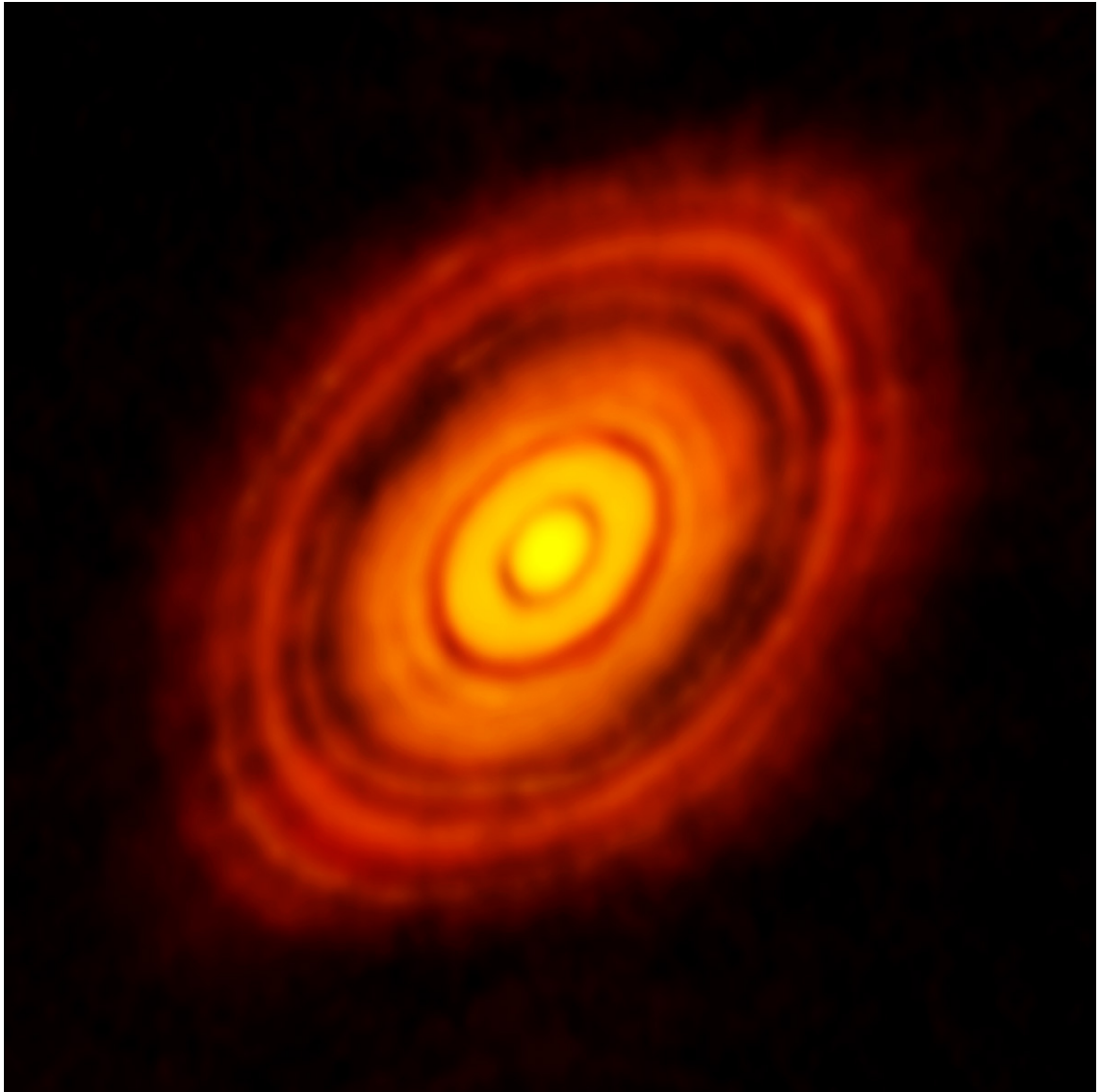
Figure 1.18: Radio image of the protoplanetary disk around the young star HL Tau, taken by ALMA. The dark gaps are thought to be formed by protoplanets sweeping out the dust around their orbits. (Brogan et al., 2015).

can allow us to infer information about the orbital parameters of the planetary system as well as characterising the planet's composition and atmosphere. With this knowledge established, we examined and analysed the current exoplanetary census leading to a discussion on how this feeds into our understanding of the formation mechanisms of planetary systems.

From our review of the literature here, we have seen that it is important for a high-resolution spectrograph designed for exoplanet science applications to:

- Resolve individual molecular/atomic lines - as the line centres are what is used to calculate the radial velocity shifts.

- Have a broad spectral coverage in the waveband of interest for a specific science case - as the signal-to-noise ratio of the cross-correlation-function scales with $\sqrt{n}$, where n is the number of identified spectral lines.

- Be stable - as the radial velocity measurement is a reference measurement, the change in the instrument profile must be minimal or characterizable in order to obtain precise radial velocity measurements.

We will elaborate on this and further describe the design process and requirements for high-resolution spectrographs in chapter 2.

In chapter 3, this design approach is applied to a low-cost, compact, high-resolution spectrometer concept is outlined. Further discussed is the construction process of this system, which led to the production of a functioning instrument, QMSPEC.

Following this, the design and construction of the necessary subsystems for on-sky testing of the spectrograph, a fibre coupling system and a data reduction pipeline, will be outlined in chapter 4. The on-sky testing of these sub-systems, along with the QMSPEC spectrograph, will then be reported before the conclusion of this chapter, with a focus on method, experimental testing and results.

With the knowledge gained thus far, a preliminary design study is carried out for NEREA; a stable, compact, high-resolution spectrometer concept for the GTC. The science case for the instrument, design process and as-designed performance will be discussed in chapter 5.

In chapter 6, the knowledge gained in the design and construction of high-resolution spectrographs, from the proceeding projects, is channeled into the production of a 'spectrograph design tool-kit' software. This allows users to assess spectrograph performance and analyse its dependence upon the specifications of the components placed into the spectrometer. This software is then tested in a design case-study for the collimating/re-focusing lens of a compact spectrograph, EXOhSPEC.

Finally, we will conclude in chapter 7 by summarising the studies outlined in this thesis and speculating on their future impact on the field of exoplanet science and beyond.

2 Achieving High Spectral Resolution with the Echelle Spectrometer Concept

Spectrometers are powerful tools in astronomy. Amongst their many applications, they allow us to remotely measure the temperature of objects, probe their chemical make-up and infer their motion.

There are four main resolving power regimes in which optical, NIR and IR spectrometers operate: low-resolution, intermediate-resolution, medium-resolution and high resolution; as illustrated in figure 2.1. Low-resolution spectrometers typically consist of a prism, which uses refraction to disperse the light into its constituent wavelengths. This form of spectrometer is only able to resolve differences in wavelength down to $\sim 10nm$ leaving it capable of displaying the continuum shape of the spectra only. Intermediate- and medium-resolution spectrometers may also use prisms or they can disperse the light through diffraction from a diffraction grating. In order to achieve this, the diffraction grating is operated in a low diffraction order and a filter (which only allows wavelengths of the order of interest to pass through) is used to select the required order. Spectrometers of this type can distinguish differences in wavelength of a few nanometers and can begin to distinguish spectral features. High-resolution spectrometers primarily apply diffraction gratings operating in the high diffraction orders to disperse their light. With this method, they are able to distinguish differences in wavelength down to the order of $10pm$ and are able to resolve individual molecular absorption/emission lines.

2.0.1 Echelle-Type Design

The Echelle-type spectrometer, first pioneered by Nagaoka & Mishima (1923) in 1923, has become the staple design for astronomical high-resolution, visible-IR spectroscopic applications. The design applies blazed grating facets to maximise throughput in higher diffraction orders. Typically a prism or another grating is
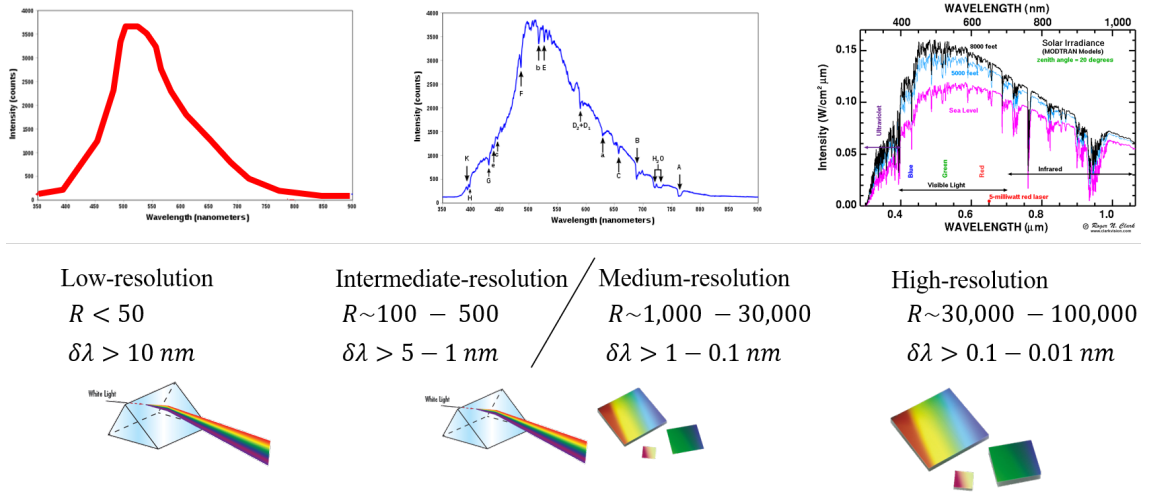
Figure 2.1: Illustration of the spectrograph operation regimes demonstrating the overall spectrum characteristics and the instrument components that facilitate their production.

used as a cross-disperser, to spatially separate each of the diffraction orders; as displayed in figure 2.2. This spectrometer design produces a 'ladder-like' spectrum with orders which are spatially separated, as demonstrated in figure 2.3. In a monochromatic sense, this spectrometer design can be seen as a simple re-imager such that each resolution element of the spectrum is a monochromatic re-image of the input fibre head or input slit; depending on whether the instrument is fibre or slit fed.

2.0.2 Diffraction Gratings

A reflectance diffraction grating, commonly found in use as the principle diffractive element in an Echelle-type spectrometer, consists of a series of periodic and regular reflective facets. Light incident on the grating will 'reflect' off of the facet centres and interfere. Constructive interference in this case occurs following the grating equation which highlights the relationship between diffraction angle and wavelength,

$$\frac{m\lambda}{d} = \sin\alpha + \sin\beta\,, \tag{2.1}$$

where the integer m denotes the diffraction order, λ is the wavelength of interest, d is the separation between the centre of adjacent facets, α is the incident angle and β is the diffraction angle. These parameters are highlighted in figure 2.4.

Under this simplified view, one might believe that the resultant intensity pattern due to this centre-centre diffraction is periodic and symmetric for all diffraction
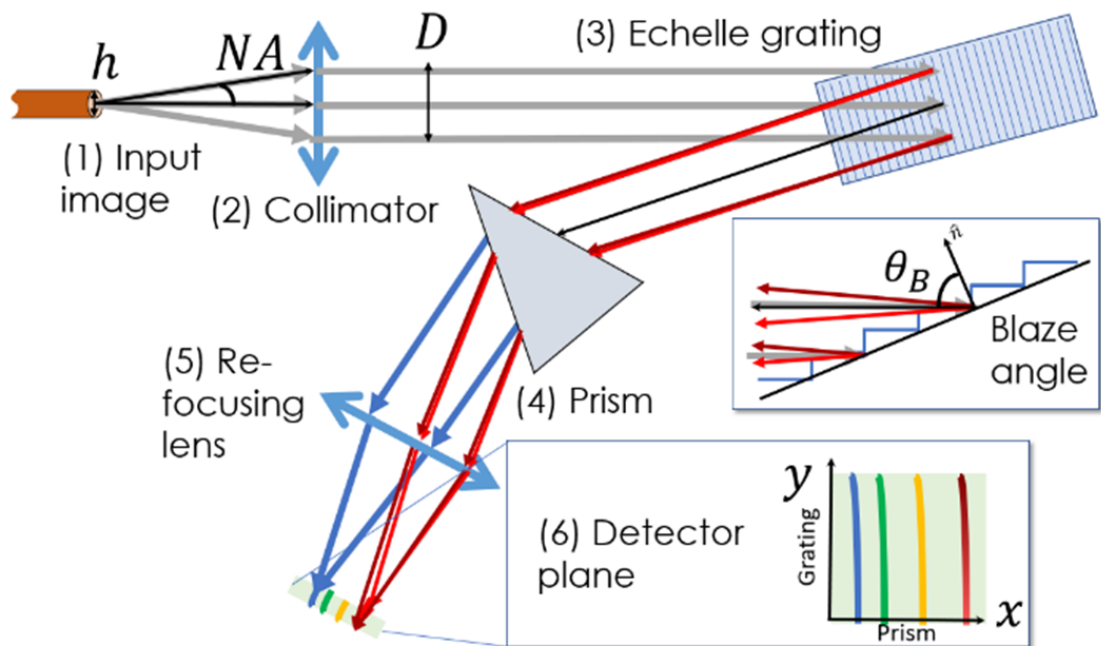
Figure 2.2: Schematic diagram depicting the layout of an Echelle type spectrometer. Light enters through a fibre or slit (1), is collimated by the collimating lens (2), dispersed in high-resolution out of the plane of the page by the Echelle grating (3), cross-dispersed parallel to the plane of the page by the prism, spatially separating the orders (4), whereby the light is then re-focussed onto a detector by the refocussing lens (5). Item (6) depicts the resultant Echelle spectrum.
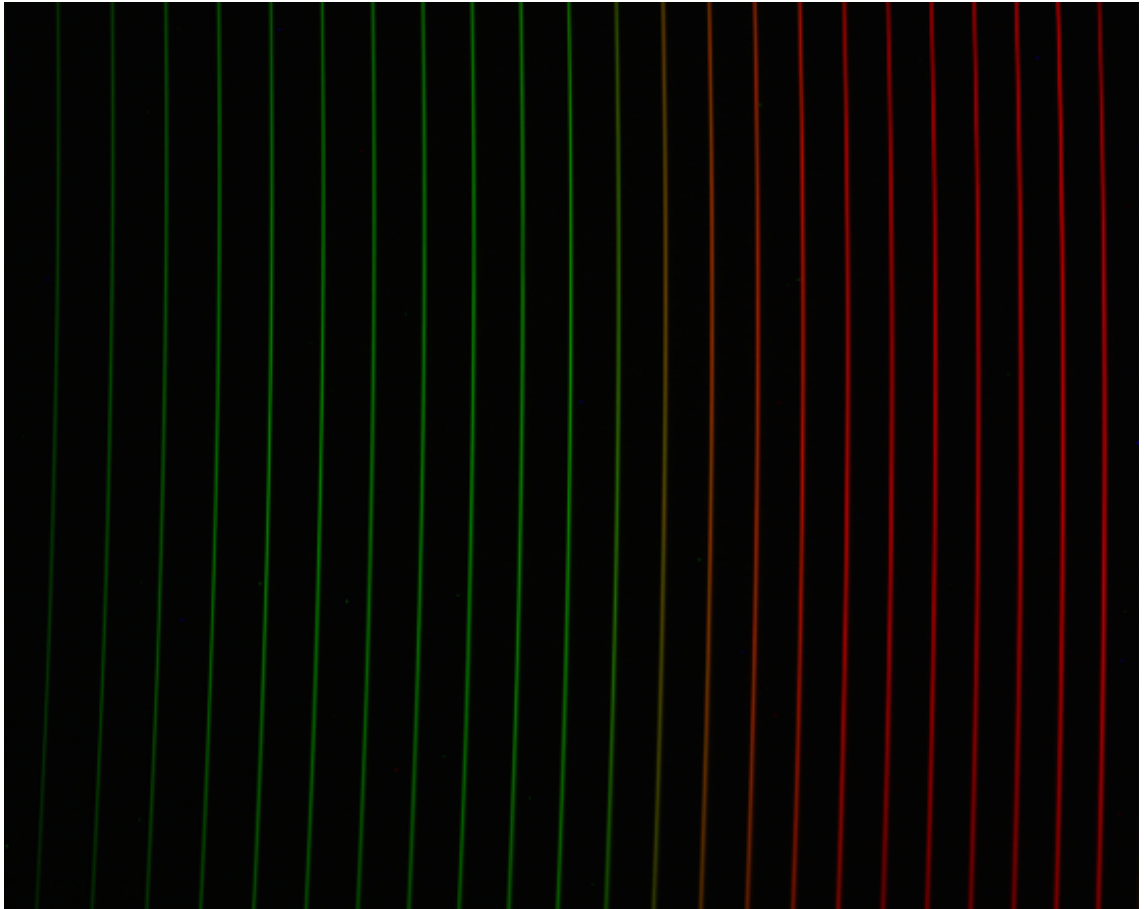
Figure 2.3: Example Echelle spectrum image from QMSPEC. Vertically the spectra are dispersed in high-resolution by the diffraction grating and the orders are spatially separated horizontally by the cross-disperser; in this case the cross-disperser is a prism.
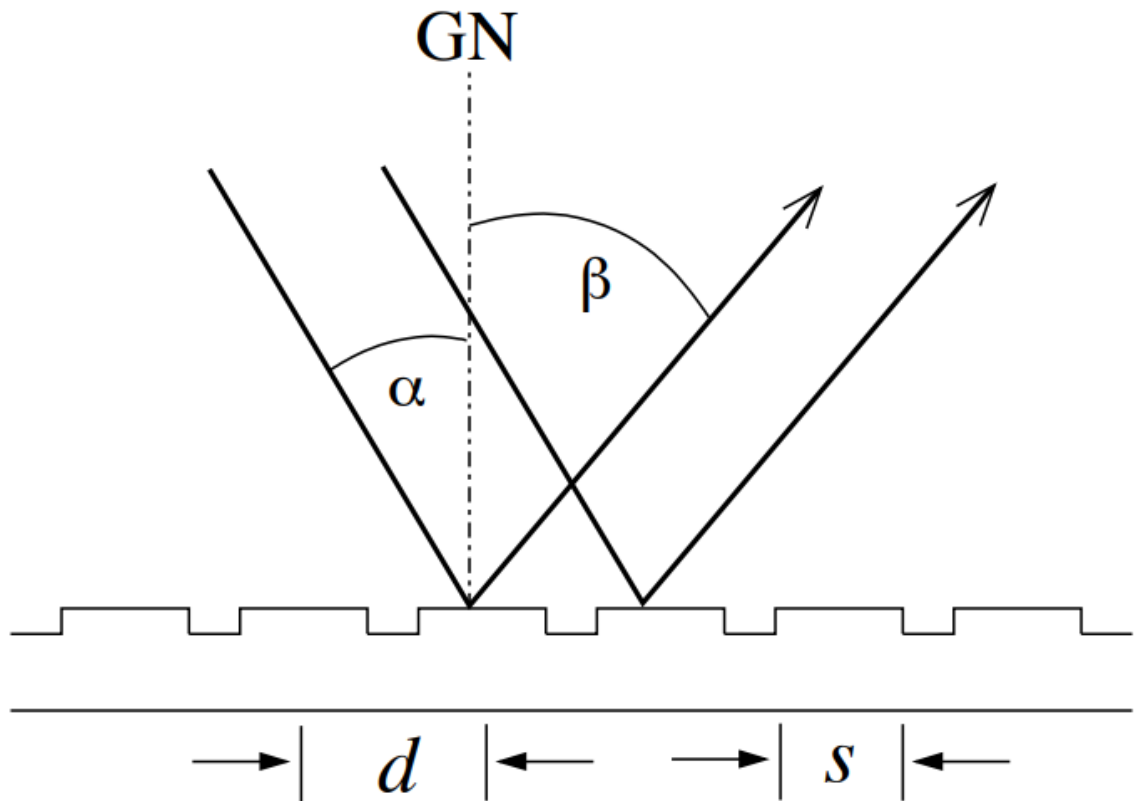
Figure 2.4: Schematic diagram of a reflection grating showing the individual grooves, or facets. The facets are characterized by their edge–to–edge lengths, s, and centre–to–centre separation, d. The incoming light has an angle of incidence, α, measured with respect to the grating normal, GN. Interference of the reflected wave-fronts yields a diffraction angle, β, which is a function of wavelength phase differences (Churchill, 2009).
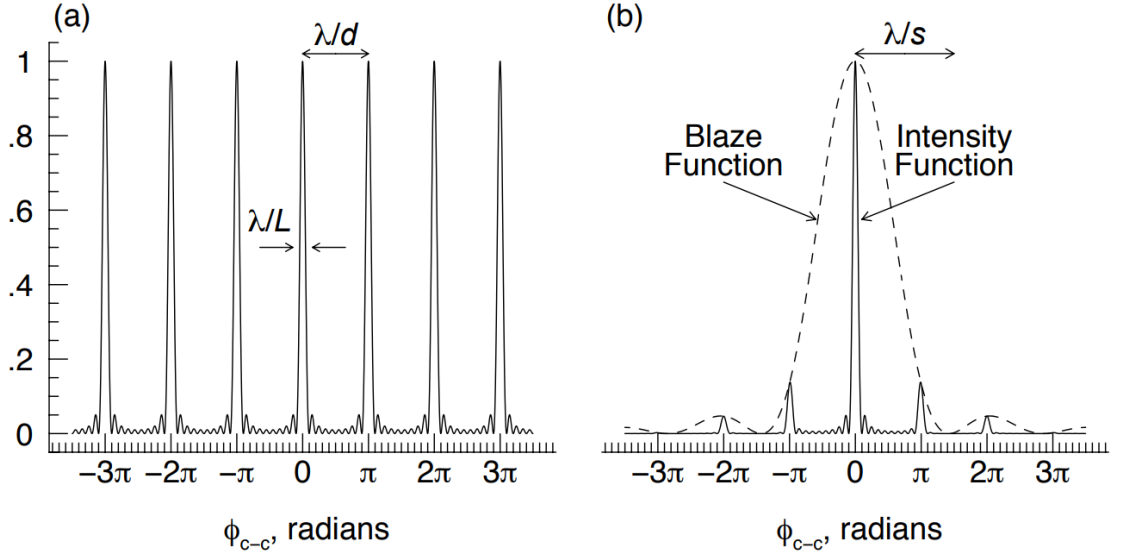
Figure 2.5: (a) The periodic interference function which results from the facet centre–to–centre interference, plotted as a function of the phase difference (in units of radians) for an arbitrary wavelength, λ. Note that the peaks occur at $m\pi$, where m is an integer. The width of peaks in the phase domain are characterised by λ/L, where L is the length of the grating, and the separation between orders is characterised by λ/d, where d is the separation between the centre of adjacent grating facets. (b) The blaze function, equation 2.2, which results from facet centre–edge interference is also plotted as a function of the phase difference of the centre–centre diffraction. The width of the blaze function is governed by the facet sizes and is characterised by λ/s in the phase domain. The blaze function modulates the interference function, giving the overall intensity pattern shown (Churchill, 2009).

orders, m. However, there are additional phase modulations which occur due to the interference phases between the centre and edge of each grating facet. This produces an envelope over the intensity distribution which is centred about $m = 0$ and characterised by the blaze function,

$$I_b = I_0 \frac{\sin^2 m\pi(s/d)}{[m\pi(s/d)]^2} \,, \tag{2.2}$$

where I_b is the intensity distribution of the blaze envelope, I_0 is the normalisation factor and s is the width of a grating facet (Churchill, 2009). The principles of the blaze function are demonstrated in figure 2.5.

For high-resolution applications, we wish to operate in the highly dispersive regime of the diffraction grating, found in the high orders. Hence, a blaze function with an intensity peak centred around $m = 0$ is highly undesirable.
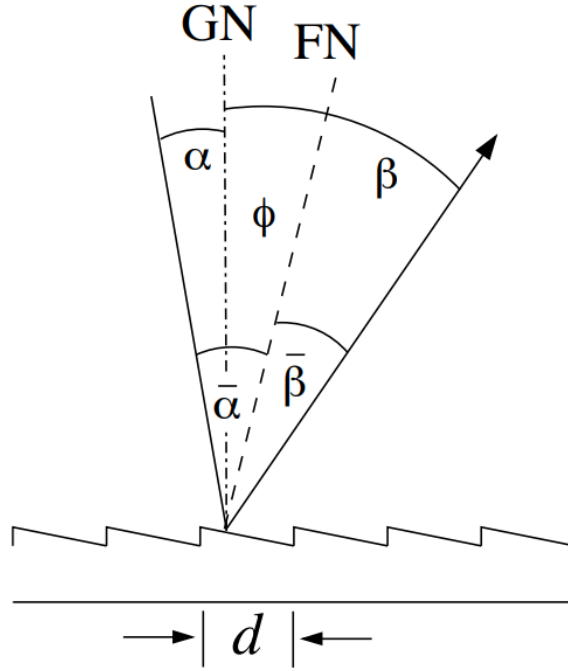
Figure 2.6: To maximize the diffraction illumination pattern for $m > 0$, a phase shift is introduced to the centre–edge diffraction interference by grooving the facets at an angle ϕ, which also defines the facet nornal, FN. The blaze function then peaks when $\overline{\beta} = -\overline{\alpha}$ (Churchill, 2009).

In order to maximise the throughput in higher orders, the peak of the blaze function must be 'shifted' in phase such that it is centred at the desired order, m. This is achieved by tilting the grating facets by an angle, ϕ, which phase shifts the centre-edge diffraction pattern. This angle is known as the blaze angle and is demonstrated in figure 2.6. The resultant blaze function for a blazed grating is then represented by,

$$I_b = I_0 \frac{\sin^2 \frac{\pi s}{\lambda}[\sin \overline{\alpha} + \sin \overline{\beta}]}{[\frac{\pi s}{\lambda}[\sin \overline{\alpha} + \sin \overline{\beta}]]^2} \, , \qquad (2.3)$$

where, for a blazed grating, s is now characterised by $s = d \cos \phi$ and, defining the incident angle with respect to the facet normal, we have $\overline{\alpha} = \alpha - \phi$ and $\overline{\beta} = \beta - \phi$, as shown in figure 2.6 (ϕ, α and $\overline{\alpha}$ are defined as positive and β and $\overline{\beta}$ are defined as negative).

The Littrow condition is defined where the incoming and diffracted beam are aligned with the facet normal, such that $\alpha = -\beta = \phi$ and hence, $\overline{\alpha} = 0$ and $\overline{\beta} = 0$. Under this condition the grating operates with maximum throughput efficiency and so this is the ideal operating condition for astronomical purposes (Palmer, 2014).

From equation 2.3 we see that the first minima of the blaze function occurs where $\frac{\pi s}{\lambda}[\sin \overline{\alpha} + \sin \overline{\beta}] = \pi$. Hence, by assuming that the incoming beam follows the

Littrow condition, such that $\overline{\alpha} = 0$, it is possible to determine a useful equation for the maximum angular span of the outgoing diffracted angles,

$$\overline{\beta}_{\pm}^{max} = \pm \sin^{-1}\left(\frac{2\tan\phi}{m}\right), \tag{2.4}$$

which is an important parameter in the design of the re-focusing lens of the spectrograph.

2.0.3 Prisms

The method by which prisms disperse light is refraction. The material that the prism is constructed from, as with all materials, will have a refractive index that varies with wavelength. This refractive index dependence on wavelength will vary from material to material; as such, material selection is an important tool in prism design.

An optimally aligned dispersing prism is one such that it deviates the incoming beam of a given wavelength by the minimum deviation angle. For a prism in air, this angle is characterised by,

$$\delta_{min} = 2\sin^{-1}\left(n\sin\frac{\gamma}{2}\right) - \gamma, \tag{2.5}$$

where δ_{min} is the minimum deviation angle of the prism, n is the refractive index of the prism material for a given wavelength and γ is the wedge angle of the prism (Mungan, 2001). As such, it can be seen the deviation angle, and hence dispersion, introduced by a prism is dependent upon refractive index of the material for a given wavelength, the way in which this refractive index varies with wavelength and the wedge angle of the prism.

For the prisms discussed in this thesis, the minimum deviation angle of the prisms have been chosen to occur for the wavelength that appears in the centre of the central order produced by the diffraction grating for the instrument's wavelength range of interest. The prism's dispersion is also designed such that the resultant cross-dispersed spectra will fit onto the detector and fill it effectively; ensuring that orders are separated sufficiently to avoid cross-talk (light from one order overlaying another). Another consideration is throughput, one should choose a material with a high transmittance and ideally minimise the length of the optical path through the material. Similarly, to maximise compactness of the instrument, one should strive to achieve the required dispersion by creating a prism with a small wedge angle,

consisting of a highly dispersive material, as opposed to a large wedge angle and low dispersion material.

2.0.4 Resolving Power

The resolving power of a spectrometer is a measure of its ability to resolve features of the electromagnetic spectrum. Resolving power, R, is defined by the ratio of the smallest resolvable wavelength difference at a given wavelength, $\delta\lambda$, and that given wavelength, λ; such that $R = \frac{\lambda}{\delta\lambda}$.

Spectrometers are highly constrained systems. Spectrograph design can be seen fundamentally as the trade-off between four main parameters: 'Resolving Power', 'Collimator Focal Length', 'Diffraction Grating Blaze Angle' and the 'Size of Input'; either fibre size or slit width. This is well demonstrated through the 'Theoretical Resolving Power Equation', equation 2.6. I provide the details for the derivation here, as understanding this relation is crucial to the design choices discussed throughout this thesis.

If we consider the spectrometer in the high resolution axis only, the prism can be ignored, as depicted in figure 2.7. In this simplified view, the system can be seen as composed of a collimating lens (lens 1), a grating and a re-focussing lens (lens 2). For a re-imaging system consisting of the two lenses only, an object such as the fibre head of height h, when collimated through lens 1 will produce a beam with angle θ such that $\tan\theta = \frac{h}{f_1}$, where f_1 is the focal length of lens 1. Similarly, when this beam is re-imaged through lens 2 the image of the fibre head has height $h_2 = f_2 \tan\theta$. Now for 2 wavelengths, λ and $\lambda + \delta\lambda$, separated by $\delta\lambda$, the diffraction grating will introduce a difference in beam angle of ϵ, see figure 2.7. When these beams are re-focussed, they will have a spatial separation of $h_2' = f_2 \tan\epsilon$. As a simplification, ignoring diffractive and aberration effects, we state that in order to distinguish a difference in wavelength of $\delta\lambda$, h_2' must be greater than or equal to h_2; hence $f_2 \tan\epsilon \geq f_2 \tan\theta$. Simplifying this gives a critical value when $\tan\epsilon = \frac{h}{f_1}$. Now consider the grating equation, $m\lambda = nd\left(\sin\alpha + \sin\beta\right)$ where m is the diffraction order, d is the groove density (often quoted in *Grooves/mm*), α and β are the incoming and outgoing angles at the grating, respectively, and n is the refractive index of the medium that the system is in. For this example we shall take the medium to be vacuum, such that $n = 1$. For some wavelength, λ_L, we shall take the Littrow condition to be satisfied, giving $\alpha = -\beta = \phi$; where ϕ is the blaze angle of the grating. This simplifies the grating equation to $m\lambda_L = 2d\sin\alpha$. For a wavelength separated from λ_L by $\delta\lambda$, the outgoing angle from the grating will have an additional angle ϵ, such
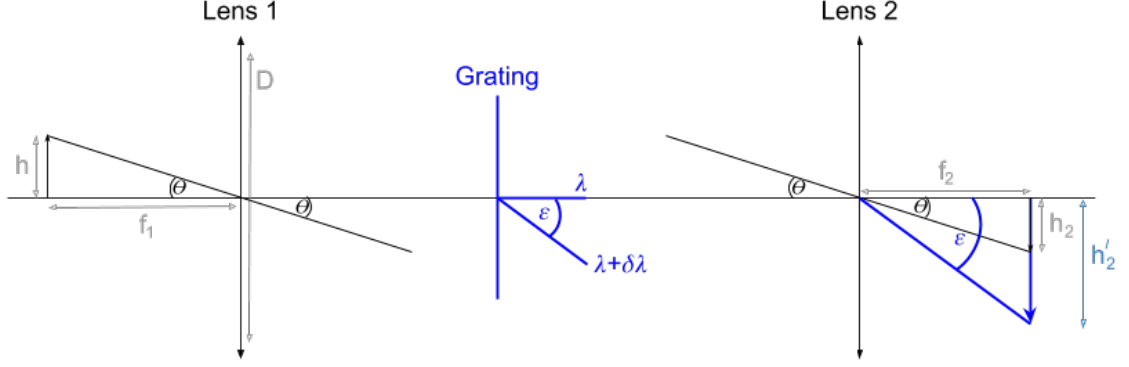
Figure 2.7: Diagram depicting a simplified spectrometer system, considering the high-resolution dispersion axis only. This figure demonstrates the key parameters used in the derivation of the 'Theoretical Resolving Power Equation', equation 2.6.

that $m(\lambda_L + \delta\lambda) = d(\sin(\alpha) + \sin(\alpha + \epsilon))$. Subtracting and re-arranging these two equations result in $\delta\lambda = \epsilon d \cos(\alpha)/m$. Taking a small angle approximation for ϵ, we see that $\frac{h}{f_1} = \epsilon$, therefore $\delta\lambda = hd\cos(\alpha)/mf_1$. The definition of resolving power is given by $R = \lambda/\delta\lambda$. Through substitution of the simplified grating equation and our value of $\delta\lambda$, we see that

$$R = \frac{2f_1 \tan(\alpha)}{h} . \tag{2.6}$$

It is to be noted here that resolving power is not explicitly dependent on grating facet number or focal length of the refocussing lens. The grating facet number only regulates the wavelength span of the individual diffraction orders and the refocussing lens focal length will alter magnification of the final image.

Furthermore, it is possible to relate the telescope diameter to the resolving power of the overall telescope and spectrometer system. In order to maximise throughput, the size of the input fibre, h, must match the physical size of a point source imaged to the focal plane of the telescope. For a telescope of focal length, f_t, the angular image size, ω, is related to the physical image size by $\omega = h/f_t$, where it is assumed that ω is a small angle. For a star, this is of the order of 1 arcsec. Following the definition of the F-number, the telescope's F-number is described by $F_t = f_t/D_t$, where D_t is the diameter of the telescope. With the aim to conserve etendue (further discussed in section 2.0.8), the F-number of the spectrometer, F_s, and the telescope must be matched; such that $F_t = F_s = F$. Following this, it can be seen that $h = \omega F D_t$ and $f_s = F D_s$. Substituting these expressions into equation 2.6, we see that

$$R = 2\frac{D_s}{D_t}\frac{\tan(\alpha)}{\omega} . \tag{2.7}$$
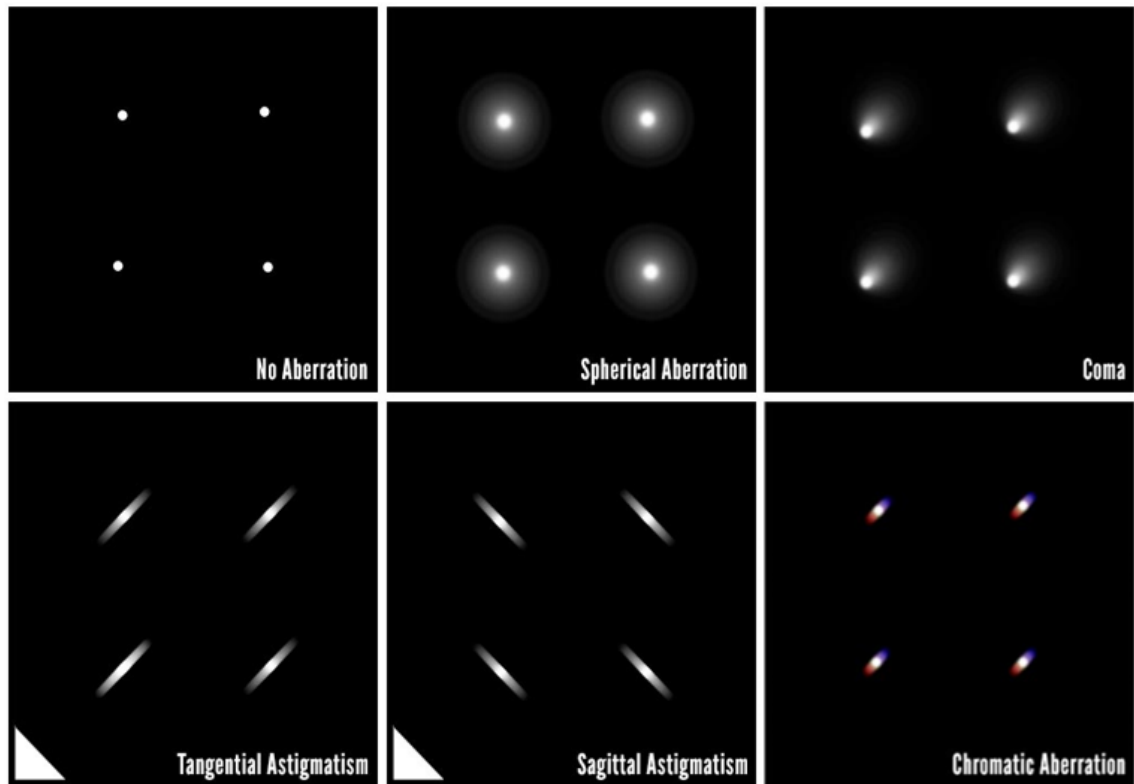
Figure 2.8: Image outlining the effects of a series of aberrations on the image of a point source (Norman, 2015).

2.0.5 Diffraction Limit and Aberration Theory

Equation 2.6, the expression for the resolving power, is a good estimate of the theoretical limit of the spectrometer's resolution but it doesn't tell the full story. The imaged fibre head can be thought of as a complex object composed of infinite point sources. As discussed in section 1.2.4, when a point source is imaged through a aberration-free, diffraction limited, ideal, focused optical system, the resultant image PSF will have a physical size due to diffraction alone. In general, real-world optical systems are not ideal and aberration-free, they have some degree of aberrations which degrade the optical performance.

Aberrations are defined as a property of an optical system which causes light to be spread out spatially as opposed to focused to a point. Aberrations are introduced due to the geometry of the optical surfaces in an optical system and through refraction from the materials of the optical system. Figure 2.8 outlines the effects of some of the Seidel aberrations on the image of a point source.

We shall not go into detail on aberration formation and geometric optics theory here as one could easily write a book on those topics, in fact many have. The books

which best align with my school of thought on the topic are 'Aberrations of Optical Systems' by Welford (1986a) and 'Astronomical Optics' by Schroeder (1999a). The key point for this thesis is that aberrations exist and through changing the geometric and refractive properties of an optical system one can alter the aberration's severity; i.e. how much they increase the size and effect the shape of an imaged point source, degrading resolution.

With this in mind, in summary, there are two phenomena which feed into the spot size (the image of a point source) of a real-world optical system:

1. Diffraction: Diffraction causes the image of a point source to have physical size. For a diffraction limited system (with an assumed circular aperture), the spot size will be characterised by the Airy disk. This will set the absolute lower physical limit on the spot size and therefore set the upper limit on imaging resolution. For a monochromatic source of wavelength, λ, the radius of this spot size, x, is characterised by,

$$x = 1.22 \frac{\lambda f}{D} \,, \tag{2.8}$$

   where f is the focal length of the imaging optics and D is the diameter of the system's aperture stop.

2. Aberrations: Irrespective of diffraction effects, optical aberrations will alter the size and shape of the spot. An optical designer's aim is to design the optical system such that the effect of the optical aberrations are balanced in such a way that the spot size from aberrations is less than the spot size from diffraction. When this criteria is met, the system is reaching its absolute classical physical limit in performance and is classed as 'diffraction limited'.

To elaborate on this, when the spot size from aberrations is smaller than the Airy disk, the system is diffraction limited and the spot size is dictated purely by the Airy disk. On the other hand, when the aberration spot size is larger than the Airy disk, the system is aberration limited and the spot size is given by the aberration spot size.

As described, the image of a complex object such as a fibre head is comprised of infinite point images, hence the resultant image is a convolution of a perfect image of the fibre head (one without diffraction or aberration) and the PSF; a full treatment of this relation can be found in Ahi & Anwar (2016). Therefore, the diameter of each resolution element (the size of the imaged fibre head), U, is the sum in quadrature

of the diameter of the perfect image of the fibre head, h, and the diameter of the PSF (the spot size), p, such that,

$$U = \sqrt{h^2 + p^2}\,. \tag{2.9}$$

Furthermore, due to this sum in quadrature, one can allow the the spot size to reach close to the value of h without substantial increase in U; and hence loss in resolution.

2.0.6 Nyquist–Shannon Sampling Theorem

To avoid aliasing, Nyquist theorem for discrete sampling states that two samples per resolution element are required for unambiguous resolution of images which are just resolved according to the Rayleigh criterion (Schroeder, 1999b). Therefore, spectrometers should be designed in such a way that the pixel size is less than or equal to half the size of the imaged fibre, $U/2$.

When a Doppler shift is measured on an Echelle-type spectrometer, the spectra will drift along the high dispersion axis, i.e. along the orders. For a spectrometer with a resolving power of $R = 100,000$ in the visible regime, the resolution will be approximately $\delta\lambda = 5.5pm$. With two pixels per resolution element, this means the system has a dispersion of $2.75pm/pixel$. From equation 1.1, we see that the RV shift measured from a pixel's worth of dispersion at $550nm$ is given by $\Delta V_{rad} = c\frac{\Delta\lambda}{\lambda} = c\frac{2.75pm}{550nm} = 1500m/s$. Therefore, an RV drift, of say a hot-Jupiter around a G-type star, on the order of $1m/s$ will only induce a shift of $\frac{1}{1500}^{th}$ of a pixel. A typical pixel may be $7\mu m$, thus we are talking about measuring a shift of only $5nm$. This highlights the importance of the cross-correlation technique, and its contemporaries (as discussed in section 1.3.1), in the measurement of these sub-pixel radial velocity drifts.

2.0.7 Anamorphic Magnification and The General Grating Equation

When the spectrometer's diffraction grating is operating perfectly on Littrow (for the one wavelength per order where this applies), the diffracted beam, and resultant image formed by that beam, will have a magnification of unity (assuming equal focal length of the collimating and re-focusing lens). As discussed by Schweizer (1979), once the beam moves away from the Littrow condition an anamorphic magnification of the resolution element occurs of a factor $r = \frac{\cos\alpha}{\cos\beta}$, where α is the incident beam angle and β is the diffracted beam angle. Hereby, when the grating is operated

under-Littrow ($\beta > \alpha$), there is an elongation of the resolution elements and when one operates the grating over-Littrow ($\alpha > \beta$) there is a compression of the resolution elements.

As discussed, only one wavelength per order will perfectly follow the Littrow condition, so all Echelle spectrometers will have some level of anamorphic magnification across their total field of view. This can be minimised by using a grating with a lower number of *grooves/mm*, such that it has a smaller blaze width; spreading the wavelengths across more orders to compensate for this.

It is often necessary in the physical alignment of the spectrograph to operate the grating off of the grating facet normal axis. This is achieved by rotating the grating such that the incoming beam projects an angle B from the grating facet normal in the cross-dispersion plane; as demonstrated in figure 2.9. In this alignment (in air), the grating properties are dictated by the general grating equation,

$$\frac{m\lambda}{d} = \cos B \left(\sin \alpha + \sin \beta \right) . \tag{2.10}$$

Note that for a constant α and λ, β is a function of B, such that an imaged object will be tilted and elongated with increasing B; as shown in figure 2.10 (Konidaris, 2014). This effect is known as Beta-anamorphism and is also the reason why the orders of Echelle spectrometers appear curved (Schroeder, 1999c). A subtle case of this phenomena can be observed in the spectra produced by QMSPEC, depicted in figure 2.3. The effect of classical and Beta-anamorphism is also exhibited in the image of a resolution element of QMSPEC, as shown in figure 2.11.

2.0.8 Etendue and Efficient Coupling

The next technical challenge in the design of a spectrograph is the efficient coupling of the spectrometer to the telescope. This is achieved through the conservation of etendue.

Etendue, G, is defined as the product of the surface area of the beam focal spot, S, and the solid angle that the focusing/dispersing beam subtends, Ω; therefore $G = S\Omega$ (Chaves, 2017).

For effective coupling, one aims to match the F/number of the telescope to the F/number of the spectrograph fibre whilst also matching the size of the telescope's focal spot to the size of the fibre head. Matching the F/numbers is achieved through the use of a focal reducer, which is a re-imaging optical device which collimates the telescope beam and refocusses it with the required F/number. To determine the
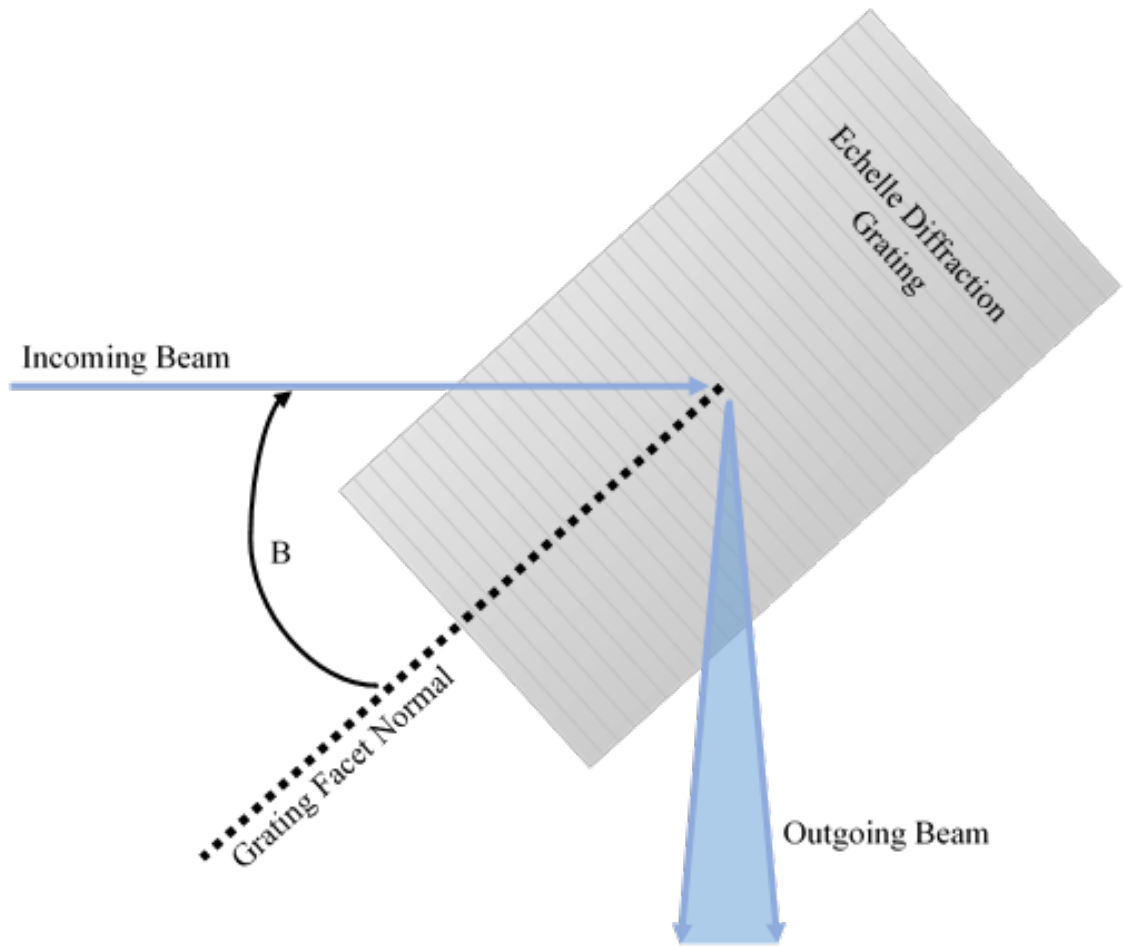
Figure 2.9: Schematic top down view (in the cross-dispersion plane) of the tilted Echelle diffraction grating as it is positioned in a spectrometer system. In the physical placement of the grating in the instrument it is often necessary for the incoming beam to approach the grating off of the grating facet normal in the cross-dispersion axis. The angle between the incoming beam and the facet normal is denoted as B. Note that the outgoing beam is dispersed in some capacity in the cross-dispersion plane, this is due to Beta-anamorphism.

B = 0*deg* B = 45*deg* B = 90*deg*
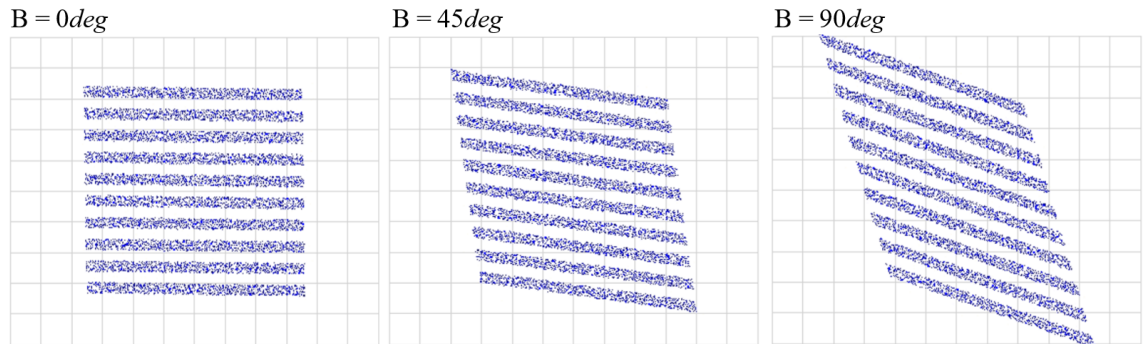
Figure 2.10: Demonstration of the effect of Beta-anamorphism for a monochromatic image of a series of horizontal lines which are re-imaged by the spectrometer system. As the grating is rotated and the B angle is increased, the effect of Beta-anamorphism is increased, leading to a tilting and elongation of the monochromatic image (Konidaris, 2014).

Figure 2.11: Image of the Sodium D-doublet spectrum produced by an early prototype of the QMSPEC instrument. Each of the resolution elements are a monochromatic image of the optical fibre head which feeds the instrument. The effect of Beta-anamorphism is clear with the circular fibre head imaged as a tilted and elongated ellipse.

spot size after the beam has passed through the focal reducer, h', conservation of etendue can be applied to derive a useful equation.

First note that the surface area of a focused image spot is proportional to x^2 (as $S = \pi(x/2)^2 \propto x^2$), where x is the diameter of the focused image spot, assuming diffraction limited performance. It is also the case that the solid angle subtended by the telescope focal beam is proportional to θ^2 (as $\Omega = 4\pi sin^2(\theta/2) \propto \theta^2$ for small angles), where θ is the angle of the focusing/dispersing beam from the optical axis. From the definition of the F/number, $F/ = f/D = \frac{1}{2tan(\theta)} \propto \frac{1}{\theta}$ for small angles, where f is the focal length of the optic and D is the diameter of its associated aperture. Thus, it can be seen that for small angles, $G \propto (x \times \frac{1}{F/})^2$. Therefore, through conservation of etendue it can be shown that,

$$h' = F/^S \times x^T \times \frac{1}{F/^T} \, , \qquad (2.11)$$

where h' is the diameter of the focal spot after the focal reducer. x^T and $F/^T$ are the focal spot diameter and F/number of the telescope without the focal reducer, respectively. $F/^S$ is the F/number of the beam after passing through the focal reducer; this should be matched to the F/number of the spectrograph fibre.

Ideally, for optimal coupling, h' will be equal to the diameter of the fibre head, h.

2.0.9 Optical Fibres

Beyond just fibre size, a number of other fibre parameters must be considered.

As discussed, for efficient coupling, the F/number of the telescope must be matched to the F/number of the spectrograph using a focal reducer. Therefore, the F/number of the optical fibre must be matched to the spectrograph. However, when discussing optical fibres, it is to be noted that the acceptance cone of an optical fibre is often quoted in an alternative but equivalent term to F/number, known as 'numerical aperture' (NA). Numerical aperture is defined by $NA = n\sin(\kappa)$, where n is the refractive index of the surrounding medium and κ is the acceptance angle of the fibre. For small angles in air, the numerical aperture and F/number can be converted between via the relation, $NA \sim \frac{1}{2 \times F/number}$; hence, for example, a NA of 0.1 is approximately equivalent to F/5.

In addition to NA matching, another factor will effect the efficiency of the system: transmission. Typically, off-the-shelf optical fibres in the visible-NIR waveband will have a throughput of $90-99\%$ per m, with transmission dropping most substantially at the blue end of the spectrum. As such, it is most efficient to minimise the length

of optical fibre required by the design of an instrument.

Another consideration in the selection of optical fibres is a phenomena called modal noise. Modal noise is an instability in the output illumination of the optical fibre seen in multimode fibres. This can be caused by incomplete filling of the fibre, where some fibre modes aren't filled, or intermodal phase variations/dispersion, where the input signal is spread out in time because the propagation velocity of the optical signal is not the same for all modes. This instability can lead to variability in the PSF of the spectrograph's resolution elements by causing the centroid of the resolution element to shift. This introduces RV noise and, furthermore, reduces the RV precision of the instrument.

Modal noise is proportional to λ/h, where λ is the wavelength being coupled to the fibre and h is the diameter of the fibre (Baudrand & Walker, 2001). As such, smaller fibres are more susceptible to model noise and require robust modal noise reduction solutions in order to be applicable in high precision RV spectrographs.

One such solution to mitigate modal noise is by applying fibres with different core shapes. In their paper, Chazelas et al. (2010) demonstrate that fibres with octagonal and square cores can show improvements in near-field mode scrambling by a factor 5 to 10 compared to the circular fibre. This is further corroborated by the work of Avila (2012).

Other modal noise suppression solutions include double scramblers, that exchange near- and far-field filling of the fibre to ensure complete filling, and fibre stretchers, which modulate the phase between modes, stabilising the PSF for any modal content.

2.0.10 Noise

In addition to purely optical phenomena, noise will also impact the fidelity of our observations.

If we consider the spectrometer system as heavily photon noise dominated and assume that photon noise can be modelled by Poisson statistics, then a basic estimate of the signal-to-noise ratio (SNR) of a measurement can be calculated. The signal is the total number of photons detected on a given pixel, I_s. If the signal is recorded a large number of times under identical conditions, the mean signal is $\langle I_s \rangle$ with a statistical fluctuation in the number of detected photons about the mean. This fluctuation is due to the random arrival rate of photons and the random selection of those that are detected. The noise introduced by photon noise will be given by the standard deviation of the photon distribution. As the variance of a Poisson distribution is equal to the mean of the distribution, e.g. the number of photons,

$\langle I_s \rangle$, the standard deviation can be seen to be $\sigma_s = \sqrt{\langle I_s \rangle}$. Taking these definitions for the signal and noise at a specific pixel, the signal to noise ratio for a pixel can be shown to be given by,

$$SNR = \frac{Signal}{Noise} = \frac{I_s}{\sqrt{I_s}} = \sqrt{I_s} \, . \tag{2.12}$$

Hence, this is why the full well capacity of the instrument's detector limits the maximum signal to noise that the system can capture.

Realistically, in addition to photon noise, there are many other sources of noise which contribute to the measurements taken by the instrument. We shall discuss these sources briefly here:

Background Noise

Dust, molecules and clouds scatter photons from our astronomical source in addition to light from other sources (e.g street lighting, sunlight and moonlight) into our telescope. These molecules in the atmosphere also emit light. Due to this, the night's sky is not perfectly dark, but acts as a noisy background to the light detected from astronomical objects. The sky background can be brighter than faint stars, making the detection of faint sources difficult.

This source of noise is also a Poisson counting process and as such, the noise associated with the background can be expressed as $\sigma_b = \sqrt{\langle I_b \rangle}$, where $\langle I_b \rangle$ is the mean number of photons detected from background sources.

In their paper, Roy et al. (2020) propose some innovative techniques which apply sky monitoring to remove background sources of noise and aid in reaching $10cm/s$ RV precision. They discuss three methods for background removal: (1) subtraction of the CCF produced by a dedicated sky fibre from the science CCF, where the sky fibre has the same spectral properties (resolution and throughput) as the target fibre, (2) subtraction of a scaled model solar spectra from the science spectrum, applying the sky fibre CCF to scale the model, and (3) using simultaneous broadband measurements of the background sky to scale a template solar spectrum which can be subtracted from the science spectra. Their findings suggest that applications of these methods can, in principle, reduce RV errors to well below the $10cm/s$ level.

Thermal Noise

For instruments operating in the NIR-IR wavebands, this source of noise is especially important. Components of the instrument thermally emit at room temperature in

the IR with photons in the Wien's tail reaching NIR wavelengths. This emission can reach the instrument's detector and contribute to the noise of a detection. For this reason, NIR-IR instruments are often cooled to cryogenic temperatures to minimise these emissions.

Unfortunately, the story doesn't end there. Measurement in CCD's are produced by photons exciting electrons from the valence band of the sensor to the conduction band. However, it is also possible to excite electrons into the conduction band via thermal excitation. Electrons excited in this way are indistinguishable from photo-electrons and hence, introduce noise known as dark current. This noise is again of the form $\sigma_d = \sqrt{\langle I_d \rangle}$.

The effect of this noise can be mostly mitigated through the subtraction of dark frames.

Read-Out Noise

Ideally every photon that comes in contact with the CCD would produce one electron in a pixel, which would be measured as one count by the analogue-to-digital converter (ADC).

The read-out electronics measure the voltage across a capacitor, which is about one micro-volt for each electron in the pixel. Unfortunately, this voltage cannot be measured with perfect accuracy, which introduces a readout-noise in the charge measured in every pixel. In a good CCD, the readout-noise can be found to be on the order of $3e^-$ per pixel. Such that even if every pixel contained a uniform number of photo-electrons, the read-out value would vary by approximately $3e^-$ pixel to pixel.

This noise is time independent and is not dictated by Poisson statistics, so we shall label it of the form $\sigma_r = r$.

Signal-To-Noise Ratio

As all of these noise sources are independent, the resultant variance is the sum of the variances for all of these Gaussian variables, such that the total noise is given by $\sigma_{tot} = \sqrt{I_s + I_b + I_d + r^2}$. Therefore the total SNR is represented by,

$$SNR = \frac{I_s}{\sqrt{I_s + I_b + I_d + r^2}}\,. \tag{2.13}$$

In terms of photo-electrons generated for a given photon flux, this expression can be rewritten as,

$$SNR = \frac{sQt}{\sqrt{sQt + bQt + dt + r^2}}\,, \tag{2.14}$$

where Q is the quantum efficiency of the detector, t is the length in time of the exposure, s is the photon flux of the signal, b is the photon flux of the background and d is the dark counts per second (Schroeder, 1999d).

Let us consider a spectrometer system undertaking an observation of exposure time, t, for an object emitting constant flux in a given waveband. If the spectrometer system's resolving power is increased, the constant amount of flux is spread over a larger number of resolution elements. Hence, for a high-resolution spectrometer system, the number of photons incident on the detector would need to be increased in order to achieve the same SNR as that achieved by a low-resolution spectrometer. Rewriting equation 2.13 in terms of its dependence on resolving power R, we see that,

$$SNR = \frac{P_s/R}{\sqrt{P_s/R + P_b/R + P_d/R + r^2}}, \qquad (2.15)$$

where P_s, P_b and P_d are the photons detected by the entire detector from the signal source, background and dark current respectively. The dependence of SNR with resolving power is depicted in figure 2.12.

This relation shows that as the resolving power of the spectrometer increases, the SNR for the same observation decreases. This highlights why it is important that high-resolution spectroscopic observations receive a high number of photons for each science frame taken. This is achieved either by increasing the length of your exposure, t, or where possible increasing the light collected from the object of interest. Hence, why the size of our telescopes limit our ability to make measurements of faint objects and why cutting-edge high-resolution spectroscopic studies are conducted at the world's largest telescopes.

The resolving power $R = 100,000$ is the 'sweet spot' for such spectroscopic studies. This is because it provides the necessary resolution to resolve molecular lines, thereby supplying enough spectral lines to allow accurate measurement of radial velocities, whilst also not spreading the photon flux too thin in order to allow sensible SNR values to be achieved (on the order of $SNR = 100$) for 'faint'[1] objects with sensible exposure times (on the order of $t = 10 minutes$) (Fischer et al., 2016). This is why

---

[1]The definition of a 'faint' object for RV study varies upon the diameter/collecting ability of the telescope and the throughput efficiency of the instrument. As a rough figure, a spectra of resolving power $R \sim 100,000$, with $SNR \sim 100$, can be produced with an exposure of approximately 30 minutes on a 2m aperture telescope, with a $\sim 10\%$ efficient spectrograph, for a star of magnitude ~ 6. This will scale following the definition of magnitude for larger collecting areas. As an example, the faintest star noted on the 'The Extrasolar Planet Encyclopedia' to have had a companion object, specifically a brown dwarf, detected with the radial velocity technique is Cha Ha 8 with an apparent V magnitude of 20.1; this was achieved with UVES at the VLT (Roques, 2020; Joergens et al., 2010).
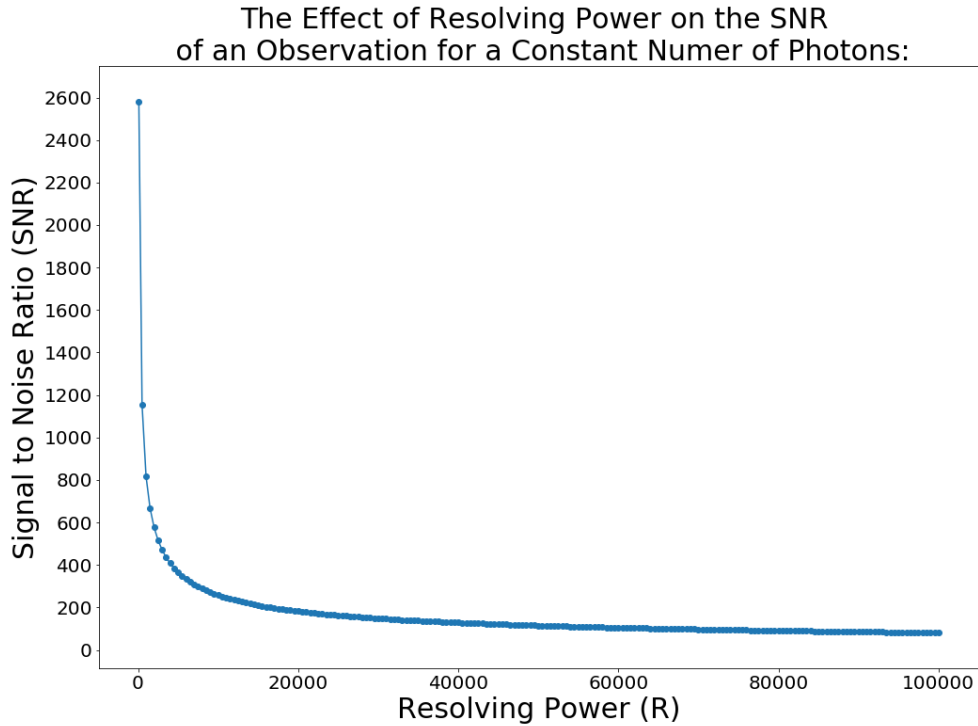
Figure 2.12: Plot of resolving power (from 100 to $100,000$) against SNR for a spectrometer system with a constant number of photons incident on the instrument detector for all resolving powers. For this plot, $P_s = 10^9$ total photons were detected by each of the instruments such that an instrument with $R = 100$ would detect 10^7 photons per pixel and an $R = 100,000$ spectrometer would detect $10,000$ photons per pixel. P_b, P_d and r were set to values typical of CCD detectors, with $P_b = 0.3P_s$, $P_d = 0.2P_s$ and $r = 5$. It can be seen that while an $R = 100$ spectrometer system can achieve a $SNR \approx 2600$, for the same observation with the same telescope an $R = 100,000$ spectrograph would only achieve a $SNR \approx 100$. This highlights why larger aperture telescopes are required for high-resolution spectroscopic studies.

$R = 100,000$ is the resolving power that most spectroscopic instruments designed for exoplanet science aim to achieve.

2.0.11 Considerations for High-Resolution Spectrograph Design

As highlighted by equation 2.6, the resolving power of a high-resolution spectrometer is dictated by the focal length of the collimating lens, the size of the optical fibre (or slit) and the blaze angle of the diffraction grating. However, within these terms, a number of other specifications of the optical system are encoded.

Principally, the size of the diffraction grating will set the aperture of the system and, hence, the diameter of collimated beam which can be efficiently incident upon the grating. For an optical fibre with its given NA (or F/number), a limit is set on the maximum focal length of the collimating lens. This limit ensures that the collimating lens produces a collimated beam, from the light of that fibre, with a diameter smaller than the size of the grating aperture. This demonstrates how the spectrograph instrument is a highly constrained system.

Further to the resolving power, the decisions made in the selection of these components also impact the size of the optics and overall instrument, in addition to the cost of the instrument; as larger optics are typically of higher cost to manufacture.

Another design requirement which has an impact on the cost of the instrument is throughput efficiency. In order to maximise signal-to-noise for a given exposure time, the efficiency of the spectrograph should be maximised. There are a number of ways to do this. Typically, the most 'lossy' component of the instrument is the diffraction grating, which can be anything as low as $10 - 20\%$ efficient for low-cost gratings. Hence, investment should be made in a precisely ruled grating to maximise throughput. Next, the prism and lens elements should be made from materials with a high transmittance and be coated with anti-reflective (AR) coatings to minimise Fresnel reflection losses. Typically, the more AR coating layers applied to the surface, the better the transmittance, which has a direct impact on the manufacturing cost of the optics. A high throughput optical fibre solution should be implemented and the selection/arrangement of the optics should avoid any vignetting. Finally, a detector for the instrument should be chosen which has a high quantum efficiency, maximising the reading efficiency of the incident photons.

Furthermore, the chosen detector should also have minimal noise sources intrinsic to the detector; such as thermal noise and read-out noise. Currently this is best achieved with CCD detector technologies, but advancements in CMOS technologies

may make these detector types feasible for photon-starved, astronomy applications in the future. The spectrograph design and detector selection are also intrinsically linked in their mutual collaboration in fulfilling the Nyquist sampling criterion. The image magnification produced by the spectrograph is controlled by the ratio of focal length of the collimating lens and re-focusing lens, while the pixel size is set by the detector selection. Hence, by selecting magnification and pixel size parameters which are consistent with Nyquist sampling, aliasing of detected signals can be avoided.

2.1 Conclusion

In this chapter, the theoretical concepts required to understand the design of high-resolution, Echelle-type spectrographs, and how these feed into the realisation of instrumental requirements, were outlined.

The physical relations dictating the function of the dispersing elements, the diffraction grating and the prism, were discussed with an emphasis on the aspects which are important factors in the spectrograph design process.

The derivation of the 'resolving power equation' was investigated, highlighting the factors which impact the resolution of a high-resolution spectrometer. This then fed into discussion on the resolution element and the two optical phenomena that can impact its size: diffraction and optical aberrations. The necessity and requirement for spectrograph instruments to meet the criteria outlined in Nyquist–Shannon sampling theorem was outlined, with discussion on this topic concluding with the effects of anamorphic magnification on the shape and size of the resolution element.

The conservation of etendue and way in which this factors into the design of fibre coupling systems, which allow efficient coupling of the telescope to the spectrograph, was summarised. The impact of this on the specifications of the optical fibre were then highlighted, followed by a deeper investigation into the optical fibre requirements of fibre-fed spectrometer systems.

A breakdown of noise sources was undertaken with a discussion on how these sources can be minimised, as well as how they impact the signal-to-noise performance of high-resolution spectrographs.

The chapter then concluded by discussing some of the consideration that go into the design of high-resolution spectrometers.

In the following chapter, the application of the theory discussed in the preceding chapters will be examined in the design of a compact, low-cost, high-resolution spectrograph: QMSPEC.

3 QMSPEC: A Highly Replicable, Low-Cost, Portable, General-Purpose, High-Resolution Spectrometer with Applications in Stellar Studies and Exoplanet Science

Abstract

High-resolution spectrometers have proven to be an important tool for astronomical observations and continue to have an ever expanding set of applications, such as high resolution IFS (Integral Field Spectroscopy). With this in mind, presented here is an alternative approach to the design and construction of Echelle type spectrometers. The usual approach is to drive high resolving power through the use of large gratings and long focal length collimators, leading to great production costs in the order of $1,000,000$. This compact, proof-of-concept prototype, via the coupling of adaptive optics, achieves comparable performance and resolution to those instruments; with a theoretical resolving power $R > 80,000$ in the Vis-NIR regime ($500nm - 1\mu m$) at a cost $< \$10,000$. This is attained through the use of commercially-off-the-shelf (COTS) and economically designed components. The overall device footprint is compact, measuring the size of a 'shoe-box', approximately $30cm \times 15cm$. The spectrometer prototype is fibre-fed with a single $10\mu m$ fibre and follows a double-pass design; applying a custom designed, $108.24mm$ focal length, collimating and re-focussing lens. The system follows an Echelle type design with high resolution achieved through the use of a compact R4 diffraction grating and a prism as the cross-disperser.

3.1 Introduction

As discussed in section 2, optical spectrometers are devices that take an input light source and separate that source into its constituent wavelengths to produce a resultant output spectrum of wavelength against respective intensity. High resolution spectrometers are spectrometers that are able to resolve difference in wavelength to smaller increments than medium and low-resolution spectrometers; these are generally defined in the visible regime as able to resolve differences in wavelength down to the order of $10pm$.

High resolution spectroscopy has proven to be an important tool in modern astronomy, with applications varying from galaxy redshift surveys (such as those completed with the DEIMOS instrument) to stellar evolution studies (using for example the N∃SIE instrument) and exoplanet discovery/characterisation with the Doppler method (Faber et al., 2003; Kintziger et al., 2018; Struve, 1952).

There are numerous ways to design high resolution spectrometers. The layout chosen here is the classic Echelle design, first pioneered by Nagaoka & Mishima (1923). This design uses blazed grating facets to maximise throughput in higher diffraction orders and applies a prism cross-disperser to separate each of the diffraction orders. This spectrometer design produces a 'ladder-like' spectrum with orders which are spatially separated, as demonstrated in figures 2.2 and 2.3.

With large scale contemporary instrumentation projects hindered by technology readiness level (TRL) set-backs and ever-increasing budget requirements, such as the production of E-ELT HIRES, the question is raised as to whether projects of this size, and larger, are feasible going forward. As such, we suggest that the design of instrumentation should be approached in a different way (Ramsay et al., 2016). With this mind-set, we aim to demonstrate that a compact high-resolution spectrometer with applications in astronomy can be produced in a replicable manner at a low cost.

3.2 Design Overview

3.2.1 Basic Considerations for the Echelle Design

Following from the calculations discussed in section 2.0.4, we see that the performance of a high-resolution spectrometer can be measured using the metric of resolving power. This is characterised by $R = \frac{2f_1 \tan(\alpha)}{h}$, equation 2.6. This relation shows that resolving power can be increased by either increasing the focal length

of the collimating optic (which in turn increases the beam size and the size of the required grating), increasing the blaze angle of the grating or decreasing the size of the optical fibre.

By applying equations 2.7 and 2.11 it can be seen that a spectrometer which has been designed to be coupled to small telescope systems can also be effectively coupled to some of the world's largest telescopes through the application of adaptive optics. The spectrometer discussed here has been designed to be coupled to a $0.5m$ telescope with an $F/ = 4.51$ such that its focal length is $2.255m$. By forcing the telescope beam to fit the numerical aperture of commercially available optical fibres ($NA \sim 0.11$), the physical image of a point star becomes $10\mu m$ for a seeing limited beam with a seeing of $1 arcsecond$. The diffraction limited image of such a telescope would have a diameter of approximately $4\mu m$. Hence, for a spectrometer that is designed to operate at the seeing limit of this telescope, the input is 2.5 times larger than it would strictly need to be for a diffraction limited instrument. It can be shown that this relation holds for telescopes of arbitrary sizes. As long as a moderate performance AO (Adaptive Optics) system is operational (which can correct the image to smaller than 2.5 times the diffraction limit of the instrument), the spectrometer discussed in this chapter can be efficiently coupled to any arbitrarily large aperture[1].

Hence, with AO, a small inexpensive spectrometer could be effectively coupled to a telescope as large as the EELT or, more productively, an array of high-resolution spectrometers could be fed by an integral field fibre array, opening a wide-array of observational possibilities. This offers a scalable way (linear with the number of units) to equip large telescopes with high resolution spectrometers; and enables new exciting science cases, as discussed by Snellen et al. (2015).

3.2.2 Top-Level Requirements

The spectrometer aims to be applicable to atomic and molecular spectroscopy. Given the typical conditions in main sequence stars, this can be achieved with a resolving power of $R > 50,000$. However, $R \approx 100,000$ typically provides the 'sweet-spot' between high spectral resolution and light collection efficiency (Fischer et al., 2016). The optical-NIR bands are required for most exoplanet science cases (Fischer et al., 2016). With this in mind, this spectrometer prototype is designed to operate between $500nm$ and $1\mu m$ with the overall aim of achieving as broad a wavelength range as possible in a single device. The device must be low-cost, with the prototype

---

[1]It is to be noted here that adaptive optics can, in theory, allow us to reach the diffraction limit but never surpass it.

having a total component value less than \$15, 000 and with a finalised replicable unit manufacturable for under \$10, 000. A summary of these and other requirements are given in table 3.1.

3.2.3 Technical Specifications and Constraints

Minimising instrument cost is a key requirement of the chosen design approach. This restricts the instrument to the use of COTS diffraction gratings, which mainly consist of replica gratings. While the availability of COTS gratings in recent years is far greater than it has ever been before, the number of available options are still limited. Due to this, the grating was the first component to be chosen; beginning the process of constraining the system design. The Thorlabs GE2550-0875 Echelle Grating (79.0 $grooves/mm$, $75deg$ Blaze Angle, $25mm \times 50mm$ face dimensions) was selected due to its large, almost R4, blaze angle at a very low-cost; along with its ease of availability. Ideally a grating with a lower number of $grooves/mm$, such as Thorlabs' 31 $grooves/mm$ offering, would have been chosen. This is more desirable as it would form a spectra with a larger number of shorter orders, leading to a squarer shaped echelle spectrum. Hence, the amount of anamorphic magnification observed in the system would be reduced, as discussed in section 2.0.7. This would also allow the spectrum to better fit onto conventional CCD sensors. Unfortunately, this grating is only offered with an R2 blaze angle, which would not allow the required resolution to be achieved.

With the diffraction grating chosen, the diffraction grating blaze angle parameter is set to $75deg$. The diffraction grating width of $25mm$ sets the upper limit on the size of the aperture stop for the system, this is because the width of the diffraction grating places a constraint on the collimated beam diameter that the diffraction grating can accept. The resultant beam diameter for the system was chosen to be $24mm$ to avoid using the very edge of the grating where it is expected that performance is degraded through the grating's manufacturing process. Ideally the grating would have a height of $100mm$, such that when it is operated at R4, the projected aperture is $100mm \cos 75deg = 25.88mm$; encompassing the entire beam. Unfortunately, Thorlabs only produce gratings of height $50mm$, giving a projected aperture of $50mm \cos(75deg) = 12.94mm$, which is less than the $24mm$ beam diameter. Fortunately, due to the geometry of a circular, gaussian beam incident on a rectangular grating cross-section projection, the majority of the light intensity in the beam cross section is accommodated by the grating.

As can be seen in equation 2.6, another way to increase resolving power is to

Table 3.1: Outline of QMSPEC's top-level requirements.

Property:	Technical Requirement:	Goal:
Spectral Resolution	$> 50,000$, sufficient to resolve atomic and molecular spectral lines on main sequence stars and planets. This resolution is also sufficient to resolve the signature of Earth atmospheric molecular gases. Satisfying this condition requires both careful selection of the spectrometer's dispersive elements and stringent constraint on the system's image quality.	100,000 achievable in a slightly reduced throughput mode by reducing the size of the input image. Such a mode could be very useful in high-S/N applications (solar and air gas analysis).
Wavelength Coverage	$600 - 900nm$. This is the wavelength range where: adaptive optics systems perform well (in the optical), nearby sun-like stars down to red-dwarfs have most of their flux, and numerous Earth atmosphere gases have strong spectral signatures (eg. O_2, H_2O). This wavelength range also covers wavelengths where toxic gases such as HCl and HF have numerous absorption features.	$500 - 1000nm$. On the blue end, it would add substantially more information on Sun-like stars, and on the red end it would enable monitoring of additional gases with strong absorption bands at $\sim 1\mu m$ (eg. CH_4, C_2H_2, NH_3, e.t.c.). Furthermore, at this wavelength range, commercially-of-the-shelf, Si based detectors have good quantum efficiency ($> 75\%$) across the entire waveband, enabling the production of low cost instruments.
Wavelength Calibration & Stability	Able to provide $\sim 5m/s$ precision in the measurement of Doppler shifts of stellar or telluric atmospheric lines during integrations of $\sim 600sec$. This mainly imposes constraints on mechanical and temperature stability.	$< 2m/s$ precision for $60sec$ integration on Solar observations and bright stars.
Efficiency (from input to detector)	$> 6\%$ for $600 - 900nm$ to remain competitive with existing echelle spectrometers. Moderately high efficiency is also needed to keep integration times low in high-contrast imaging applications.	$> 10\%$ for $500 - 1000nm$, at least on specific ranges where Quantum Efficiency (QE) of the detectors is higher.
Abs. Wavelength Calib.	$< 2m/s$ precision per calibration set (before and after each observation).	$< 2m/s$ precision (once per night).
Size	$360mm \times 260mm \times 120mm$, the size of a conventional shoe-box.	$300mm \times 100mm \times 100mm$, the size of a $3U$ cube-sat.
Cost	$\$15,000$	$\$10,000$

Table 3.2: Summary table of key design parameters once constrained to a feasible combination of COTS components.

Fibre size	Fibre NA	System F/#	Collimating Lens Focal Length	Blaze Angle	Facets (Grooves/mm)	Theoretical Resolving Power
$10\mu m$	0.11	4.51	108.24mm	75deg	71	81,000

reduce the size of the optical fibre. It is to be noted that the image size and the numerical aperture are set by the image size and numerical aperture producible by the telescope with a focal reducer, for efficient coupling. As discussed in section 3.2.1, a fibre size of $10\mu m$ with 0.11 NA allows for the efficient coupling of the spectrometer with a $0.5m$ aperture telescope. The closest COTS optical fibre to this is the Thorlabs M65L, which has a 0.1 NA. This was used for prototype testing and due to this, the current prototype has some loss in throughput. A 0.11 NA fibre could be cheaply manufactured for the final system to remedy this. With this value chosen, the third constraint on the spectrometer system is set; this now limits our last component of interest: the collimating lens. As the fibre will accept and re-emit light with a numerical aperture of 0.11, or equivalently an F/number of 4.51, we can determine the required focal length of the collimating lens, f_s, from the definition of the F/number and the required beam diameter of $24mm$: $f_s = F/ \times D_s = 4.51 \times 24mm = 108.24mm$. As such, the collimating lens requires a $108.24mm$ focal length to produce the required $24mm$ beam diameter with the 0.11 NA optical fibre.

   With these key parameters set, the theoretical resolving power of the system can be estimated. Using equation 2.6 with $f_1 = 108.24mm$, $\alpha = 75deg$ and $h = 10um$, it is found that $R = 81,000$.

   Through the use of such a compact grating (with the resulting small collimated beam size and the short collimating lens focal length that comes from this), an instrument can be constructed with a high resolving power and a highly compact size; at around the size of a shoe-box. The key parameters of this design are summarised in table 3.2.

3.3 Preliminary Testing

Prior to substantial investment in the design and procurement of the full instrument, a preliminary proof of concept was constructed. This consisted of the essential components of an Echelle spectrometer: a diffraction grating (Thorlabs GE2550-0363:
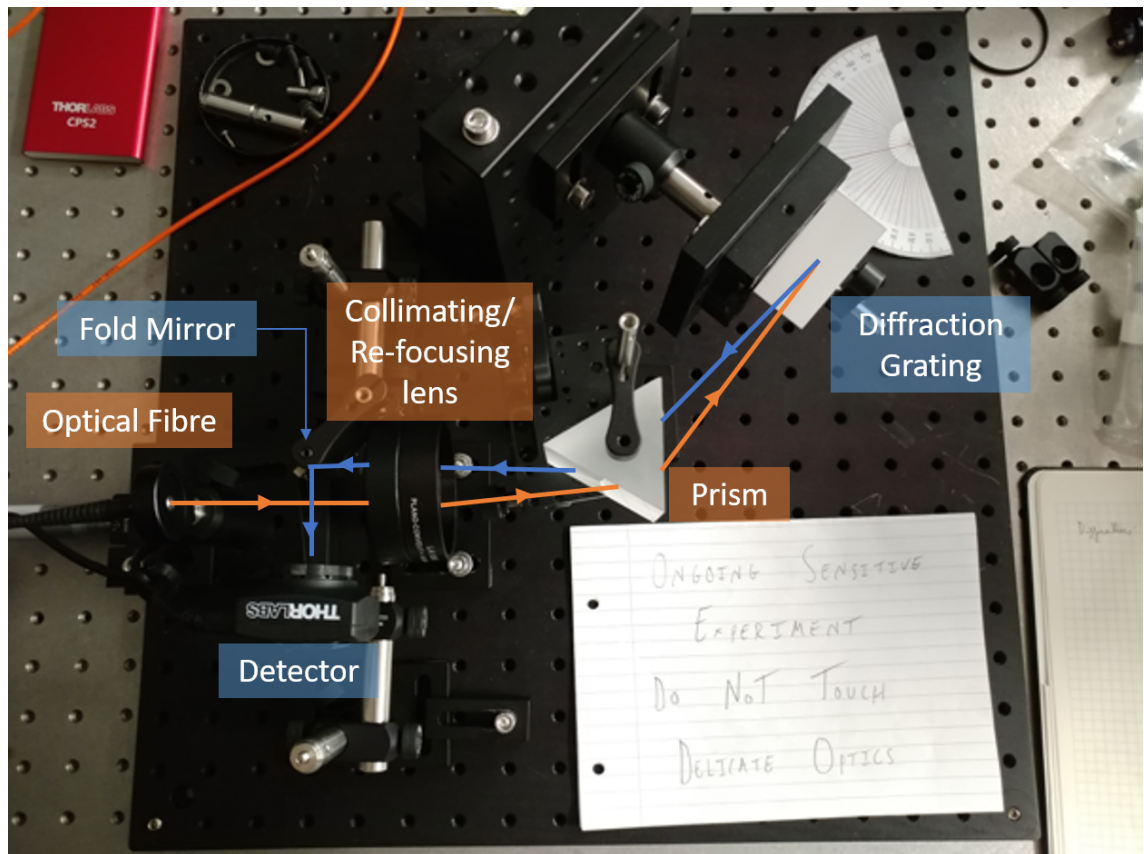
Figure 3.1: Annotated image of the preliminary spectrograph breadboard test.

R2, $31.6 grooves/mm$), a prism (Thorlabs PS854: F2 Equilateral Prism, $50mm$), a singlet collimating/re-focusing lens (Thorlabs LA1050: N-BK7 Plano-Convex Lens, $\varnothing 2''$, $f = 100mm$), a small fold mirror (Thorlabs ME05S-G01), the Thorlabs M65L optical fibre and a low-cost CMOS detector (Thorlabs DCC1645C). The entire system was assembled using off-the-shelf kinematic mounts as shown in figure 3.1. The total system cost is on the order of approximately £500.

Following equation 2.6, the theoretical maximum resolving power of this system is $R = 39,252$. For a small field and wavelength range, it was possible to align the system such that it can achieve a resolving power of $R = 17,833 \pm 2,000$. This was measured using the pixel separation and resolution element size observed in the Sodium D-doublet, as shown in figure 3.2, and comparing this to the known separation in wavelength of the Sodium D-doublet.

This experiment demonstrated that high-resolving power can be achieved in a compact Echelle system, proving the feasibility of the base concept and suggesting that further study may produce an innovative instrument.

It was determined that the limiting component in this instrument set-up is the
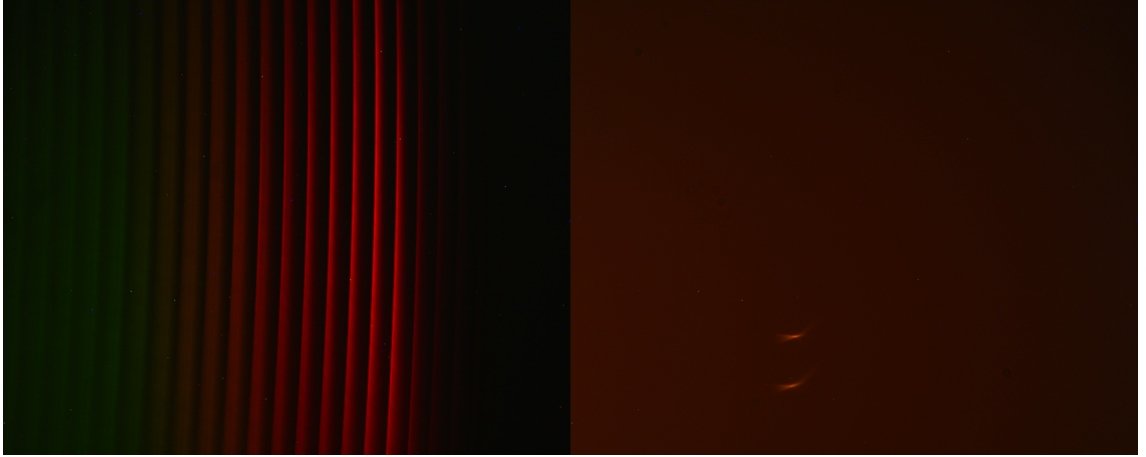
Figure 3.2: (Left Pane) Image of the Echelle spectrum produced by the preliminary spectrograph test. (Right Pane) Image of the Sodium D-doublet produced by the preliminary spectrograph test with optimal alignment of the field and wavelength region in which the Sodium D-doublet resides.

singlet lens. This lens introduces significant optical aberrations, limiting its ability to resolve objects at fields greater than $0.1deg$ from the optical axis and over wavelength ranges larger than a few nanometers. As such, it was decided that primary focus of this project should be made in the study, design and construction of the collimating and re-focussing optics.

3.4 Optical and Mechanical Design

As discussed in section 2.0.4, the focal length of the re-focussing lens is a free parameter in terms of resolving power performance. However, the ratio of the collimating lens and re-focussing lens' focal lengths determine the magnification of the spectra image in the focal plane. Given this, the main aim of the re-focussing lens' design is to magnify the spectra image to allow optimal Nyquist sampling on the chosen detector.

With this in mind and with the aim of keeping the system as compact as possible, the approach taken to the optical layout of the spectrometer was given substantial scrutiny. There are two ways the optical layout can be designed:

- Single pass, where the system has a separate collimating and re-focussing lens, shown in figure 2.2 and as seen in the design of UVES or HARPS (Dekker et al., 2000; Pepe et al., 2000).

- Double pass, where the system uses one lens for both the collimating and

re-focussing of the beam, as seen in PFS (Crane et al., 2006).

Both of these optical layouts have their intrinsic pros and cons. For this system, the double pass design was chosen to maximise compactness and to minimise the number of components; reducing overall system cost. In addition to this, the beam reflection angle at the grating (in the cross-dispersion axis) can be substantially reduced for a compact double pass system, leading to a more symmetric system, hence reducing anamorphic magnification effects (Schroeder, 1999e).

3.4.1 The Aperture Stop

A very important item of note in the design of spectrometer systems is the location of the aperture stop. This can be defined as the point where all of the principle rays of the system cross each other at the optical axis (Welford, 1986b). In a spectrometer system the location of this aperture stop can be seen to be at the location of the diffraction grating, as that is where all of the principle rays cross the optical axis during the process of dispersion. In the majority of commercial lens system, such as camera lenses, the aperture stop is located within the lens itself. As such, a custom optic must be designed for the purpose of the collimating/refocussing lens of this instrument.

3.4.2 Optical Design Parameters and Requirements

The collimating/refocussing lens, henceforth known as the lens, was designed to have the aperture stop 135mm away from the front element of the lens. This was chosen as a good estimate to the placement of the diffraction grating, accommodating the physical placement of both the prism and the grating. This aperture stop placement allows the lens to accommodate beams traveling away from the optical axis when they reach the lens' front element, focussing them back towards the image plane. Figure 3.3 demonstrates the lens' function and how this differs from a standard camera lens.

With the aperture stop placement set, the next most important set of requirements for the lens design are field angle acceptance and required wavelength range. The latter of which was chosen to be 500nm-1um, with the aim to achieve diffraction limited performance across this entire range.

Ideally, one would design the lens to accept the largest field angle possible, but this becomes an issue as there is a trade off with spot size performance and optimised field acceptance angle. The larger your accepted optimised field, the larger the angle
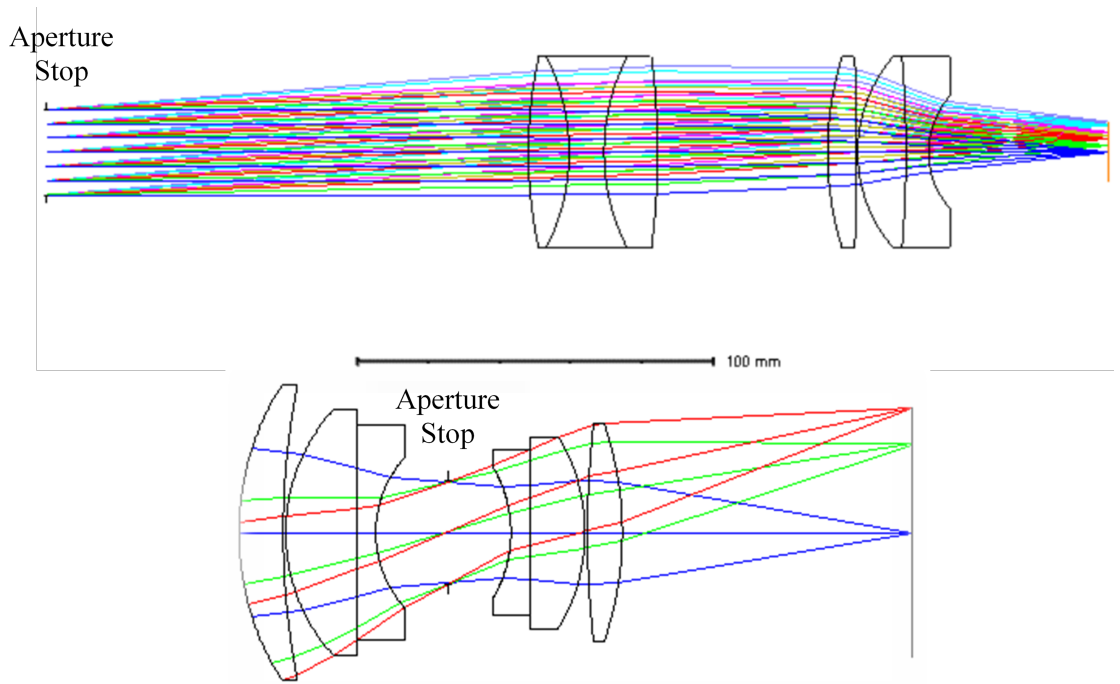
Figure 3.3: Schematic diagram depicting the location of the aperture stop for a spectrometer's collimating/re-focussing lens (Top Panel) and a conventional lens; a Double-Gauss design in this case (Bottom Panel).

where the lens performance must be optimised and hence the worse the performance across the entire field becomes[2]. Therefore, it is prudent to only optimise the lens for the fields required. In order to determine the field angle acceptance required by the lens, the dispersion angles produced by the diffraction grating and the prism must be characterised.

For the diffraction grating, the maximum dispersion angle of interest is determined by the first minima of the blaze function. This field angle is calculated as discussed in section 2.0.2, using equation 2.4: $\overline{\beta}_{\pm}^{max} = \pm \sin^{-1}\left(\frac{2\tan\phi}{m}\right)$.

Using the grating equation for a grating with 79.0 $grooves/mm$ and a 75deg blaze angle, a test wavelength of 800nm is found to be in order 30. Substituting these values into equation 2.4, the first minima of the blaze intensity function is found at 3.692deg. Note that the blaze function is widest at the lowest order, so the lower orders down to order 24 at a wavelength of 1μm should be expected to be slightly wider than this. As such, the lens should be designed to accept at least a field angle from the optical axis of $\sim 3.8deg$.

The dispersion of the prism is characterised at the angle of minimum deviation

---

[2]The same effect is seen for wavelength range as well as field angle.

by equation 2.5: $\delta_{min} = 2\sin^{-1}\left(n\sin\frac{\gamma}{2}\right) - \gamma$.

For an N-BK7 prism with a dispersion angle of $\gamma = 45deg$, the total deviation in field angle between the lowest and highest order is found using equation 2.5. The refractive index for our extreme wavelengths are as follows, $n_{500nm} = 1.5214$ and $n_{1000nm} = 1.5075$. Hence, substituting into equation 2.5 we find $\delta_{500nm} = 26.21deg$ and $\delta_{1000nm} = 26.47deg$, leaving the difference in dispersion angle of $\Delta\delta = \delta_{1000nm} - \delta_{500nm} = 0.745deg$. Therefore, the total deviation in field angle introduced by a $45deg$ N-BK7 prism is $0.745deg$. Further to this, it is found that this prism gives a separation of on average 5.2 fibre widths between orders, allowing for a compact spectrum as required.

Following these two field acceptance requirements, set by the grating and prism, the lens should be designed to accept a minimum field from the optical axis of $3.8deg$. It was decided to set the minimum field acceptance angle from the optical axis to be $5deg$, giving $10deg$ of field acceptance in both directions. This allows for the introduction of some additional field angle from the beam reflection angle at the grating (in the cross-dispersion axis), which is required for the double pass layout. In addition, this extra field freedom gives the opportunity, later in the design process, to alter the optical layout or use a grating with a wider blaze function.

3.4.3 Imaging Performance Target

As discussed in section 2.0.5, point source objects will be imaged through the spectrometer to a finite size due to the diffraction limit and optical aberrations. The fibre head has finite size and so it can be thought of as made up of an array of 'many' point sources. The image produced by the fibre is hence a convolution of the fibre's perfect image and the point source image. Hence, the size of the final image will be given by equation 2.9: $U = \sqrt{h^2 + p^2}$.

Given the fibre head size is $10\mu m$, the spot diameter of the lens' re-imaging of a perfect point source can be allowed to reach approximately $6\mu m$ with minimal increase in image size and hence loss in resolution.

3.4.4 Detailed Lens Design and Manufacturability

Throughout the lens design process, the aim was to minimise the number of optical surfaces in order to maximise throughput. Initial testing in both in the laboratory and using Zemax models found, as expected, that singlet and doublet lenses do not have the necessary degrees of freedom to achieve the near diffraction limited

performance across the field and wavelength range required. As theoretically understood, a triplet lens has the lowest number of elements required to provide the necessary number of degrees of freedom to correct for all of the Seidel aberrations (Welford, 1986c). Whilst, ideally, a triplet would be applicable as our double pass lens system, we aim to produce the spectrometer at a low-cost. Hence, our glass selection is greatly reduced to that which is readily available and low in cost. With this limitation in glass selection, and hence limitation in refractive index and Abbe number of the lens elements, it was found that the minimum number of elements required to achieve near diffraction limited performance following our wavelength and field criteria was 6 elements.

The initial lens design was based on the well-studied Double Gauss lens with the aperture stop placed at the required $135mm$ away from the front element of the lens. The Double Gauss was selected due to its high resolution, diffraction limited imaging performance at large field angles across a wide wavelength range. It was found, as expected, that applying such a significant stop shift to the lens caused its properties to vary significantly from its initial design. With this began the optimisation and re-design process.

Through the use of Zemax optical studio, the lens was re-optimised and redesigned until its imaging performance met the $10\mu m$ spot diameter criteria or, if it came first, diffraction limited performance for the field and wavelength requirements specified. It is to be noted that at this stage of the design process, the lens was optimised purely as a re-focussing lens. The design was approached in this way as when the lens was placed into the full spectrometer model, due to the double pass set-up, the number of degrees of freedom for Zemax to optimise were too great to lead to applicable results in a reasonable timescale. Once a design that fit the design criteria was found, the manufacturability/procurement process was begun.

Prior to contacting manufacturers, the lens tolerances were tested using Zemax's tolerancing tools. This comprised of setting tolerances for all of the lens parameters and running a series of, say 3000, Monte-Carlo simulations. This produces a series of systems within the parameter space set by the tolerances and allows the performance of these systems to be observed. If less than 95% of the systems performed as expected, the tolerances were tightened where necessary. The Zemax tolerancing tools highlight which tolerances have the largest effect on performance, allowing the adjustment of tolerances which are required and enabling those which do not effect performance to be left looser. This was repeated until the performance of 95% of the simulated systems performed as required.

The procurement stage of the optical design was unexpectedly the longest single

stage of the entire instrument design. Between an applicable design being created in Zemax and a manufacturable, low-cost, procurable design being reached was approximately 9 months of design work. The design went through 8-10 major redesigns with input from manufacturers. The process would commence as follows: a manufacturer would be approached and they would give a list of criteria to meet in order to bring the lens to a manufacturable state. In terms of design, these criteria would generally relate to glass selection, lens thickness, edge thickness, surface curvature or overall system tolerances. In addition to this, each of the lens parameters would require reasonably loose tolerances in order to be manufactured at the required low-cost. Once a design was iterated with the manufacturer a number of times until it met these criteria and also still fulfilled our performance requirements, we would return to the manufacturer for a quote. Unfortunately, we found on multiple occasions that manufacturers would either no longer be interested in producing a small batch of lenses, the quote would beyond the scope of this project or the tolerances required would be too tight. This then began a cycle until we contacted Kingsview Optical (Kingsview Optical, 2019). We can highly recommend their services, they worked closely with us during the manufacturing iteration process, giving clear feedback throughout.

Unfortunately, this lens was designed was prior to Zemax's optimisation system including a 'design for manufacturability' merit function operand. This recently introduced operand allows for robust optimisation to maximise manufacturability by finding designs with loose tolerances that achieve close to nominal performance. As such, whilst designing the system, the required tolerances of a design were effectively beyond control. The designer had to accept the tolerances that the design required, which made the procurement process far more difficult. Note, the TOLR operand (Optical Studio's operand for optimising tolerance sensitivity) was applied but this was found to be minimally effective with our design. Zemax's new 'design for manufacturability' option greatly improves the ease of the design and procurement process.

During the design stage, it was possible to significantly improve spot size performance across the field and wavelength range by ignoring lateral chromatic aberration during the optimisation process. This was possible due to the nature of the spectrometer system; as each of the images formed in the image plane will be a monochromatic re-image of the fibre head at every wavelength down to the resolution of the spectrometer. Given that each of the images will be monochromatic, one does not need to be concerned with the lateral chromatic shift effecting resolution, it will only change the location of the image. The location will also change minimally

over the course of an individual order as the wavelengths are all sufficiently close together.

With the final iteration of the manufacturable lens, the design was refined to have only 9 surfaces with 6 elements; as 4 of the surfaces were cemented while maintaining the required optical performance, see figure 3.4. Each of the elements were set to 2″ in diameter in order to maximise ease of manufacturability and ease of mounting; allowing all of the elements to be placed in a 2″ tube with toleranced spacers to ensure the required element separation.

Another approach used to reduce manufacturing cost on this prototype was to apply only a single layer MgF2 anti-reflective coating on the outer element surfaces. Further production runs of the lens system, now that the optical performance has been proven to be sufficient, should be produced with higher performance anti-reflective coatings on all surfaces, increasing the cost per lens in the order of \$500 but greatly increasing throughput.

It was found that the key tolerances for the final design were the lens curvatures, specifically the low radii elements which had to be set to within the order of $10\mu m$ from the nominal value. Element thickness, tilt and decentre were all able to be set to standard uniform values of $5\mu m$, $0.01deg$ and $4\mu m$, respectively. The Abbe number tolerance was set to 0.2% and the refractive index was set to $\pm 5 \times 10^{-4}$, both following industry standards (Schott AG, 2011).

In order to test the lens' performance, after each iteration it was placed into a model spectrometer in Zemax using the double pass layout, see figure 3.5 (top panel). The performance of the resultant spectrometer system was measured through the spot size of a number of wavelengths outlining the centre and the extreme edge wavelengths in each of the diffraction orders.

For the nominal final lens design and spectrometer layout, it can be seen that diffraction limited performance is achieved across the entire spectrum, see figure 3.5 (bottom panel). The worst performing version of the lens found in 3,000 of Zemax's tolerance Monte-Carlo simulations, was placed into the spectrometer system. This system was found to have close to diffraction limited performance across the entire spectra. Given this, we were then sufficiently happy with the lens design in order to move into procurement and have the system manufactured.

The lens, with mounting in a tube to the tolerances dictated above and procured in a batch of 2, was quoted to be manufacturable for \$5500 per lens. This is the highest cost component of the spectrometer but now that the tooling is produced, with production of higher quantities, the cost per lens has been quoted to drop below \$1500; making this design replicable at a low cost.
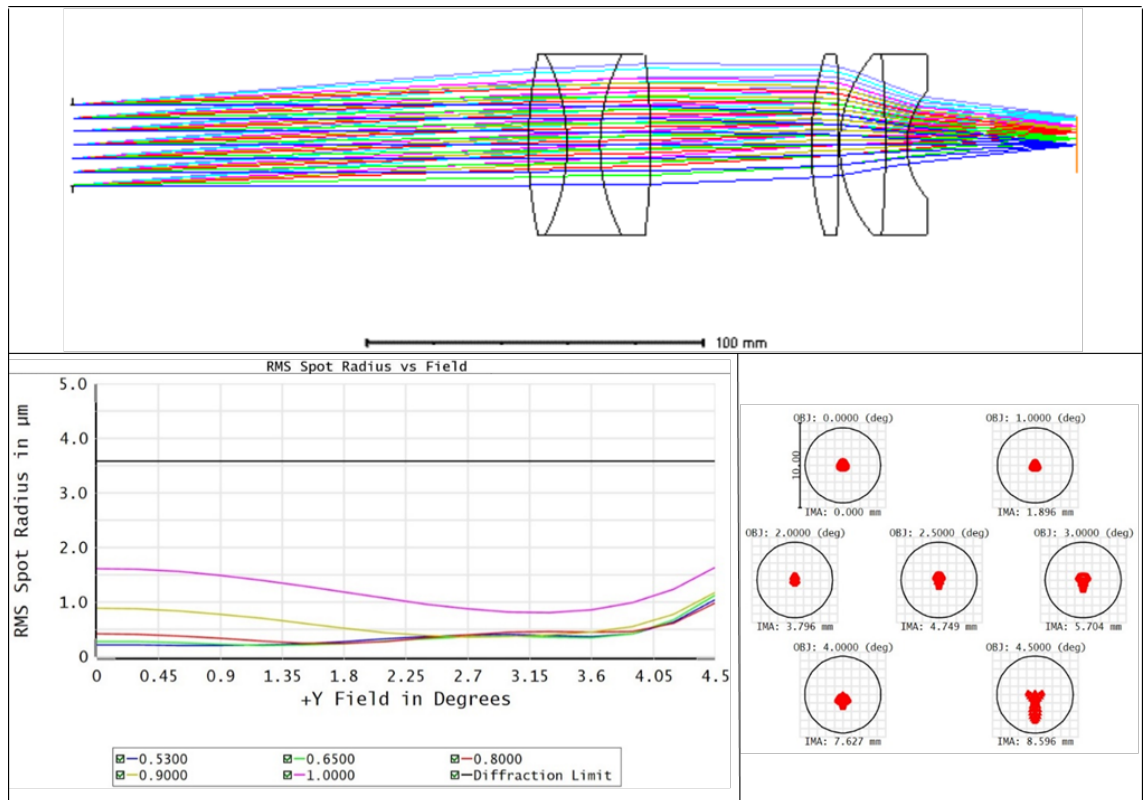
Figure 3.4: (Top panel) Schematic depicting the geometry of the finalised manu-
facturable lens design. (Bottom-right panel) Spot diagram for the lens
design, with a sub-plot for each of the chosen field angle values from $0deg$
to $4.5deg$. The red spots depict the aberration limited spot size and the
black circles depict the diffraction limit for the system. (Bottom-left
panel) Graph of field angle against RMS spot radius for the lens system.
The black line represents the diffraction limit value, the blue line rep-
resents $530nm$, the green line represents $650nm$, the red line represents
$800nm$, the yellow line represents $900nm$ and the pink line represents
$1000nm$. It can be seen that the lens is diffraction limited across this
field and wavelength range.
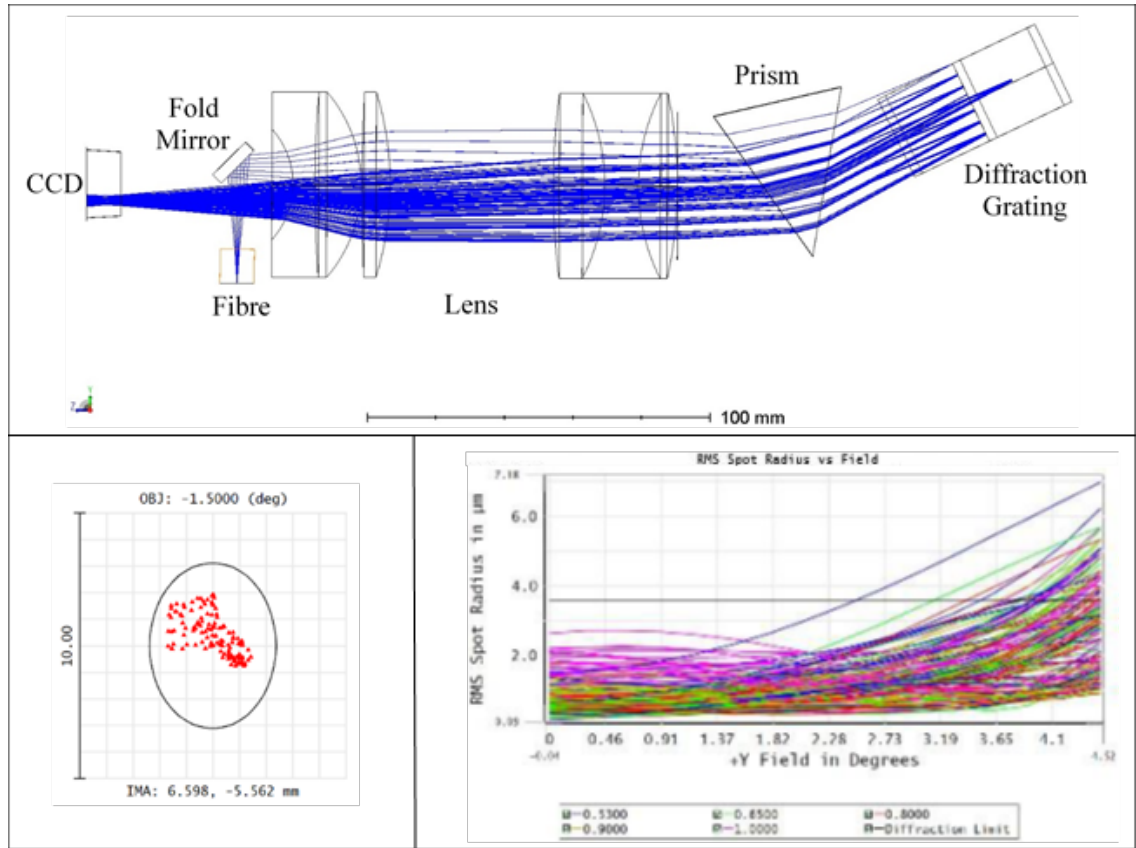
Figure 3.5: (Top Panel) Schematic layout of the finalised double-pass spectrometer system. (Bottom-left) An example plot of the spot diagram for the spectrometer system at $530nm$, which is at a field of $1.5deg$ for this spectrometer system. The red spots depict the aberration limited spot size and the black circles depict the diffraction limit for the spectrometer. The RMS radius of this spot is $1.2\mu m$ and the diffraction limit is $2.92\mu m$. (Bottom-right) Graph of field angle against RMS spot radius for the manufacturable lens system. This plot contains data for 3000 lens systems that have been generated by Monte-Carlo simulation, taking lens parameter values from within the accepted tolerances. The black line represents the diffraction limit value, the blue line represents $530nm$, the green line represents $650nm$, the red line represents $800nm$, the yellow line represents $900nm$ and the pink line represents $1000nm$. It can be seen that the lens is diffraction limited across most of the field for all of our chosen wavelengths, with acceptable aberration limited performance seen in most of the 3000 systems beyond a field of $3deg$.

The detector should be chosen to allow Nyquist-Shannon sampling. The resultant fibre image with aberration effects is expected, following equation 2.9 and noting that in the double pass system there is no image magnification, to be approximately $12 - 14\mu m$. Following Nyquist-Shannon sampling, when it comes to pixel size, one should aim to have at least 2 pixels per fibre head image. Given this, pixels for this instrument should be smaller than $6 - 7\mu m$. For the prototype, a Starlight Xpress SXVR-H16 was applied due to ease of availability. It has a Kodak CCD chip: 2048×2048 square pixels in a $15.15 \times 15.15mm$ array with each pixel of $7.4\mu m$. This sensor is under-sampling the spectrum and the square sensor shape does not fit the rectangular shaped Echelle spectrum well. A detector like the Atik 490EX with 3379×2703, $3.69\mu m$ pixels in a $12 \times 10mm$ array guarantees that the spectrum would be well sampled under Nyquist sampling theorem, with 3.79 pixels per resolution element (ATIK Cameras, 2018). Its size is also more than sufficient to cover the entire image of the Echelle spectrum, with its approximately $12mm$ high resolution dispersion from grating and $2mm$ cross-dispersion from the prism.

Another option would be a CMOS sensor, which have far better read-out rates and read-out noise performance. Unfortunately, these options are still early in development and as such remain too expensive for current low-cost systems; but this is likely to change in the next few years. An inexpensive CMOS detector, the Thorlabs DCC1645C, was used for alignment and optical quality measurements; which are made far easier with the fast read out rates of CMOS technologies. Unfortunately, this detector's sensor is too small and prone to thermal noise to be used for science data.

3.4.5 Lens Testing and Characterisation

Once the procured lens was brought into the laboratory, it was characterised to ensure that its performance was as expected from the Zemax model, with tolerances considered. To characterise the lens' optical performance, a test was devised whereby light from a fibre at the focal point of the lens would be collimated. The collimated beam would then be reflected back into the lens by a plane mirror, where the lens would then re-focus the fibre image onto a detector; the experimental layout is highlighted in figure 3.6. The resultant full-width-half-maxima of the imaged fibre was measured as a proxy for the diameter of the fibre. This test was repeated multiple times, changing the fibre size, altering the field of the lens used by rotating the mirror and varying the wavelength of the input source. It was found that the image of a $400\mu m$ fibre was re-imaged to $400\pm10\mu m$ and a $10\mu m$ fibre was re-imaged
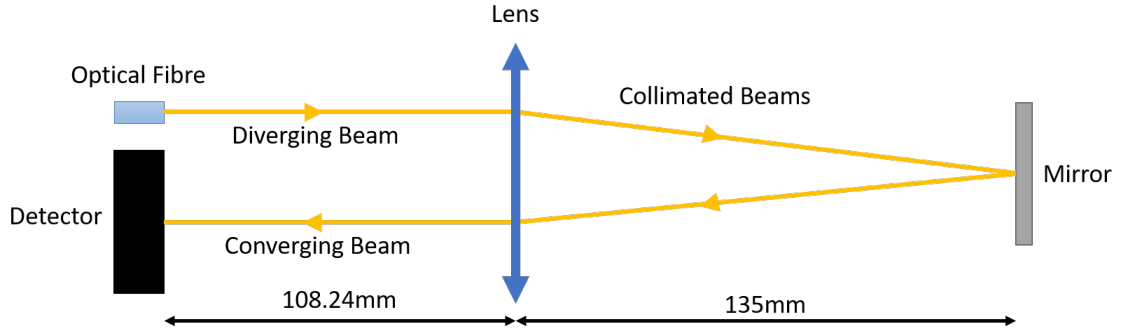
Figure 3.6: Schematic diagram outlining the experimental layout for the lens imaging performance test. The location of the fibre and detector (perpendicular to the optical axis), in addition to the tilt of the mirror, were altered to characterise the total field acceptance of the lens.

Table 3.3: Table of throughput seen for the lens system on a single pass for a variety of wavelengths.

Wavelength:	$532nm$	$672nm$	$779nm$
Throughput:	82%	93%	95%

to $10 \pm 1.8 \mu m$. Thus, proving that the optical performance of the lens alone is at the required standard.

In order to test the lens' throughput, a series of lasers were passed through the optical axis of the lens in a single pass, with the intensity of the laser measured before and after passing through the lens. The resultant attenuation for each wavelength is shown in table 3.3.

To summarise, lens throughput is measured at approximately 82%-95% between $532nm$-$779nm$ per lens pass. This could be improved in the next iteration through the use of higher cost, higher throughput lens coatings as discussed in section 3.4.4.

Following confirmation that the lens performance was as required, a series of pre-prototype spectrometers were constructed using breadboarding optical mounts. These were found to be a good proof of concept but the physical size of the breadboarding mountings made setting up the spectrometer in the optimal layout close to impossible. The fibre input's fold mirror was especially difficult to mount and manipulate without the beam vignetting due to the compactness of that space. The entire system also had too many degrees of freedom; making alignment difficult. To combat this a custom mechanical mount was designed.

3.4.6 Mechanical Mounting

In order to align the optics in the optimal layout found using the Zemax model, an investigation was undertaken as to whether it would be possible to produce a mechanical mount within which all of the optical components could be placed, such that optimal alignment is achievable with relative ease.

The mount was produced by taking the spectrometer alignment set-up from Zemax and exporting it as a CAD file. This CAD file was then opened in a CAD manipulation program, with a derivative part created by taking the negative of the optical alignment from a 'block of CAD material'. This 'block' was then carved away, removing unnecessary parts until a basic mount shape was formed. Ideally, one could 3D print or machine this part, place the optical components in it and have the system function as designed in Zemax. Unfortunately, due to expected error in the manufacturing and the looseness of tolerances, some degrees of freedom are required to adjust the final set-up. These required degrees of freedom were heavily scrutinised.

As an overview, the camera and fibre alignment are critical to the resolution across the field, as the fibre and sensor chip must both be well aligned to the lens' focal plane. The prism, lens, input mirror and grating alignment, whilst they must not vignette, are thought to be non-critical and can be set by the model; being allowed to vary by the tolerances set on the mount manufacture.

The camera and fibre alignment must be fine tuneable, through mechanical alignment parts, but are to be designed to remain stable over long periods of time. The camera will require 3 translational d.o.f. due to uncertainty on sensor placement and 2 rotational d.o.f. to align the sensor with the focal plane. The fibre head placement is better defined and so may only require 1 translational d.o.f. perpendicular to focal plane as well as 2 rotational d.o.f.

Taking these degrees of freedom into account, a first pass CAD mount was designed and 3D printed using PLA; with a print tolerance accuracy of $100\mu m$. The resultant mount can be seen in figure 3.7.
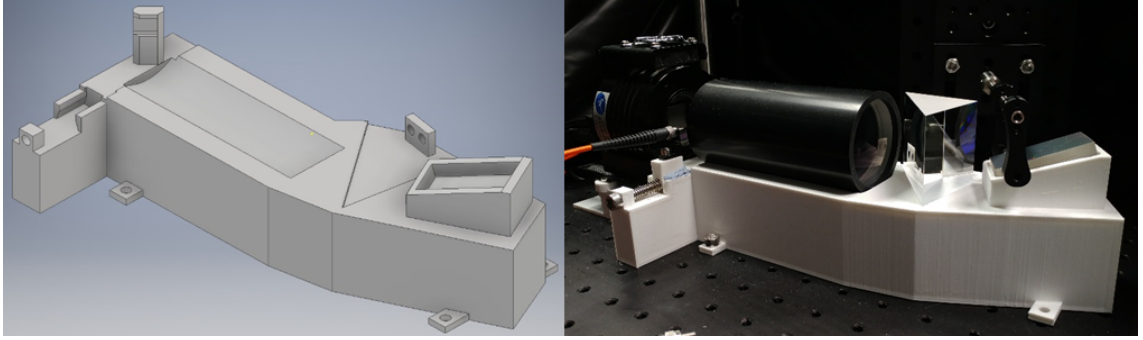
Figure 3.7: (Left panel) Image of CAD model mechanical mount design. (Right panel) Image of assembled 3D printed mount with spectrometer components fitted.

3.5 Laboratory Testing

3.5.1 Mechanicals Stability Test Using Flat-Lamp Exposures

With the finalised iteration of the spectrometer assembled in the mechanical mounting, a brief investigation into the short and long term stability of the spectrometer was undertaken. The effects of exposure to fluctuating temperature and pressure, along with other mechanical disturbances experienced in the lab, were examined.

A flat lamp source was coupled to the fibre which feeds the spectroscope. The spectrometer was then left for an hour with a frame taken at a cadence of 6 seconds; of which, 1 second was of exposure and 5 seconds was of sensor read-out. With an initial frame chosen as a reference frame, each row of each subsequent frame was cross-correlated with the corresponding row in the reference frame in order to measure the shift from this initial frame. The peak three points of the CCF (cross-correlation function) were then used to describe a parabola with the peak of which taken as the centre of the CCF; allowing sub-pixel precision to be achieved on the shift of each row. With the centre of the CCF found for each row, the median value was taken to describe the overall shift of the image on the sensor. An example of the resultant time series can be seen in figure 3.8.

The test was repeated multiple times. It can be seen on figure 3.8 that when the spectrometer is left without interference, after approximately 15 minutes the system oscillations level out. The following analysis is undertaken on the 'level' section of the time-series. The point to point RMS was measured for this time-series to be $(9.1 \pm 0.01) \times 10^{-3}$ pix. Gaussian noise was then injected into this data to represent random photon noise. The point to point RMS of this time-series with noise was
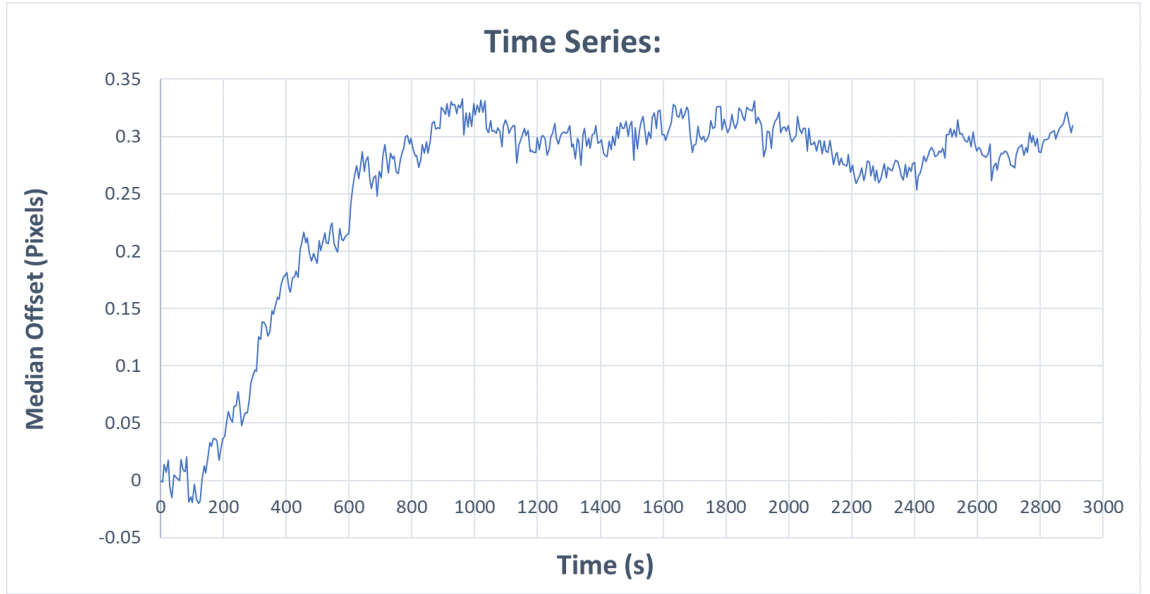
Time Series:

Figure 3.8: Graph of the time series for an example stability test. Time elapsed in seconds is plotted against median offset in pixels seen from the cross-correlation of the frame taken at a given time against the reference frame taken at $t = 0$.

found to be unchanged within the margin of error. This suggests that the stability is not photon noise dominated.

Allan-Variance analysis of the system, computing the variance using pairs of points separated by a varying time-lag, found that stability variability is not consistent over the course of this time-series; see figure 3.9. This further suggests that the stability of the system is primarily affected by either systematic error or under-sampling.

Interestingly, in these tests it is seen that the system's stability has a high variance value for a time-scale of 5-10 minutes. The laboratory is located above a London Underground train-line and the mechanical disturbance of the trains passing is noticeable. This time-scale aligns well with the train timetable, so further tests in another location should be carried out to determine whether this variance is purely mechanical.

Using Doppler theorem, we see that $v/c = \delta\lambda/\lambda = 1/R$, where c is the speed of light. Hence, velocity span is given by $v = c/R$. Taking, for example, a resolving power, R, of $60,000$ we ascertain a velocity span of $v = 5km/s$. With a spot size of $14\mu m$ we can estimate our resolution element to be approximately 2 pixels, therefore the velocity span per pixel is $v/pixel = 2.5km/s$. Our RMS point to point variability is $(9.1 \pm 0.01) \times 10^{-3}pix$, multiplying this with $v/pixel$ gives us the pixel variability in radial velocity of $v_{rad} = 22.9m/s$. As we have taken point to point values for our
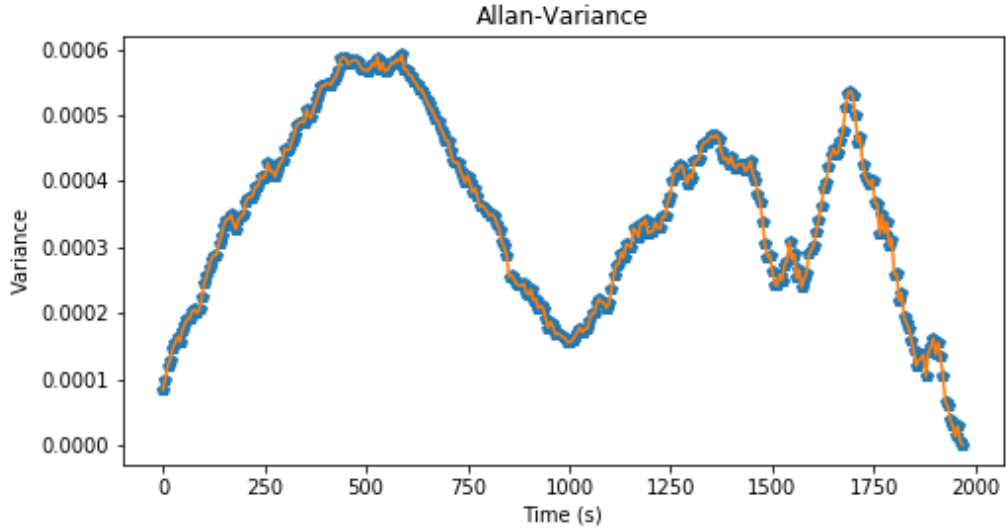
Figure 3.9: Graph of the Allan-Variance analysis undertake on the 'level' section of the time series seen in figure 3.8. Time-lag used in the variance calculation (in seconds) is plotted against variance.

measurement, there is also uncertainty in the location of both points, which add in quadrature, as such a better estimate of radial velocity stability is given by dividing by a factor of $\sqrt{2}$, yielding $v_{rad} = 16.2m/s$.

Given that the system currently has no stability control system beyond the passive mechanical stability of the optical bench, and that the stability is currently dominated by systematic error, the radial velocity performance has scope to improve substantially. By reducing the point to point variability by a factor of ~ 8, the system goal would be reached. We are confident this can be achieved with an active temperature control system, a vacuum chamber and improved mechanical isolation.

3.5.2 Blaze Angle Inconsistency

It was found that the measured separation between the sodium D-lines doublet in the spectrum was lower than theoretically expected. The separation was measured on Littrow to be $666\mu m$. Using $m\delta\lambda = \epsilon d\cos\alpha$, derived in section 2.0.4, we can see that the grating dispersion angle is given by $\epsilon = m\delta\lambda/(dcos\alpha)$. By rearranging the grating equation, it can be seen that $m/d = 2\sin\alpha/\lambda$, hence substituting this into our equation for grating dispersion, we find that $\epsilon = 2\frac{\delta\lambda}{\lambda}\tan\alpha$. Hence, the separation seen at the focal plane for a difference in wavelength $\delta\lambda$ is given by,

$$S = \epsilon \times f = 2f\frac{\delta\lambda}{\lambda}\tan\alpha\,. \tag{3.1}$$

Using the values from the sodium doublet and the spectrometer parameters, $\delta\lambda = 0.6nm$, $\lambda = 589nm$, $f = 108.24mm$ and $\alpha = 75deg$, we find that the predicted separation is $S = 840\mu m$. Given this, there is a disparity between the measured and theoretical separation of the Sodium doublet. Let it be noted that even though the sodium doublet in not on Littrow for this set-up, the change in separation seen by moving up the diffraction order is a higher order effect and has minimal effect on the separation value seen here, hence it has been ignored here for brevity.

In order for the theoretical separation to match the measured value, the blaze angle would have to be set to $71deg$. To investigate whether this was the case, the grating angle was increased using a micrometer until the required separation was achieved. It was found that the intensity of the sodium doublet decreased by over a factor of 5 when at this grating angle. If this intensity reduction was caused by vignette due to the decrease grating surface projection, the intensity should only fall by a factor of 0.2. As such, it would appear that the manufactured blaze angle of the grating varies from the quoted value and it is possible that the manufactured blaze angle has a tolerance of a few degrees. This is compounded by prior investigation which found that for the $63deg$ blaze angle Thorlabs Echelle grating, the laboratory set-up only matched the Zemax model when the model's grating angle was set to $66deg$. It was also found that altering the grating in the lab system to $63deg$, incurred a substantial decrease in spectral intensity, suggesting that the blaze angle for that grating is more likely $66deg$. Following discussion with Thorlabs it appears that this uncertainty in the blaze angle of the gratings is due to wear on their master grating which is used in the manufacture of these replica gratings.

There are two take-away points from this, in the next mechanical mount design, the grating angle should be made an alterable degree of freedom as it would appear that no two grating blaze angles are the same. Secondly, the performance of our system is currently limited by the availability and quality of the diffraction grating. With the current grating, high resolution of the order R=80,000 could be achieved with low throughput or R=60,000 can be achieved with maximal throughput. Further testing with Thorlabs gratings will be required to determine whether one can be obtained with a blaze angle of 75deg (or greater) in order to gain the maximum resolving power achievable by the system at a nominal throughput.

This suggests that to further the replicability of this system or systems like this, the investment should be made into manufacturing a template grating to the required specifications. Whilst this would cost in the order of $10,000$ to procure, replica gratings could then easily be produced in the order of $100. Along with the current lens production offering, this would result in a low cost and easily replicable system.

3.6 Results

A prototype, low-cost, high-resolution spectrometer has been produced as depicted in figure 3.10. The total spectrometer's footprint is $300mm \times 140mm \times 90mm$, fitting well within the technical requirements. Beyond ground-based telescopes (of arbitrary size, if moderate AO is available), the instrument could also be easily implemented on space-based telescopes of arbitrary size. For example, with a minimal re-design of the mechanical mount, the system would easily fit within a 3U cube-sat chassis and possibly even a 2U chassis with a re-working of the optical design. The total parts cost of this prototype was less than $10,000$ but if produced as part of a larger batch, this would be reduced to below $5,000$; reaching our goal of a low-cost spectrometer.

The system has been successfully designed to achieve the goal wavelength coverage of $500nm$-$1000nm$ at close to diffraction limited performance across this range.

Mounted in the current prototype 3D-printed mechanical mount, in an on Littrow set-up, the spectrometer performs with a resolving power of $R = 60,000$; surpassing the technical requirement. To go beyond this and reach the goal of $R = 100,000$, the current limitations have been identified as the diffraction grating and the stability/adjustability of the mount.

Analysis suggests that the grating limits performance in 2 ways: The manufactured blaze angle of the grating appears lower than expected, such that to achieve the required throughput, the spectral separation is decreased, decreasing resolution. Secondly, the grating is only $50mm$ in height as opposed to ideal $100mm$, causing some of the collimated beam to vignette. The vignette of the beam alone isn't a great issue but this also acts as an aperture in the dispersion direction, which limits the spot size to $11\mu m$ in the dispersion direction irrelevant of how good the aberration performance of the optics are. One solution to this issue is to have a template grating produced with the optimal parameters for systems like this, allowing replica gratings to be produced at a low cost. Alternatively one could apply a Virtually Imaged Phase Array (VIPA) as the high-resolution dispersing element (Bourdarot et al., 2018); further study of this option appears to be fruitful.

The current prototype mount was designed to minimise degrees of freedom but it is missing some necessary adjustable parameters, such as grating blaze angle. Whilst a blaze angle adjustment solution has been retroactively produced using kinematic mounts, the alignment of this system is not ideal. In addition to this, due to the relatively loose tolerances in the manufacturing of this mount, some alignment parts (such as the fibre mounting), which should be ideally aligned as per the CAD model,
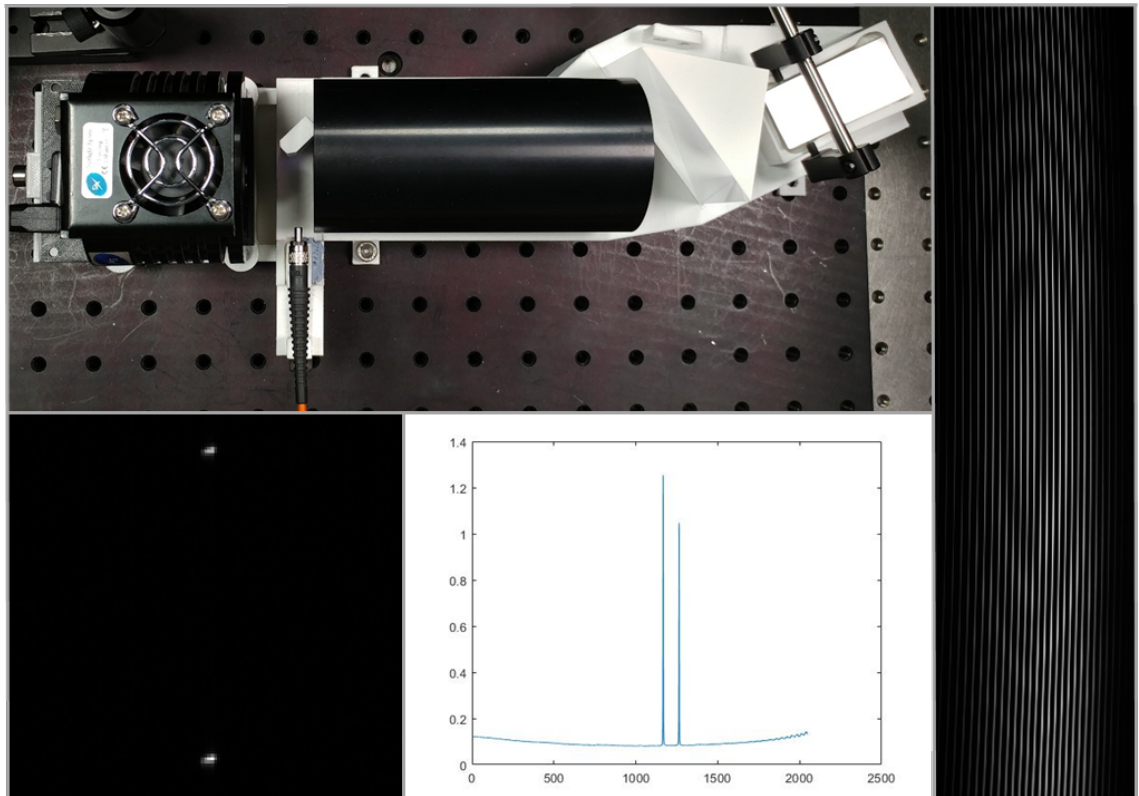
Figure 3.10: (Top-left panel) Image of the spectrometer assembled in the 3D printed mechanical mounting following the optical layout shown in figure 3.5. (Right panel) A section of the CCD image displaying the full Echelle spectra of a flat lamp. (Bottom-left panel) A section of the CCD image displaying the spectrum of the Sodium D-doublet. (Bottom-middle) The unprocessed extracted spectra of the Sodium D-doublet where pixel number (x-axis) is plotted against relative intensity (y-axis).

are partially misaligned of the order of $0.3deg$. Future designs should either have tighter tolerances or have micro-adjustment for such parameters.

For the parameters which do have degrees of freedom, the translational stages function as required but the rotational degrees of freedom are too coarse. A further redesign would give us the accuracy in alignment to achieve maximum performance across the CCD.

Regarding stability, measurements with precision down to a radial velocity of $16.2m/s$ are achievable with the current set-up. This must be reduced by a factor of 4 to reach the technical requirement and a factor of 8 to reach the goal. The current system is exposed to all laboratory variations, it has no temperature or pressure control system and is under the influence of mechanical variations of the environment. As such, it would be fair to speculate that with a stability control system and a mount constructed of a more robust material (such as high-carbon steel and carbon-fibre), the stability of the system could be improved substantially. The long-term stability of the system requires further study.

The throughput of the system also requires further study. An educated estimate for the current system, taking the grating efficiency to be approximately 35%, is of the order of 6.6%. Efficiency of the fibre and CCD are included in this value. This value is approximately half the throughput of some of the most refined Echelle spectrometers, which often have an efficiency of $\sim 12\%$. The grating is the most lossy component of the system, as even with a blazed grating, if the grating facets are not manufactured to be sharp, a curvature on the edge of the facets can send light into other direction; as has been observed with this grating.

3.7 Conclusion

This prototype spectrometer has proven the concept that a compact, low-cost spectrometer can be produced in a replicable fashion. Devices such as this could be coupled to enthusiast grade telescopes across the world, opening the opportunity to be involved with high-resolution spectroscopic science to a wide audience. Alternatively, systems like this could be effectively coupled to some of the world's largest telescopes, allowing banks of these low-cost, high-resolution spectrometers to be employed in an integral field array; bringing about many exciting new science cases. Beyond ground-based applications, there is a science case for the use of systems like this in pioneering space-based, high-resolution spectroscopy.

4 QMSPEC: Sub-Systems and On-Sky Testing

Abstract

Following the successful design, construction and lab testing of the QMSPEC spectrometer system, the sub-systems necessary for on-sky observations were developed and subsequently tested at the 'QMUL AU Observatory'.

- FRONT-END: A fibre coupling device was optically designed, assisted by the use of the Zemax Optical Studio Software, to allow the spectrometer's F/4.51 optical fibres to be efficiently coupled to the F/7 STARWAVE 110ED-R telescope. With an optical design in place, a mechanical mount was derivatively designed in CAD format and 3D printed to the necessary tolerances.

- BACK-END: In order to extract line-spectra from the CCD output of the Echelle spectrograph, a custom data reduction pipeline was written in Python. This pipeline removes bias/dark frames, traces the orders from a flat calibration spectra, extracts the spectra from the science frames and, through the use of the FOX algorithm, effectively divides the science spectra by the flat spectra to give the resultant science spectra. Wavelength calibration is planned to be achieved in the first instance using a reference solar/lunar spectrum.

With the front-end and back-end systems functioning as necessary, the entire instrument system was tested on-sky. A lunar spectra was successfully observed and extracted.

4.1 Introduction

In order to test the QMSPEC instrument on-sky, a number of subsystems are required to facilitate the efficient coupling of light into the spectrometer and the extraction of spectra data from the CCD. A fibre coupling system ensures that the telescope beam is at the correct F/number to maximise light entering into the spectrometers fibre and also facilitates the alignment of the telescope pointing such that light from the object of interest is being fed into the fibre. The data reduction pipeline takes the Echelle CCD image and converts it into a line-spectra, preserving resolution and measurement accuracy. In this chapter we will discuss the design and construction of these sub-systems and their effective testing on-sky at the Queen Mary Astronomy Unit Observatory, applying the STARWAVE 110ED-R telescope. The STARWAVE 110ED-R is a 110mm aperture extra-low dispersion (ED) refractor telescope with a 770mm focal length.

4.2 Sub-Systems

4.2.1 Front-End Fibre Coupling System

The initial fibre coupling system designed for QMSPEC was loosely based on the principles of the system found on HARPS (Pepe et al., 2000). A schematic for this design can be found in figure 4.1. This design places a $45deg$ mirror centralised at the on-axis focal point of the telescope. This mirror has a hole on the order of $\sim 20\mu m$ in diameter at it's centre. When the system is misaligned the light from the target star will be reflected onto an eyepiece, where if the star is observed through this eyepiece it can be concluded that the system is misaligned. If the system is aligned correctly, the focussed light will pass through the mirror hole and re-disperse as it passes the focal point. The dispersing light is then refocused by a singlet lens onto the fibre head with the correct F/number.

Following initial lab assembly investigation, and the results of Kintziger et al. (2018) in the design of a comparable system for the TIGRE telescope, it was decided that on the budget allocated, the required alignment of such a device would not be feasible.

Adhering to the design suggestions discussed in Kintziger et al. (2018), a new fibre coupling system with less critical alignment parts was designed. The system, shown in fig 4.2, essentially re-images the fibre head plane through an eye-piece such that the observer can directly observe whether the light from the target object is going
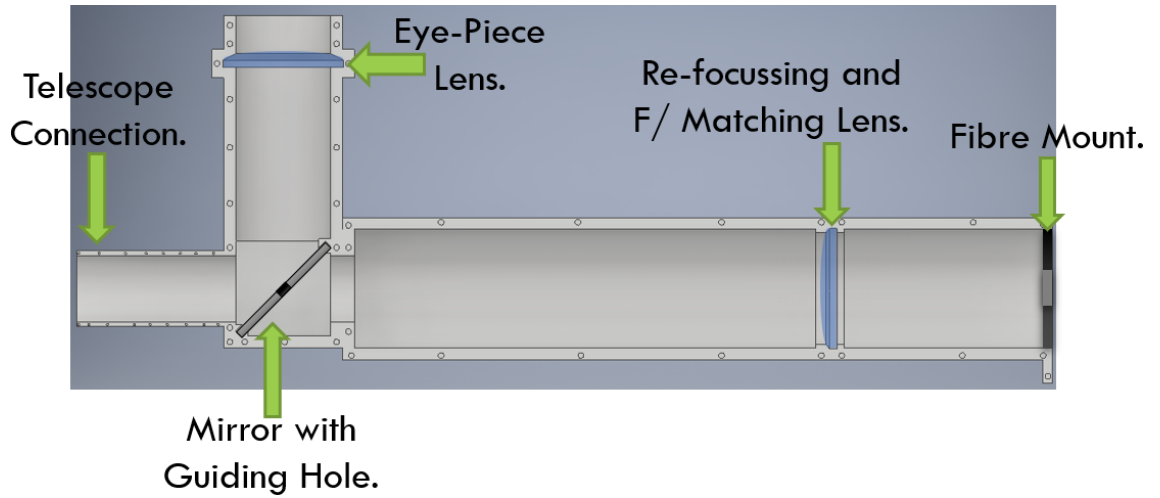
Figure 4.1: Schematic layout of the initial proposed fibre coupling system for QM-SPEC.

into the fibre head.

Light from the telescope passes through a 90/10 (T/R) beam-splitter (where 10% of the light is lost) and is then focused by a singlet lens, which acts as the F/number matching optic. This brings the F/7 telescope beam down to F/4.51 to match the 0.11 NA optical fibre and subsequently, the F/4.51 spectrometer. This beam comes to focus for the first time on the plane of the optical fibre head, such that if the telescope pointing is correct, the light from the object of interest will be injected into the fibre.

The fibre mount (which is at the fibre head plane) is reflective, such that if the light from the target object isn't injected into the fibre, it will be reflected back on itself. This reflected light will pass through the singlet lens and the beam will be reconverted to F/7. This F/7 beam will pass through the beam-splitter again, where now 10% of the beam will be directed to the eyepiece lens. This eyepiece lens then collimates the beam for ease of observation with the naked eye. Hence, throughout the entire observation, the user can view the fibre head plane to determine whether the object of interest is being injected into the fibre for observation by the spectrometer.

The focal reducer employs a Thorlabs LA1145 $f = 74.8mm \pm 0.1mm$ singlet lens, a part which retails for £34.70, with it's back surface at $66.4mm \pm 0.1mm$ from the fibre head plane; to convert the F/7 STARWAVE 110ED-R telescope beam to the required F/4.51 beam for efficient coupling. Modelled performance computed using Zemax Optical Studio of this system, assuming diffraction limited telescope performance, can be seen in figure 4.3.
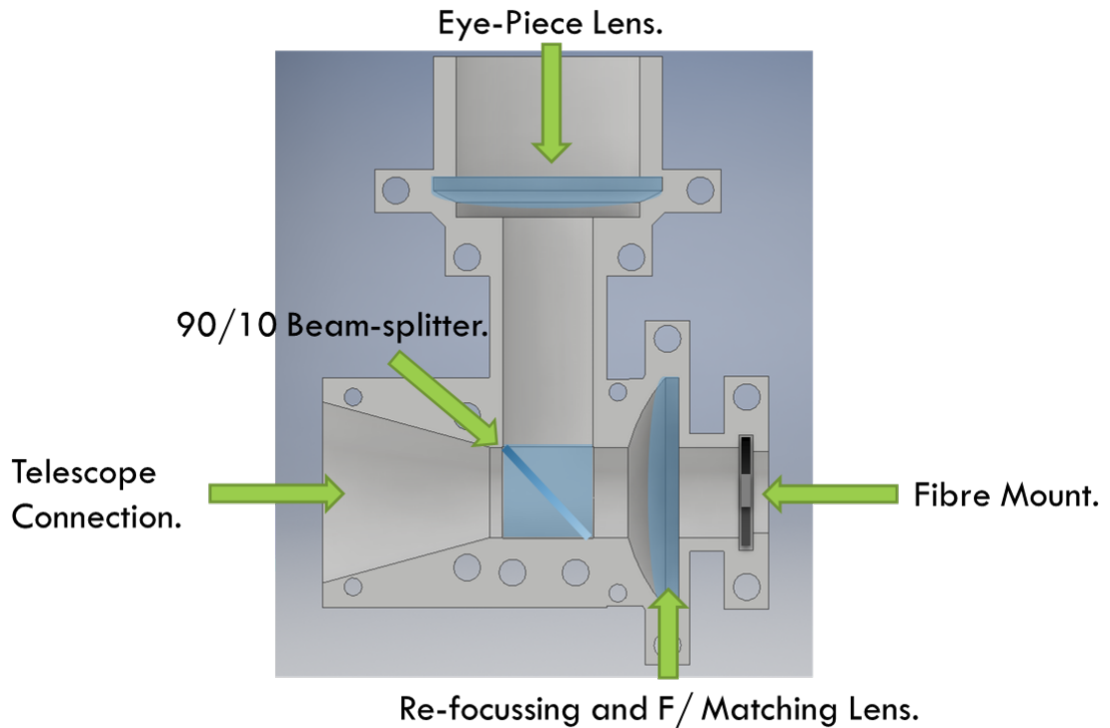
Figure 4.2: Schematic layout of the fibre coupling system for QMSPEC.
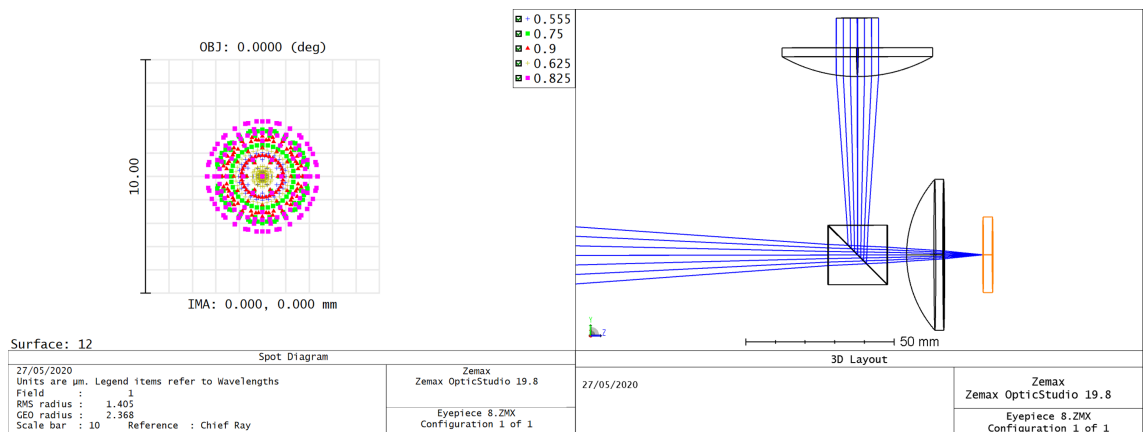
Figure 4.3: Modelled performance of the QMSPEC fibre coupling system. (Left panel) Spot size performance of the focal reducer at the fibre head plane. (Right Panel) Zemax model layout of the fibre coupling system as demonstrated in figure 4.2.

As can be seen in figure 4.3 (left pane), the RMS spot size radius observed by the focal reducer is less than $1.5\mu m$. This model of the fibre coupling system was tested while coupled to a nominal design of the STARWAVE 110ED-R telescope. Assuming that the manufactured model of the telescope has moderate aberrations producing a spot size of radius up to $5\mu m$, the system would still achieve efficient coupling to the $10\mu m$ diameter fibre.

Due to the small aperture and hence focal length of this telescope at F/7, the diffraction limited spot size will be larger than the seeing limited spot size; hence why adaptive optics is not effective on small telescopes. With this in mind and applying equations 2.8 and 2.11, it can be calculated that the diffraction limited spot size diameter of the combined telescope and fibre coupling system is $5.5\mu m$. This allows the system to operate in the aberration limited regime with effective coupling still seen to our $10\mu m$ fibre.

With a functioning model optical design completed, a mechanical design was undertaken following the process outlined in section 3.4.6. Briefly recapping this procedure here, the functioning and optimised optical design model was exported from Zemax Optical Studio as a CAD file and imported to Autodesk Inventor; a CAD manipulation software. In the CAD software, the optical CAD design was used to make a derivative part from a 'block' of CAD material. The block was then fashioned into the required shape such that it can couple to the $2''$ telescope port and allow light to pass through the optical components without vignette. The resultant mechanical design is shown in figure 4.4.

The required tolerance on components in the optical design of this fibre coupling system was found to be on the order of $\sim 0.5mm$. 3D printing with PLA using the facilities at 3D People (2019) allows print tolerances to be set at $100\mu m$. Hence, it was possible to produce a low cost mechanical design that the optical components could be seated into without the need for additional adjustable parameters. The resultant 3D printed opto-mechanical mount is displayed in figure 4.5.

The beam-splitter is a 20mm Thorlabs BS044. This beam-splitter has an anti-reflective coating which allows 90% of $675nm - 900nm$ light to pass but only allows $\sim 30\%$ of $400nm$ light to penetrate. Under use with QMSPEC this is not an issue as the spectrometer's performance cuts off at $500nm$ and the blue end of the spectrum is unused.
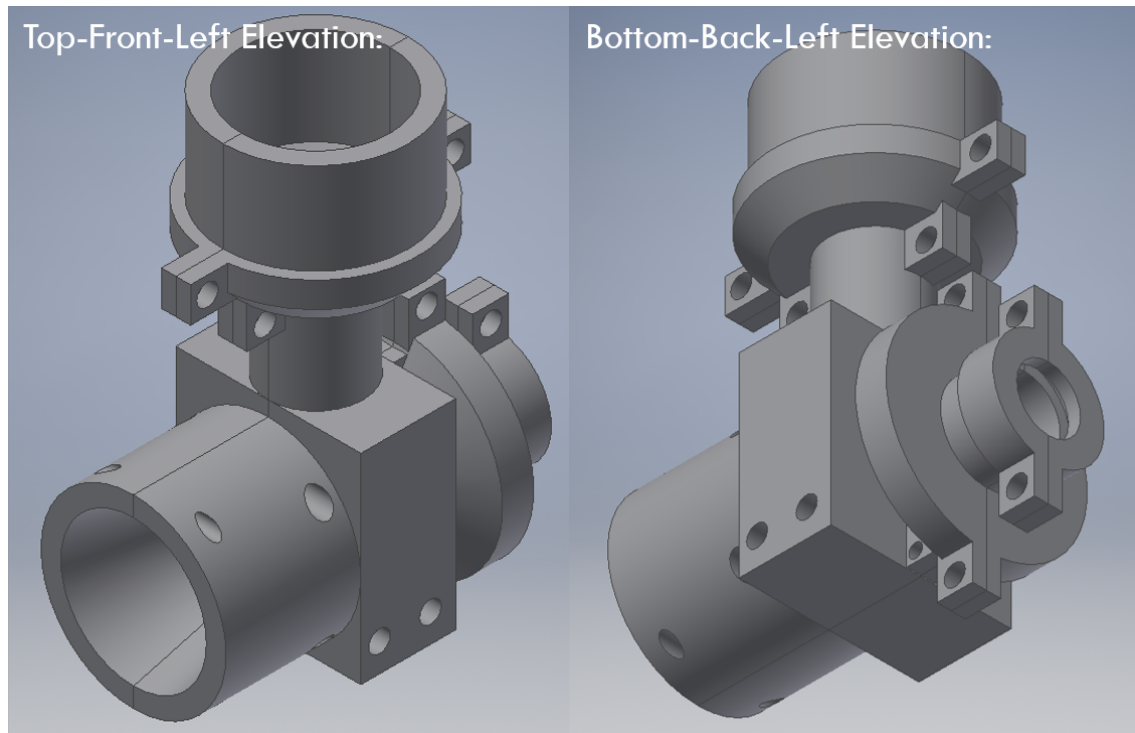
Figure 4.4: Image of the finalised assembled CAD design for the mechanical mount of the QMSPEC fibre coupling system. (Left panel) Top-Front-Left elevation of the design. (Right panel) Bottom-Back-Left elevation of the design.
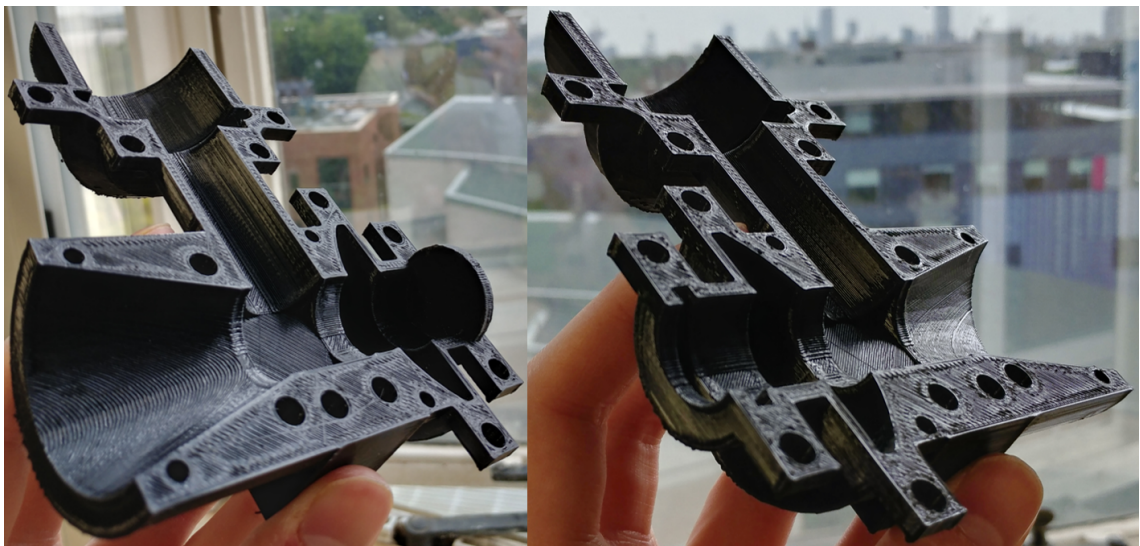
Figure 4.5: Image of the realised 3D printed opto-mechanical mount for the QMSPEC fibre coupling system.
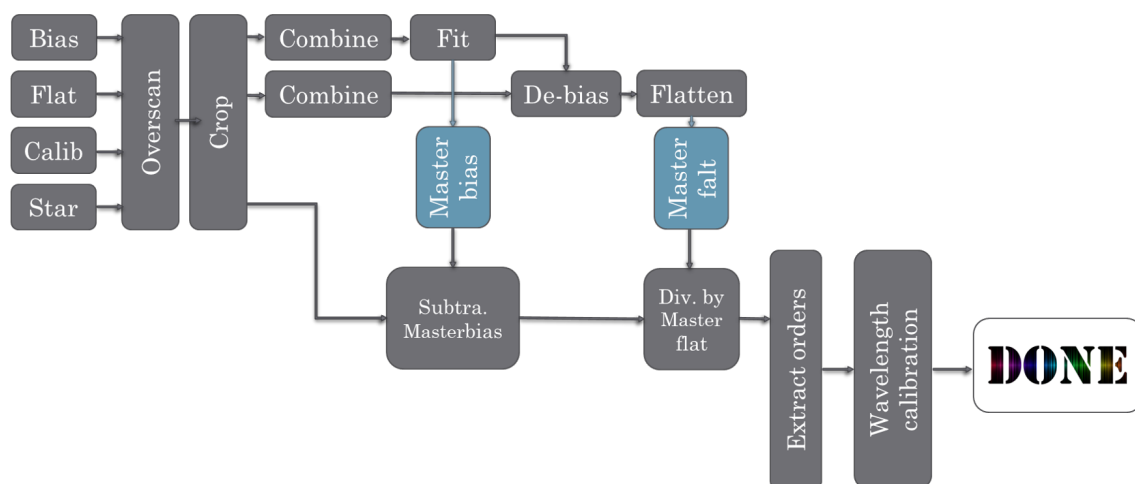
Figure 4.6: Flow-chart depicting the processes undertaken by the data reduction pipeline.

4.2.2 Back-End Data Reduction Pipeline

The aim of this data reduction pipeline was to be lightweight and simplistic, so that it could be run on a microcomputer like a 'Raspberry Pi'. This would allow the spectrometer to be operated portably as a stand-alone unit for applications beyond astronomy; such as the detection of trace gases in caves and mines or in the detection of allergens in food. In order to run natively on a 'Raspberry Pi', the pipeline was written in Python. The basic data-flow of the pipeline follows the flow-chart depicted in figure 4.6.

To ensure a simple and light-weight system, the pipeline follows the procedures outlined in early extraction systems, such as INTER-TACOS on ELODIE (Queloz, 1994). The pipeline process is as follows:

1. For each observation, a science frame, flat frame (from a continuum calibration lamp) and a dark or bias frame are all taken. These frames are taken in the .fits file format from the CCD.

2. Using the 'Astropy' python package, the frames are imported into the pipeline and converted into 'Numpy' arrays for lightweight manipulation. The frames are then cropped to remove the CCD overscan.

3. The scaled dark frame or bias frame is subtracted from the science and flat frame to remove background noise, stray light and read-out noise. If multiple dark/flat frames are taken, these are co-added to form a master dark/flat frame, which is used instead.
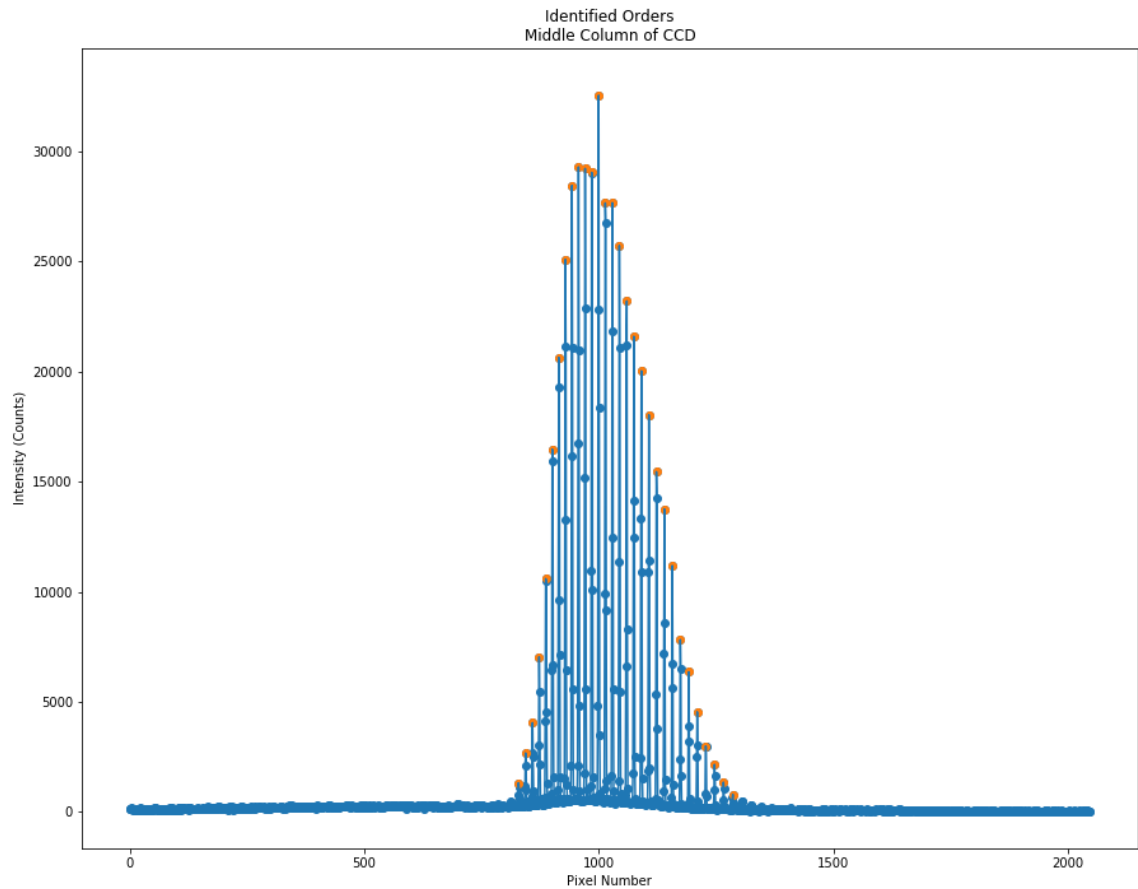
Figure 4.7: Scatter plot of the middle column of the CCD for a flat frame spectra. The orange points represent an identified peak and hence, the centre of an order.

4. The resultant flat frame is used to trace the orders of the Echelle spectrum. The algorithm starts at the middle column of the CCD and finds all of the peaks; as demonstrated in figure 4.7. The middle of the CCD is chosen as typically this is where the spectra is brightest. Each of these peaks is one of the Echelle orders; a threshold is set so that noise isn't recognised as an order. To trace the orders, from one of the peak pixels identified as an order, the 3 adjacent pixels in the column next to it (above, level and below the current pixel) are compared to see which has the largest value. The algorithm then moves to the brightest pixel and repeats until it reaches the edge of the CCD. This is done in both directions from the middle of the CCD and for all of the orders. The resultant traced orders are displayed in figure 4.8.

5. With the orders traced, using these order pixel positions, the values across the orders for the science and flat frames are found. Using the Flat-relative optimal
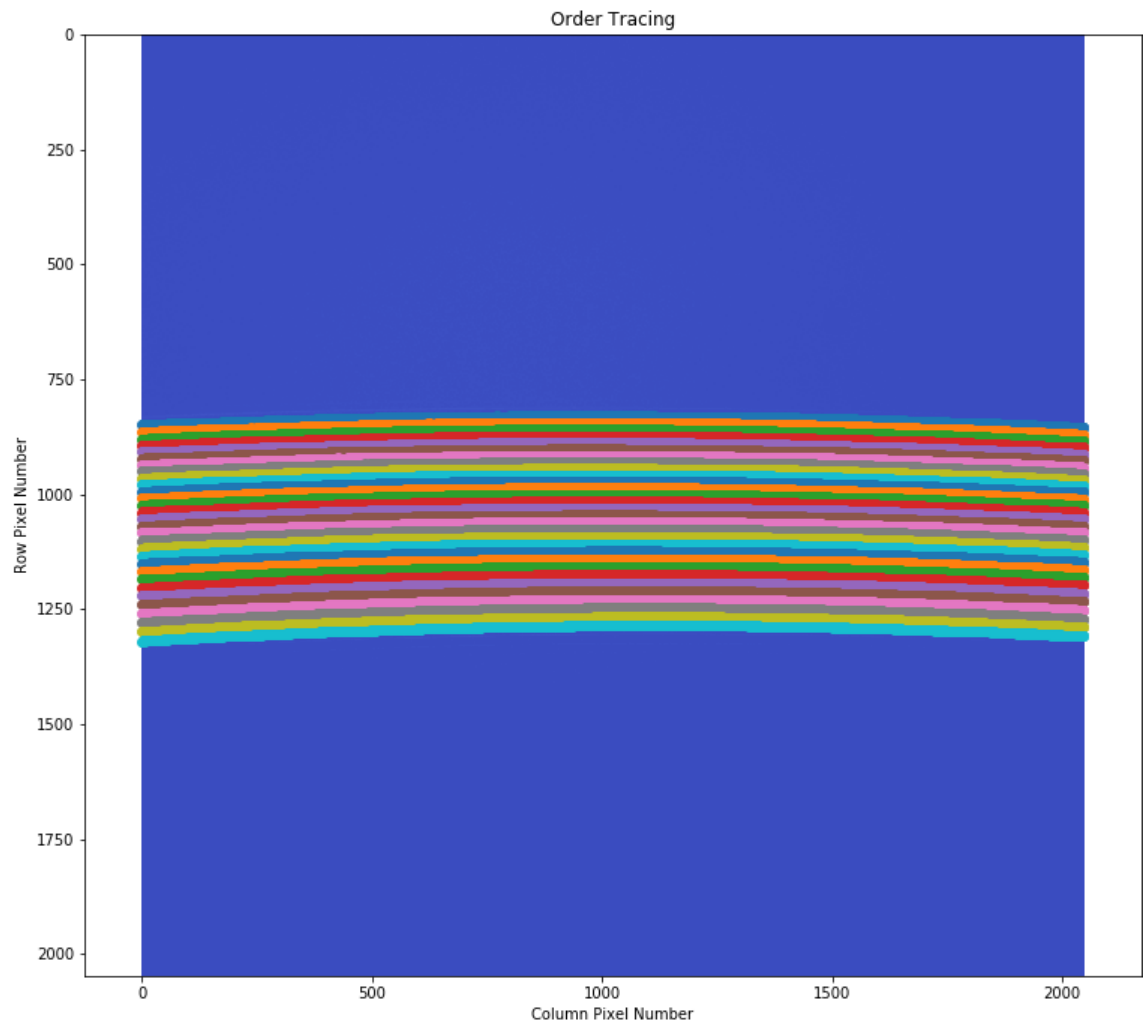
Figure 4.8: Plot of the CCD output for a flat frame spectra with the traced orders over-plotted.

extraction (FOX) algorithm (Zechmeister et al., 2014), the science frames are flattened, which essentially equates to dividing the science frame by the flat frame to remove any areas of non-uniform sensitivity of the instrument; such as that which can be caused by vignette at the edge of the frame. With this, a line spectra is extracted with pixel position against the resultant flattened science frame intensity.

6. In order to produce a line spectra of wavelength against intensity, the spectra must be wavelength calibrated. As no hollow cathode lamps, or other calibration sources are available for this project, this is to be achieved in the first instance using a solar or lunar spectra as the calibration spectrum and matching pixel position with well characterised absorption lines, as well as telluric lines, and using a second or third order polynomial fit to accurately complete the wavelength calibration.

Following this process, the Echelle spectra on the CCD are converted to calibrated line spectra, ready for analysis.

An extracted spectra of a neon lamp using this data reduction pipeline with QMSPEC can be seen in figure 4.9.

4.3 On-Sky Testing

4.3.1 Instrument Set-Up

Prior to observations, the spectrometer was re-aligned in the lab to ensure maximal resolution across the frame. The re-alignment process consisted, initially, of a flat lamp exposure to ensure that the grating blaze angle was set correctly; such that the centre of the blaze of the orders was centred on the middle of the CCD (which was fixed at the correct height by the mechanical mount). Then, a combination of calibration sources, a sodium lamp and a series of lasers, were used to measure the size of the resolution elements across the spectral range. The position along the optical axis of the fibre and CCD, in addition to the tip/tilt angle of the CCD, were adjusted until the resolution element size was minimised for all of the sources measured. Following this procedure, the resolution of the instrument was measured using the Sodium D doublet and was found to produce a spectra of resolving power $R \sim 60,000$. The instrument was then moved from the laboratory to the observatory.
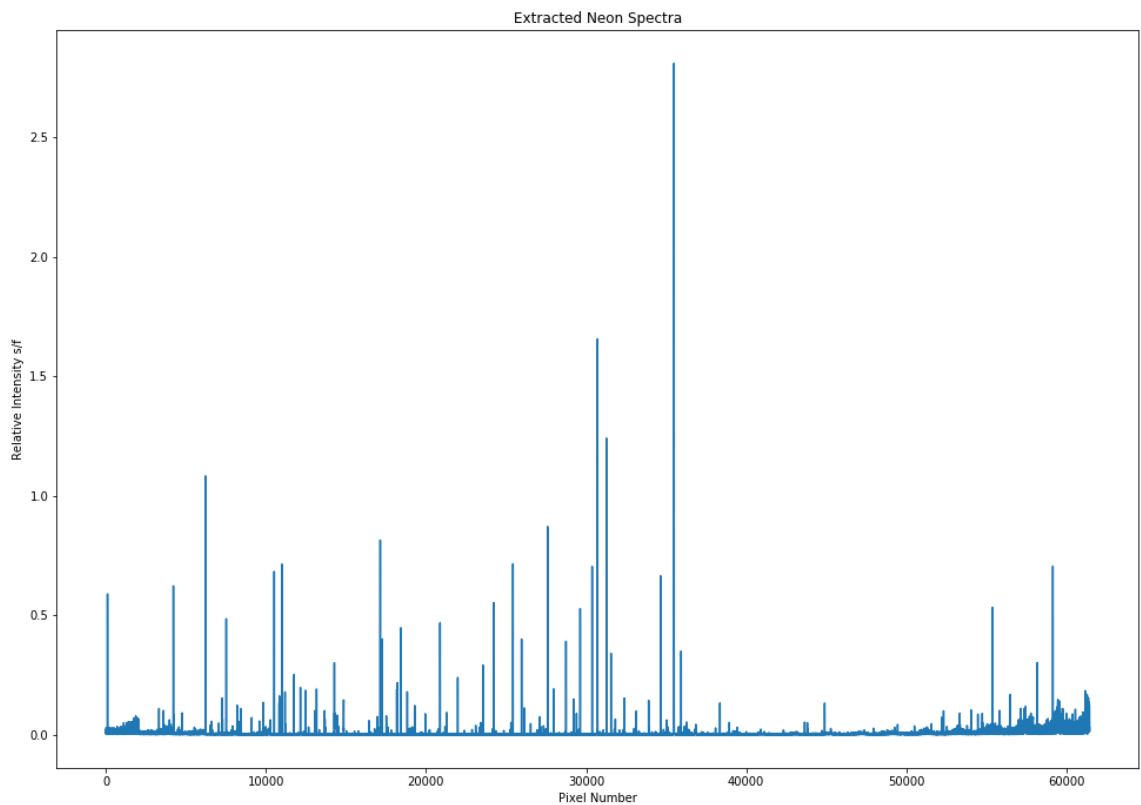
Figure 4.9: Complete extracted line spectra of neon produced using QMSPEC and the data reduction pipeline. Note: this spectra is not wavelength calibrated, each order is plotted adjacently in pixel number, the orders are not merged.

4.3.2 Fibre Coupling System Test

The fibre coupling system was found to couple well to the $2''$ telescope connector, as shown in the left pane of figure 4.10. Unfortunately, the telescope's flange did not extend enough in order for the fibre coupling system to come to focus on the fibre head plane. This is something that couldn't have been calculated previously as the telescope manufacturer's specification and opto-mechanical designs are not publicly available. To overcome this issue and gain the necessary back focal length, a $2''$ extension tube was placed between the telescope and the fibre coupling system. With this in place it was possible to bring a telescope image of an object at infinity to focus on the fibre head plane, as shown in the right panel of figure 4.10. Here an image of the Moon is focused on the fibre head plane and re-imaged through the eye-piece. An extended object like the Moon is useful to focus the system by eye as it is far easier to observe when the lunar surface details are most resolved as opposed to when a star image appears smallest. Of course, if one were to focus the optics using an automated system, it would be far easier to write a routine which minimises star image size.

It was found that the telescope mounting system, which is of a high-end amateur level and controlled by SkyX softare (Bisque, 2020), was more than adequate to slew to the Moon and have it centralised on the fibre head. Whilst the pointing was accurate enough for extended objects, it required some correction in order to align a star image on the $10\mu m$ fibre head.

Further compounding this issue is the inaccuracy in the tracking. Over the period of a 10 minute exposure, several pointing corrections were necessary to keep the Moon image over the fibre head. Unfortunately, this made it impossible with the current set-up to take spectra of a star; as once the star was placed over the fibre head, within the period of a few seconds, the starlight was no longer reaching the spectrometer. This made the required exposures, on the order of 10 minutes in length, unfeasible.

To improve this system, a camera could be placed at the eyepiece of the fibre coupling unit. Light can be coupled to the spectrometer end of the fibre to be emitted in the fibre coupling device, this can then be used to locate which pixel on the eyepiece camera holds the fibre head. With this pixel position known, and assuming the system is stable, a centroiding code can be written to measure the star position on the fibre head plane. Using a closed feedback loop, the pointing of the telescope can be controlled in order to ensure that the starlight is always entering the fibre; allowing extended exposures.
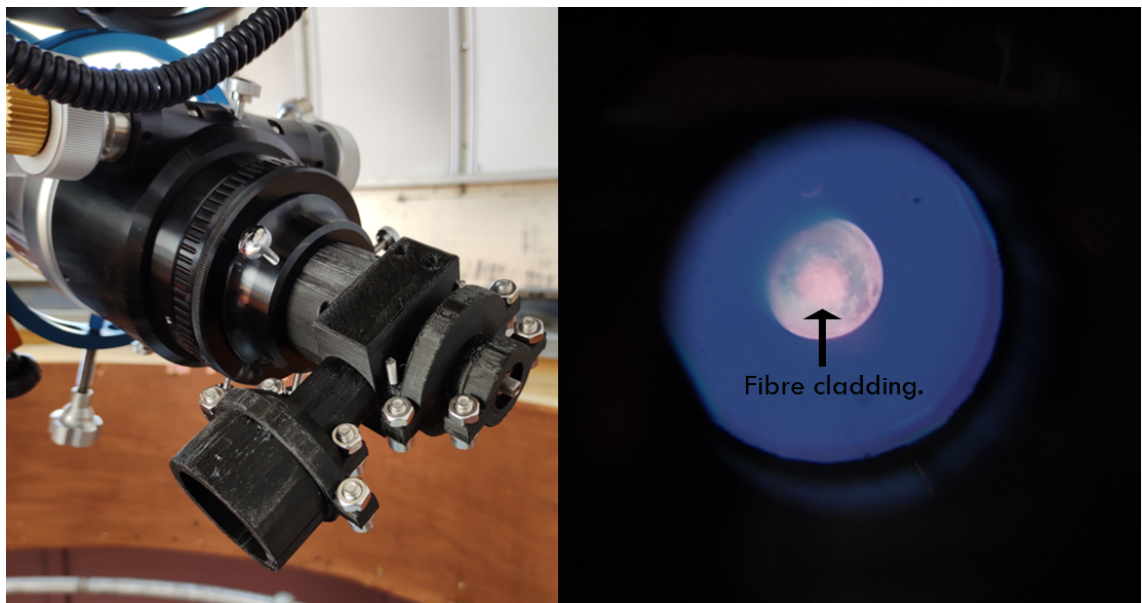
Figure 4.10: (Left Pane) Image of the fibre coupling system attached to the STAR-WAVE 110ED-R telescope. (Right Pane) Image through the eyepiece of the fibre coupling system with the Moon focused on the fibre head plane. The red disk at the centre of the lunar image is the fibre cladding. Note: This optical system was precisely aligned, however the documentation of this image with a smartphone camera introduced 'halos' and vignetting to the image depicted here; making the fibre and lunar image appear off-centre and, in parts, defocused. In reality, this was not the case.
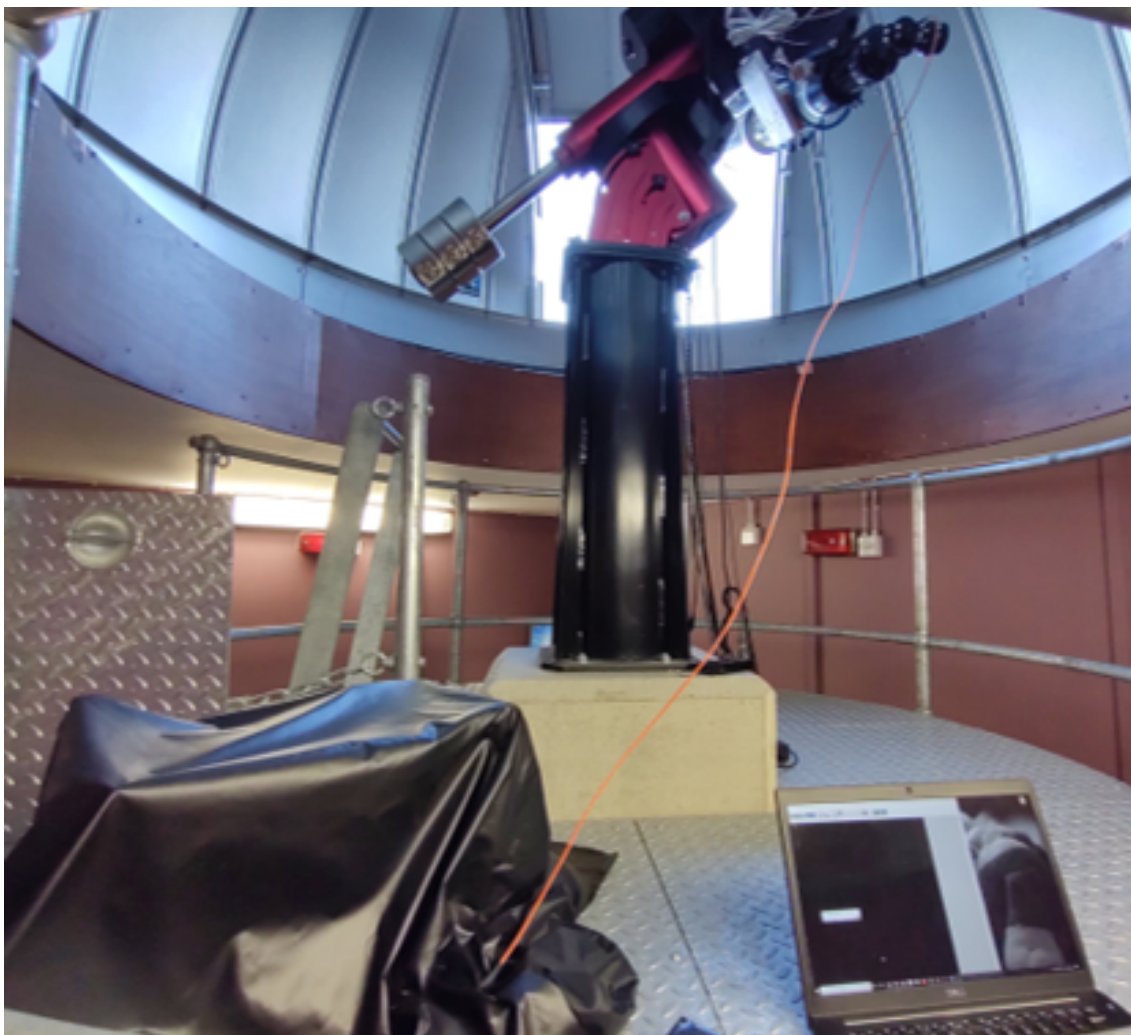
Figure 4.11: Image of the on-sky experimental set-up. QMSPEC is kept under a black light shield to stop stray light.

4.3.3 On-Sky Spectra with QMSPEC

As discussed, with the current fibre coupling solution, star spectra were not attainable; but lunar spectra can be taken with promising results. The experimental set-up is shown in figure 4.11; the fibre coupling system is connected to the telescope and the fibre is then feeding QMSPEC.

A raw lunar spectra exposure of 20 minutes (with a dark frame subtracted) can be seen in figure 4.12. This spectra has a signal to noise ratio of $SNR \approx 100$, suggesting that objects of up to magnitude -1 to 0 could be observed with this instrument/observatory set-up; assuming an improved pointing/guiding system. With a larger aperture telescope, fainter objects could be observed. For example, with a 1m diameter telescope, objects of approximately magnitude 5 could be observed.
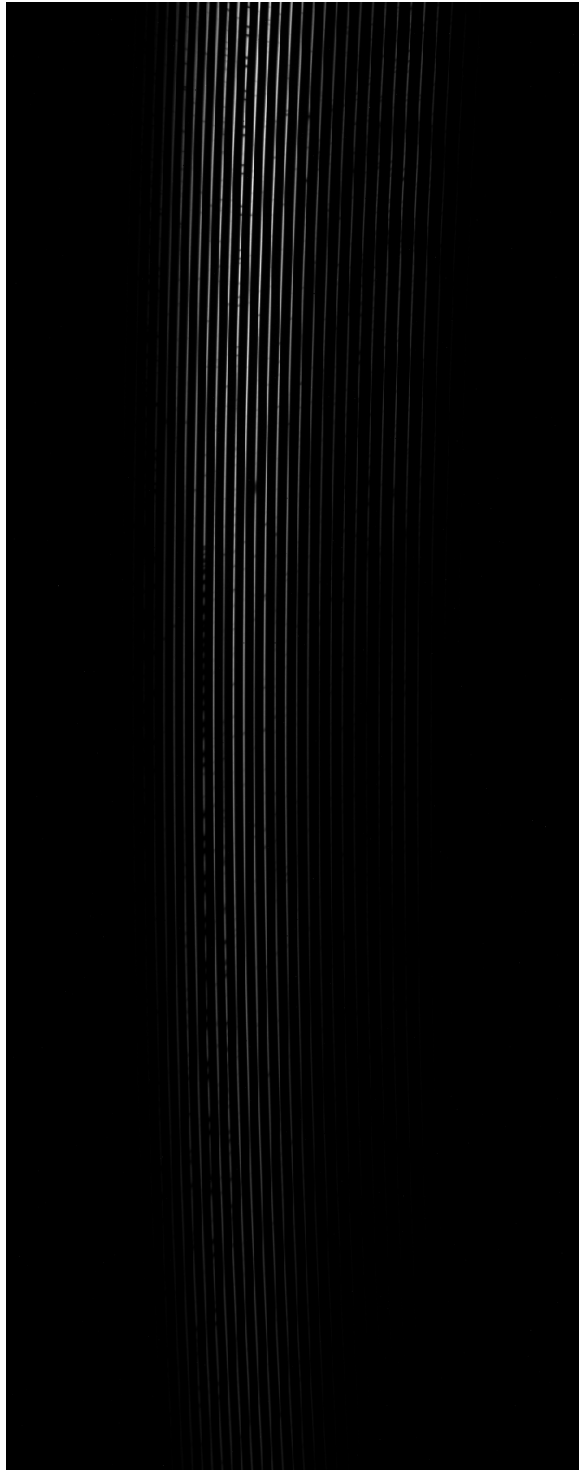
Figure 4.12: Image of a raw 20 minute lunar spectra exposure, with a dark frame subtracted, taken with QMSPEC. Note: For optimal alignment, the most intense region of the blaze would be aligned with the centre of the CCD. However, for this frame, the blaze angle was slightly misaligned due to an alignment error prior to this experiment. This experiment would have been repeated, however the laboratory was closed shortly following this experiment due to the COVID-19 pandemic.
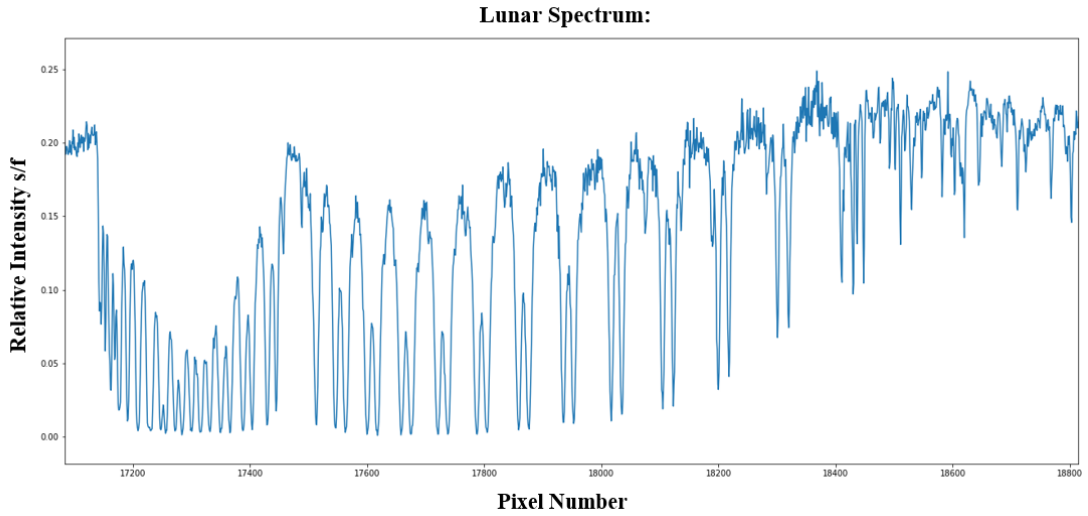
Lunar Spectrum:

Figure 4.13: Extracted order of a 20 minute exposure lunar spectra, clearly exhibiting telluric lines. Pixel number is plotted against relative intensity.

Feeding this lunar spectra through the data reduction pipeline produces a lunar line spectra; one of the extracted orders is shown in figure 4.13. This order displays the O_2 B-band telluric absorption lines. By measuring the separation of the $688nm$ doublet in this order, at 18 pixels, and measuring the resolution element size from a non-broadened line as 3 pixels, it is possible to calculate the on-sky resolving power of QMSPEC at $R \sim 45,000$.

This is a positive result as the spectrometer had been disturbed and vibrated substantially between its alignment in the laboratory and set-up in the observatory. It is safe to assume that if an optical bench and alignment facilities were available in the observatory that an on sky spectra of beyond $R \sim 50,000$ could be attained. Following this experiment, the spectrometer was returned to the laboratory and the resolving power was measured using the Sodium D doublet. This found the spectrometer's resolving power to be $R \sim 40,000$, suggesting that the $R \sim 45,000$ on-sky value is reliable.

4.4 Conclusion

In order to test QMSPEC's on-sky performance, a series of subsystems were required; a fibre coupling system and a data reduction pipeline. Custom solutions were designed and produces for both of these system.

A fibre coupling device was constructed which successfully couples the spectrometer fibre to the telescope with an efficient coupling solution. The system allows

the pointing of the telescope to be assessed to ensure that light from the object of interest is fed into the fibre. However, further work is required in the guiding system; such as through the application of a closed feed-back loop, to ensure that the object is tracked as needed for high SNR exposures.

A custom, light-weight data reduction pipeline was written in Python. This code successfully converts the Echelle spectra in the CCD image to line spectra, while conserving resolution and SNR. Further work is required to produce an accurate wavelength solution but prior to this work being undertaken, the spectrometer should be housed on an optical bench in the observatory and stabilised to ensure that this calibration solution remains accurate between the calibration procedure and the observation.

With the subsystems in place, a lunar spectra was observed and extracted. Using the extracted spectra it was possible to measure QMSPEC's on-sky resolving power at $R \sim 45,000$. It is expected that with alignment facilities in the observatory, such that the instrument can be set up and left to stabilise there, that a higher on-sky resolving power could be achieved. With an improved guiding solution and observatory alignment facilities it would be possible to measure radial velocities to a greater precision than $20m/s$ with QMSPEC; for a total instrument budget of $<£15,000$.

5 NEREA (Near Earths and high-Res Exoplanet Atmospheres): A Red/Near-IR Spectrograph Concept for the GTC

Abstract

NEREA is a stable, compact, high-resolution spectrometer concept for the GTC. The spectrometer is designed with two science goals:

1. The discovery and characterisation of planets around late-M type stars. Using the GTC's large 10m collecting area, NEREA would be capable of reaching out for planets around cooler, smaller and dimmer stars than current facilities; contributing to completing the census of small planets in our stellar neighbourhood (<30pc).

2. The characterization of planetary atmospheres from Hot-Jupiters to Super-earths. NEREA would be capable of detecting species including H_2O, CH_4, CO_2 and ionized metals in planetary atmospheres; as well as detecting and resolving individual Na I, Hα and He I line profiles, improving our understanding of the physical and chemical evolution of planetary atmospheres. Due to the GTC's collecting area, the current planetary sample size can be expected to increase by $\sim$40 times.

The spectrometer preliminary design follows a single-pass Echelle type layout and is fibre-fed with both, a rectangular $22\mu m \times 198\mu m$ science fibre and a $29\mu m$ calibration fibre. The system is designed to achieve a resolving power of 100,000 in the red-NIR regime (0.7-1.7μm). The device footprint is approximately $0.5m \times 1.5m \times 0.1m$, allowing the system to be temperature and pressure stabilised ($< 50cm/s$) in a small, compact container. The concept applies a $320mm \times 90mm$, R4 blazed, diffraction grating as the disperser and a 60.6deg, P-SF67, prism as the cross-disperser. A 325mm focal length, off-axis, parabolic mirror is employed as the collimator and the camera consists of a custom designed 325mm re-focussing lens. The instrument is designed to efficiently couple to the GTCAO system, for which we assume moderate performance of $0.3arcsec$ in our wavelength range. The spectrometer would also be able to perform efficiently without adaptive optics at a resolving power of 40,000 or, with losses, at a resolving power of 70,000-100,000.

5.1 Introduction

From the proposal of the 'Doppler Method' in 1952 (Struve, 1952) to its wide spread application in exoplanet science, beginning in the mid 1990's (Mayor & Queloz, 1995), the use of precision radial velocity measurements in the discovery and characterization of exoplanets has proven to be a powerful tool. Not only in advancing our understanding of planetary features and distribution but also in the study of the dynamics and formation of extrasolar planetary systems as a whole (Udry et al., 2007; Taylor, 2019). Thus, the Doppler method has given great insight into the formation of our solar system, Earth and its place in the greater universe.

In order to implement the Doppler method with the simultaneous reference technique, ultra-stable, high-resolution spectrographs are required (Baranne et al., 1979). These instruments accurately and reliably measure the red and blue shift of the spectral lines from, for example, the line of sight 'wobble' of a star in order to infer the existence, mass and orbital characteristics of a star's planetary system (Pepe et al., 2014b; Mayor et al., 2014).

Furthermore, high resolution spectrographs (with a resolving power, R>50,000) are required to measure atomic and molecular transition lines, allowing the atmospheres of exoplanets to be probed and characterized through the cross-correlation and transit spectroscopy techniques (de Kok et al., 2014; Birkby et al., 2013a; Brogi & Line, 2019). These investigations give great insight into the physical/chemical processes and evolution of planetary atmospheres; and one day might provide the opportunity to detect biomarker signatures, which could hint at the existence of life beyond our planet (Pallé et al., 2009).

In this chapter, we will outline the science goals, design requirements and preliminary design of a stable, compact, NIR, Echelle-type, high-resolution spectrometer concept: NEREA. This design review is completed as a 'pre-phase A' study to demonstrate the feasibility of an instrument with these top-level requirements. The findings of this report will support the funding proposal for a full phase A study once the GTC issues the funding call. The phase A study will produce a further detailed design review encompassing all of the systems and sub-systems which is beyond the aim and scope of this report.

The resultant instrument, NEREA, is to be coupled to the GTC for near-Earth exoplanet discovery and atmospheric characterization science cases.

5.2 NEREA Science Case

With the combination of the GTC's large collecting area and NEREA's proposed technical specifications (notably, its stability and high-resolution in the NIR regime), two main science goals are set to be achieved: *The discovery and characterisation of planets around late-M type stars* and *The characterization of atmospheres from Hot-Jupiters to Super-Earths.*

1. *The exploration of the nearest planets to Earth*: Currently there is a wealth of discovered exoplanets, over 4000 and growing. With this, the interest in the field is shifting from finding more planets to finding those more amenable for detailed physical and atmospheric characterization. The TESS mission, already in operation, will provide hundreds of transiting planet candidates around bright stars, followed in the late 2020's by ESA's PLATO mission. Both will need a Northern Hemisphere stable high-resolution spectrograph mounted on a 10-m class telescope for follow-up studies, to obtain precision radial velocities of stars with small planets near or in their habitable zones. A large fraction (>50%) of these planets will be around M dwarfs (Lada, 2006). NEREA will be uniquely suited to carry out such follow-ups. However, because of the geometric bias, only about 2% of planets are seen to transit their host star when observed from Earth; thus, the other 98% remain undetected (Koch, 2004). The main goal of NEREA is to conduct a radial velocity search for our closest exoplanets, surveying a volume-limited sample of nearby late-M type stars. It will build on the successful CARMENES project, but reach out for planets around cooler, smaller and dimmer stars, where the collecting area sets a limitation (Quirrenbach et al., 2014). A 4-m class telescope can only survey a handful of stars ($\sim$10) with spectral types later than M6. The GTC could bring this number up to a few hundred potential targets, representing the immediate Solar System neighbourhood within 30pc. Recent evidence (e.g., TRAPPIST-1 and others) shows that ultra-cool dwarfs host very rich planetary systems thus boosting the chances of success of blind surveys (Grimm et al., 2018).

2. *The characterization of atmospheres from Hot-Jupiters to Super-Earths*: Observations with high-resolution spectrographs are quickly becoming a key tool for exploring exoplanet atmospheres. One of the major advantages of high-resolution spectroscopy is that not only are we able to detect chemical species in the atmosphere of exoplanets but we are also able to resolve their individual spectral features. If the SNR of the final transmission spectrum is high

enough, it is possible to obtain the temperature/pressure profiles of the higher atmosphere by adjusting thermal models to different regions of the lines (from core to wings), which arise from different layers of the atmosphere. The cross-correlation technique has already allowed the detection of several species in planets from Hot-Jupiters down to Neptune-size, including H_2O, CH_4, CO_2, CO, and ionized metals (de Kok et al., 2014). Complementary, employing the transmission spectroscopy technique, ground-based studies have been able to resolve the individual line profiles of Na I, $H\alpha$ and He I lines (Redfield et al., 2008; Cabot et al., 2020; Wyttenbach et al., 2017; Keles et al., 2020; Zhang et al., 2020). This allows the exploration of atmospheric escape, an important process for understanding atmospheric physical and chemical evolution (Žák et al., 2019). All of these studies have been conducted over a limited sample of planets with bright host stars, applying spectrographs operating in the visible and near-IR wavelength regime at 3-4m class telescopes. NEREA at the GTC would allow us to vastly increase this sample, providing the capability to measure atmospheric escape down to the super-Earth regime and for a much more numerous stellar sample (potentially 40 times larger).

As mentioned previously, while being designed with these specific science cases in mind, NEREA will be a very versatile spectrograph; filling the current capability gap of high-resolution spectroscopy at the GTC. It is expected that NEREA will become a common user instrument, for open use by the community for a variety of science cases.

5.3 Instrument Concept and Top-Level Requirements

To achieve the science cases, outlined above, a number of top-level requirements for the high-resolution spectrometer have been derived, which are listed in table 5.1.

NEREA is designed to be a primarily adaptive optics assisted instrument, this minimises cost and allows the system to be compact while achieving the desired resolution. This compact nature, in turn, allows the system's stability to be greater; as it is easier and more efficient to actively temperature and pressure stabilise a compact tank (Stefánsson et al., 2016).

Table 5.1: Outline of NEREA's top-level requirements.

Property:	Technical Requirement:	Goal:
Input	Fibre-fed spectrograph with a front-end throughput efficiency of $>70\%$.	Fibre-fed spectrograph with a front-end throughput efficiency of $>80\%$.
Spectral Resolution	$>70,000$, sufficient to resolve atomic and molecular spectral lines on main sequence stars and planets. This resolution is also sufficient to resolve the signature of Earth atmospheric molecular gases.	$110,000$.
Wavelength Coverage	$800 - 1700nm$.	$700 - 1700nm$.
Efficiency (from input to detector)	$>10\%$ for $800 - 1700nm$, comparable with existing echelle spectrometers.	$>15\%$ for $700 - 1700nm$.
Abs. Wavelength Calib.	$<2m/s$ hard-ware stability.	$<50cm/s$ sky stability.
Adaptive Optics Requirement	Moderate AO requirement with an input image size: $0.3arcsec$	
Size	$1.5m \times 1.5m \times 1m$.	$1m \times 1m \times 0.5m$.
Hard-ware Budget	€$3million$	€$2million$
Other Requirements	Compact design, behind an AO system, also able to operate under seeing limited conditions ($R \sim 30,000$, or $70,000$ with high losses).	

5.4 Front End Preliminary Design

5.4.1 Fibre Coupling System Optical Design

NEREA would couple to the GTC at the exit of the beam path from GTCAO and before the beam enters the main GTCAO instrument, FRIDA (Cuevas et al., 2006). The aim of the fibre coupling system is to efficiently couple GTCAO to NEREA without intrusion into the set-up of the current/planned instrumentation on the GTCAO optical bench. As such, the NEREA Fibre Coupling System, NEREAFCS, is designed to sit around current instrumentation on the empty spaces of the optical bench. Between GTCAO and FRIDA there is a magnetic platform which is used for GTCAO calibration. This can be easily interchanged, without affecting performance of either instrument, with a fold mirror which will redirect the beam into NEREA's fibre coupling system, see figure 5.1.

NEREAFCS follows a conventional fibre coupler design; similar to that seen in HARPS (Pepe et al., 2000). The redirected beam from GTCAO is allowed to come to focus. At the focal plane there is a $45deg$ plane mirror with a $75\mu m$ diameter pinhole in the centre, cut parallel to the incoming optical axis. The mirror is aligned such that when the beam passes through this hole it will couple efficiently to the science fibre; see figure 5.2. Following the mirror is a low-cost Edmund Optics $f = 49.9mm$ doublet (AC 127-050-C) which will re-collimate the beam. Subsequently, the beam is re-imaged onto the fibre by another commercially-off-the-shelf Edmund Optics doublet of $f = 12.8mm$ (AC 064-013-C). The optics of the focal reducer are chosen such that the F/number of the NEREAFCS exit beam is matched to that of the fibre, F/4.2. Low-cost, commercially-off-the-shelf doublets can be used for this purpose whilst still achieving close to diffraction limited performance as the beam path of the marginal rays are close to the optical axis, such that minimal optical aberrations are introduced; this is demonstrated in figure 5.3. When the system is misaligned, the mirror will reflect the beam to a camera system which, using centroiding, will adjust the pointing of the telescope to re-align the fibre coupling system. The GTC's pointing accuracy is within 2 arcseconds, NEREAFCS can accommodate the centroiding of off-axis beams up to 5 arcseconds, leaving ample redundancy.

The GTC has an F/number of 16-17, depending on where this is defined. For this analysis, the GTC is taken to have a focal length of $169.9m$ and a diameter of $10.4m$, such that it produces a $F/^T = 16.33$ beam. Using the $f = 49.9mm$ doublet as a re-collimator, a $3.06mm$ diameter collimated beam is produced. Re-focussing this with the $f = 12.8mm$ doublet produces an F/4.18 beam which can be efficiently
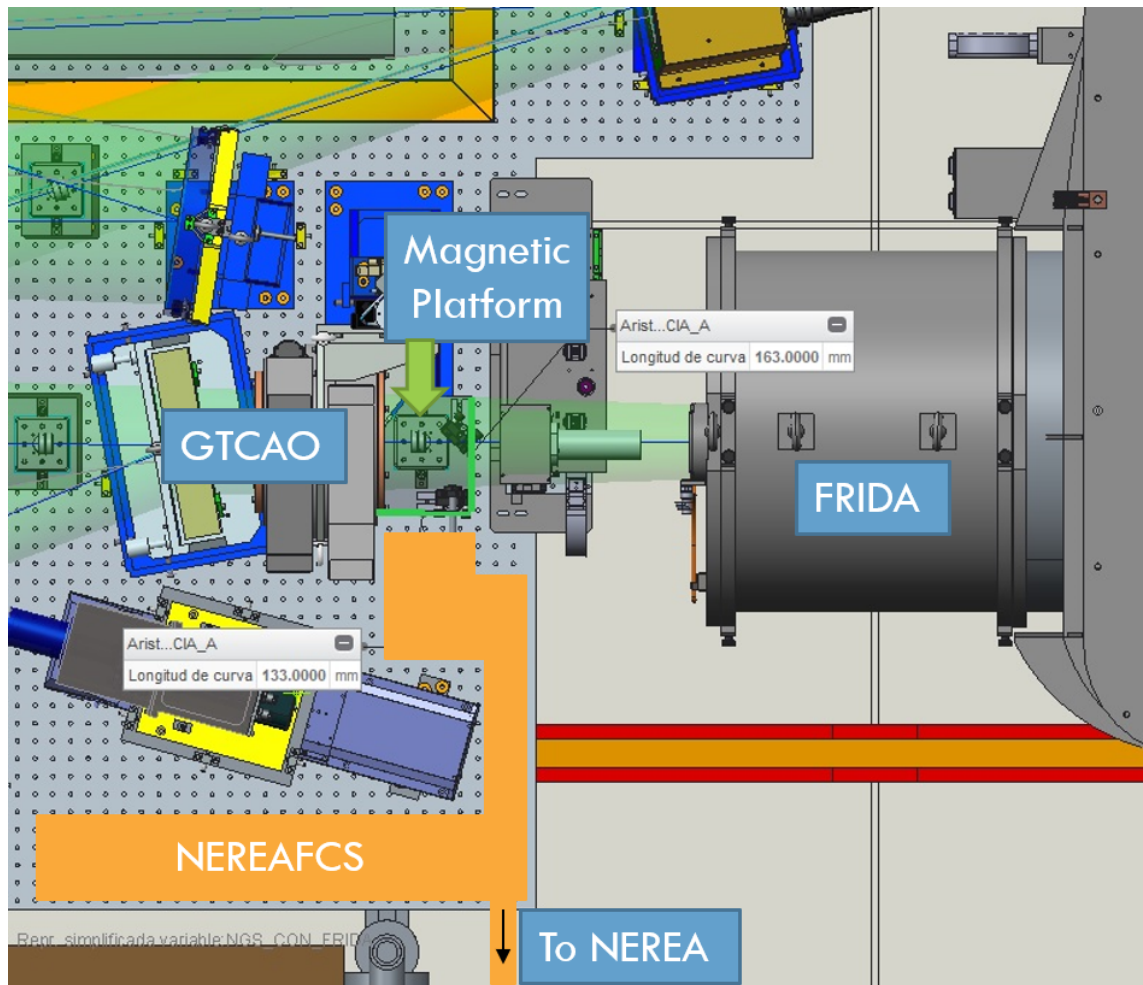
Figure 5.1: Schematic depicting the NEREA fibre coupling system on the current GTCAO/FRIDA optical bench. The magnetic platform alows the GTCAO calibration system to be interchanged with a fold mirror which re-directs the beam into NEREAFCS (the functional placement and dimensions of which are demonstrated by an orange box).
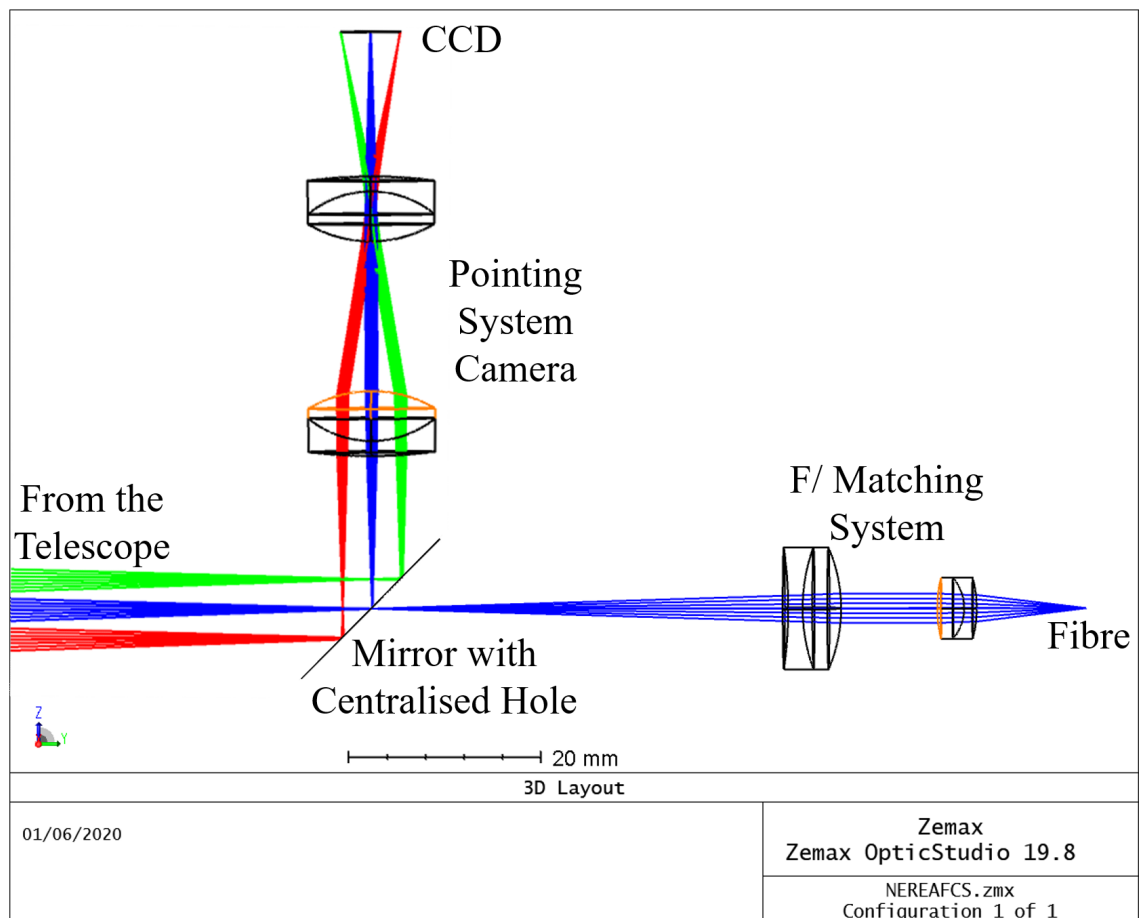
Figure 5.2: Annotated schematic layout of a Zemax model of the NEREAFCS system.

Figure 5.3: Spot diagram of the fibre coupling system Zemax model. This demonstrates that the optical performance of the low-cost components are sufficient to produce a system with close to diffraction limited performance; with geometric spot sizes less than $10\mu m$ across the entire instrument wavelength range. This is more than sufficient performance to allow efficient coupling to any applicable optical fibre.

coupled to an F/4.2 fibre.

5.4.2 Optical Fibre Selection

NIRPS, a spectrograph at ESO La Silla, uses an F/4.2 fibre (Wildi et al., 2017). By using the same F/number we can build on the experience gained by the team on that project to build a proven and maximally efficient fibre coupling, scrambling and splitting system.

If the GTC was not seeing limited, one could achieve a diffraction limited spot size of diameter, $x = 1.22\lambda \times F/^T = 31.6\mu m$ at $\lambda = 1.6\mu m$. GTCAO is not designed to operate at diffraction limited performance in NEREA's wavelength range but, after analysis of the system, it is safe to assume that it will be able to bring the seeing limit down from 1" to 0.3" resolution; or ~ 8.5 times the diffraction limit in the $0.7 - 1.7\mu m$ wavelength regime. Hence, applying equation 2.11, $h' = F/^S \times x^T \times \frac{1}{F/^T}$, it is found that $h' = 4.2 \times (8.5 \times 31.6\mu m) \times \frac{1}{16.33} = 69.08\mu m$. As such, h' is small enough to couple efficiently to a standard, readily available $h = h_S = 66\mu m$ and $F/ = F/^S = 4.2$ octagonal optical fibre. This is especially prudent as it is likely that GTCAO will bring the telescope spot size below 8.5 times the diffraction limit and that the majority of the spot intensity will be in the centre of the PSF. The system is also designed to operate in circumstances where no AO is available, either due to unfavourable weather conditions or a fault with the AO system. In this situation, the seeing limited spot image from the GTC, having passed through the focal reducer and been converted to F/4.2, would be $212\mu m$ in diameter. As such the spectrometer could either operate at full resolution with losses in efficiency or one could instead couple efficiently to the secondary science fibre, a $200\mu m$ octagonal fibre, leading to a reduction in resolving power. Octagonal fibres are chosen due to their significant improvement in scrambling performance over comparable circular fibres (Chazelas et al., 2010; Avila, 2012).

NEREA will also have a third fibre input, a $h_C = 29\mu m$ and $F/^C = 4.2$ octagonal calibration fibre for concurrent on-sky analysis or calibration. Both of the science fibres will pass through a mode scrambling system. The primary science fibre is to be spliced in three and efficiently coupled to a $22\mu m \times 198\mu m$, $F/^S = 4.2$ rectangular fibre. The secondary science fibre is to also be spliced in three and efficiently coupled to a $66\mu m \times 300\mu m$, $F/^S = 4.2$ rectangular fibre, see figure 5.4.

Telescope Focus: Spectrometer Input:

212μm, F/4.2, Science Fibre, Coupled to telescope.

66μm, F/4.2, Science Fibre, Coupled to telescope.

Scrambling/splitting /coupling systems.

198X22μm, F/4.2, Rectangular Science Fibre.

300X66μm, F/4.2, Rectangular Science Fibre.

~ 140μm (5 res. elements)

29μm, F/4.2, Calibration Fibre, Coupled to calibration source.

29μm, F/4.2, Calibration Fibre
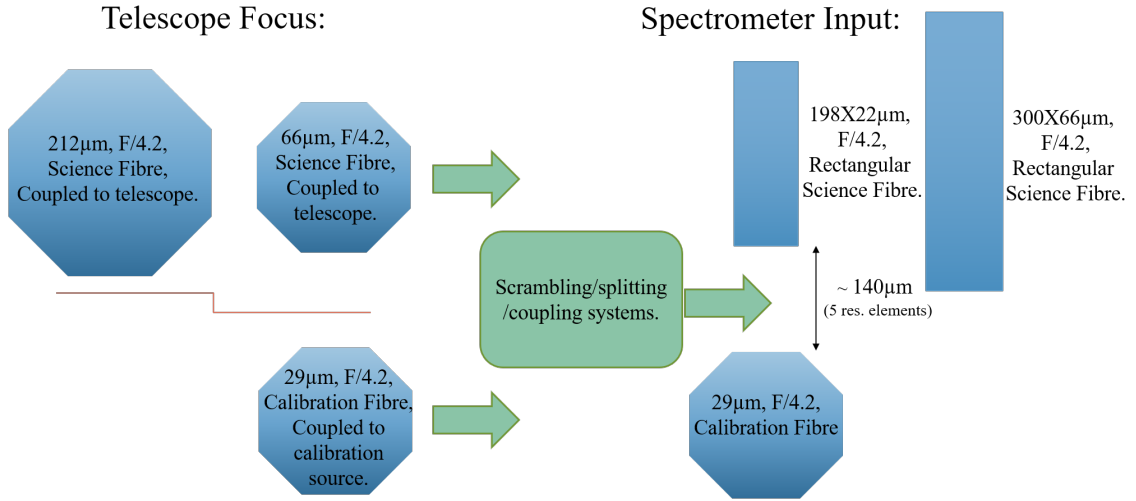
Figure 5.4: Schematic diagram of the fibre system layout.

5.4.3 Fibre Mode Scrambling System

As discussed in section 2.0.9, modal noise is defined as the instability in the output illumination of an optical fibre caused by either intermodal phase variations or an incomplete filling of the fibre. This instability leads to variability in the PSF of the spectrograph's resolution elements, shifting the centroid of the resolution element and introducing RV noise; reducing the RV precision of the instrument. Modal noise is proportional to λ/h, where λ is the wavelength being coupled to the fibre and h is the diameter of the fibre (Baudrand & Walker, 2001). As such, the primary fibre with its smaller diameter, enabled by AO, will be more susceptible to model noise.

To combat this modal noise, a strong and proven fibre scrambling solution will be implemented, following the success of the NIRPS system (Wildi et al., 2017). The system will utilise:

- Octagonal and rectangular fibres (Chazelas et al., 2010; Avila, 2012).

- Double scramblers that exchange near- and far-field filling of the fibre, to ensure complete filling.

- Fibre stretchers which modulate the phase between modes and stabilise the PSF for any modal content.

With these solutions a sub $2m/s$ RV precision will be achievable.

5.5 NEREA Preliminary Design Overview

5.5.1 Basic Considerations For NEREA's Design

NEREA's preliminary design was constructed such that it meets the top-level requirements set out in table 5.1 while maximising design simplicity and ease of manufacture. Minimising the number of components is also considered, to increase stability performance, throughput and to minimise cost; this is expanded further through the use of readily available/manufacturable components where feasible. The system has been designed to perform as reliably as possible via the use of standard industry solutions and well-understood solutions inherited from previous projects. This is particularly the case in the state-of-the-art AO-coupling, mode scrambling and splitting of optical fibres.

5.5.2 Preliminary Optical Design

Components and Instrument Layout

The spectrograph follows the classical Echelle-type design. It consists of:

- a $f_{coll} = 325.08mm$, $20deg$ off-axis parabolic mirror as a collimator.

- a $13grooves/mm$, R4 ($76deg$ blaze), $90mm \times 320mm$ Echelle diffraction grating.

- a $60.6deg$, $240mm \times 240mm$ faced P-SF67 prism.

- a custom designed $f_{cam} = 325.08mm$ refocussing camera lens.

- a Hawaii 4RG (4096×4096) detector with $10\mu m$ pixels.

The optical path, shown in figure 5.5, is as follows:

1. The beam leaves the science and on-sky/calibration fibre at F/4.2.

2. The parabolic mirror, which also acts as the aperture stop of the system, collimates the beam and redirects it to the grating.

3. The grating diffracts the beam and redirects it to the prism with the diffracted region of interest within $3.52deg$ of the optical axis.

4. The prism cross-disperses the beam separating the diffraction order.

5. The resultant beam is focussed onto the CCD by the re-focusing camera lens.
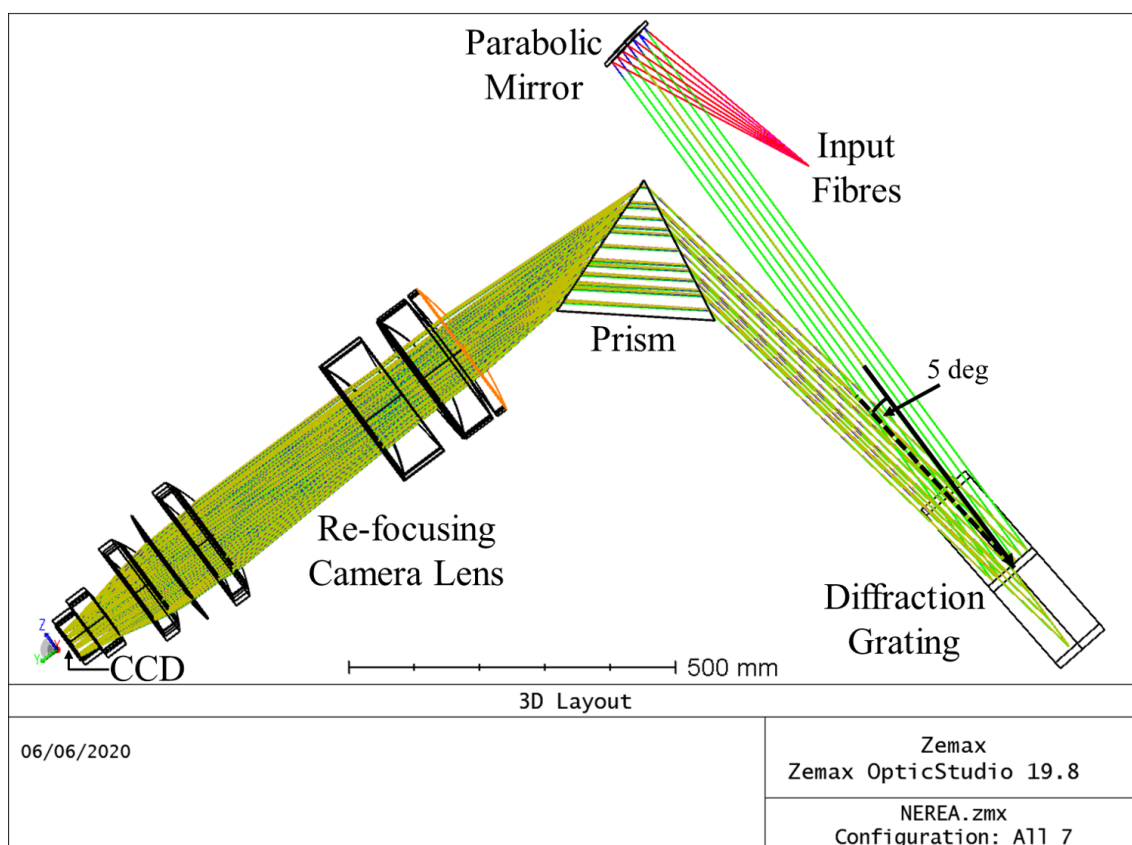
Figure 5.5: Annotated schematic layout of the optical design of the NEREA spectrograph. The 5*deg* input beam angle at the diffraction grating is labelled. Note: This preliminary design is subject to change and refinement with further design reviews but the top-level design specifications will remain broadly consistent.

Between the prism and the grating an additional plane fold mirror shall be placed to reduce the footprint of the instrument and allow the use of a compact cylindrical vacuum chamber. The optical design and testing of the system preliminary design is undertaken using Zemax Optical Studio.

Resolving Power

The goal resolving power of the spectrograph is 110,000 and the requirement is 70,000. The theoretical maximum resolving power of a spectrometer system (in the form referenced in Baker et al. (2019)) can be described by $R = (2f_{coll}tan(\alpha))/h_S$; where α is the blaze angle of the diffraction grating. Using this equation, it can be seen that this NEREA preliminary design can achieve a theoretical resolving power of $R = 118,500$. This is a suitable starting theoretical value as it contains some redundancy for the resolution to decrease with anamorphic effects, aberrations and

manufacturing tolerance allowances whilst still enabling close to the goal resolving power to be achieved across the entire field and wavelength range. When the AO system is not in use and NEREA is fed by the secondary science fibre, a theoretical resolving power of 39,500 can still be achieved.

Detector

The chosen Hawaii 4RG (4096×4096) detector has a high quantum efficiency in NEREA's wavelength range ($> 50 - 70\%$ QE at $0.8\mu m - 1.5\mu m$), low read-out, photon and shot noise as well as minimal dark current without the need for a cryogenic system through the use of tuned sensitivity (Teledyne Scientific and Imaging, 2019). With its $10\mu m$ pixels it has an active region of $40.96mm \times 40.96mm$. As the spectrometer operates at $1:1$ magnification, the resolution element will have a size comparable to that of the fibre, at $22\mu m$. With the $10\mu m$ pixels this gives a sampling of approximately 2.2 times, which surpasses the Nyquist requirement.

Diffraction Grating

Following discussion with manufacturers, it was discovered that Bach Research would be able to produce a grating to the specification of that manufactured for the NIRPS spectrograph (Wildi et al., 2017) at a greatly reduced cost, using the tooling from that instrument. This grating has specifications close to our requirement and is producable for 10% of the cost of an equivalent custom grating. Hence, by using this grating, approximately €700k is reduced from the required hard-ware budget.

The $13grooves/mm$, R4 ($76deg$ blaze), $90mm \times 320mm$ Echelle diffraction grating gives a maximum beam size of $320mm \times \cos 76deg = 77.4mm$. Following the grating equation, it places $700nm$ in order $m = 213$ and $1.6\mu m$ in order $m = 87$. Applying equation 2.4, $\overline{\beta}_{\pm}^{max} = \pm \sin^{-1}\left(\frac{2\tan\phi}{m}\right)$, we see that order $m = 87$ has a total blaze width of $\overline{\beta}_{\pm}^{max} = \pm 5.29deg$ from the optical axis which with a $325.08mm$ camera corresponds to a $60mm$ blaze width on the CCD. Due to the blaze intensity peaking at the centre of the blaze function, 96% of blaze intensity is captured within $3.52deg$ from the optical axis. This corresponds to a total $39.9mm$ blaze width on the CCD plane, which fits onto the $40.96mm$ detector, see figure 5.6. Of course, from the blaze intensity equation (equation 2.2) we see that for higher orders, the blaze width is smaller, such that the sensor will capture more of the blaze function for all of the proceeding higher orders.
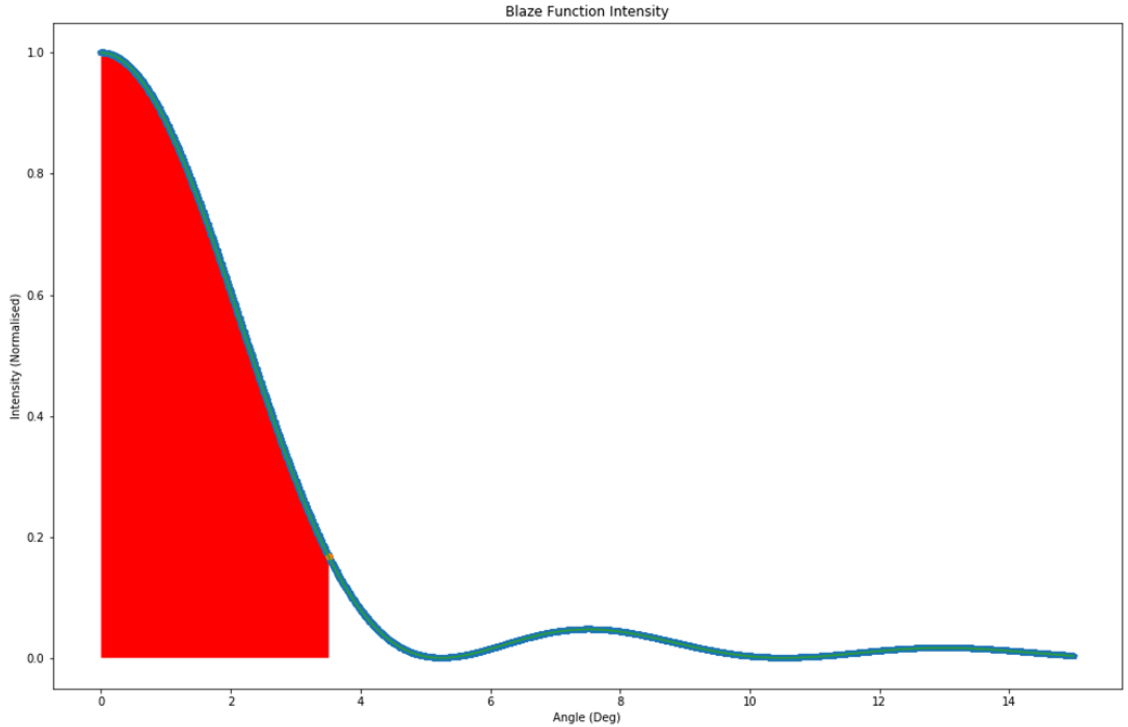
Figure 5.6: Plot of the blaze function of order m=87 with the region of blaze intensity captured by the CCD, up to $3.52deg$, highlighted in red.

It is noted that it is often useful for wavelength calibration and stability measurement if an overlap of the same wavelengths are seen in multiple orders, as is the case for ESPRESSO (Pepe et al., 2010). With this in mind, NEREA is designed to have substantial order overlap across all of the orders down to order 90, see figure 5.7. This has the effect of increasing the accuracy of the wavelength solution of the spectrograph, enabling more accurate RV measurements. However, for a given exposure length, this will reduce the amount of light measured in an order for a given wavelength. This is because it will be spread across across two (or more) different places on the CCD; with the strength of the intensity distribution between those positions dictated by the blaze function intensity at those positions for the order in which they lie. This has the effect of reducing the SNR for that spectral line measurement at a given point, reducing the precision of the measurement. In practice, however, this is not an issue as an observer would increase their exposure time to ensure that they are reaching the SNR requirement for their science case.

Prism

The prism is chosen to give maximal separation between orders, to avoid crosstalk, while ensuring that all of the orders fit onto the sensor. With a $60.6deg$ P-
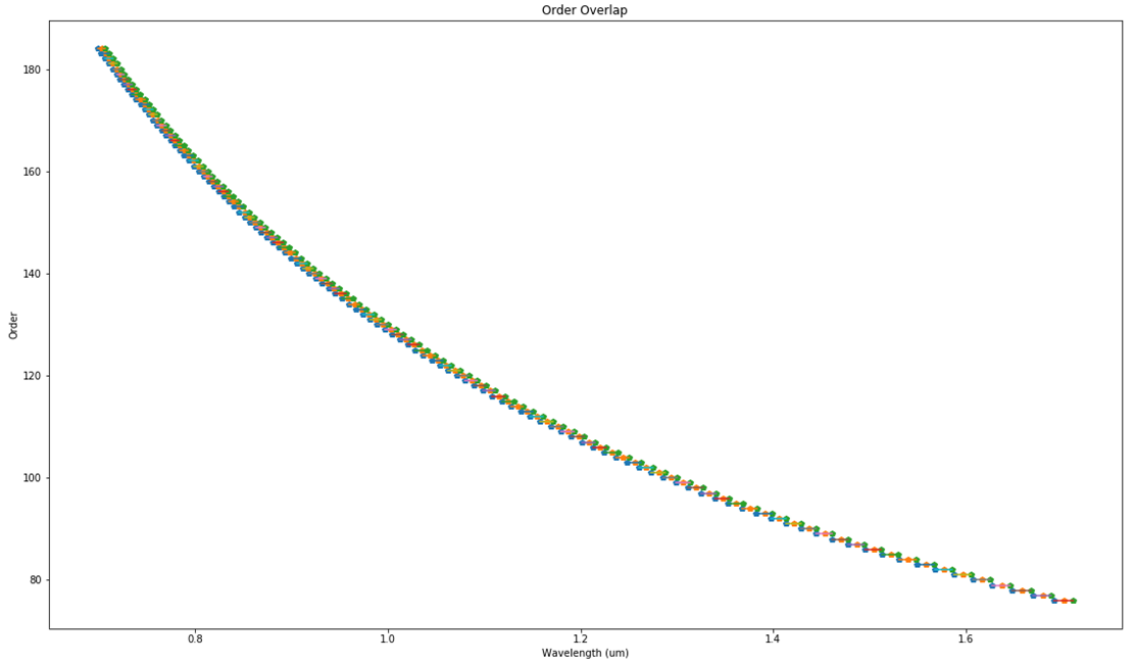
Figure 5.7: Plot of the order overlap of wavelength against order. The green, orange and blue points show the upper, central and lower wavelength of each order. This plot shows that there is substantial wavelength overlap between adjacent orders down to approximately order 90.

SF67 prism, this is achieved. Dispersion is close to constant across the wavelength range, giving a consistent separation between the centre of orders of $0.28 - 0.42mm$; as displayed in figure 5.8. At the minimum separation of $0.28mm$, the distance between the edges of science orders is $82\mu m$, which is equivalent to 3.73 resolution elements, minimising the risk of cross-talk. The resultant total separation of orders is $40.4mm$ ($3.55deg$ field), fitting within the $40.96mm$ detector. The P-SF67 glass has a throughput of $> 99.8\%$ per mm in the $0.7 - 1.7\mu m$ wavelength range, leading to a total throughput of $> 90\%$ for the $60.6deg$, $240mm \times 240mm$ faced P-SF67 prism.

Re-focusing Camera Lens

In order to maximise resolving power, the longest collimating focal length which fills the $77.4mm$ beam acceptance of the diffraction grating should be used. Following this criteria for a F/4.2 diverging beam, the focal length of the parabolic mirror is set to $f_{coll} = 325.08mm$. Noting manufacturing considerations, the parabolic mirror is chosen to be $20deg$ off-axis. This allows the beam to be compactly redirected to the grating whilst ensuring that there is no vignette from the fibre (and its associated
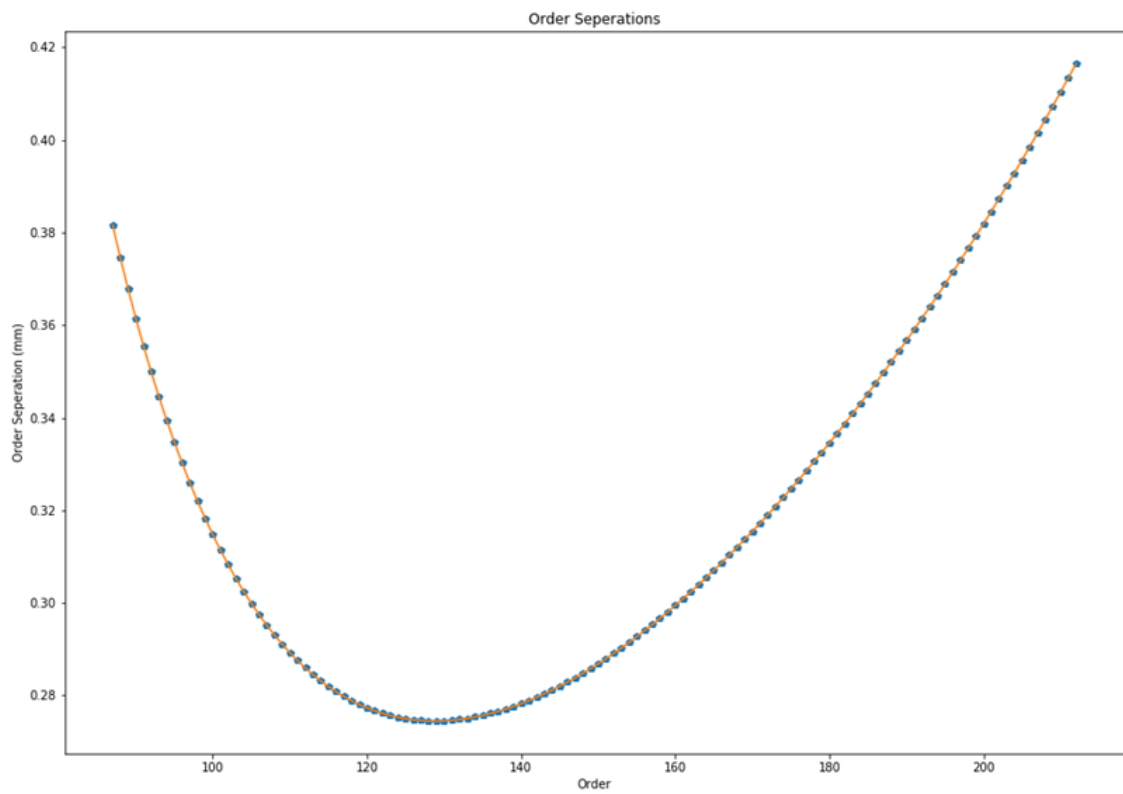
Figure 5.8: Plot of order against the separation of the order and its adjacent order on the CCD plane induced by the dispersion of the prism, for a $f = 325.08mm$ re-collimation camera lens.

mounting).

With this design, a $1 : 1$ magnification system was found to give the best trade-off between filling the sensor in the dispersion and cross-dispersion directions and the pixel sampling per resolution element. As such, a $f_{cam} = 325.08mm$ refocussing camera lens was designed; as demonstrated in figure 5.9. In this early preliminary design for the camera lens, a ten element optical system was constructed using readily available, low-cost glass selections from Schott and Ohara. The front element of the lens system has a diameter of approximately $223mm$, to avoid vignetting of the dispersed beams, however this is reduced for subsequent elements where possible in order to reduce cost and maximise compactness of the system. The ten elements were chosen to ensure the maximal aberration correction. The performance of this lens should be strongly diffraction limited to ensure correction for the off-axis aberrations introduced by the physical size of the fibre array collimated by the parabolic mirror. The lenses were chosen to be non-cemented to minimise manufacturing cost. This can have positive and negative effects on stability. Notably, not being cemented leaves the lenses prone to more independent drift, but this also stops elements from putting stress on each other with expansion and contraction. Further trade-off analysis should be conducted on the issue of lens design stability and material selection for this system. The resultant preliminary design for the collimating lens has diffraction limited performance across the entire necessary field and wavelength range; an example spot performance plot is displayed in figure 5.10.

The resultant resolution element image produced by the spectrometer is a convolution of the size of the imaged object and the size of the spot formed by imaging a perfect monochromatic point source through the system; where this spot size is dictated by either optical aberrations or the diffraction limit of the system (Ahi & Anwar, 2016). As such, the resultant image size can be given by the sum in quadrature of the $22\mu m$ resolution element size and the RMS spot size. Given this, the RMS spot radius of the resultant spectrometer system can be allowed to reach $11\mu m$ before a substantial decrease in the resolution of the spectrometer is seen.

Optical Design Results

The resultant spectrometer system designed using these components is depicted in figure 5.5. This system is found to have an RMS spot radius $< 11\mu m$, as required, across the entire operating wavelength range and CCD field. This spot size performance is demonstrated in figure 5.11.

This design has proven that a system can be constructed that meets the top-level
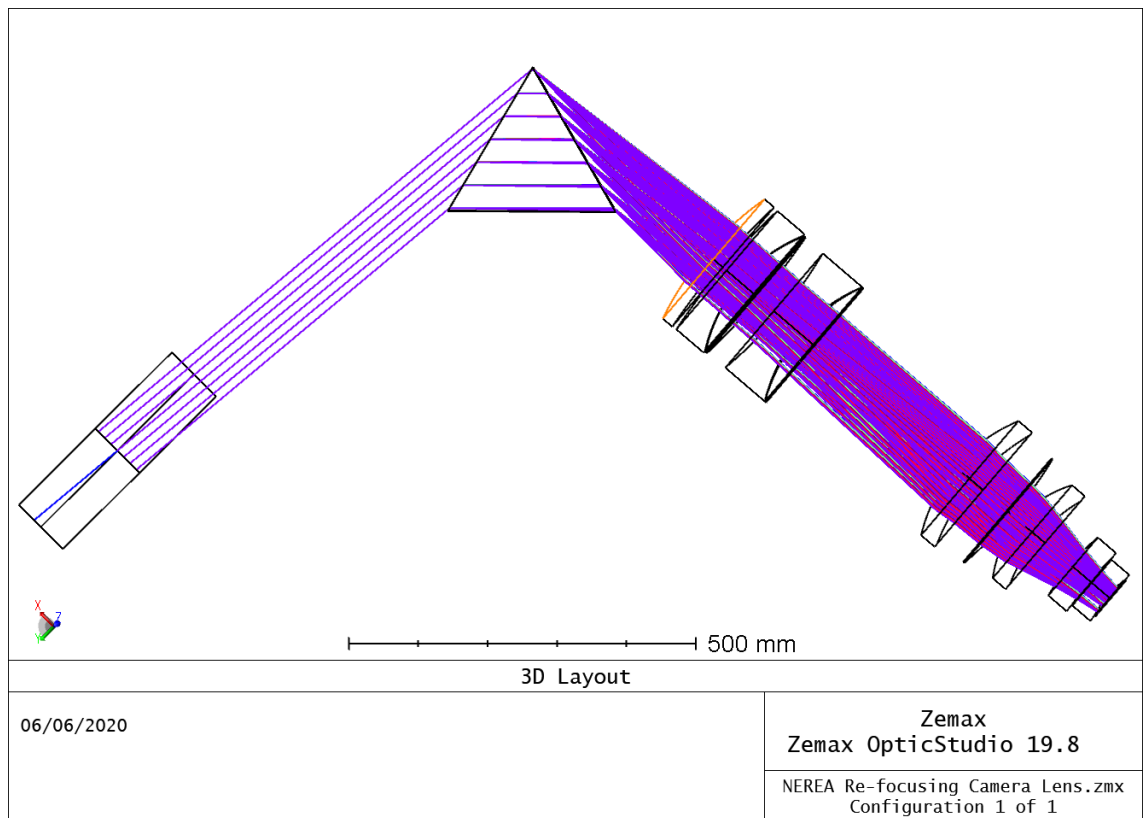
Figure 5.9: Schematic layout of the NEREA re-focusing camera lens model. The system layout depicts the set-up in which it was designed.

☑ ▲ 1.2

OBJ: -5.0000, 0.0000 (deg)   OBJ: -5.0000, -1.0000 (deg)   OBJ: -5.0000, -2.0000 (deg)   OBJ: -5.0000, -3.0000 (deg)

20.00

IMA: 7.158, 0.000 mm   IMA: 6.964, -5.762 mm   IMA: 6.381, -11.503 mm   IMA: 5.408, -17.202 mm

OBJ: -5.0000, -3.5000 (deg)   OBJ: -5.0000, -4.0000 (deg)   OBJ: -5.0000, 1.0000 (deg)

IMA: 4.775, -20.030 mm   IMA: 4.044, -22.841 mm   IMA: 6.964, 5.762 mm

OBJ: -5.0000, 2.0000 (deg)   OBJ: -5.0000, 3.0000 (deg)   OBJ: -5.0000, 3.5000 (deg)   OBJ: -5.0000, 4.0000 (deg)

IMA: 6.381, 11.503 mm   IMA: 5.408, 17.202 mm   IMA: 4.775, 20.030 mm   IMA: 4.044, 22.841 mm

Surface: IMA

Spot Diagram

06/06/2020
Units are μm.   Airy Radius: 4.813 μm. Legend items refer to Wavelengths

Field	:	1	2	3	4	5	6	7	8	9	10	11
RMS radius	:	1.024	0.964	0.793	0.532	0.466	0.806	0.969	0.811	0.571	0.541	0.853
GEO radius	:	1.708	1.727	1.702	1.503	1.315	1.752	1.727	1.702	1.503	1.315	1.752
Scale bar	: 20	Reference : Chief Ray										

Zemax
Zemax OpticStudio 19.8

NEREA Re-focusing Camera Lens.zmx
Configuration 1 of 1

Figure 5.10: An example spot diagram produced by the NEREA re-focusing camera lens. This example demonstrates the spot size performance of the lens system across a field range from $-4deg$ to $4deg$ at a wavelength of $1.2\mu m$. In the footnote of this plot, values are given for the RMS spot radius and GEO spot radius at each of the plotted field angles. The value of the RMS radius is the root-mean-square deviation for all of the ray bundles traced through the system at that field angle; as such, it gives a sense of the radius within which the majority of the light intensity is focused. The GEO radius is the geometric spot radius, which tells us the radius within which all of the light rays traced through the system at that field angle will focus; as such, it includes regions of the PSF which may be of low intensity and have little impact on the measured spot-size performance. As is demonstrated, the spot size performance is consistent across the entire field range and is heavily diffraction limited. The spot radius requirement of $11\mu m$ is surpassed substantially, with the RMS spot radius found to be less than $1\mu m$ for the majority of fields specified here. The performance demonstrated in this plot at $1.2\mu m$ is consistent across the entire wavelength range $(0.7\mu m - 1.7\mu m)$.

☑ + 0.991388

OBJ: -0.00, -118.29 mm

20.00

IMA: -0.167, 0.000 mm

OBJ: 0.01, -118.39 mm

IMA: -0.258, 0.053 mm

OBJ: -0.01, -118.39 mm

IMA: -0.258, 0.075 mm

OBJ: 0.01, -118.19 mm

IMA: -0.075, -0.075 mm

OBJ: -0.01, -118.19 mm

IMA: -0.075, -0.053 mm

Surface: IMA

Spot Diagram					
06/06/2020					Zemax
Units are µm. Airy Radius: 4.907 µm. Legend items refer to Wavelengths					Zemax OpticStudio 19.8
Field : 1 2 3 4 5					
RMS radius : 0.220 3.338 3.530 3.599 3.400					
GEO radius : 0.825 6.688 7.059 7.326 6.909					
Scale bar : 20 Reference : Chief Ray					NEREA.ZMX
					Configuration 4 of 7

Figure 5.11: An example spot diagram produced by the model NEREA spectrometer demonstrated in figure 5.5. The five points depicted here demonstrate spot performance for the centre and four corners of the primary science optical fibre for a fibre emitting $0.991\mu m$ light. This wavelength is re-imaged through the spectrometer at the centre of order 150. Spot size performance is consistent with that demonstrated here across the entire spectrometer's operating wavelength range. RMS spot radius is less than the required upper limit of $11\mu m$.

requirements of the instrument. However, this is an early preliminary optical design and is limited by the resources of this study. With further design stages the system has the opportunity to be improved and refined further. Notably, the camera lens' ten non-cemented elements are likely to impact system throughput. A more highly designed component may have twice the efficiency of the proposed preliminary design whilst still achieving comparable optical performance. A four element lens system is currently under investigation.

5.5.3 Stray Light Analysis and Throughput

Whilst this is a purely academic exercise as the final optical design is likely to vary from the one described, stray light analysis of the camera section of the preliminary optical design was undertaken using the non-sequential mode of Zemax Optical Studio. It was found that no significant ghost imaging was present in the system and that the stray light contribution to the resultant spectral image is at a contrast ratio of less than 10^{-4}.

A pessimistic and coarse efficiency analysis of the model system suggests that this design, where all optical components have the relevant high-throughput AR coatings in the $700nm - 1.7\mu m$ wavelength range, should have a throughput greater than 10%.

5.5.4 Fibre Orientation

To maximise compactness of the system, a $5deg$ reflection angle at the diffraction grating (in the cross-dispersion plane) is introduced. This is depicted in figure 5.5. This minimises the required diameter of the re-focussing optics and hence, reduces cost. However, this introduces some Beta-anamorphism to the imaging system (Konidaris, 2014), leading to a tilting and elongation of the resolution elements and hence the spectra as a whole. An example of this effect is depicted in figure 5.12 (upper panel).

The effect of the tilt on the spectra can be mitigated, making the extraction process simpler, by pre-tilting the fibre to account for the effects of beta-anamorphism. It was found that by pre-tilting the fibre $30.3deg$, the resultant fibre image is re-aligned to level; as displayed in figure 5.12 (lower panel).
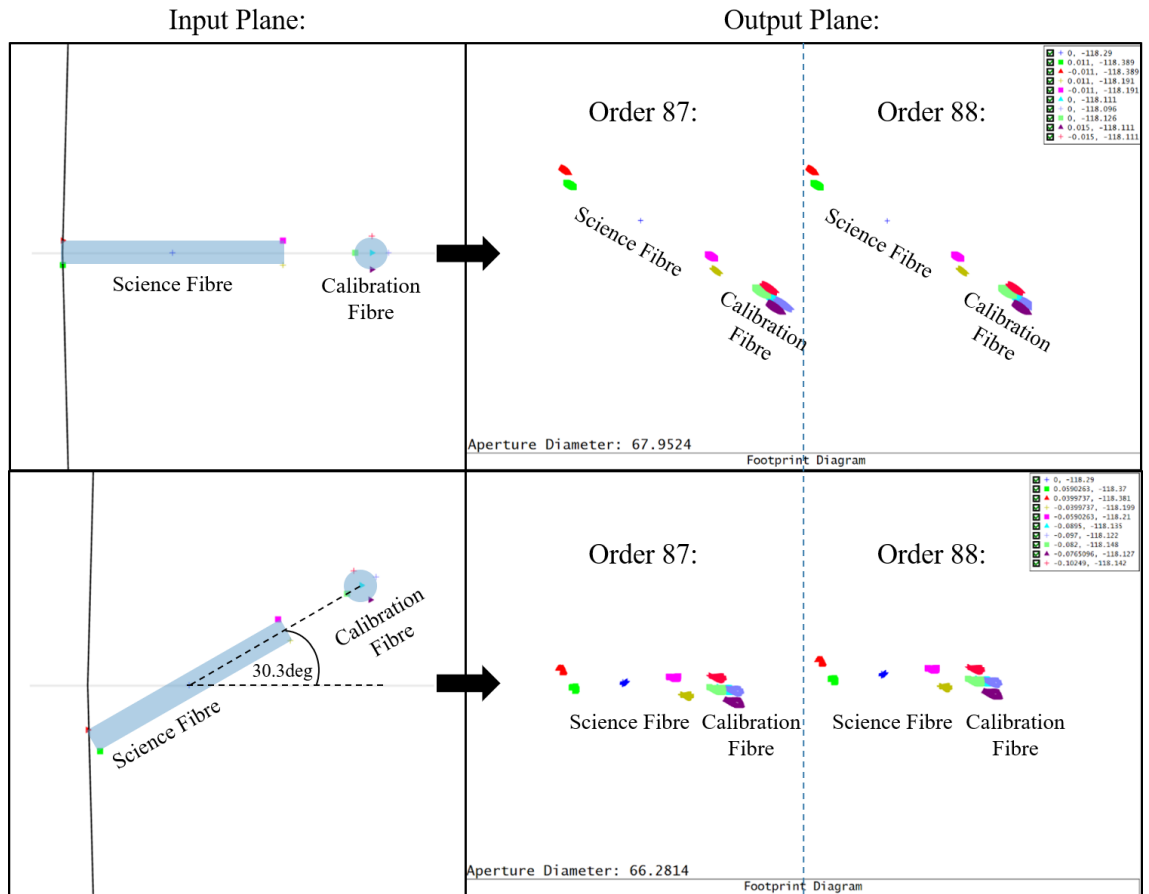
Figure 5.12: Annotated footprint diagram displaying the effect of beta-anamorphism on the resolution element re-imaged by the spectrometer for a given input object. A central point and four corner points for each of the fibres are imaged through the system to observe the effect on the shape and orientation of the resolution elements; these points are colour coded on the plot for ease of tracing through the system. The panels on the left hand side display the optical fibres on the object plane. The monochromatic resolution elements produced by the spectrometer for those fibres at the edge of orders 87 and 88 are shown in the right hand side of the figure. (Upper Panel) The science and calibration fibres are orientated parallel to the cross-dispersion axis, the resultant resolution elements are tilted and elongated in the high-resolution axis. (Lower Panel) The science and calibration fibres are pre-tilted by 30.3deg from the cross dispersion axis, resulting in resolution elements parallel to the cross-dispersion axis.

Table 5.2: NEREA spectrograph hardware budget.

Component:	Cost:
Diffraction Grating	€60k
Custom Re-focussing Optics	€120k
Prism	€60k
Collimating Parabolic Mirror	€120k
Detector	€750k
Mechanical Mounting (Thermal/Pressure Control)	€500k
Fibre Systems	€100k
Total	€1.7million

Table 5.3: Total NEREA hardware budget.

Component:	Cost:
NEREA Spectrograph	€1.7million
Calibration Unit (Including HCL Lamps & Fabry-Perot)	€200k
Control Computers, Software, and Operations Infrastructure	€100k
NEREAFCS	€50k
Facility Interventions	€50k
Total	€2.1million

5.6 NEREA Budget and Project Timeline Considerations

5.6.1 Hardware Budget Estimate

Following completion of the preliminary design of this spectrograph concept, industry and manufacturing contacts were consulted for design for manufacture (DFM) consideration. With manufacturability in mind, this system was designed to maximise performance metrics to reach those required by the science goals while minimising budgetary requirements where possible. A pessimistic budget for this early design concept is noted in table 5.2.

Through the use of readily available and manufacturable components, such as the NIRPS diffraction grating and fibre systems, and by ensuring a compact system, a substantial amount is saved on the overall hard-ware budget.

Including the spectrograph's sub-systems, a total hardware budget estimate can be seen in table 5.3.

5.6.2 Total Budget Estimate

Personnel requirements for the instrument design and construction are estimated at 25 FTE (25 person-years), with a total cost estimate of approximately €1.5million. Although, the actual funding needs will be highly dependent on whether participating institutes can dedicate part of their own personnel or whether all of the FTEs will need to be new contracts.

With this in mind, we believe that a fully operational, stable, high-resolution spectrometer, opening up cutting edge exoplanet science opportunities at the GTC could be constructed for as little as €3.6million.

5.6.3 Proposed Project Time-Line

For NEREA to maximise its scientific impact, it should be operational 3-5years before E-ELT/HIRES and other extremely large class telescopes come on-line towards the end of the decade. This timescale will also allow synergetic observations with JWST. As such, a simplistic and well understood design, such as the the one proposed here, would aid in the rapid manufacture and construction of such a spectrograph.

The proposed project plan is as follows:

1. Preliminary design phase (months 0-12): An initial trade-off study (0-3 months) will decide an initial concept. This will be iterated until month 9 where the 'Initial Design Review' will take place. Following the decisions made at that review, the instrument will be further iterated until the 'Preliminary Design Review' at month 12, where the system will be fully specified.

2. Final design phase (months 12-18): Here the design will be refined and iterated with manufacturers to ensure that all parts can be procured. The 'Initial Final Design Review' will take place at month 16 to ensure manufacturability and to assess the performance/cost budget of the system. The 'Final Design Review' will take place at month 18 to sign off the final design.

3. Procurement phase (months 18-24).

4. Optical bench assembly & system architecture assembly (months 24-36).

5. Full system lab testing & data reduction pipelines (months 36-42).

6. Observatory deployment (months 42-46): First light achieved at month 46.

7. Commissioning (months 46-48).

Given this, the first scientific spectra from NEREA can be expected within 4 years of initial funding.

5.7 Conclusion

A successful 'pre-phase-A' concept study has been completed on the proposed NEREA spectrograph[1]. This study has proved that a system can be designed which fulfils the technical specifications of the instrument within the budgetary requirements of the project. This design concept follows one of the most basic, well-studied and tested, Echelle layouts in order to ensure the ease of manufacture and construction of the system. The concept utilises readily available components where possible to keep costs low; and where custom components are required, it ensures DFM issues are considered. The spectrograph uses a combination of industry standard solutions and expertise inherited from previous projects to ensure a that all aspects of the system are feasible. The instrument is designed to be compact, with a footprint smaller than $1m \times 1m \times 0.5m$. This will allow the system to be housed in a compact vacuum tube for high performance temperature and pressure stabilisation. The system has considerations for calibration with wavelength overlap between orders, a separate simultaneous calibration fibre and the ability to couple the science fibre to the calibration fibre for concurrent calibration using the same parts of the optics and sensor as the science spectra.

This preliminary study is limited by the resources available to it and hence, the design produced is an early preliminary design. Thus, the final instrument design is subject to change and, if funded, will be further explored, refined and improved upon in the planned eighteen month design phases.

NEREA at the GTC would be a great asset to the exoplanet community. Its contribution to the completion of the planetary census of our solar neighbourhood, as well as its capability to vastly increase the number of attainable targets for atmospheric characterisation, would be unmatched by current instrumentation. The investigations that NEREA would enable will aid in filling the blanks of our understanding of planet formation and evolution; not only improving our understanding of our own solar system but also the origin and place of our own planet within it.

---

[1]The work undertaken in this design study was completed by Clark Baker with input from those in collaboration on this project, Dr. Enric Pallé, Dr. Roberto López López, Dr. José Luis Rasilla and Dr. Guillem Anglada-Escudé, in the specific areas of the science case for the instrument, feasibility of the fibre solution and in discussion of the overall design requirements.

6 Spectrometer Design Tool-Kit Software and EXOhSPEC Contributions

Abstract

In order to facilitate the rapid prototyping and modelling of Echelle spectrometer systems, a 'Spectrometer Design Toolkit' software was produced in Python. This software allows a user to enter the specifications of the components of the spectrograph and outputs a report which outlines the design parameters and performance of the system. This allows the designer to make rapid iterations and improvements to the design of the instrument.

With this software successfully operational, a test case study is outlined in the re-design of the collimating/re-focusing optics of EXOhSPEC; The EXOplanet high resolution SPECtrograph for the Thai National Telescope. Using the 'Spectrometer Design Toolkit', the system is characterised in order to provide the parameters required to design the system optics. Applying these results, the optics are designed for manufacturability in Zemax Optical Studio and the resultant optical system is presented for procurement.

6.1 Introduction

Echelle Spectrometers are highly constrained systems. One of the key design phases in the production of one of these instruments is the selection of components and the process of modeling how they will all interact together. Previously, throughout this thesis, the relation between components and how that would effect the resultant Echelle spectra formed on the CCD had been calculated on a case-by-case basis by hand. This is effective for single designs with minimal component choice, like QMSPEC, but for larger scale systems with many layers of design decisions, like NEREA, this is not time efficient. To solve this issue a 'Spectrometer Design Toolkit' software was created to automate these calculations.

Throughout the period of this PhD, I have collaborated closely with the EXOhSPEC team at The University of Hertfordshire. They are designing and constructing a compact, double-pass, spectrograph system for the upcoming 2m class telescope at the National Astronomical Research Institute of Thailand's (NARIT) Thai National Telescope. They are currently undergoing a re-design of their system, including the collimating/re-focusing optics. The design of this replacement collimating/re-focusing optics is being undertaken as a part of this thesis and provides an opportunity to test the effectiveness of the 'Spectrometer Design Toolkit'.

6.2 Spectrometer Design Toolkit

During the process of designing NEREA, the performance of GTCAO (which feeds the spectrometer), as well as the necessary features of the spectrograph, were subject to change. As such, rapid redesigns of the instrument were required in order to develop a spectrograph concept that meets all of the necessary criteria.

To be able to rapidly and 'on-the-fly' produce these design concepts on the time-scales required, it was not possible to recalculate all of the instrument parameters by hand. Hence, applying the concepts and relations outlined in section 2, a spectrometer design tool-kit was written in Python which allows a user to enter in the specifications of their spectrograph components (e.g. grating blaze angle, number of *grooves/mm* and aperture, prism angle, size and material, fibre size and numerical aperture, collimating lens focal length, refocussing lens focal length and CCD pixel size and sensor area) and produce a series of outputs which allow the instrument designer to assess the effectiveness of the design. An example series of such output plots are shown in figures 6.1, 6.2 and 6.3.

The primary applications of this toolkit are as follows:
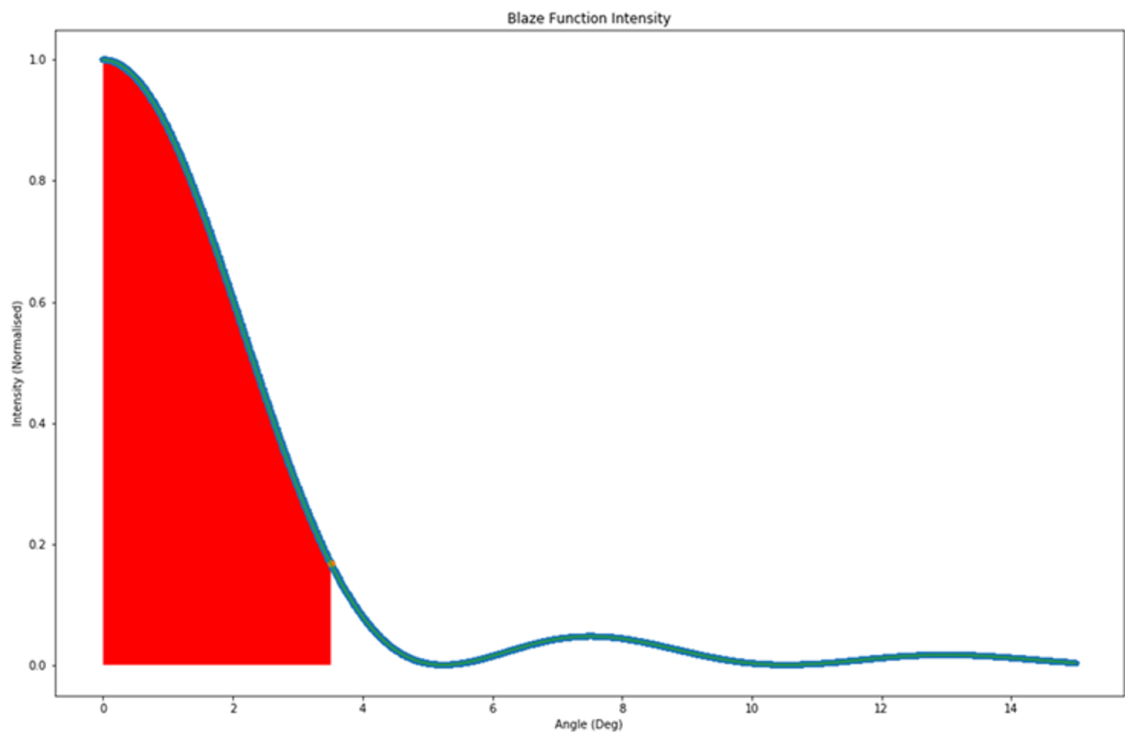
Figure 6.1: Plot of angle from the optical axis against blaze function intensity for a diffraction order to demonstrate the angular dependence of the light intensity leaving the diffraction grating. The red shaded portion of the plot demonstrates the field angles which will reach the detector. In this case 95% of the light leaving the diffraction grating in this order is within a field that will be detected by the CCD.
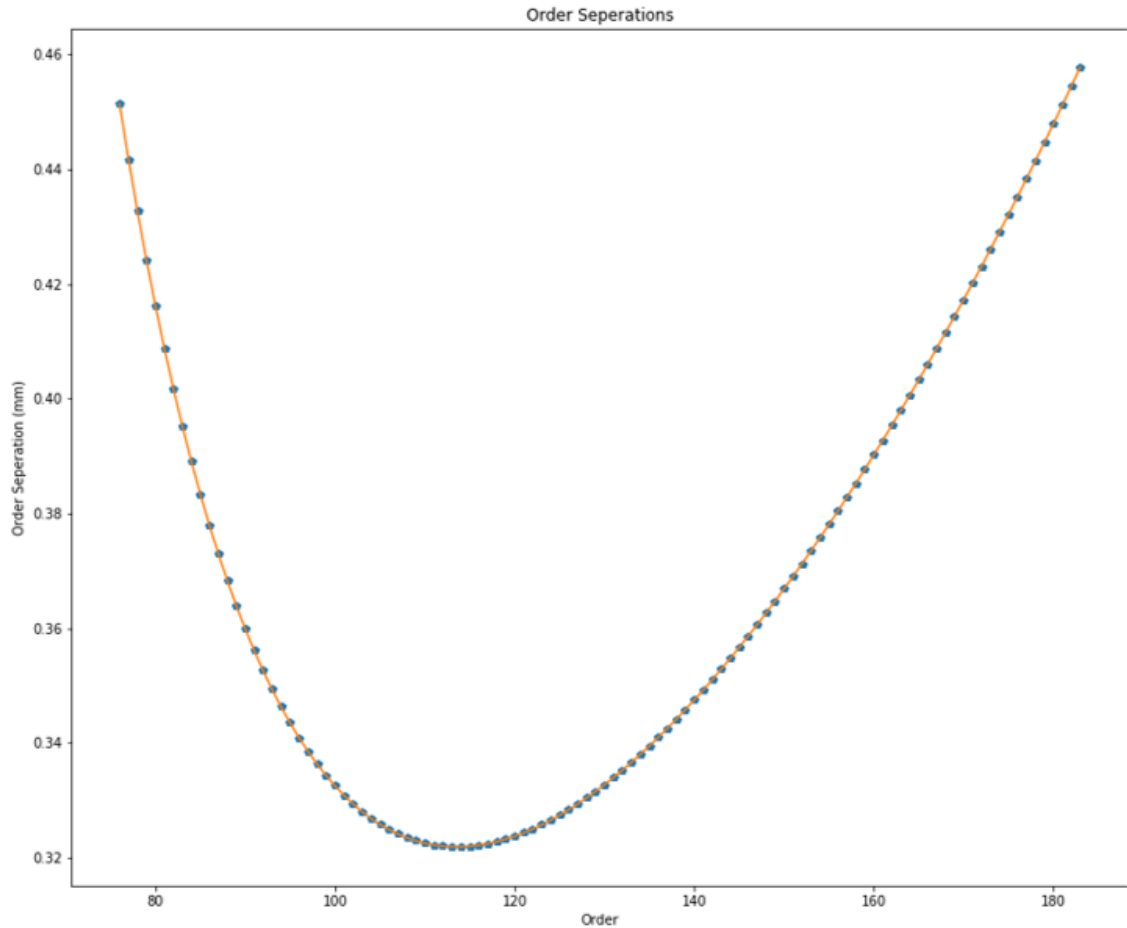
Figure 6.2: A plot of diffraction order number against separation between adjacent orders introduced by cross-dispersion from the prism and measured on the CCD plane, following imaging by the re-focusing lens. This allows the separation of the imaged orders within the spectrograph to be assessed in order to minimise the likely-hood of cross-talk between diffraction orders. This also allows the total width of the Echelle spectra to be assessed in the cross-dispersion axis, to ensure that the CCD area is filled effectively.
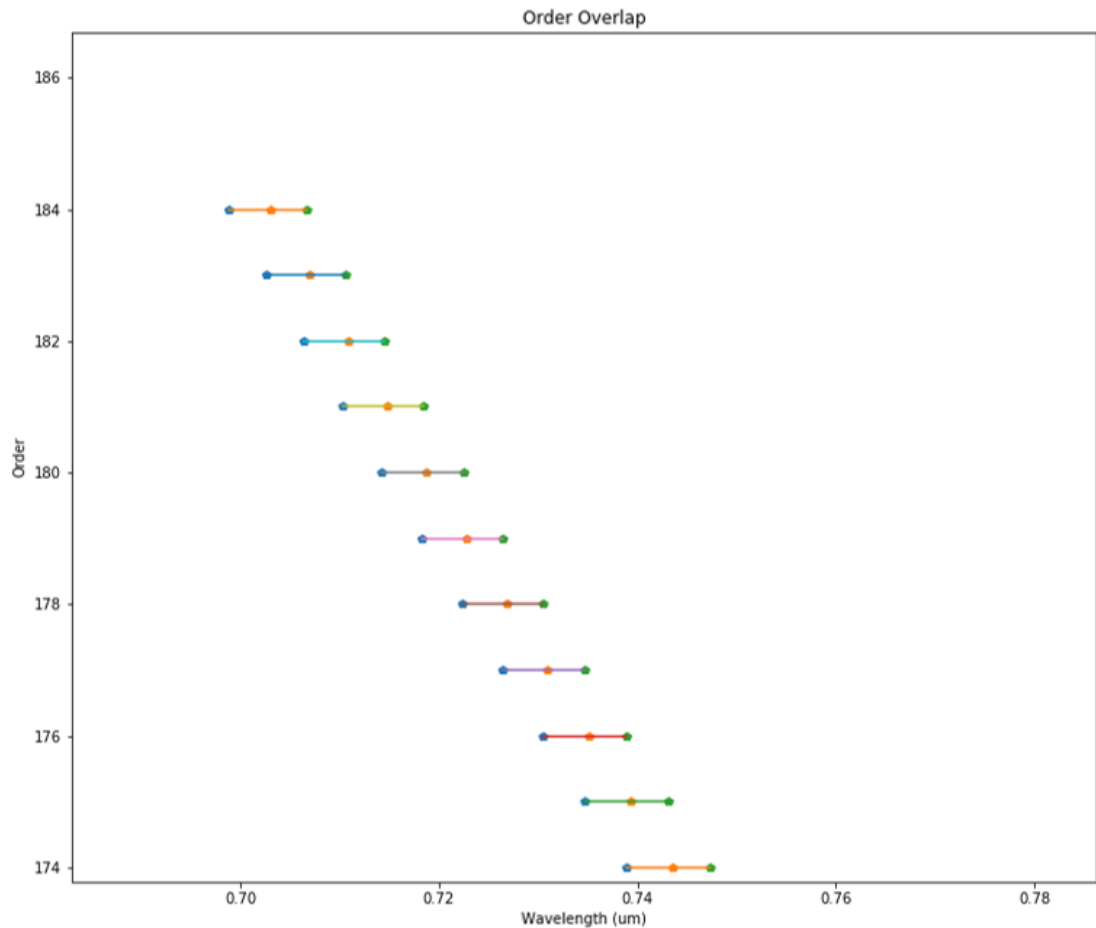
Figure 6.3: Plot of wavelength span against order. Each line consists of the wavelength span of each order; the three point on each line display the lower, upper and central wavelength of each order. This plot allows the wavelength overlap of orders to be assessed. This is a useful metric to study as having a large wavelength overlap between orders improves the wavelength calibration fit accuracy (Pepe et al., 2010).

1. To assess the blaze function spread on the CCD for the lowest order (the one which contains the longest wavelengths and has the widest blaze function with respect to angle from the optical axis), in order to ensure that sufficient amounts of the order will fit onto the CCD (say, $> 60\%$ of the light in the order) and also that the CCD area is used effectively and isn't being under-filled.

2. To assess the cross-dispersion of all of the orders by the prism in order to ensure that the CCD is efficiently filled and that the orders are sufficiently separated to reduce cross-talk. This utility has also proven useful in the design of prisms. The Sellmeier dispersion equation is a formalism which dictates the refractive index of a material with respect to the wavelength of light refracting through it. The coefficients of the equation for each material can be found in the optical glass manufacturer's technical specifications (Schott AG, 2011). Combining the Sellmeier dispersion equation with the prism wedge angle and applying Snell's law, it is possible to rapidly assess the dispersion of different combinations of materials and prism wedge angles across the entire wavelength range of interest to ensure that the prism performs as required. With a prism design completed, the software can export the prism parameters required for the component to be directly copied into the optical design software, Zemax Optical Studio.

3. To measure the theoretical maximum resolution of the instrument.

4. To ensure that Nyquist sampling theorem is fulfilled at the CCD.

5. To characterise the wavelength overlap between orders, which is a useful feature to maximise in order to improve calibration accuracy; as discussed in figure 6.3 (Pepe et al., 2010).

6. To test the baseline parameters of the spectrograph so that they can be modelled in detail in optical design software such as Zemax Optical Studio. This tool allows parameters to be checked quickly before committing to producing a time and resource intensive Zemax model.

This model currently does not simulate the effects of classical and beta anamorphic magnification but, in future developments, this is a feature that is to be added in order to allow more accurate resolving power estimates to be made across orders. In further future work, a GUI is planned to be implemented in order to allow more intuitive entry of instrument parameters.

Table 6.1: Requirements for EXOhSPEC collimating/re-focusing system.

Specification:	Requirement:
f, Collimating/Re-focusing Lens Focal Length	$250mm$.
Lens Diameter	$80mm$ – all lenses same diameter.
Wavelength Range	$400 - 800(900)nm$.
Back Focal Length	$220mm$.
Distance from Front Element to Stop	$130mm$.
Lens Total Thickness	$< 100mm$.
D, Instrument Aperture	$50mm$.
Distance from Front Element to Stop	$130mm$.
Grating Specifications	$27grooves/mm$, $70deg$ blaze angle, $60 \times 150 \times 25mm$.
Off-Axis Grating Field Requirements	$1.5deg$ (from optical axis) reflection at grating.
Prism Specifications	$80mm$ face, $60deg$ N-BK7 or better.
Fibre Specifications	$10\mu m$, $0.10NA$.
Sensor Specifications	CMOS, $53.4mm \times 40mm$, $3.76\mu m$ pixel size.

6.3 EXOhSPEC Collimating/Re-focusing Lens Redesign

The current design of EXOhSPEC is outlined in Lhospice et al. (2019). The system is a double-pass, high-resolution ($R < 70,000$) spectrograph operating between $400nm$-$700nm$.

6.3.1 EXOhSPEC Collimating/Re-focusing Lens Requirements

The redesigned system requirements are outlined in table 6.1. The main priorities of this redesigned collimating/re-focusing optic are high throughput and consistent, close to diffraction limited performance over a larger wavelength range ($400nm$-$900nm$) and across the entirety of the field of the detector. This would allow a consistent resolving power of $R \sim 100,000$ to be achieved.

6.3.2 Lens Design Requirements Set By Specifications

Prism

It was found through modelling the optical aligment of the system that an 80mm face, 60deg, N-BK7 prism would introduce substantial vignette to the instrument. To correct for this a 100mm face, 60deg, N-BK7 prism would be necessary; but this would require a substantial volume of glass, which would raise the component cost unnecessarily. A more efficient solution would be to replace the material with a more dispersive glass, so that a smaller prism angle is required. Using the 'Spectrometer Design Toolkit' it was found that a 100mm face, 30deg, F2 prism could offer the dispersion necessary.

The F2 prism produces a total separation between the orders of $77(900\mu m)$ to $174(400\mu m)$ of $6.68mm$ for a $250mm$ focusing lens; or equivalently a total dispersion angle of $1.53deg$. The resultant separation between orders from this cross-dispersion is shown in figure 6.4. Given this, the cross-dispersion fits easily within the $40mm$ width of the detector.

The minimum separation between the centre of orders is $43\mu m$, which leaves $33\mu m$ between the edges of the closest orders. This is more than three times the size of a resolution element, which is ample separation to avoid cross-talk.

Figure 6.5 shows how the refractive index of the F2 glass changes with wavelength. In order to gain consistent separation between cross-dispersed orders, the change in refractive index must compensate for the difference in separation of the central wavelengths between orders.

Diffraction Grating

A diffraction grating with $27grooves/mm$ operated at a $70deg$ blaze angle will produce a blaze function of the form shown in figure 6.6 at $900nm$. The lowest order with the longest central wavelength is chosen here as it is the widest; hence, if this order fits on the sensor, all of them will.

Within $2deg$ of field from the optical axis, 84.8% of the blaze intensity is captured. This is more than an adequate quantity; as beyond this, the SNR of the spectra is degraded considerably (less than 40% of the maximum value) compared to the centre of the order.

Hence, if operating on axis, the re-focusing lens can be designed to capture and operate most effectively at a maximum field of $2deg$. This can accommodate a detector of width $2 \times 250mm \tan(2deg) = 17.46mm$; the factor of 2 is to accommodate
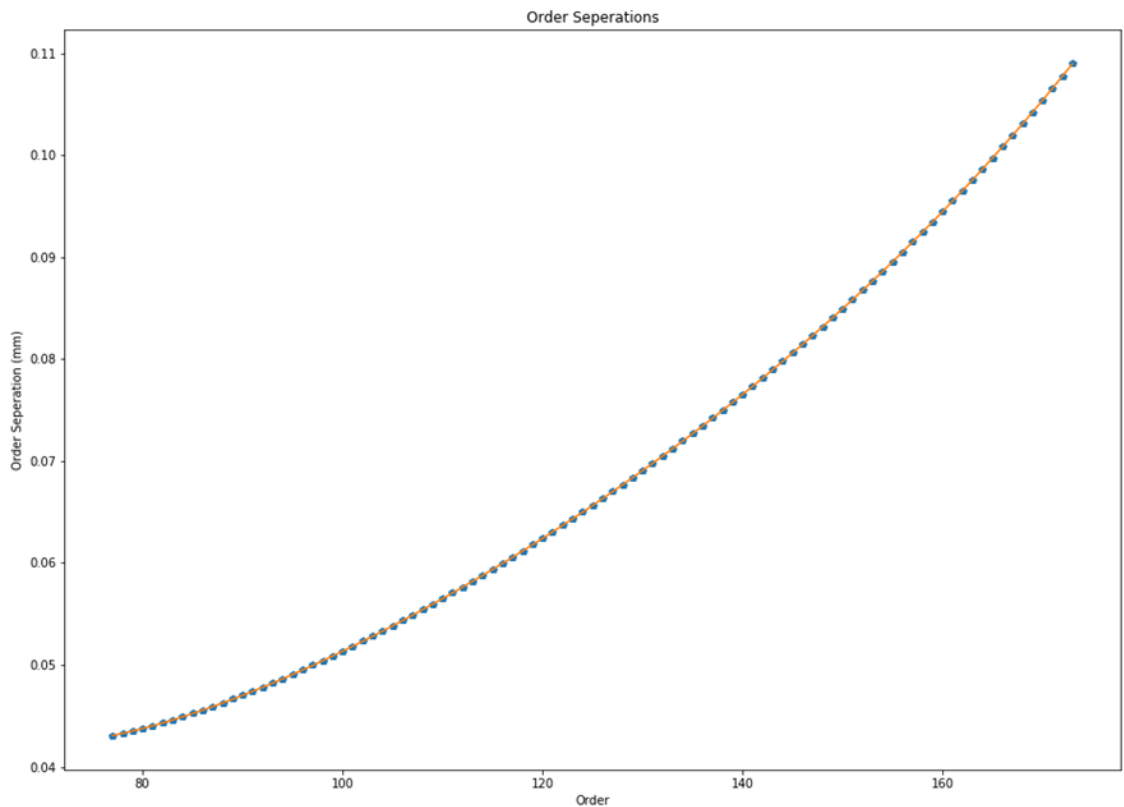
Figure 6.4: A plot of diffraction order number against the separation between adjacent orders introduced by the 100mm face, 30deg, F2 prism and measured on the CCD plane, following imaging by the 250mm re-focusing lens. Separation between orders varies from $43\mu m$ to $109\mu m$.
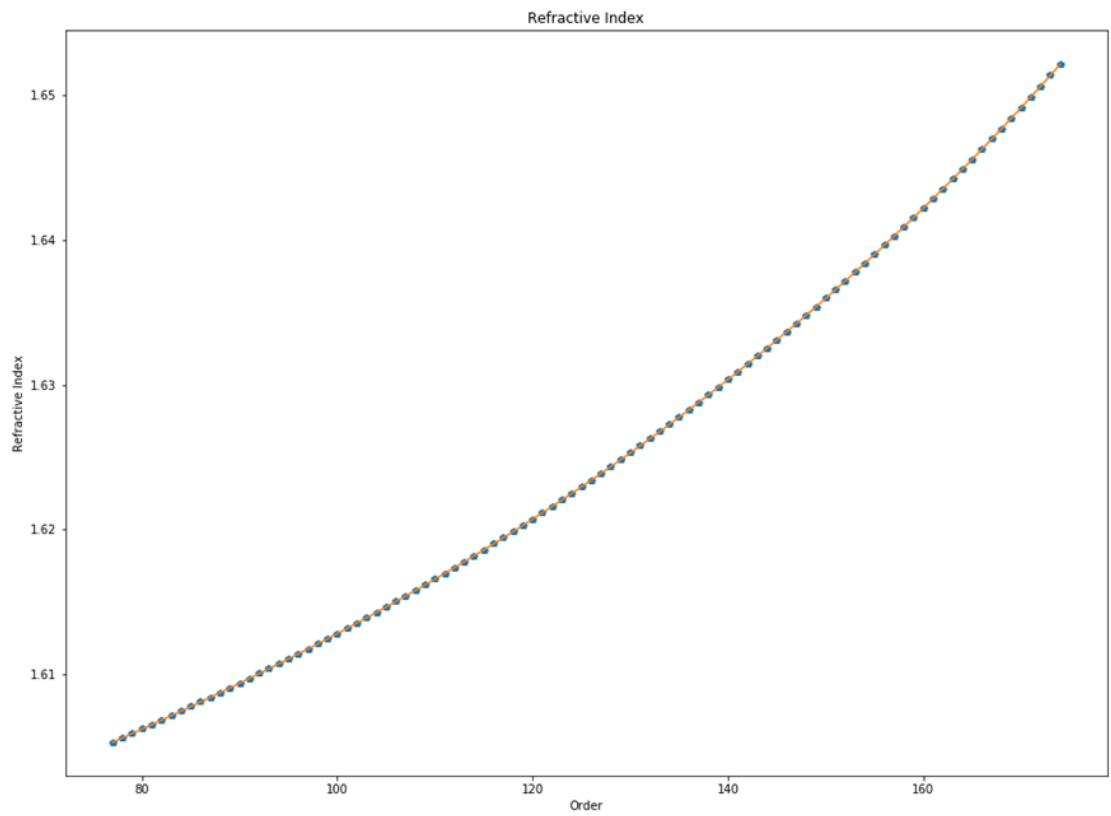
Figure 6.5: A plot of diffraction order number against refractive index of the F2 glass.
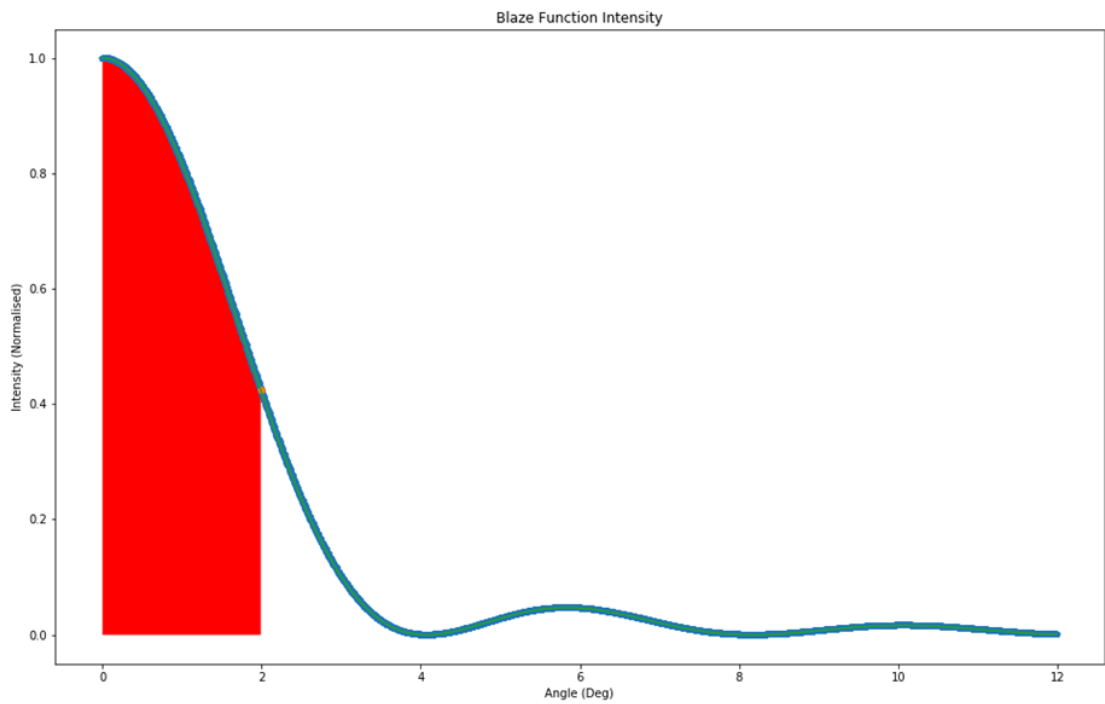
Figure 6.6: Plot of angle from the optical axis against blaze function intensity for a diffraction grating with $27 grooves/mm$ and a $70 deg$ blaze angle operating at an order containing $900 nm$. The red shaded portion demonstrates the amount of blaze intensity within $2 deg$ from the optical axis.

either side of the optical axis. This will easily fit within the large 53.4*mm* detector height.

This spectrometer is double pass and as such is operating 1.5*deg* off of the optical axis, due to reflecting the beam off of the grating; 3*deg* total. Therefore, including the additional $(1.53/2)deg$ field from the prism, the lens must accommodate a full field of $\sqrt{(1.5 + (1.53/2))^2 + (2)^2} = 3.02deg$ in order to accept the beam which forms the edge of the furthest order from the optical axis.

Design Operating Parameters

With these calculations completed, in addition to the design parameters collated in table 6.1, the lens must accommodate a 1.5*deg* x, 2*deg* y field (from optical axis). This is mimicking the beam reflection from grating.

The lens design should also minimise the number of surfaces in order to maximise throughput efficiency. The minimum theoretical lens design with enough degrees of freedom to accommodate diffraction limited performance is a triplet (Welford, 1986a). For spherical only surfaces, due to the limitation in available glass materials and manufacturability of surface radii, it is often not possible to achieve real-world diffraction limited performance from a triplet. However, for this design, conic surfaces are applied to increase the number of degrees of freedom available.

6.3.3 Optical Design

An initial triplet design meeting the focal length requirement was sketched by hand and imported into Zemax Optical Studio. This was optimised in order to meet the rest of the lens requirements, using the Optical Studio Optimisation Tool. After a series of optimisations, glass material substitutions and redesigns, a manufacturable design was reached that met or exceeded all of the system requirements. A model layout of this system is shown in figure 6.7 and an example of the system's nominal spot size performance across the entire field is displayed in figure 6.8. The achieved system performance criteria are listed in table 6.2.

As figure 6.8 suggests, diffraction limited (or close-to diffraction limited) performance is achieved across the entire field and wavelength range while maintaining a greater than 220*mm* back focal length. The separation in the focal plane (which is both the object and image plane in a double pass system) between the fibre and edge of closest order is 9.75*mm*. This gives ample space for the mechanical mounting of the optical fibre, a fold mirror and the detector.
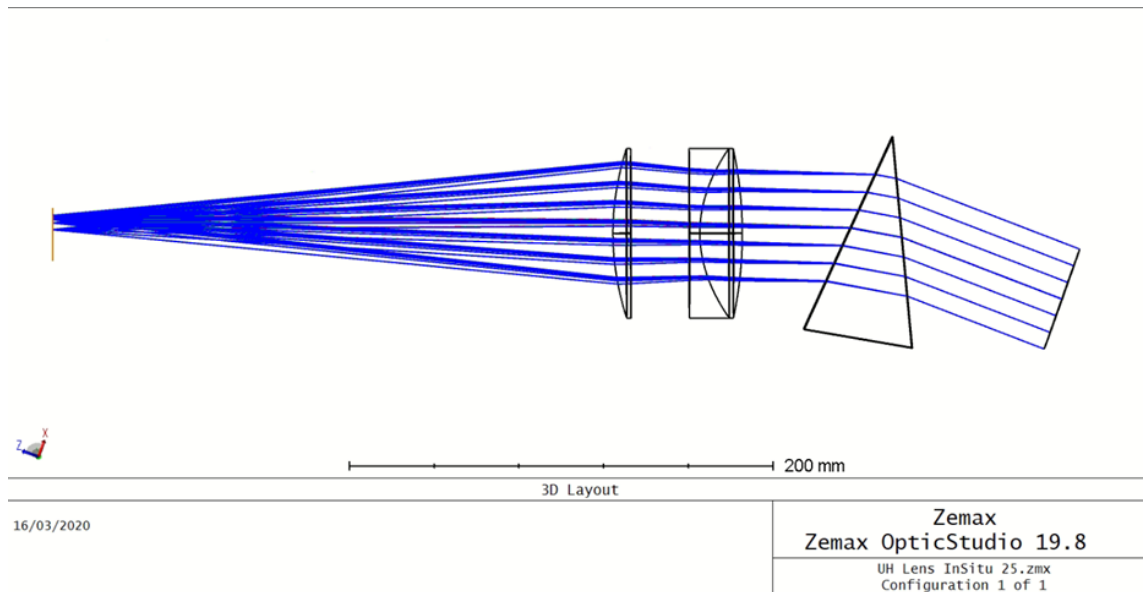
Figure 6.7: Top elevation of EXOhSPEC collimating/re-focusing lens model layout. Plotted here is the image plane, the triplet lens, the 100mm face, 30deg, F2 prism and the aperture stop.

Table 6.2: Criteria achieved for the EXOhSPEC collimating/re-focusing system.

Operating Parameter:	**Requirement:**
f, Collimating/Re-focusing Lens Focal Length	$250mm$.
Lens Diameter	$80mm$ – all lenses same diameter.
Wavelength Range	$400 - 900nm$.
Back Focal Length	$264.423mm$.
Distance from Front Element to Stop	$156.794mm$.
Lens Total Thickness	$61mm$.
D, Instrument Aperture	$50mm$.
Field Requirement	1.5deg x, 2deg y (from optical axis). Mimicking beam reflection from grating.
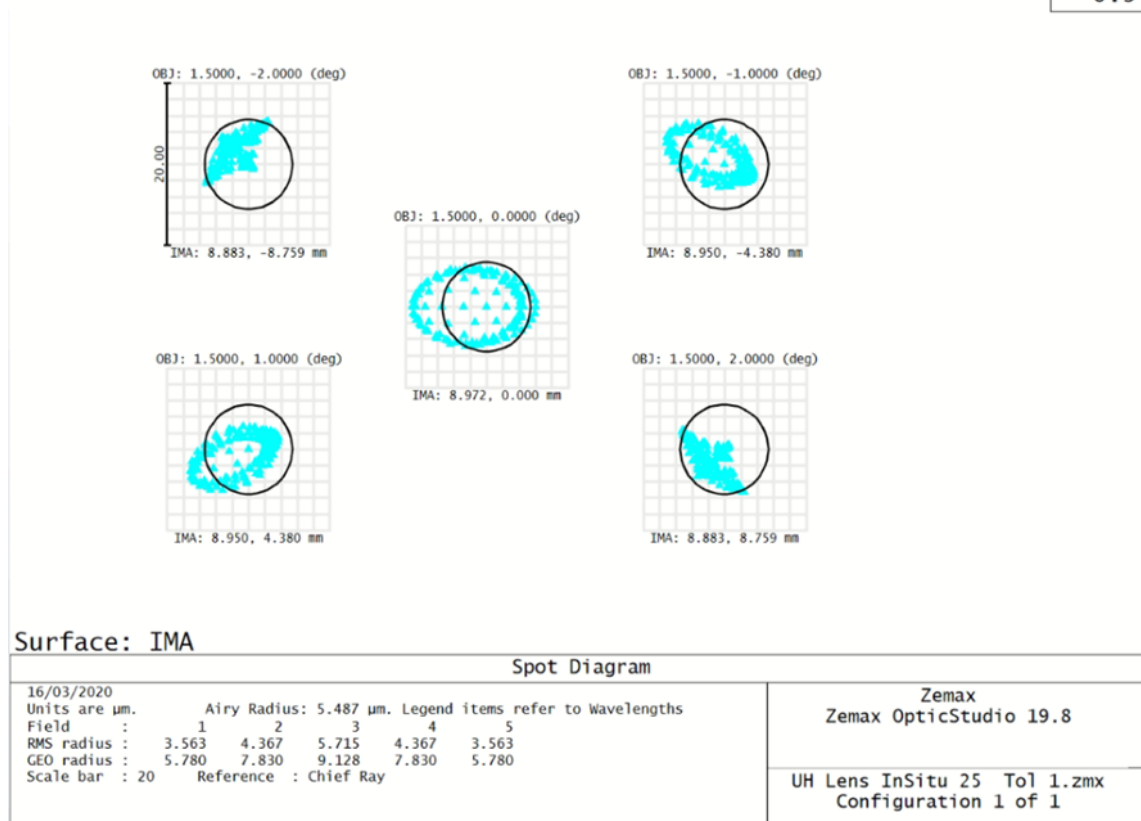
Figure 6.8: Plot of the spot size produced by the imaging system across the field range specified in section 6.3.2 for a $900nm$ source. The blue spots are those produced by aberrations in the optical system and the black circles depict the diffraction limited spot performance at each of the field positions. In the footnote of this plot, values are given for the RMS spot radius and GEO spot radius at each of the plotted field angles. The value of the RMS radius is the root-mean-square deviation for all of the ray bundles traced through the system at that field angle; as such, it gives a sense of the radius within which the majority of the light intensity is focused. The GEO radius is the geometric spot radius, which tells us the radius within which all of the light rays traced through the system at that field angle will focus; as such, it includes regions of the PSF which may be of low intensity and have little impact on the measured spot-size performance.

One of the lens surface pairs is combined into a single cemented surface to maximise throughput, leaving a resultant design comprised of a cemented doublet and a singlet. Due to the compact nature of this lens system, aberration correction is shared across all of the elements.

Two of the exposed lens surfaces are planar to maximise manufacturability and minimise production cost; one can achieve high tolerances on a plane surface for a relatively low-cost compared to a spherical or conic surface. As these planar surfaces are the only two internal exposed surfaces, this also makes mounting of the lenses simpler as the filler tube can have two planar ends; allowing much tighter tolerances at a lower cost comparable to conventional spherical designs.

As discussed in section 2.0.5, the spot size performance of an optical system is dictated by optical aberrations and diffraction through the system. The diffraction through the system limits the spot size to a physical 'best case' smallest spot size. On the other hand, optical aberrations, which cause deviations in the geometric spot focal point from the perfect spot, due to the geometry of the optics and chromatic effects, can be less than the diffraction limit; and hence allow the system to operate in a 'diffraction limited' state. The aberration spot sizes achieved for EXOhSPEC, as shown in figure 6.8, are larger (relative to the diffraction limit) than those seen for both QMSPEC and NEREA. This is due to the critera for EXOhSPEC's design being different to the aforementioned spectrographs. EXOhSPEC has a larger aperture than QMSPEC but the optics budget is comparable, hence, the number of optical elements has been reduced to keep production costs under control. This has the positive effect of increasing the throughput of the optical system but it also decreases the number of degrees of freedom the optical designer has to combat optical aberrations. However, in this case, the spot sizes are still diffraction limited (or close to it), so the resolution performance will be minimally impacted.

Furthermore, all spot sizes have an RMS radius $< 6\mu m$, so that applying equation 2.9 with a $10\mu m$ diameter fibre size, we can see that there will not be a significant increase in resolution element size and hence no substantial degradation in image quality for the resultant spectrometer.

Lens surface 2 is a pro-late ellipse, close to a parabola, and lens surface 5 is a hyperbola; which are both within manufacturing capabilities of most custom optics manufacturers. All other surfaces are spherical.
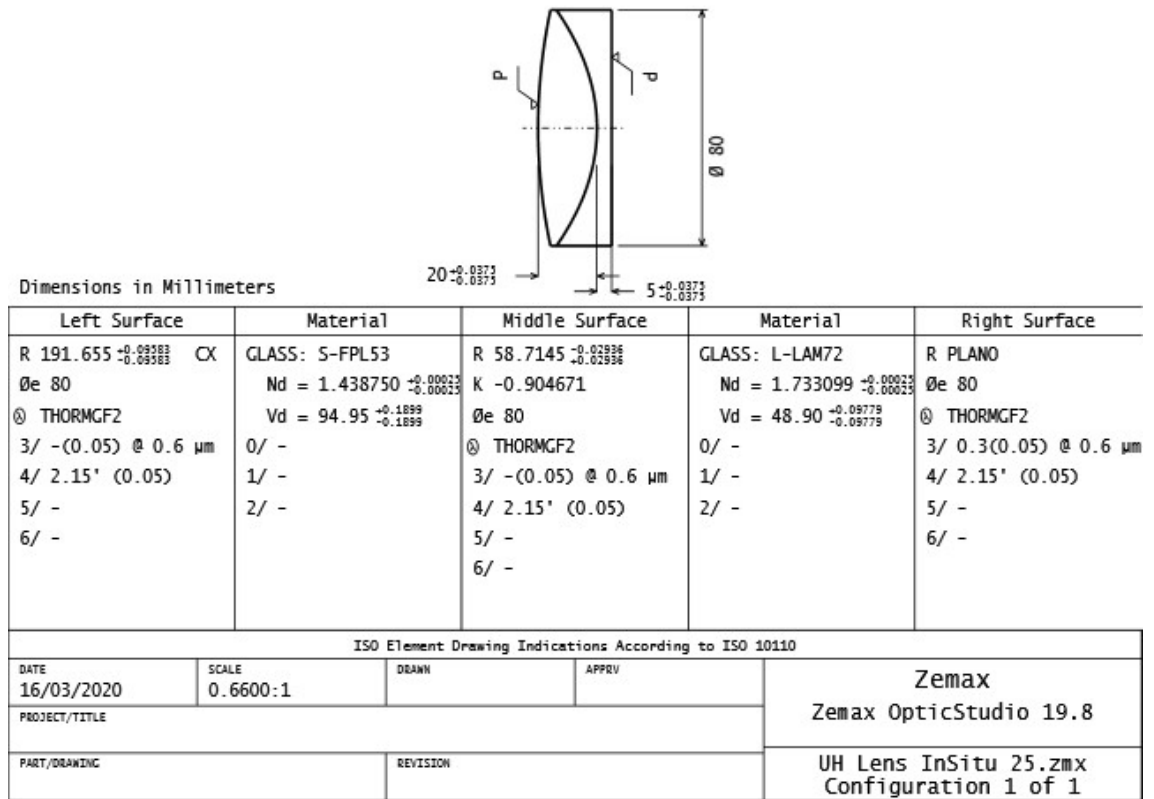
Figure 6.9: ISO 10110 Standard Element Drawing for the cemented doublet element of the triplet lens system. This table displays the element parameters and their tolerances.

6.3.4 Tolerancing and Manufacturability

By applying Zemax Optical Studio's Tolerancing Tool, a series of tolerances were set on each of the lens parameter. Three hundred Monte-Carlo simulations where then run to explore the lens designs within this parameter space and measure their performance. These tolerances were found to be too loose, so they were tightened and the process repeated until all of the modelled systems met the required, close to nominal, performance.

The resultant tolerances are outlined in figures 6.9 and 6.10, and the performance of three thousand Monte-Carlo simulations of spectrometers within this parameter space are shown in figure 6.11.

From figure 6.11 it can be seen that even in the worst case system within these tolerances operating with a $900nm$ beam at a field close to the optical axis, the RMS spot size doesn't pass beyond $8.5\mu m$ with the majority of the spot radii at approximately $4\mu m$. Applying equation 2.9 with the $10\mu m$ fibre diameter, it can be

Dimensions in Millimeters

8.43306 +0.0373 / -0.0373

Left Surface	Material	Right Surface
R PLANO	GLASS: S-LAH96	R 123.153 +0.06158 / -0.06158 CX
Øe 80	Nd = 1.763850 +0.00023 / -0.00023	K -1.37446
Ⓐ THORMGF2	Vd = 48.49 +0.09698 / -0.09698	Øe 80
3/ 0.3(0.05) @ 0.6 μm	0/ -	Ⓐ THORMGF2
4/ 2.15' (0.05)	1/ -	3/ -(0.05) @ 0.6 μm
5/ -	2/ -	4/ 2.15' (0.05)
6/ -		5/ -
		6/ -

ISO Element Drawing Indications According to ISO 10110				
DATE 16/03/2020	SCALE 0.6600:1	DRAWN	APPRV	Zemax Zemax OpticStudio 19.8
PROJECT/TITLE				
PART/DRAWING		REVISION		UH Lens InSitu 25.zmx Configuration 1 of 1

Figure 6.10: ISO 10110 Standard Element Drawing for the singlet element of the triplet lens system. This table displays the element parameters and their tolerances.
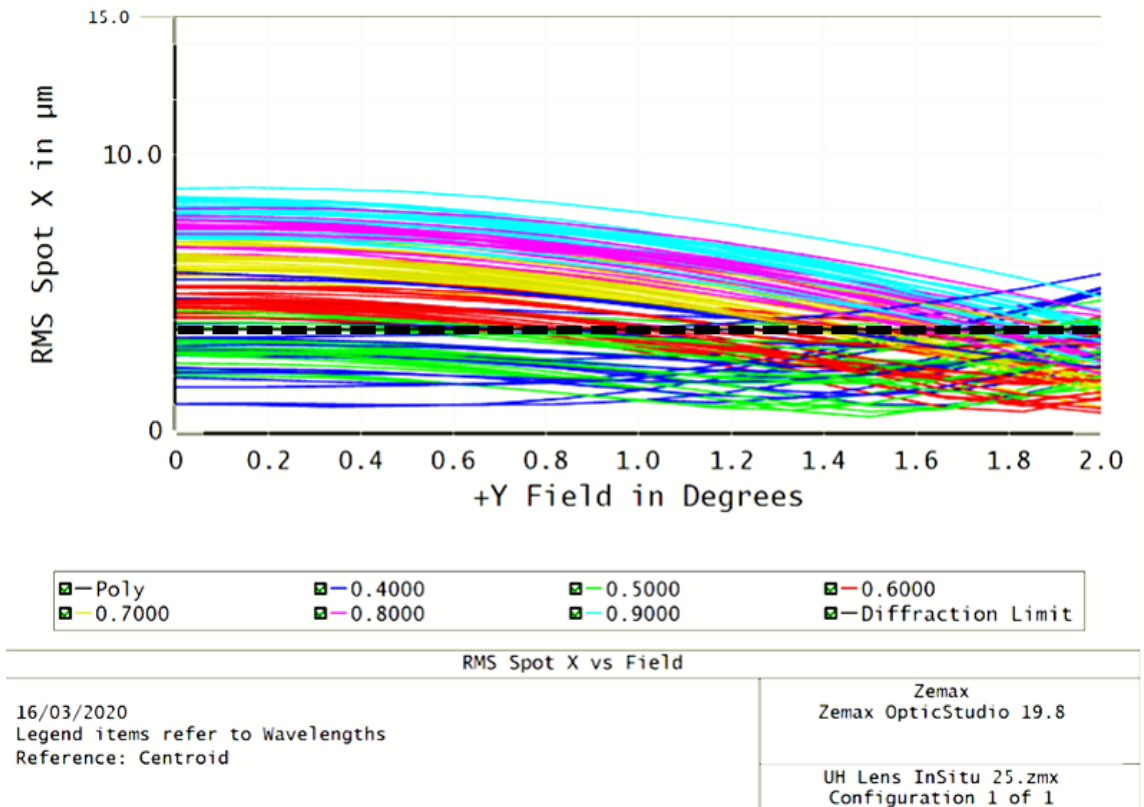
Figure 6.11: Plot of the field from the optical axis along the dispersion axis against RMS spot size for 300 Monte-Carlo simulation spectrometer systems exploring the parameter space set by the tolerances. The black dashed line shows the diffraction limit of the system. The dark blue lines are the spot size of $400nm$ light. The green lines are the spot size of $500nm$ light. The red lines are the spot size of $600nm$ light. The yellow lines are the spot size of $700nm$ light. The pink lines are the spot size of $800nm$ light and the light blue lines are the spot size of $900nm$ light.

seen that on average the resolution elements will have a diameter of approximately $12.8\mu m$ across the spectrograph's field and wavelength range. Hence, minimal performance loss is seen in comparison to the ideal aberration free system.

6.3.5 Procurement

With a manufacturable design reached and tolerances set such that the required performance is achieved, the system is now (as of writing) out for procurement.

6.4 Conclusion

A 'Spectrometer Design Tool-kit' software was successfully developed to streamline the spectrometer design and parameter selection process (prior to the production of a full optical design model). This preliminary model gives design intuition into the resultant Echelle spectra layout for a given set of component specifications. The system's accuracy could be improved through the modelling of further phenomena, such as classical and beta anamorphism. However, this isn't key at the preliminary design stage and is easily modelled in software like Zemax Optical Studio, once component specifications are chosen. The software could further be improved through the introduction of a GUI for easier user input and interpretation.

Following the completion of this tool-kit, the functioning software was tested in a design case-study of a collimating/re-focussing lens solution for the EXOhSPEC redesign. The parameters of the redesigned instrument were easily, rapidly and accurately modelled using the 'Spectrometer Design Tool-kit', providing all of the necessary data required in the design of the collimating/re-focussing lens. A compact, efficient and highly manufacturable collimating/re-focussing lens solution was designed with the aid of Zemax Optical Studio and tested in a spectrograph model. With a design meeting the required performance achieved, the lens tolerances were set and tested to ensure that the manufactured lens would also meet those requirements. With the selection of the necessary tolerances completed, the lens design was circulated to manufacturers for procurement.

7 Conclusion

At the beginning of this thesis I proposed the questions 'how did we come into being?' and 'could others come about in the same way, are we really alone?'. I used these questions to place the work discussed in this thesis in the context of the bigger picture. We discussed how the universe is the best laboratory for answering these types of questions and how by studying the formation of planetary systems and their characteristics, we can gain greater insight into the formation of our own planet. Beyond this, by searching for biomarkers and the planets that could support life, we will gain a greater insight into the environment required for life, the formation of life on our own planet and the proclivity of life in the universe itself.

Current studies on the conditions required for the prebiotic chemistry to occur that likely proceeds the production of life as we know it suggests that the principle situation where these criteria can be fulfilled is on the surface of an Earth-like planet orbiting a Sun-like star. With current technology and instrumentation we have neither the direct imaging capability to distinguish the 10^{-10} flux ratio of such a system or the high dispersion spectrographic stability to measure the $9cm/s$ radial velocity signal of an Earth-like planet around a Sun-like star.

Current investigations suggest that the combination of integral field high dispersion spectroscopy and high contrast imaging could allow us to reach the necessary 10^{-10} flux ratios required to study these possible life producing and supporting planetary systems.

With contemporary high-resolution spectrograph design, each instrument is large (the size of a car) and expensive (on the order of £1million). This is not conducive to the construction of the arrays of these systems required for integral field high dispersion spectroscopy. As such, a different approach must be taken; and this is what is studied in this thesis. A proof-of-concept instrument was developed and tested which can achieve comparable resolving power performance to the large scale systems but is compact (the size of a shoe box) and low-cost (hardware cost $\sim$£10,000).

The principles applied in the construction of this instrument were then utilised in the production of a design concept for a high-resolution spectrograph for the GTC,

NEREA. If produced, this instrument would increase the number of investigatable planets in our stellar neighbourhood by a factor of 10, aiding in the completion of the planetary census. NEREA at the GTC would potentially also increase the number of exoplanetary atmospheres that can be characterised by a factor of ~ 40.

Furthermore, applying the experienced gained in these projects, in order to increase the efficiency of the design process of Echelle spectrometer systems, a 'Spectrometer Design Tool-kit' was developed. This software aids in the selection of component specifications at the preliminary design phase. This system was then tested in a redesign of the collimating/re-focussing lens for EXOhSPEC; another compact, high-resolution spectrograph instrument.

Chapter 1 and 2 - Introduction and Theory

In chapter 1 we began by introducing the motivations for studying exoplanets and, by extension, the work discussed in this thesis. We proceeded to outline the methods used in the discovery of exoplanets and conducted a detailed discussion on the characterisation techniques that are possible through the application of high-resolution spectroscopy. After briefly recapping the current state of the exoplanet field, we broke down the ways in which the high precision radial velocity data required for the aforementioned science can be extracted from high resolution spectra. This set us up in chapter 2 to conclude the introduction by investigating the prerequisite theory required to examine the results produced in this thesis. This section showcased the derivations of the relations relevant to this thesis in a format which is conducive to explaining the work undertaken.

Chapters 3 and 4 - QMSPEC

In chapters 3 and 4 we discussed the design, construction and testing of QMSPEC; a highly replicable, low-cost, portable, general-purpose, high-resolution spectrometer with applications in stellar studies and exoplanet science.

An instrument design was developed and constructed that produces a theoretical resolving power $R > 80,000$ in the Vis-NIR regime ($500nm - 1\mu m$) at a cost $\sim$£$10,000$. It is compact, measuring the size of a 'shoe-box', approximately $30cm \times 15cm$ and the proof-of-concept prototype is consistently capable of producing a resolving power of $R \sim 60,000$, a feat only attained by instruments an order of magnitude greater in cost.

The instrument applies commercially-off-the-shelf (COTS) and economically designed components. The Echelle-type spectrometer prototype is fibre-fed with a

single $10\mu m$ fibre and follows a double-pass design; applying a custom designed, $108.24mm$ focal length, collimating and re-focussing lens. High resolution is achieved through the use of a compact COTS R4 diffraction grating and a prism as the cross-disperser.

The diffraction grating is found to be the limiting factor in achieving the theoretical resolution; all other optical components are found to be operating at or above resolution requirements. In future work, this could be improved through the manufacture of a custom grating to the required specifications and tolerances.

The prototype spectrograph was tested on-sky at the QMUL AU Observatory. In order to achieve this, two sub-systems were required; a front-end fibre coupling system and a back-end data reduction pipeline.

A fibre coupling solution was successfully developed which, through the use of a beam-splitter, allows the observed object to be viewed throughout the observation on the fibre head plane to ensure that the object is successfully coupled. A singlet is used as a focal reducer to match the F/7 telescope to the F/4.51 spectrograph system. Due to the on- and close-to- optical-axis design, minimal aberrations are introduced by the singlet and so efficient coupling is achieved to the $10\mu m$ fibre. This system has some issues with tracking, so a future design should place a detector in the eye-piece and use centroiding to ensure that the observed object remains on the fibre.

A light-weight data reduction pipeline was designed and produced that is capable of converting the Echelle spectra produced on the QMSPEC CCD into a line spectra for analysis. Further work is required to finalise the wavelength calibration routine.

With these sub-systems in place, QMSPEC was tested on sky. A series of lunar spectra were successfully observed and extracted. These spectra were then used to measure the on-sky resolving power of the instrument, finding a value of $R \sim 45,000$. Further on-site alignment and calibration is expected to increase this value.

The design principles concluded from the design and construction of QMSPEC were then applied to a concept study for NEREA.

Chapter 5 - NEREA

A preliminary design study was carried out for NEREA; a stable, compact, high-resolution spectrometer concept for the GTC. A manufacturable design was reached which can achieve a resolving power of $R \sim 100,000$ in the red-NIR regime (0.7-$1.7\mu m$) and is compact, with a device footprint is approximately $0.5m \times 1.5m \times 0.1m$. This will allow the system to be easily temperature and pressure stabilised to a radial

velocity precision of $< 50cm/s$.

The instrument in it's primary mode will be fed by a $22\mu m \times 198\mu m$ rectangular science fibre, for improved mode scrambling, and a $29\mu m$ octagonal calibration fibre. For dispersion, the concept applies a $320mm \times 90mm$, R4 blazed, diffraction grating and a $60.6deg$, P-SF67, prism as the cross-disperser. A $325mm$ focal length, off-axis, parabolic mirror is used as the collimator and the camera consists of a custom designed $325mm$ re-focussing lens. The instrument is designed to efficiently couple to the GTCAO system but will also be able to perform efficiently without adaptive optics at a resolving power of 40,000 or, with losses, at a resolving power of 70,000-100,000.

This design is found to meet all of the instrument requirements and each of the components are found to be manufacturable within the project budget, with a hardware cost of $\sim$€$2.1million$.

Further work on the design and construction of this system is to be carried out with the successful allocation of funding.

With the completion of the design of QMSPEC and NEREA it was noted that the spectrometer design process could be made more efficient with the automation of the calculations required for component selection. To achieve this a 'Spectrometer Design Toolkit' software was conceived.

Chapter 6 - Spectrometer Design Toolkit and EXOhSPEC

A functioning 'Spectrometer Design Toolkit' software was developed (in Python) which allows the user to assess the resultant Echelle spectra layout produced by the specifications of their chosen components. This has proven to be useful in the preliminary design stage of an instrument, allowing rapid testing of component combinations.

As a test design case, the software was applied in the selection of design requirements for the re-design of the EXOhSPEC collimating/re-focusing lens system. The software was found to greatly increase the efficient selection of design parameters.

With these parameters chosen, a $250mm$ focal length double-pass triplet lens was designed which is able to achieve close to diffraction limited performance across the entire field and wavelength regime of interest ($400nm$-$900nm$). The lens employs a cemented surface to maximise throughput and two planar surface to increase manufacturability and ease of mounting. The lens system was tested in a spectrometer model and found to perform as required.

With an applicable design reached, the tolerances for the manufacture of the lens

were set and tested. A set of attainable tolerances were found that ensure that all possible manufactured lenses within these tolerances would perform as required, with near nominal performance. With this, the lens system is now out for procurement.

The 'Spectrometer Design Toolkit' has proven its worth and further development could improve its accuracy, although this is not necessary for its intended purpose. A GUI would increase its usability and ease of user interpretation.

Future Work

With the availability of further resources, the compact, low-cost, replicable, high-resolution spectrometer proof-of-concept, QMSPEC, could be developed into a fully functioning instrument. This study has proven that such an instrument is possible. I would like to work further to finalise the sub-systems and maximise instrument stability by producing a temperature and pressure control system. With this in place, I expect to be able to produce an accurate and efficient radial velocity instrument at a fraction of the cost of its contemporaries. This would open up a number of astronomical science cases to smaller observatories, such as stellar activity studies, galactic evolution surveys, investigation of the chemical composition of the interstellar medium and of course Doppler spectroscopy of exoplanetary systems (Faber et al., 2003; Kintziger et al., 2018; Struve, 1952). Furthermore, with minor alterations to the current prototype QMSPEC instrument, it would be possible to accommodate a multiplexing mode; where multiple (3-4) separate spectra from different fibres could be produced simultaneously by the same instrument. This would allow some level of integral field unit applications to be achieved with a single instrument, such as spatially resolving observed objects, observing two separate objects simultaneously in a survey application or increasing the sampling of a single PSF.

I plan to maintain my involvement in the NEREA concept proposal and its potential subsequent design stages and implementation. I have produced an upcoming publication outlining the current design concept and will continue to contribute to the instrument proposal process. This is an exciting concept, an instrument with the specifications of NEREA at the GTC, with its large 10m aperture, would greatly increase the number of investigatable planetary systems in our stellar neighbourhood and allow us to study the atmospheres of potentially up to 40 times the number of planets possible with current instrumentation. Principally, with further resources, I would re-design the current prototype's re-focusing camera lens to produce a system with comparable performance to the current design but with a lower number of optical elements to improve throughput efficiency.

7 Conclusion

As I continue to grow my spectrometer design experience, I will continue to add to and improve the 'Spectrometer Design Toolkit' software, ultimately bringing it to a condition where it is intuitive for anyone to use. With this achieved I would release it alongside a brief letter describing the theoretical methods that the model is applying.

Following successful procurement and implementation of the EXOhSPEC lens system, I would like to remain involved with the instrument and, in the short term, contribute to its testing during the upcoming planned guest instrument observing run at the Isaac Newton Telescope later this year. In the longer term, I plan to remain involved in the design of further iterations of the instrument.

In 2018, Bourdarot et al. (2018) unveiled a compact, high-resolution spectrometer prototype which, unlike most comparable systems, uses a virtually imaged phase array (VIPA) as the dispersion element. VIPAs are compact optical elements consisting of a rectangular cuboid piece of, for example, glass; such that two of the faces form parallel plates. A high reflectance coating ($\sim 100\%$) is applied to one face and the opposite face has a semi-reflective ($\sim 95\%$) coating. When light is injected into the VIPA, it will leave through the semi-reflective coating face and interfere via the phase difference introduced by internal reflection within the VIPA. VIPA's have a number of advantages over diffraction gratings. Primarily, where as a blazed diffraction grating would need to tilted to a large blaze angle to achieve the dispersion required for high resolving powers, necessitating a large and expensive diffraction grating, a VIPA can be produced which is able to achieve greater dispersion at a fraction of the size. In addition to being more compact, VIPA's are also simpler to manufacture than diffraction gratings. A VIPA capable of achieving dispersion and efficiency comparable to a £100k diffraction grating could be procured for on the order of £3,000 (Light Machinery, 2020). This allows an extremely compact, low-cost and high-resolution instrument to be produced. With this, the design of a VIPA based instrument is something that I believe would be fruitful. The primary issue with the QMSPEC in terms of both resolution and throughput is the diffraction grating, the low-cost gratings perform incredibly well for the cost of a few hundred pounds but they have limited us to achieving a maximum resolving power of $R = 60,000$. With a VIPA based system, high dispersion is achieved sufficiently easily, that achieving a resolving power of $R = 100,000$ with high efficiency is not an issue. The instrument discussed by Bourdarot et al. (2018) is able to achieve a resolving power of $R = 80,000$ in the H-band ($1.5\mu m - 1.75\mu m$) within an instrument footprint of $400mm \times 260mm$. Comparatively, QMSPEC is able to achieve a resolving power of $R = 60,000$ over a larger wave-band in the

VIS-NIR regime ($0.5\mu m - 1.0\mu m$) within a more compact instrument footprint of $300mm \times 150mm$. However, from the instrument layout displayed in Bourdarot et al. (2018), there are a number of ways in which the system could be made more compact. Furthermore, with alternative reflective coatings on the VIPA, the waveband of the instrument could be increased substantially. In regards to throughput, Bourdarot et al. (2017) demonstrate that a low-cost commercial VIPA can achieve a throughput of greater than 60%, this is a feat only achieved by high-end, highly machined blazed diffraction gratings. An equivalently priced commercial blazed diffraction grating may only achieve an efficiency of $10 - 20\%$. Another benefit to the design of a VIPA-based system is that as almost arbitrarily large dispersion is achievable, the optical performance of the rest of the optical system is not as critical. One could allow the resolution element size to grow substantially larger than that required by a grating based system without seeing a reduction in resolving power below $R = 100,000$. Thereby allowing the use of low-cost optics (as close to diffraction-limited spot performance is not required) or allowing the use of larger, higher throughput optical fibres than those applied by QMSPEC. Utilizing a VIPA as the high dispersion component in a spectrometer is something that I believe may revolutionise high-resolution spectroscopy, and allow the miniaturisation of efficient, high-resolution spectrographic systems.

Apart from large scale missions like the STIS on the Hubble Space Telescope or ACS-MIR on the ExoMars Trace Gas Orbiter, high-resolution spectroscopy in space is not commonplace (Woodgate et al., 1998; Trokhimovskiy et al., 2015). Furthermore, there are currently no space-based high-resolution spectrometers tailored to exoplanet science requirements. If an instrument like QMSPEC (which would fit within a 3U cubesat chassis) were connected to a space based telescope, it would be able to take stellar spectra at high resolving powers without the telluric lines from the Earth's atmosphere. This would increase the number of usable stellar lines, improving the SNR of the resultant CCF (or equivalent) produced when taking RV observations. This would allow systems to be studied that otherwise wouldn't be possible from an equivalently sized ground-based observatory. Furthermore, a space based observatory of this form would also allow higher SNR study of planetary atmospheres that have a similar composition to that of Earth's. In addition to looking outwards, there is a growing demand for looking inwards with Earth observation and climate study missions. Instruments are being developed for the space-based tracking of greenhouse gases. One example of this is NanoCarb, a compact Fourier transform spectrometers system specifically designed to study CO_2 and CH_4 under the Space CARBon Observatory (SCARBO) framework (Gousset et al., 2019).

7 Conclusion

The SCARBO framework is a study funded by the European Union's Horizon 2020 research and innovation programme to assess the feasibility of a small sat constellation in order to provide spatially resolved measurement of climate altering aerosols (European Union's Horizon 2020 Research and Innovation Programme, 2020). If a mission such as this applied an instrument like QMSPEC (but designed for a mid-IR waveband), instead of a fourier transform spectrometer, it would be able to detect and track a much larger number of molecules than just CO_2 and CH_4. It would also be capable of tracing, for example CO, H_2S and Methane; and if the waveband was increased to include either the optical or longer IR: O_2, SO_2, nitrogen, ozone, hydrogen halides and water would be detectable. This would greatly increase the use case of the satellite system, with applications in, for example, the detection of the spread of toxic gases after natural disasters; like volcanic eruptions. With multiplexing on a single instrument, this would allow spatial resolution to be achieved with an individual cube-sat. I am of the opinion that a compact, low-cost, high resolution spectrometer system like the one discussed in this thesis could provide a number of novel use cases in space based applications, from cube-sat systems to missions of greater scale.

As discussed previously in this thesis, Rimmer et al. (2018) suggest that for what is thought to be the necessary life forming prebiotic chemistry to occur (for life as we know it), liquid water must be present and sufficient UV radiation must be incident on the surface of the planet. This criteria is principally fulfilled for systems analogous to Earth-like exoplanets orbiting around Sun-like stars. Unfortunately, current spectroscopic and direct imaging instrumentation is limited to observing planet/star systems with a contrast ratio of down to 10^{-5}; where as Earth orbiting the Sun has a contrast ratio of 10^{-10}. To overcome this, Snellen et al. (2015) proposed an instrument which combines high dispersion spectroscopy (HDS) and high contrast imaging (HCI) to achieve the necessary contrast ratio of 10^{-10}. It achieves this by placing a fibre bundle at the focal plane of a high contrast imaging system, with each of the fibres connected to a high-resolution spectrometer system. The spectrometer system is then able to distinguish the planetary signal from residual starlight speckle left by the coronagraph of the high contrast imaging system. The cost (on the order of £1million) and size (comparable to a car) of high-resolution spectrometer systems was prohibitive to the design of such an instrument, as this instrument would require more than 100 of these such spectrographs. However with the advent of compact, low-cost and replicable high-resolution spectrometer systems, like QMSPEC, the cost of such an instrument is reduced from billions of pounds to several million pounds, which is comparable to a single conventional high-resolution spectrograph.

Haffert et al. (2018) outline a concept instrument, the 'Leiden Exoplanet Instrument' (LEXI), demonstrating this instrument concept as a pathfinder for future E-ELT instruments. As the high dispersion spectrograph for this instrument, they utilize a single mode fibre fed $R = 92,000$ spectrometer which operates in the $600nm - 800nm$ wavelength range; in a device footprint of $350mm \times 250mm$. Alongside QMSPEC, this cements that a HCI+HDS coupled instrument is feasible and of a sufficient technology readiness level for further larger scale study.

Jovanovic et al. (2017) discuss a project outline for a combined instrument at the Subaru Telescope. They propose coupling the AO system of SCExAO to the IRD spectrograph in the H-band. Similarly, they discuss using the IRD spectra to separate the residual stellar speckle left over by SCExAO. However, as only one spectrograph is available, the planet position must be known in order for the optical fibre to be placed correctly. Even with this caveat, this is an exciting, large scale test case for the coupling of HCI+HDS.

With systems like MUSE connected to the Adaptive Optics Facility (AOF) at the VLT demonstrating the effectiveness of IFU spectroscopy in the medium resolution regime, in addition to the studies aforementioned laying down the groundwork for coupled HCI+HDS, I believe that such a coupled instrument should be considered for phase A study as a common user instrument at the E-ELT (Bacon et al., 2010). High resolution spectroscopy is a photon limited observation. As such, we are currently limited in the systems that we can observe with acceptable signal to noise. With this, NEREA would greatly increase the number of observable systems utilising the GTC's 10m diameter collecting area over the conventional 3-4m class telescopes currently in use for this science. The E-ELT's almost 40m diameter collecting area would potentially increase the signal strength for a comparable exposure length at the GTC by 16 times. High resolution spectroscopy at the E-ELT will allow us to study fainter and further planetary systems with weaker signals. It will also enable studies of planetary atmospheres (through transits, reflected light or planetary thermal emission) that are currently beyond the noise limit. With this, we can begin to search for planets with habitable atmospheres and, more importantly, signs of biomarkers.

As it stands, the E-ELT will not have a high-resolution spectrograph capable of achieving this science initially. In my opinion this is a great fallacy, a HCI+HDS instrument should be considered for phase 1. This instrument could be small scale initially, employing a few spectrographs at the centre of the PSF where most of the signal is strongest. This could then be expanded easily by adding larger fibre bundles and more replicable spectrometers as the concept is verified. As we have discussed in chapter 3, even a single compact spectrometer like QMSPEC could be efficiently

coupled to the E-ELT. With a project of the E-ELT's scale, there is no reason such a crucial instrument should not be considered. This is even more prudent when there are available options that could be rapidly developed on budgetary scales that are negligible to the overall project.

I also believe that direct imaging will have a promising future. Both of NASA's upcoming decadal mission concepts, HabEx and LUVOIR aim to directly image habitable planets by achieving the necessary contrast ratios of 10^{-10} (Martin et al., 2019; Pueyo et al., 2019). Whilst the TRL of this technology is up for debate, lab test-bed demonstrations applying hybrid lyot coronagraphs show promising results (Trauger et al., 2011; Seo et al., 2019).

Just as how the field of applications for low-cost, hand-held, low-resolution spectrometers has exploded in recent years with the advent of consumer friendly devices, I believe the same could occur with a consumer low-cost, compact, high-resolution spectrometer. Consumer grade low-resolution spectrometer systems have seen applications in food testing, falsified medicine detection, low-resolution space-based spectroscopy and counterfeit alcohol identification; amongst many other use cases (Ellis et al., 2015; Wilson et al., 2017; Hausgen et al., 2015; Ellis et al., 2017). In addition to fulfilling these functions, a consumer high-resolution spectrometer could have applications such as the detection of trace gases in caves and mines, the identification of allergens in food and other substances, the detection of contraband materials at airports, in the field biological/chemical studies or, as discussed previously, pollutant tracking from a CubeSat.

Over the course of the PhD, a number of external academic and industry sources have shown interest in the compact, high-resolution spectrometer system. Within astronomy, we have had inquiries ranging from small-scale amateur telescope systems to large-scale observatories who are interested in acquiring one of the spectrometers. Beyond astronomy, representatives of chemical/pharmaceutical companies, such as GlaxoSmithKline, have shown interest in and see a use-case for the instrument. Now that the PhD is completed and we have a functioning prototype instrument, these opportunities are something that can be explored further.

Bibliography

3D People 2019, Design Guide, https://www.3dpeople.uk/design-guide

ATIK Cameras 2018, Atik 490EX Camera, https://www.atik-cameras.com/product/atik-490ex

Addison B., 2016, Spin-orbit alignments for three more WASP planets, https://wasp-planets.net/2016/03/21/spin-orbit-alignments-for-three-more-wasp-planets/

Agol E., Steffen J., Sari R., Clarkson W., 2005, Monthly Notices of the Royal Astronomical Society, 359, 567

Ahi K., Anwar M., 2016, in Anwar M. F., Crowe T. W., Manzur T., eds, Vol. 9856, Terahertz Physics, Devices, and Systems X: Advanced Applications in Industry and Defense. SPIE, pp 57 – 74, doi:10.1117/12.2228680, https://doi.org/10.1117/12.2228680

Anglada-Escudé G., Butler R. P., 2012, The Astrophysical Journal Supplement Series, 200, 15

Armitage P. J., 2018, A Brief Overview of Planet Formation. Springer International Publishing, Cham, pp 2185–2203, doi:10.1007/978-3-319-55333-7˙135, https://doi.org/10.1007/978-3-319-55333-7_135

Australian Telescope National Facility 2018, Adaptive Optics, https://www.atnf.csiro.au/outreach/education/senior/astrophysics/adaptive_optics.html

Auvergne et al., 2009, A&A, 506, 411

Avila G., 2012, in McLean I. S., Ramsay S. K., Takami H., eds, Vol. 8446, Ground-based and Airborne Instrumentation for Astronomy IV. SPIE, pp 1437 – 1443, doi:10.1117/12.927447, https://doi.org/10.1117/12.927447

Babcock H. W., 1953, Publications of the Astronomical Society of the Pacific, 65, 229

Bacon R., et al., 2010, in McLean I. S., Ramsay S. K., Takami H., eds, Vol. 7735, Ground-based and Airborne Instrumentation for Astronomy III. SPIE, pp 131 – 139, doi:10.1117/12.856027, https://doi.org/10.1117/12.856027

Bibliography

Baker C., Anglada-Escudé G., Jones H., Martin W., 2019, in Shaklan S. B., ed., Vol. 11117, Techniques and Instrumentation for Detection of Exoplanets IX. SPIE, pp 511 – 530, doi:10.1117/12.2529290, https://doi.org/10.1117/12.2529290

Baranne A., Mayor M., Poncet J., 1979, Vistas in Astronomy, 23, 279

Baranne A., et al., 1996, A&AS, 119, 373

Baudrand J., Walker G. A. H., 2001, Publications of the Astronomical Society of the Pacific, 113, 851

Beaulieu J.-P., et al., 2006, Nature, 439, 437

Birkby J. L., 2018, arXiv e-prints, p. arXiv:1806.04617

Birkby J., de Kok R., Brogi M., Schwarz H., Albrecht S., de Mooij E., Snellen I., 2013a, The Messenger, 154, 57

Birkby J. L., de Kok R. J., Brogi M., de Mooij E. J. W., Schwarz H., Albrecht S., Snellen I. A. G., 2013b, Monthly Notices of the Royal Astronomical Society: Letters, 436, L35

Birkby J. L., de Kok R. J., Brogi M., Schwarz H., Snellen I. A. G., 2017, The Astronomical Journal, 153, 138

Bisque 2020, SkyX Software, https://www.bisque.com/product/theskyx-pro/

Bond I. A., et al., 2004, The Astrophysical Journal, 606, L155

Bond I. A., et al., 2017, Monthly Notices of the Royal Astronomical Society, 469, 2434

Borucki W. J., Summers A. L., 1984, Icarus, 58, 121

Borucki W. J., et al., 2010, Science, 327, 977

Bourdarot G., Coarer E. L., Alecian E., Rabou P., Bonfils X., 2017, in Cugny B., Karafolas N., Sodnik Z., eds, Vol. 10562, International Conference on Space Optics — ICSO 2016. SPIE, pp 684 – 692, doi:10.1117/12.2296210, https://doi.org/10.1117/12.2296210

Bourdarot G., et al., 2018, in Evans C. J., Simard L., Takami H., eds, Vol. 10702, Ground-based and Airborne Instrumentation for Astronomy VII. SPIE, pp 1798 – 1809, doi:10.1117/12.2311696, https://doi.org/10.1117/12.2311696

Bowler B. P., 2016, Publications of the Astronomical Society of the Pacific, 128, 102001

Brogan C. L., et al., 2015, The Astrophysical Journal, 808, L3

Brogi M., Line M. R., 2019, The Astronomical Journal, 157, 114

Bibliography

Brogi M., Snellen I. A. G., de Kok R. J., Albrecht S., Birkby J., de Mooij E. J. W., 2012, Nature, 486, 502

Brown R. A., 2009, The Astrophysical Journal, 702, 1237

Burdanov A., Delrez L., Gillon M., Jehin E., 2018, SPECULOOS Exoplanet Search and Its Prototype on TRAPPIST. Springer International Publishing, Cham, pp 1007–1023, doi:10.1007/978-3-319-55333-7˙130, https://doi.org/10.1007/978-3-319-55333-7_130

Cabot S. H. C., Madhusudhan N., Welbanks L., Piette A., Gandhi S., 2020, Monthly Notices of the Royal Astronomical Society, 494, 363

Cameron A. C., Horne K., Penny A., James D., 1999, Nature, 402, 751–755

Chauvin Lagrange, A.-M. Dumas, C. Zuckerman, B. Mouillet, D. Song, I. Beuzit, J.-L. Lowrance, P. 2004, A&A, 425, L29

Chauvin Lagrange, A.-M. Dumas, C. Zuckerman, B. Mouillet, D. Song, I. Beuzit, J.-L. Lowrance, P. 2005, A&A, 438, L25

Chaves J., 2017, Introduction to Nonimaging Optics. CRC Press, https://books.google.co.uk/books?id=e11ECgAAQBAJ

Chazelas B., Pepe F., Wildi F., Bouchy F., Perruchot S., Avila G., 2010, in Atad-Ettedgui E., Lemke D., eds, Vol. 7739, Modern Technologies in Space- and Ground-based Telescopes and Instrumentation. SPIE, pp 1458 – 1466, doi:10.1117/12.856874, https://doi.org/10.1117/12.856874

Churchill C., 2009, Spectrographs, NMSU Lectures, http://astronomy.nmsu.edu/cwc/Teaching/ASTR605/Lectures/spectra.pdf

Crane J. D., Shectman S. A., Butler R. P., 2006, in McLean I. S., Iye M., eds, Vol. 6269, Ground-based and Airborne Instrumentation for Astronomy. SPIE, pp 972 – 982, doi:10.1117/12.672339, https://doi.org/10.1117/12.672339

Cuevas S., et al., 2006, New Astronomy Reviews, 50, 389

Davies M. B., Adams F. C., Armitage P., Chambers J., Ford E., Morbidelli A., Raymond S. N., Veras D., 2014, in Beuther H., Klessen R. S., Dullemond C. P., Henning T., eds, Protostars and Planets VI. p. 787 (arXiv:1311.6816), doi:10.2458/azu˙uapress˙9780816531240-ch034

Deeg H. J., Alonso R., 2018, Transit Photometry as an Exoplanet Discovery Method. Springer International Publishing, Cham, pp 633–657, doi:10.1007/978-3-319-55333-7˙117, https://doi.org/10.1007/978-3-319-55333-7_117

Deibert E. K., de Mooij E. J. W., Jayawardhana R., Fortney J. J., Brogi M., Rustamkulov Z., Tamura M., 2019, The Astronomical Journal, 157, 58

Bibliography

Dekker H., D'Odorico S., Kaufer A., Delabre B., Kotzlowski H., 2000, in Iye M., Moorwood A. F. M., eds, Vol. 4008, Optical and IR Telescope Instrumentation and Detectors. SPIE, pp 534 – 545, doi:10.1117/12.395512, https://doi.org/10.1117/12.395512

Dumusque 2018, A&A, 620, A47

Eggenberger Udry 2010, EAS Publications Series, 41, 27

Ehrenreich D., et al., 2020, Nature

Ellis D. I., Muhamadali H., Haughey S. A., Elliott C. T., Goodacre R., 2015, Anal. Methods, 7, 9401

Ellis D. I., Eccles R., Xu Y., Griffen J., Muhamadali H., Matousek P., Goodall I., Goodacre R., 2017, Scientific Reports, 7, 12082

European Union's Horizon 2020 Research and Innovation Programme 2020, SCARBO, https://scarbo-h2020.eu/

Faber S. M., et al., 2003, in Iye M., Moorwood A. F. M., eds, Vol. 4841, Instrument Design and Performance for Optical/Infrared Ground-based Telescopes. SPIE, pp 1657 – 1669, doi:10.1117/12.460346, https://doi.org/10.1117/12.460346

Fischer D. A., et al., 2016, Publications of the Astronomical Society of the Pacific, 128, 066001

Foo G., Palacios D. M., Swartzlander G. A., 2005, Opt. Lett., 30, 3308

Fressin F., et al., 2013, The Astrophysical Journal, 766, 81

Gaudi B. S., Winn J. N., 2007, The Astrophysical Journal, 655, 550

Gillon M., et al., 2017, Nature, 542, 456

Goldreich P., Tremaine S., 1979, ApJ, 233, 857

Gousset S., Croizé L., Le Coarer E., Ferrec Y., Brooker L., 2019, in . p. 111803Q (arXiv:1907.05617), doi:10.1117/12.2536053

Griffin R., 1973, Monthly Notices of the Royal Astronomical Society, 162, 243

Grimm S. L., et al., 2018, A&A, 613, A68

Haffert S. Y., et al., 2018, in Close L. M., Schreiber L., Schmidt D., eds, Vol. 10703, Adaptive Optics Systems VI. SPIE, pp 692 – 702, doi:10.1117/12.2314199, https://doi.org/10.1117/12.2314199

Hartmann J., 1900, magazine for instrument science. No. v. 20, Springer, https://books.google.co.uk/books?id=dV_HjQqYruUC

Hausgen P. E., Bradshaw G. K., Wilt D., Jenkins P. P., 2015, in 2015 IEEE 42nd Photovoltaic Specialist Conference (PVSC). pp 1–6, doi:10.1109/PVSC.2015.7355862

Holman M., Murray N., 2005, Science (New York, N.Y.), 307, 1288

Hsu D. C., Ford E. B., Ragozzine D., Ashby K., 2019, The Astronomical Journal, 158, 109

Joergens Müller, A. Reffert, S. 2010, A&A, 521, A24

Jovanovic N., et al., 2017, arXiv e-prints, p. arXiv:1712.07762

Kane S. R., Ciardi D. R., Gelino D. M., von Braun K., 2012, Monthly Notices of the Royal Astronomical Society, 425, 757

Kant I., Johnston I., Crowe I., 1755, Universal Natural History and Theory of the Heavens, Or, an Essay on the Constitution and the Mechanical Origin of the Entire Structure of the Universe Based on Newtonian Principles. Richer Resources Publications, https://books.google.co.uk/books?id=3eFIPgAACAAJ

Keles E., et al., 2020, Monthly Notices of the Royal Astronomical Society, 498, 1023

Kingsview Optical 2019, Kingsview Optical, Optics Manufacturer, https://www.kingsviewoptical.com

Kintziger C., Rauw G., Desselle R., Rochus P., Loicq J., 2018, in Evans C. J., Simard L., Takami H., eds, Vol. 10702, Ground-based and Airborne Instrumentation for Astronomy VII. SPIE, pp 1490 – 1509, doi:10.1117/12.2312586, https://doi.org/10.1117/12.2312586

Koch D., 2004, in Norris R., Stootman F., eds, IAU Symposium Vol. 213, Bioastronomy 2002: Life Among the Stars. p. 85

Koch D. G., et al., 2004, in Mather J. C., ed., Vol. 5487, Optical, Infrared, and Millimeter Space Telescopes. SPIE, pp 1491 – 1500, doi:10.1117/12.552346, https://doi.org/10.1117/12.552346

Konidaris N., 2014, Classical and β Anamorphism in Spectrographs, https://nickkonidaris.com/2014/10/17/anamorphic-factor/

Kreidberg L., 2017, Exoplanet Atmosphere Measurements from Transmission Spectroscopy and Other Planet Star Combined Light Observations. Springer International Publishing, Cham, pp 1–23, doi:10.1007/978-3-319-30648-3˙100-1, https://doi.org/10.1007/978-3-319-30648-3_100-1

Lada C. J., 2006, The Astrophysical Journal, 640, L63

Leigh C., Cameron A. C., Horne K., Penny A., James D., 2003, Monthly Notices of the Royal Astronomical Society, 344, 1271

Lessard L., 2011, PhD thesis

Lhospice E., et al., 2019, in Shaklan S. B., ed., Vol. 11117, Techniques and Instrumentation for Detection of Exoplanets IX. SPIE, pp 312 – 326, doi:10.1117/12.2529044, https://doi.org/10.1117/12.2529044

Light Machinery 2020, VIPAS Catalogue, https://lightmachinery.com/optics-catalog/vipas/

Lovis C., Fischer D., 2010, Radial Velocity Techniques for Exoplanets. pp 27–53

Lyot M. B., 1939, Monthly Notices of the Royal Astronomical Society, 99, 580

Marcy G. W., Butler R. P., 1992, Publications of the Astronomical Society of the Pacific, 104, 270

Martin S., Kuan G., Stern D., Scowen P., Krist J., Mawet D., Ruane G., 2019, in Shaklan S. B., ed., Vol. 11117, Techniques and Instrumentation for Detection of Exoplanets IX. SPIE, pp 66 – 84, doi:10.1117/12.2530737, https://doi.org/10.1117/12.2530737

Martins J. H. C., Figueira P., Santos N. C., Lovis C., 2013, Monthly Notices of the Royal Astronomical Society, 436, 1215

Martins et al., 2015, A&A, 576, A134

Martins J. H. C., Santos N. C., Figueira P., Melo C., 2016, Origins of Life and Evolution of Biospheres, 46, 487

Mayor M., Queloz D., 1995, Nature, 378, 355

Mayor M., Lovis C., Santos N. C., 2014, Nature, 513, 328

McLaughlin D. B., 1924, Popular Astronomy, 32, 558

Morton T. D., Bryson S. T., Coughlin J. L., Rowe J. F., Ravichandran G., Petigura E. A., Haas M. R., Batalha N. M., 2016, The Astrophysical Journal, 822, 86

Mungan C. E., 2001, Angle of Minimum Deviation through a Prism, USNA, https://www.usna.edu/Users/physics/mungan/_files/documents/Scholarship/MinimumDeviation.pdf

Muterspaugh M. W., et al., 2010, The Astronomical Journal, 140, 1657

Mégevand D., et al., 2014, in Ramsay S. K., McLean I. S., Takami H., eds, Vol. 9147, Ground-based and Airborne Instrumentation for Astronomy V. SPIE, pp 553 – 570, doi:10.1117/12.2055816, https://doi.org/10.1117/12.2055816

NASA Exoplanet Science Institute 2020, NASA Exoplanet Archive, https://exoplanetarchive.ipac.caltech.edu/exoplanetplots/

Bibliography

Nagaoka H., Mishima T., 1923, ApJ, 57, 92

Nave R., 2016, The Rayleigh Criterion, http://hyperphysics.phy-astr.gsu.edu/hbase/phyopt/Raylei.html

N'diaye M., Pueyo L., Soummer R., 2015, The Astrophysical Journal, 799, 225

Noll R. J., 1973, J. Opt. Soc. Am., 63, 1399

Norman I., 2015, A Practical Guide to Lens Aberrations and the Lonely Speck Aberration Test, https://www.lonelyspeck.com/a-practical-guide-to-lens-aberrations-and-the-lonely-speck-aberration-test/

Ohta Y., Taruya A., Suto Y., 2005, The Astrophysical Journal, 622, 1118

Pallé E., Osorio M. R. Z., Barrena R., Montañés-Rodríguez P., Martín E. L., 2009, Nature, 459, 814

Palmer C., 2014, Diffraction Grating Handbook (7th edition)

Pepe F., et al., 2000, in Iye M., Moorwood A. F. M., eds, Vol. 4008, Optical and IR Telescope Instrumentation and Detectors. SPIE, pp 582 – 592, doi:10.1117/12.395516, https://doi.org/10.1117/12.395516

Pepe Mayor, M. Galland, F. Naef, D. Queloz, D. Santos, N. C. Udry, S. Burnet, M. 2002, A&A, 388, 632

Pepe F. A., et al., 2010, in McLean I. S., Ramsay S. K., Takami H., eds, Vol. 7735, Ground-based and Airborne Instrumentation for Astronomy III. SPIE, pp 209 – 217, doi:10.1117/12.857122, https://doi.org/10.1117/12.857122

Pepe F., et al., 2014a, Astronomische Nachrichten, 335, 8

Pepe F., Ehrenreich D., Meyer M. R., 2014b, Nature, 513, 358

Perryman M., 2018, The Exoplanet Handbook. Cambridge University Press, https://books.google.co.uk/books?id=ngtmDwAAQBAJ

Perryman M., Hartman J., Bakos G. Á., Lindegren L., 2014, The Astrophysical Journal, 797, 14

Platt B. C., Shack R., 2001, Journal of Refractive Surgery, 17, 5

Pueyo L., et al., 2019, in Shaklan S. B., ed., Vol. 11117, Techniques and Instrumentation for Detection of Exoplanets IX. SPIE, pp 37 – 65, doi:10.1117/12.2530722, https://doi.org/10.1117/12.2530722

Queloz D., 1994, ELODIE, INTER-TACOS, http://www.obs-hp.fr/www/guide/elodie/manuser.html

Queloz D., Eggenberger A., Mayor M., Perrier C., Beuzit J. L., Naef D., Sivan J. P., Udry S., 2000, A&A, 359, L13

Bibliography

Quirrenbach A., et al., 2014, in Ramsay S. K., McLean I. S., Takami H., eds, Vol. 9147, Ground-based and Airborne Instrumentation for Astronomy V. SPIE, pp 531 – 542, doi:10.1117/12.2056453, https://doi.org/10.1117/12.2056453

Rajpaul V. M., Aigrain S., Buchhave L. A., 2020, Monthly Notices of the Royal Astronomical Society, 492, 3960

Ramsay S., et al., 2016, in Evans C. J., Simard L., Takami H., eds, Vol. 9908, Ground-based and Airborne Instrumentation for Astronomy VI. SPIE, pp 543 – 554, doi:10.1117/12.2232407, https://doi.org/10.1117/12.2232407

Redfield S., Endl M., Cochran W. D., Koesterke L., 2008, The Astrophysical Journal, 673, L87

Ricker G. R., et al., 2014, Journal of Astronomical Telescopes, Instruments, and Systems, 1, 1

Rimmer P. B., Xu J., Thompson S. J., Gillen E., Sutherland J. D., Queloz D., 2018, Science Advances, 4

Roques F., 2020, The Extrasolar Planets Encyclopaedia, http://exoplanet.eu/

Rossiter R. A., 1924, ApJ, 60, 15

Rowe J. F., et al., 2014, The Astrophysical Journal, 784, 45

Roy A., et al., 2020, The Astronomical Journal, 159, 161

Safronov V. S., 1972, Evolution of the protoplanetary cloud and formation of the earth and planets.

Schott AG 2011, Optical Glass Catalogue, https://www.schott.com/d/advanced_optics/094a6f8c-f648-45cd-a5fe-ca7df5474fcb/1.2/schott-optical-glass-pocket-catalog-europe-october-2011-eng.pdf

Schroeder D., 1999a, Astronomical Optics. Elsevier Science, https://books.google.co.uk/books?id=fu3650dUNPcC

Schroeder D., 1999b, Astronomical Optics. Elsevier Science, https://books.google.co.uk/books?id=fu3650dUNPcC

Schroeder D., 1999c, Astronomical Optics. Elsevier Science, https://books.google.co.uk/books?id=fu3650dUNPcC

Schroeder D., 1999d, Astronomical Optics. Elsevier Science, https://books.google.co.uk/books?id=fu3650dUNPcC

Schroeder D., 1999e, Astronomical Optics. Elsevier Science, https://books.google.co.uk/books?id=fu3650dUNPcC

Schweizer F., 1979, Publications of the Astronomical Society of the Pacific, 91, 149

Bibliography

Seager S., 2010, Exoplanet Atmospheres: Physical Processes. Princeton Series in Astrophysics, Princeton University Press, https://books.google.co.uk/books?id=XpaYJD7IE20C

Seager S., 2014, Proceedings of the National Academy of Sciences of the United States of America, 111, 12634

Seo B.-J., et al., 2019, in Shaklan S. B., ed., Vol. 11117, Techniques and Instrumentation for Detection of Exoplanets IX. SPIE, pp 599 – 609, doi:10.1117/12.2530033, https://doi.org/10.1117/12.2530033

Snellen et al., 2015, A&A, 576, A59

Snik F., et al., 2018, in Navarro R., Geyl R., eds, Vol. 10706, Advances in Optical and Mechanical Technologies for Telescopes and Instrumentation III. SPIE, pp 741 – 755, doi:10.1117/12.2313957, https://doi.org/10.1117/12.2313957

Spanò P., et al., 2010, in McLean I. S., Ramsay S. K., Takami H., eds, Vol. 7735, Ground-based and Airborne Instrumentation for Astronomy III. SPIE, pp 274 – 283, doi:10.1117/12.858096, https://doi.org/10.1117/12.858096

Stefánsson G. K., et al., 2016, in Evans C. J., Simard L., Takami H., eds, Vol. 9908, Ground-based and Airborne Instrumentation for Astronomy VI. SPIE, pp 2108 – 2116, doi:10.1117/12.2233443, https://doi.org/10.1117/12.2233443

Struve O., 1952, The Observatory, 72, 199

TLS Tautenburg 2020, Karl Schwarzschild Observatory, http://www.tls-tautenburg.de/TLS/index.php?id=31

Taylor S. F., 2019, , 51, 179

Teledyne Scientific and Imaging 2019, HAWAII-4RG, http://www.teledyne-si.com/products-and-services/imaging-sensors/hawaii-4rg

Thompson S. J., et al., 2016, in Evans C. J., Simard L., Takami H., eds, Vol. 9908, Ground-based and Airborne Instrumentation for Astronomy VI. SPIE, pp 1949 – 1961, doi:10.1117/12.2232111, https://doi.org/10.1117/12.2232111

Traub W. A., Oppenheimer B. R., 2010, University of Arizona Press, pp 111–156

Trauger J., Moody D., Gordon B., Krist J., Mawet D., 2011, in Shaklan S., ed., Vol. 8151, Techniques and Instrumentation for Detection of Exoplanets V. SPIE, pp 195 – 204, doi:10.1117/12.895032, https://doi.org/10.1117/12.895032

Trokhimovskiy A., et al., 2015, in Scholl M. S., Páez G., eds, Vol. 9608, Infrared Remote Sensing and Instrumentation XXIII. SPIE, pp 55 – 61, doi:10.1117/12.2190359, https://doi.org/10.1117/12.2190359

Udry S., Fischer D., Queloz D., 2007, in Reipurth B., Jewitt D., Keil K., eds, Protostars and Planets V. p. 685

Bibliography

Vanderburg A., 2020, Transit Light Curve Tutorial, `https://www.cfa.harvard.edu/~avanderb/tutorial/tutorial.html`

Welford W., 1986a, Aberrations of Optical Systems. Series in Optics and Optoelectronics, Taylor & Francis, `https://books.google.co.uk/books?id=UTRem7YLM_kC`

Welford W., 1986b, Aberrations of Optical Systems. Series in Optics and Optoelectronics, Taylor & Francis, `https://books.google.co.uk/books?id=UTRem7YLM_kC`

Welford W., 1986c, Aberrations of Optical Systems. Series in Optics and Optoelectronics, Taylor & Francis, `https://books.google.co.uk/books?id=UTRem7YLM_kC`

Wheatley P. J., et al., 2017, Monthly Notices of the Royal Astronomical Society, 475, 4476

Wiedemann G., 2000, in Bergeron J., ed., Vol. 4005, Discoveries and Research Prospects from 8- to 10-Meter-Class Telescopes. SPIE, pp 260 – 262, doi:10.1117/12.390150, `https://doi.org/10.1117/12.390150`

Wildi F., et al., 2017, in Shaklan S., ed., Vol. 10400, Techniques and Instrumentation for Detection of Exoplanets VIII. SPIE, pp 321 – 335, doi:10.1117/12.2275660, `https://doi.org/10.1117/12.2275660`

Wilson B. K., Kaur H., Allan E. L., Lozama A., Bell D., 2017, The American Journal of Tropical Medicine and Hygiene, 96, 1117

Wolszczan A., Frail D. A., 1992, Nature, 355, 145

Woodgate B. E., et al., 1998, Publications of the Astronomical Society of the Pacific, 110, 1183

Wyttenbach et al., 2017, A&A, 602, A36

Youdin A. N., Goodman J., 2005, The Astrophysical Journal, 620, 459

Žák J., Kabáth P., Boffin H. M. J., Ivanov V. D., Skarka M., 2019, The Astronomical Journal, 158, 120

Zechmeister Anglada-Escudé, G. Reiners, A. 2014, A&A, 561, A59

Zeng L., et al., 2019, Proceedings of the National Academy of Sciences, 116, 9723

Zhang Snellen, I. A. G. Mollière, P. Alonso-Floriano, F. J. Webb, R. K. Brogi, M. Wyttenbach, A. 2020, A&A, 641, A161

Zucker S., 2007, Observations of extrasolar planetary systems. Cambridge University Press, p. 3–20, doi:10.1017/CBO9780511536120.002

Bibliography

de Kok Birkby, J. Brogi, M. Schwarz, H. Albrecht, S. de Mooij, E. J. W. Snellen, I. A. G. 2014, A&A, 561, A150

van de Kamp P., 1963, AJ, 68, 515

List of Figures

List of Tables